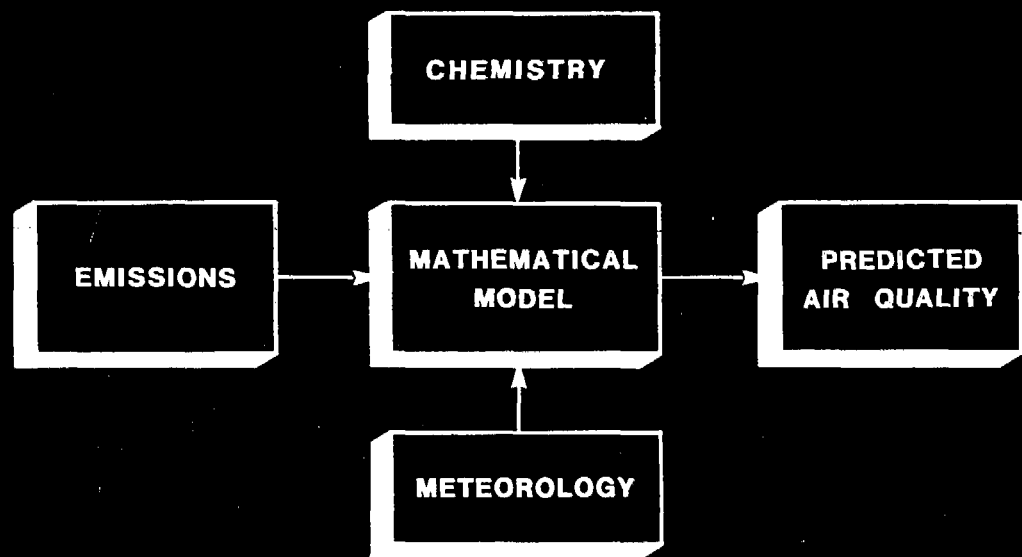




# MATHEMATICAL MODELING OF PHOTOCHEMICAL AIR POLLUTION

**GREGORY J. McRAE**  
**WILLIAM R. GOODIN**  
**JOHN H. SEINFELD**



**ENVIRONMENTAL QUALITY LABORATORY**  
**California Institute of Technology**  
**Pasadena, California 91125**



MATHEMATICAL MODELING OF PHOTOCHEMICAL AIR POLLUTION

Gregory J. McRae  
William R. Goodin  
John H. Seinfeld

Environmental Quality Laboratory  
California Institute of Technology  
Pasadena, California 91125

Final Report to the  
STATE OF CALIFORNIA AIR RESOURCES BOARD  
in

Completion of Research Under  
ARB Contract Nos. A5-046-87 and A7-187-30

EQL Report No. 18

27 April 1982

Copyright © by  
GREGORY JOHN MCRAE 1981

Dum Spiro Sperum

... While I breathe I hope

Hippocrates

## ACKNOWLEDGEMENTS

Completion of this research project would not have been possible without the assistance, advice and cooperation of a great number of individuals and organizations. Unfortunately it is not feasible to adequately acknowledge all the unique contributions and so, to those involved, the authors offer their sincere gratitude. There are however, some people who deserve special mention. Dr. John Seinfeld, the project supervisor and faculty advisor to Gregory J. McRae, has been a major source of inspiration. His scientific insights, thoughtful critiques and practical support have been invaluable.

This work was carried out under the auspices of the Environmental Quality Laboratory. The enthusiastic support of its Director, Dr. Norman H. Brooks, and the technical contributions of: Glen Cass, James Tilden, Shohreh Gharib and Pamela McMurry are truly appreciated. The superb secretarial work of Patricia Houseworth and Carol Marr, together with the graphics executed by Philip Dubé, greatly facilitated the preparation of this manuscript. Other staff members, both past and present, who have assisted with the report production include: Theresa Fall, Mary Ann Gray, Jeri Lucas, Dennis Petticoffer and Patricia Rankin.

Some sections of the report are the results of collaborative studies involving other investigators. The objective analysis procedures and numerical analysis techniques were developed jointly with Dr. William Goodin. The formulation, testing and sensitivity analysis

of the photochemical reaction mechanism was a cooperative venture that involved members of the Chemical Engineering Department: Dr. John Seinfeld, Stan Sander, Andrew Falls and Matsato Koda. Many staff members of the South Coast Air Quality Management District (SCAQMD) provided valuable assistance in compiling the needed emissions, air quality and meteorological data.

The California Air Resources Board Research Division, its chief Dr. John Holmes, and the Air Quality Modeling Section: Andrew Ranzieri, Paul Allen, Praveen Amar, Marna Johns, Kit Wagner and Timothy Woody have contributed immeasurably to the success of this venture. Financial support for the work was provided by the California Air Resources Board contracts A5-046-87 and A7-187-30\*. Additional funding was met by a Department of Energy Institutional Grant EY-76-G-03-1035. The first author was sustained by Graduate Research Assistantships and Fellowships financed by grants and gifts to the Environmental Quality Laboratory.

---

\* A requirement of these contracts is that the following disclaimer be inserted. "The statements and conclusions in this report are those of the Contractor and not necessarily those of the State Air Resources Board. The mention of commercial products, their source, or their use in connection with material reported herein is not to be construed as either an actual or implied endorsement of such products."

## TABLE OF CONTENTS

ACKNOWLEDGEMENTS	iv
ABSTRACT	vi
LIST OF FIGURES	
LIST OF TABLES	
CHAPTER 1 INTRODUCTION	
1.1 Thesis	1
1.2 Photochemical Air Pollution	1
1.3 Modeling Photochemical Air Quality	2
1.4 The Atmospheric Diffusion Equation	7
1.5 Structure of This Research	12
CHAPTER 2 FORMULATION OF AN URBAN SCALE AIRSHED MODEL	
2.1 Introduction	15
2.2 Species Continuity Equation	15
2.3 Decoupling Species and Carrier Fluid Equations	16
2.4 Turbulent Flows	20
2.5 The Turbulent Closure Problem	22
2.6 Eddy Diffusivities	25
2.7 Effect of Turbulence on Chemistry	26
2.8 The Atmospheric Diffusion Equation	31
2.9 Vertical Extent of the Airshed Boundaries	35

## TABLE OF CONTENTS (Continued)

2.10	Initial and Boundary Conditions	41
2.11	Validity and Accuracy of the Atmospheric Diffusion Equation	43
2.12	Simplified Forms of the Atmospheric Diffusion Equation	49
2.13	Conclusions	60
CHAPTER 3 OBJECTIVE ANALYSIS PROCEDURES		
3.1	Introduction	63
3.2	A Comparison of Interpolation Methods for Sparse Data: Application to Wind and Concentration Fields (Paper)	64
3.3	Weighted Interpolation Procedures	76
3.4	Generation of Triangulated Computational Domains	81
3.5	Polynomial Interpolation Over Triangles	88
3.6	Generation of Three-dimensional Wind Flow Fields	92
3.7	An Objective Analysis Technique for Constructing Three-Dimensional Urban-Scale Wind Fields (Paper)	95
3.8	Extensions of the Wind Field Generation Procedure to Incorporate the Effects of Surface Roughness	107
3.9	Solution of the Poisson Equation	114
3.10	Trajectory Integration Procedure	125
3.11	Conclusions	130
CHAPTER 4 TURBULENT DIFFUSION COEFFICIENTS		
4.1	Introduction	132
4.2	Turbulent Diffusion in the Atmosphere	132
4.3	Turbulent Transport Parameters	135

## TABLE OF CONTENTS (Continued)

4.4	Estimation of the Monin-Obukhov Length	137
4.5	Surface Roughness Estimation	140
4.6	Determination of the Friction Velocity $u_*$	144
4.7	Vertical Diffusivity Profile for Unstable Conditions	145
4.8	Vertical Diffusivity Profile for Neutral Conditions	156
4.9	Vertical Diffusivity Profile for Stable Conditions	161
4.10	Horizontal Eddy Diffusion Coefficients	165
4.11	Application and Validity of the Diffusion Coefficients	172
4.12	Conclusions	174
CHAPTER 5 CONVECTIVE DOWN MIXING OF PLUMES IN A COASTAL ENVIRONMENT		
5.1	Introduction	176
5.2	Description of Field Experiment	176
5.3	Vertical Mixing Over the Ocean	180
5.4	Mixing Times Under Convective Conditions	182
5.5	Eddy Diffusion Coefficients	186
5.6	Conclusions	186
CHAPTER 6 SURFACE DEPOSITION OF POLLUTANT MATERIAL		
6.1	Introduction	189
6.2	Deposition in the Constant Flux Layer	190
6.3	Eddy Diffusion of Momentum and Scalar Contaminants in the Surface Layer	193
6.4	Upper Limit Deposition Model	195

## TABLE OF CONTENTS (Continued)

6.5	Application of Deposition Model	197
6.6	Experimental Methods for Determining Deposition Velocities	207
6.7	Literature Survey of Deposition Velocity Measurements	213
6.8	Conclusions	215
CHAPTER 7 TREATMENT OF POINT AND AREA SOURCE EMISSIONS		
7.1	Introduction	219
7.2	Point and Area Source Emissions	219
7.3	Effective Release Height for Emissions	225
7.4	Plume Rise and Effective Stack Height	228
7.5	Plume Penetration into Elevated Stable Layers	232
7.6	Treatment of Elevated Point Sources	238
7.7	Plume Dispersion Parameters	244
7.8	Near Source Plume Chemistry	257
7.9	An Examination of the Contribution of Thermal NO Oxidation to the Formation of NO <sub>2</sub>	262
7.10	Conclusions	267
CHAPTER 8 PRACTICAL IMPLEMENTATION OF A PHOTOCHEMICAL REACTION MECHANISM WITHIN AN AIRSHED MODEL		
8.1	Introduction	268
8.2	Chemical Reaction Source Term and Mechanism Definition	270
8.3	Stoichiometric Coefficients for the Lumped Reactions	280
8.4	Specification of the Reaction Rate Constants	283
8.5	Lumped Hydrocarbon Reaction Rate Constants	288

## TABLE OF CONTENTS (Continued)

8.6	Photolytic Rate Constants	299
8.7	Calculation of Atmospheric Water Vapor Concentration	322
8.8	A Simple Box Model for Testing Photochemical Reaction Mechanisms	327
8.9	Numerical Solution Procedures	331
8.10	Smog Chamber Experiments	332
8.11	Species Conservation Constraints	346
8.12	Steady State Approximations for Ozone	347
8.13	Conclusions	352
CHAPTER 9 NUMERICAL SOLUTION OF THE ATMOSPHERIC DIFFUSION EQUATION FOR CHEMICALLY REACTING FLOWS		
9.1	Introduction	356
9.2	Governing Differential Equations	357
9.3	Coordinate Transformations	358
9.4	General Approach to the Numerical Solution of the Problem	360
9.5	Operator Splitting and the Method of Fractional Steps	362
9.6	Formulation of the Numerical Solution	366
9.7	Solution of the Advective Transport Step $T_a$	367
9.7.1	Preservation of Positive Quantities and Filtering Schemes	369
9.7.2	Conservation Properties of Different Advection Methods	376
9.8	Solution of the Diffusive Transport Step $T_d$ and Boundary Condition Treatment	380
9.9	Numerical Solution of the Chemical Kinetics	382
9.9.1	Selection of a Suitable Solution Scheme	384
9.9.2	Pseudo Steady State Approximations	385

## TABLE OF CONTENTS (Continued)

9.9.3	Asymptotic Integration Scheme	388
9.9.4	Implementation of Asymptotic Integration Scheme	392
9.10	Conclusions	393
CHAPTER 10 SENSITIVITY AND UNCERTAINTY ANALYSIS OF URBAN SCALE AIR POLLUTION MODELS		
10.1	Introduction	398
10.2	Methods for Sensitivity Analysis of Mathematical Models	399
10.3	Automatic Sensitivity Analysis of Kinetic Mechanisms (Paper)	417
10.4	Application of the Fourier Amplitude Sensitivity Test to Atmospheric Dispersion Problems	436
10.5	Sensitivity and Uncertainty of Reaction Mechanisms for Photochemical Air Pollution (Paper)	448
10.6	Sensitivity and Uncertainty of Reaction Mechanism for Photochemical Air Pollution	459
10.7	Conclusions	486
CHAPTER 11 EVALUATION OF MODEL PERFORMANCE		
11.1	Introduction	487
11.2	Performance Evaluation of the Airshed Model	487
11.3	Definition of the Region of Interest	492
11.4	The Episode of 26-28 June 1974 in the South Coast Air Basin	495
11.5	Meteorological Fields Needed for Model Evaluation	496
11.6	Emissions Inventory for the South Coast Air Basin	496
11.7	Assessment of the Accuracy of the Emissions Inventory	505
11.8	Initial and Boundary Conditions for Model Evaluation	520

## TABLE OF CONTENTS (Continued)

11.9	Location of the Airshed Boundaries of the Modeling Region	527
11.10	Summary	531
11.11	Predicted and Observed Concentrations for 26-27 June 1974	531
11.12	Statistical Analysis of Results	542
11.13	Distribution of Residuals	544
11.14	Predicted and Observed Concentration Maxima	544
11.15	Frequency Distributions	551
11.16	Observation Accuracy	551
11.17	Conclusions	554
CHAPTER 12 DIRECTION FOR FUTURE RESEARCH		
12.1	Introduction	555
12.2	Model Applications	555
12.3	Basic Research	562
12.4	Field and Experimental Measurements	564
12.5	Conclusions	567
CHAPTER 13 SUMMARY AND CONCLUSIONS		568
APPENDIX A KINETIC RATE EQUATIONS AND STEADY STATE APPROXIMATIONS		569
APPENDIX B A LINEAR FINITE ELEMENT SOLUTION OF THE CONSERVATIVE FORM OF THE ADVECTION EQUATION		
B.1	Introduction	576
B.2	Galerkin Formulation	577

## TABLE OF CONTENTS (Continued)

APPENDIX C	GRAPHICAL DISPLAY OF OBSERVED AND PREDICTED AIR QUALITY	583
	FOR THE TWO-DAY PERIOD 26-27 JUNE 1974	
References for Chapter 1		618
References for Chapter 2		622
References for Chapter 3		629
References for Chapter 4		633
References for Chapter 6		638
References for Chapter 7		641
References for Chapter 8		645
References for Chapter 10		651
References for Chapter 11		655
References for Chapter 12		660
References for Appendix B		661

## LIST OF FIGURES

<u>Figure</u>		<u>Page</u>
1.1	Ozone Isopleth Plot as a Function of the Precursor Concentration of Nitrogen Oxides ( $\text{NO}_x$ ) and Non-Methane Hydrocarbons. The Three Cases A, B, and C Indicate the Effect on Ozone, of Reducing Nitrogen Oxides	3
1.2	Schematic Structure of An Air Quality Model	4
1.3	Elements of a Mathematical Model for Relating Pollutant Emissions to Ambient Air Quality	6
1.4	Inputs to the Atmospheric Diffusion Equation and Processes Required for Numerical Solution. Numbers Represent Subsequent Chapters	14
2.1	Summary of the Steps Involved in Deriving the Atmospheric Diffusion Equation	34
2.2	Vertical Profiles of Ozone, Temperature and $b_{\text{scat}}$ over El Monte Airport (a) 1247 PDT and (b) 1656 PDT	37
2.3	Contours of Oxidant Concentrations (ppm) in the Vertical Cross Section from Santa Monica to Rialto-Miro, as Observed by Edinger (1973). (a) 0900 PDT, (b) 1200 PDT, (c) 1630 PDT 20 June 1970. Dotted curve denotes inversion base	38
2.4	Sequence of Events Leading to Entrainment of Ozone from Stable Layers Aloft into the Surface Well-Mixed Layer	40
2.5	Frequency Distribution of the Convective Mixing Time Scale Observed in the Los Angeles Marine Layer for Different Times	59
2.6	Simplified View of the Factors Involved in Relating Emissions to Atmospheric Air Quality. Numbers Refer to Subsequent Chapters	62
3.1	Some Examples of Different Weighting Functions of the Form $W(r/R)$ Where R is the Radius of Influence	77
3.2	Results of Using Different Exponents in the Weighting Function $W(r) = 1/r^a$ . The Three Cases Correspond to (a) $1/r$ , (b) $1/r^{10}$ and (c) $1/r^2$	79
3.3	The Dirichlet Tessellation (bold lines) and Delaunay Triangulation (fine lines) for a small scale Configuration	83

## LIST OF FIGURES (Continued)

<u>Figure</u>		<u>Page</u>
3.4	Procedure for Identifying Triangle Vertices	85
3.5	Triangulations of the Plane for Examples Presented in Section 3.3 (a) Air Quality Interpolation ( $n=53$ , $n_b=8$ , $n_t=96$ ) (b) Flow Over a Flat Plate ( $n=32$ , $n_b=5$ , $n_t=57$ )	86
3.6	An Example of a Linear Functional Variation Over Each Triangular Element	91
3.7	Summary of Approaches for Generating Wind Fields	94
3.8	Plot of Measured Data and Calculated Profiles for E Stability	110
3.9	Plot of Measured Data and Calculated Profiles for C-D Stability	111
3.10	Plot of Measured Data and Calculated Profiles for B-C Stability	112
3.11	Number of Iterations Required for Convergence of the Successive Over Relaxation (SOR) Method as a Function of $\omega$	123
3.12	Number of Iterations Required for Convergence of the Alternating Direction Implicit (ADI) Method as a Function of	124
3.13	Velocity at Current Position $P(x,y)$ is Determined as a Distance Weighted Mean of Wind Velocity at the Four Nearest Grid Points	127
3.14	Forward Air Parcel Surface Trajectories	128
3.15	Plot of Distance Between Actual and Perturbed Trajectories as a Function of Time	131
4.1	Structure of the Atmospheric Boundary Layer for Typical Daytime Conditions	134
4.2	Relationship between Pasquill Stability Classes, Surface Roughness, and Monin-Obukhov Length. (Solid Lines Define Stability Classes, Dotted Lines Used to Approximate Stability Region.)	138

## LIST OF FIGURES (Continued)

<u>Figure</u>		<u>Page</u>
4.3	Variation of Surface Roughness as a Function of Surface Type	143
4.4	Vertical Diffusivity Profiles for a Range of Stability Conditions Derived from Turbulence Model of Deardorff (1970)	150
4.5	Vertical Turbulent Diffusivity Profiles, Derived from Field Measurements and a Second Order Closure Calculation	152
4.6	Vertical Turbulent Diffusivity Profile Corresponding to (4.26)	154
4.7	Comparison of Diffusivity Profiles for Unstable Conditions ( $L = -30m$ , $u_* = 0.5m/sec$ , $Z_i = 500m$ )	157
4.8	Comparison of Various Models for Vertical Diffusivity Profile Under Neutral Conditions	160
4.9	Cross Wind Standard Deviation $\sigma_y$ as a Function of Travel Time. (Labeled Points Correspond to Examples in Table 4.4.)	170
4.10	Summary of Computational Procedure to Evaluate the Vertical Variation of $K_{zz}$	173
5.1	Sulfur Hexafluoride ( $SF_6$ ) Measurements Made on Board R/V Arcania 22 July 1977	177
5.2	Sulfur Hexafluoride ( $SF_6$ ) Measurements Made on Board R/V Arcania 24 July 1977	178
5.3	Intermittent Entrainment of Tracer Material by Convective Cells	181
5.4	Schematic Representation of (a) Fumigation Process and (b) Notation for Mixing Model	182
5.5	Distribution of Convective Mixing Times	185
5.6	Vertical Turbulent Diffusivity Profile for Unstable Conditions	187
6.1	Idealized Representation of the Airshed Surface	191
6.2	Variation of Surface Deposition Velocity $v_g$ as a Function of Atmospheric Stability and Pollutant $Sc/Pr$ Ratio	200

## LIST OF FIGURES (Continued)

<u>Figure</u>		<u>Page</u>
6.3	(a) Computational Cell Nomenclature	202
	(b) Discrete Approximation of Vertical Concentration Profile	202
6.4	Variation of Average Deposition Velocity as a Function of Atmospheric Stability and the Cell Height ( $z_o=0.01$ m, $u=2.5$ m/s, $v_g(z_r)=0.01$ m/s)	205
6.5	Time Evolution of a Typical Vertical Concentration Profile for an Air Parcel Traversing an Urban Airshed ( $\Delta z=20$ m, $z_o=0.01$ m, $z_r=10$ m, $v_g=0.01$ m/s)	208
6.6	(a) Diurnal Variation of Column Mass Fraction and Cell Average Deposition Velocity	209
	(b) Diurnal Variation of Vertical Diffusivity (Profiles are drawn every four hours)	209
7.1	Point and Area Source Representation	222
7.2	Selection Criteria for Ground Level and Elevated Sources	226
7.3	Limiting Plume Rise as a Function of the Buoyancy Flux Parameter F	231
7.4	Nomenclature for Plume Rise Calculations	234
7.5	Concentration Distributions Resulting from Direct Point Source Injection into the Computational Cells Indicated by Dots ( $u=v=2.2$ m/s, $t=1.6$ hrs, $\Delta x= y=3.2$ Km, $K_{xx}=K_{yy}=100$ m <sup>2</sup> /sec)	239
7.6	Plume Dispersion in Computational Grid	241
7.7	Same as Figure 7.6 except that the source injection is performed using the algorithm described in the text	243
7.8	Instantaneous Concentrations and the Effect of Temporal Averaging	245
7.9	Vertical Profile of $\sigma_w/w_*$ for Fully Convective Conditions	251
7.10	Values of $F_z$ for Elevated Releases and Near-Surface Releases During Convectively Unstable Conditions	253

## LIST OF FIGURES (Continued)

<u>Figure</u>		<u>Page</u>
7.11	Values for $F_z$ for Surface and Elevated Releases During Neutral and Stable Conditions	256
7.12	Variation of $\text{NO} + \text{NO} + \text{O}_2 \xrightarrow{k_4(T)} 2\text{NO}_2$ Reaction Rate Constant as a Function of Temperature	264
7.13	$\text{NO}_2$ Concentrations as a Function of Travel Time. Stack Conditions $T = 250^\circ\text{C}$ , $\text{O}_2 = 3\%$ , $\text{NO}_2(0)/\text{NO}_x = 0.05$ , $\text{NO}_2^b = 0.02$	266
8.1	Structure of the Falls and Seinfeld (1978) Photochemical Reaction Mechanism	279
8.2	General Ozone-Olefin Reaction Mechanism with Reaction Products as Proposed by Dodge (1978)	282
8.3	Conversion of Total Reactive Hydrocarbon Measurements, Expressed in ppbC, to an Equivalent Volumetric Concentration (ppbV) of Lumped Hydrocarbon Species. The Specific Example is for the Atmospheric Surrogate Smog Chamber Experiment SUR-119J	300
8.4	Photolysis Rate for $\text{NO}_2 + h\nu \xrightarrow{k} \text{NO} + \text{O}(^3\text{P})$ as a Function of Zenith Angle	308
8.5	Photolysis Rate for $\text{HONO} + h\nu \xrightarrow{k} \text{OH} + \text{NO}$ as a Function of Zenith Angle	308
8.6	Photolysis Rate for $\text{HNO}_3 + h\nu \xrightarrow{k} \text{OH} + \text{NO}_2$ as a Function of Zenith Angle	309
8.7	Photolysis Rate for $\text{O}_3 + h\nu \xrightarrow{k} \text{O}(^3\text{P}) + \text{O}_2$ as a Function of Zenith Angle	309
8.8	Photolysis Rate for $\text{O}_3 + h\nu \xrightarrow{k} \text{O}(^1\text{D}) + \text{O}_2$ as a Function of Zenith Angle	310
8.9	Photolysis Rate for $\text{O}_3 + h\nu \xrightarrow{k} \text{O}_2(^1\Delta) + \text{O}$ as a Function of Zenith Angle	310
8.10	Photolysis Rate for $\text{HCHO} + h\nu \xrightarrow{k} \text{H}_2 + \text{CO}$ as a Function of Zenith Angle	311
8.11	Photolysis Rate for $\text{HCHO} + h\nu \xrightarrow{k} 2\text{HO}_2 + \text{CO}$ as a Function of Zenith Angle	311

## LIST OF FIGURES (Continued)

<u>Figure</u>		<u>Page</u>
8.12	Photolysis Rate for $\text{H}_2\text{O}_2 + h\nu \xrightarrow{k} 2\text{OH}$ as a Function of Zenith Angle	312
8.13	Photolysis Rate for $\text{CH}_3\text{CHO} + h\nu \xrightarrow{k} \text{CH}_3 + \text{HO}_2 + \text{CO}$ as a Function of Zenith Angle	312
8.14	Photolysis Rate for $\text{CH}_3\text{CHO} + h\nu \xrightarrow{k} \text{CH}_4 + \text{CO}$ as a Function of Zenith Angle	313
8.15	Relationship between Latitude, Declination and Zenith Angles	318
8.16	Comparison of Calculated Diurnal Variation of $\text{NO}_2$ Photolysis Rate with Experimental Measurements of Zafonte et al. (1977)	316
8.17	Correlation between UV Radiometric Measurements and $\text{NO}_2$ Photolysis Rate.	320
8.18	Comparison of the Experimental (Circles), Theoretical (Dashed Line), and UV Scaled Theoretical (Solid Line) Diurnal Variation of the Photolytic Rate Constant for the Photolysis of $\text{NO}_2$ near Raleigh, N.C. ( $35.8^\circ\text{N}$ , $78.6^\circ\text{W}$ ) on April 28, 1975	321
8.19	Saturation Vapor Pressure as a Function of Ambient Temperature Evaluated Using the Polynomial Expression of Richards (1971)	325
8.20	Schematic Representation of a Simple Box Model	328
8.21	Predicted and Observed Concentration Profiles for Smog Chamber Experiment 119J	336
8.22	Predicted and Observed Concentration Profiles for Smog Chamber Experiment 121J	337
8.23	Predicted and Observed Concentration Profiles for Smog Chamber Experiment 126J	338
8.24	Predicted and Observed Concentration Profiles for Smog Chamber Experiment 132J	339
8.25	Predicted and Observed Concentration Profiles for Smog Chamber Experiment 133J	340
8.26	Predicted and Observed Concentration Profiles for Smog Chamber Experiment 134J	341

## LIST OF FIGURES (Continued)

<u>Figure</u>		<u>Page</u>
8.27	Predicted and Observed Concentration Profiles for Smog Chamber Experiment EC-237	342
8.28	Concentration Profiles for Major Nitrogen Containing Species for Smog Chamber Experiment 119J	348
8.29	Errors in the Photo Stationary State (PSSA) and Quasi Stationary State (QSSA) Approximations for Ozone in Smog Chamber Experiment SUR-119J	353
9.1	Results of Advection Tests Using Square Wave Form	371
9.2	Results of Advection Tests Using Triangular Wave Form	372
9.3	Results of Advection Tests Using Gaussian Wave Form	373
9.4	Application of Different Schemes to Maintain Concentration Positivity	374
9.5	Steps in the Application of the Discrete Noise Filter	376
9.6	Results of Crowley Test Problem for a Quarter and Complete Revolution of a Cone	379
9.7	Structure of the Algorithm for Solving the Advection-Diffusion Equation for Transport of Species $c_i$ in the $x$ -direction	381
9.8	Typical Eigenvalue Spectrum and Characteristic Reaction Times for the Falls and Seinfeld (1978) Photochemical Reaction Mechanism	384
10.1	Schematic Representation of the Parameter Space $\underline{k}$ and the Response Surface for State Variable $u_i(t;\underline{k})$	401
10.2	Linear and Nonlinear Sensitivity Analysis	403
10.3	Systematic Search Patterns of Parameter Space	413
10.4	Survey of Global Sensitivity Analysis Methods	415
10.5	Survey of Local Sensitivity Analysis Methods	416
10.6	Linearized Sensitivity Analysis of a Gaussian Plume Model (+ 5% Parameter Variation)	455

## LIST OF FIGURES (Continued)

<u>Figure</u>		<u>Page</u>
10.7	Fourier Amplitude Sensitivity Test (FAST) Analysis of a Gaussian Plume Model (+ 5% Parameter Variation)	456
10.8	Fourier Amplitude Sensitivity Test (FAST) Analysis of a Gaussian Plume Model (Factor of Two Parameter Variation)	457
11.1	Definition of the Origin of the Computational Grid System	493
11.2	Perspective View of the Topography of the South Coast Air Basin. (Vertical scale 1:10)	494
11.3	Typical Surface Wind Field Distribution for 27 June 1974 (a) Direction and Magnitudes at Monitoring Sites (b) Generated Ground Level Flow Field (c) Streamlines for Generated Flow Field	497
11.4	Mixing Height Distribution Above Sea Level (16:00 PST 27 June 1974)	498
11.5	Spatial and Diurnal Variations in Carbon Monoxide (CO) Emissions	506
11.6	Spatial and Diurnal Variations in Nitrogen Oxides (NO <sub>x</sub> ) Emissions	507
11.7	Spatial and Diurnal Variations in Reactive Hydrocarbons (RHC) Emissions	508
11.8	Simplified Structure of the Inventory Used in This Study	522
11.9	Location of Air Quality Monitoring Stations in the South Coast Air Basin	523
11.10	Measured Ozone Concentrations at Mt. Lee and Burbank During Episode of 26-27 June 1974	526
11.11	Illustration Procedure Used to Define Computational Region that Minimizes the Effects of Inflow Boundary Conditions	530
11.12	Definition of Computational Grid System for the South Coast Air Basin	532
11.13	Predicted and Observed Concentrations of (a) Ozone and (b) Nitrogen Dioxide at Downtown Los Angeles	536
11.14	Predicted and Observed Concentrations of (a) Ozone and (b) Nitrogen Dioxide at Pasadena	537

## LIST OF FIGURES (Continued)

<u>Figure</u>		<u>Page</u>
11.15	Predicted and Observed Concentrations of (a) Ozone and (b) Nitrogen Dioxide at Pomona	538
11.16	Predicted and Observed Concentrations of (a) Ozone and (b) Nitrogen Dioxide at Upland	539
11.17	Predicted and Observed Concentrations of (a) Ozone and (b) Nitrogen Dioxide at Riverside	540
11.18	Histograms of Concentrations Residuals (Observed-Predicted) Determined Over All Times and Locations for the Two Day Period 26-27 June 1974: (a) Ozone (b) Nitrogen Dioxide	545
11.19	Distribution of Concentration Residuals (Observed-Predicted) as a Function of Observed Values Determined Over All Times and Locations for the Two Day Period 26-27 June 1974: (a) Ozone (b) Nitrogen Dioxide	546
11.20	Distribution of Concentration Residuals (Observed-Predicted) as a Function of Time Determined Over All Locations for the Two Day Period 26-27 June 1974: (a) Ozone (b) Nitrogen Dioxide	547
11.21	Effect on a Correlation Plot of a One Hour Phase Shift in the Predicted Concentration Time Profile	548
11.22	Frequency Distributions of a Predicted and Observed Concentrations at (a) Azusa and (b) Upland	552
11.23	(a) Histograms of the Difference Between the Calibration Standards and Observed Concentrations for Oxidant Monitoring Instruments During the Period 1968-1975 (b) Ozone Predictions at Pasadena Together with the $\pm 2\sigma$ Calibration Error Bounds on the Measured Air Quality	553
12.1	(a) Emission Control Strategy Composed of Particular Tactics (b) Control Strategy Definition in Terms of Individual Tactics	557
12.2	Detailed Elements of an Integrated Approach to Least Cost Control Strategy Design	561
B.1	Linear Basis Functions for Galerkin Finite Element Model	578

## LIST OF FIGURES (Continued)

<u>Figure</u>		<u>Page</u>
C.1	Location of Air Quality Monitoring Sites within the South Coast Air Basin	584
C.2	Definition of the Origin of the Computational Grid System	585
C.3	Measured (o) And Predicted (-) Ozone and Nitrogen Dioxide Air Quality at Anaheim	587
C.4	Measured (o) And Predicted (-) Ozone and Nitrogen Dioxide Air Quality at La Habra	588
C.5	Measured (o) And Predicted (-) Ozone and Nitrogen Dioxide Air Quality at Los Alamitos-Orangewood Avenue	589
C.6	Measured (o) And Predicted (-) Ozone and Nitrogen Dioxide Air Quality at Norco-Prado Park	590
C.7	Measured (o) And Predicted (-) Ozone and Nitrogen Dioxide Air Quality at Riverside-Rubidoux	591
C.8	Measured (o) And Predicted (-) Ozone and Nitrogen Dioxide Air Quality at Riverside-Magnolia Avenue	592
C.9	Measured (o) And Predicted (-) Ozone and Nitrogen Dioxide Air Quality at San Bernardino	593
C.10	Measured (o) And Predicted (-) Ozone and Nitrogen Dioxide Air Quality at Chino-Riverside Avenue	594
C.11	Measured (o) And Predicted (-) Ozone and Nitrogen Dioxide Air Quality at Upland-Civic Center	595
C.12	Measured (o) And Predicted (-) Ozone and Nitrogen Dioxide Air Quality at Inland ARB	596
C.13	Measured (o) And Predicted (-) Ozone and Nitrogen Dioxide Air Quality at Fontana-Foothill Blvd	597
C.14	Measured (o) And Predicted (-) Ozone and Nitrogen Dioxide Air Quality at Camp Paivika-USFS	598
C.15	Measured (o) And Predicted (-) Ozone and Nitrogen Dioxide Air Quality at Camarillo-Palm	599
C.16	Measured (o) And Predicted (-) Ozone and Nitrogen Dioxide Air Quality at Point Mugu	600

## LIST OF FIGURES (Continued)

Figure		Page
C.17	Measured (o) And Predicted (-) Ozone and Nitrogen Dioxide Air Quality at Port Hueneme	601
C.18	Measured (o) And Predicted (-) Ozone and Nitrogen Dioxide Air Quality at Simi Valley	602
C.19	Measured (o) And Predicted (-) Ozone and Nitrogen Dioxide Air Quality at Ventura-Telegraph Rd	603
C.20	Measured (o) And Predicted (-) Ozone and Nitrogen Dioxide Air Quality at Thousand Oaks-Windsor Dr	604
C.21	Measured (o) And Predicted (-) Ozone and Nitrogen Dioxide Air Quality at Los Angeles-Downtown	605
C.22	Measured (o) And Predicted (-) Ozone and Nitrogen Dioxide Air Quality at Azusa	606
C.23	Measured (o) And Predicted (-) Ozone and Nitrogen Dioxide Air Quality at Burbank	607
C.24	Measured (o) And Predicted (-) Ozone and Nitrogen Dioxide Air Quality at West Los Angeles	608
C.25	Measured (o) And Predicted (-) Ozone and Nitrogen Dioxide Air Quality at Long Beach	609
C.26	Measured (o) And Predicted (-) Ozone and Nitrogen Dioxide Air Quality at Pomona	610
C.27	Measured (o) And Predicted (-) Ozone and Nitrogen Dioxide Air Quality at Lennox	611
C.28	Measured (o) And Predicted (-) Ozone and Nitrogen Dioxide Air Quality at Redondo beach	612
C.29	Measured (o) And Predicted (-) Ozone and Nitrogen Dioxide Air Quality at Whittier	613
C.30	Measured (o) And Predicted (-) Ozone and Nitrogen Dioxide Air Quality at Pasadena	614
C.31	Measured (o) And Predicted (-) Ozone and Nitrogen Dioxide Air Quality at Lynwood	615
C.32	Measured (o) And Predicted (-) Ozone and Nitrogen Dioxide Air Quality at Mt Lee Dr.-Mobile Van	616

## LIST OF FIGURES (Continued)

<u>Figure</u>		<u>Page</u>
C.33	Measured (o) And Predicted (-) Ozone and Nitrogen Dioxide Air Quality at Van 1-105 Frwy (Prop)	617

## LIST OF TABLES

<u>Table</u>		<u>Page</u>
1.1	Empirical Relationships for Predicting the Impact of Photochemical Oxidant Control Strategies	8
1.2	Physicochemical Models for Predicting the Impact of Photochemical Oxidant Control Strategies	9
1.3	Summary of Inputs Needed to Solve the Atmospheric Diffusion Equation	11
1.4	Outline of Contents of Chapters	13
2.1	Typical Reaction Rate Damkohler Numbers for a Smog Chamber Experiment	29
2.2	Sources of Invalidity in Air Quality Models	45
2.3	Sources of Inaccuracy in Air Quality Models	47
3.1	Results of Test Case Comparing Three Poisson Equation Solving Algorithms	122
4.1	Estimation of Pasquill Stability Classes	139
4.2	Coefficients for Straight Line Approximations to Golder's Plot as a Function of Stability Classes	141
4.3	Momentum and Pollutant Integrals of Different Stability Conditions	148
4.4	Typical Horizontal Eddy Diffusivities and Cross Wind Standard Deviations	171
5.1	Basic Meteorological Data Collected During Period 19-26 July 1977	180
5.2	Additional Data and Calculated Results for Period 19-26 July 1977	183
5.3	Convective Mixing Times Based on Turbulence Intensities for 22 July 1977	186
6.1	Estimates of Turbulence Constants from Surface-Layer Measurements	194
6.2	Momentum and Pollutant Integrals for Different Stability Conditions	198

## LIST OF TABLES (Continued)

<u>Table</u>		<u>Page</u>
6.3	Deposition Velocity as a Function of Stability and Ratio of Sc/Pr	199
6.4	Integrals Required to Calculate the Cell Average Deposition Velocity	204
6.5	Literature Survey of Deposition Velocity Data for Species Involved in Photochemical Reaction Processes	214
6.6	Average Deposition Velocity of SO <sub>2</sub> for Different Surface and Stability Conditions	216
6.7	Summary of Deposition Velocity Data and Concentration Ratios	217
7.1	Conversion Factors for Point and Area Sources	224
7.2	Relationship Between Pasquill-Gifford Stability Classes and Temperature Stratification	233
8.1	Chemical Mechanism Used Within Airshed Model	272
8.2	Chemical Species Participating in Photochemical Reaction Mechanism	276
8.3	Summary of Rate Constants Excluding Photolysis and Lumped Hydrocarbon Steps	285
8.4	Hydrocarbon Composition of Smog Chamber Experiment SUR-119J Excluding Methane, Acetylene, and Acetone	290
8.5	Rate Constant Data for Reaction with OH	293
8.6	Rate Constant Data for Reactions with O	295
8.7	Rate Constant Data for Reactions with O <sub>3</sub>	297
8.8	Rate Constants for Lumped Hydrocarbon Reaction Steps	298
8.9	Ground Level Actinic Irradiance as a Function of Zenith Angle and Wavelength (Photons/cm <sup>2</sup> -sec x 10 <sup>-15</sup> )	303
8.10	Quantum Yield Data Averaged over 10 nm Wavelength Interval	306
8.11	Absorption Cross Section $\sigma(10^{-20} \text{ cm}^2 \text{ molecule}^{-1})$ 10 nm Integral Averaged, Centered about	307

## LIST OF TABLES (Continued)

<u>Table</u>		<u>Page</u>
8.12	Photolysis Steps in Photochemical Reaction Mechanism	317
8.13	Application of Procedure for Calculating Atmospheric Water Vapor Concentration	326
8.14	Initial Conditions for Smog Chamber Experiment SUR-119J	333
8.15	Initial Conditions for Smog Chamber Experiments	334
8.16	Approach to the Equilibrium Nitrous Acid (HONO) Concentration	344
8.17	Predicted Concentration of Nitrogen Containing Species for Smog Chamber Experiment SUR-119J	345
8.18	Forward Reaction Rates for Smog Chamber Experiment SUR-119J	350
9.1	Test Problems for Advection Equation	369
9.2	Summary of Results of Advection Tests for Different Initial Distributions	370
9.3	Results of Advection of Triangular Wave Form After 80 Time Steps	377
9.4	Errors in Concentration Predictions After 100 Time Steps for A Spatially-Varying Velocity Field	378
9.5	Summary of Results of Two-Dimensional Cone in a Circular Wind Field ( $C_x = C_y = 0.5$ )	378
9.6	Comparison Between the Exact Calculation and the Pseudo Steady State Approximation for Different Chemical Species	386
9.7	Comparison Between Predictions of Complete System and Kinetics using Pseudo Steady State Approximations	387
9.8	Comparison of Start Up Times for EPISODE and Asymptotic Solution Schemes	391
10.1	Summary of Sensitivity Measures	405
10.2	Parameters Studied in Gaussian Plume Model	454
11.1	Summary of Input Data Needed to Carry out A Model Performance Evaluation Study	489

## LIST OF TABLES (Continued)

<u>Table</u>		<u>Page</u>
11.2	Height of 500 mb Pressure Surface During June 25-28, 1974 Oxidant Episode	491
11.3	Summary of Total Emissions Into South Coast Air Basin	499
11.4	Emissions Inventory for South Coast Air Basin	500
11.5	Composition of Reactive Hydrocarbons in Inventory Region	509
11.6	Reactive Hydrocarbon Emissions for the South Coast Air Basin	510
11.7	Reactivity Weighted Inventory of Emissions from Major Hydrocarbon Source Categories in the South Coast Air Basin	521
11.8	Splitting Factors for Converting Total Hydrocarbon Measurements into Hydrocarbon Classes for Chemical Mechanism	525
11.9	Natural (Unpolluted), Rural and Airshed Background Concentrations	528
11.10	Summary of Aerometric and Emissions Information Available for 26-28 June 1974 for the South Coast Air Basin	533
11.11	Summary Statistics Determined Over All Times and Locations for 26-27 June 1974	543
11.12	Observed and Predicted Maximum 1-hr Ozone Concentration at SCAB Stations Where $[O_3] > 0.20$ ppm and Timing of Ozone Maxima, 27 June 1974	549
12.1	Summary of Areas and Questions for Additional Research	563
12.2	Summary of Meteorological Measurements Needed for Model Evaluation	565
12.3	Summary of Needed Chemical Measurements	566
C.1	Air Quality Monitoring Sites Used in Statistical Analysis of Model Results for 26-27 June 1974	586



## CHAPTER 1

### INTRODUCTION

#### 1.1 Objectives

A particularly serious problem facing densely populated areas is the environmental degradation caused by the presence of photochemical air pollution. The problem is both pervasive and difficult to control. An important element of any rational approach directed at attempting to improve the situation is a reliable means for evaluating the air quality impact of alternative control measures. This report presents such a capability in the form of a mathematical description of the production and transport of photochemical oxidants within an urban airshed.

#### 1.2 Photochemical Air Pollution

Photochemical oxidant air pollution, or as it is more commonly known--smog, is actually a mixture of chemical compounds. In a typical urban atmosphere there are many oxidants including such species as ozone ( $O_3$ ), nitrogen dioxide ( $NO_2$ ), peroxyacetylnitrate (PAN) and hydrogen peroxide ( $H_2O_2$ ). These, and other pollutants, are produced as a result of the action of sunlight on the emissions of nitrogen oxides ( $NO_x$ ) and reactive hydrocarbons (RHC). An important characteristic of oxidants is that they are not emitted by the pollutant sources, but rather, are formed as products of chemical reactions in the atmosphere. It is this latter property that makes their control so difficult. When coupled with the fact that the amount of oxidant formed in any given urban area has a complex dependence on time of day, meteorological

conditions and the nature of the pollutant sources, the design of effective abatement programs becomes an even more complex undertaking.

Historically most pollution control measures have been based on the notion that a reduction in precursor emissions leads to a proportionate improvement in air quality. Unfortunately, the inherent non-linear nature of the chemistry of oxidant formation precludes the use of such simple approaches. Indeed, depending on the initial state of the atmosphere, it is possible to produce an increase, decrease or no change in oxidant levels from a simple strategy based on reducing one of the precursor emissions. Figure 1.1, for example, illustrates the effects on ozone concentration arising as a result of lowering the nitrogen oxides. These counter-intuitive results further highlight the need for a formal methodology capable of predicting the air quality impact of changes in emissions.

### 1.3 Modeling Photochemical Air Quality

At the core of any approach which attempts to relate changes in pollutant emissions to ambient air quality is a reliable prediction method. Whether the prediction scheme is a simple chart, formula or a complex numerical procedure there are three basic elements which must be considered; the meteorology (M), the source emissions (E) and the chemical interactions. Consider the schematic representation shown in Figure 1.2 where the function F, or air quality model, denotes the means of relating changes in contaminant emissions to the resulting air quality AQ. Mathematically F can be an algebraic or differential

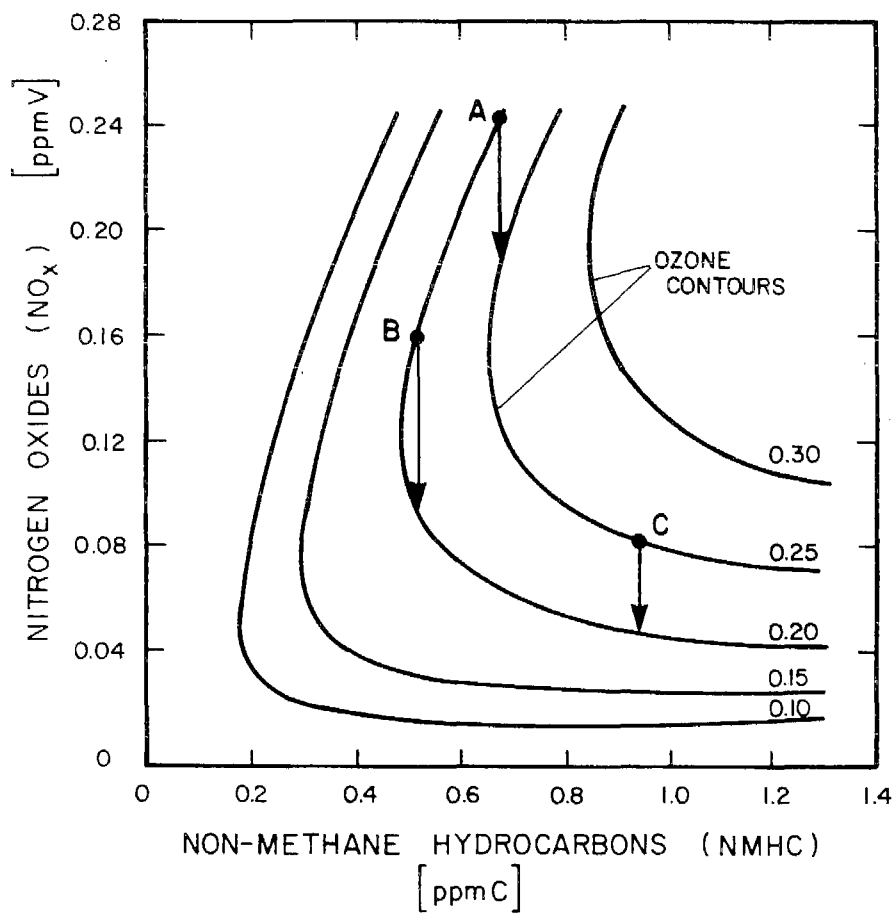


FIGURE 1.1

Ozone Isopleth Plot as a Function of the Precursor Concentration of Nitrogen Oxides (NO<sub>x</sub>) and Non-Methane Hydrocarbon (NMHC). The Three Cases A, B, and C Indicate the Effect, On Ozone, of Reducing Nitrogen Oxides. [Graph derived from Whitten and Hogo (1978).]

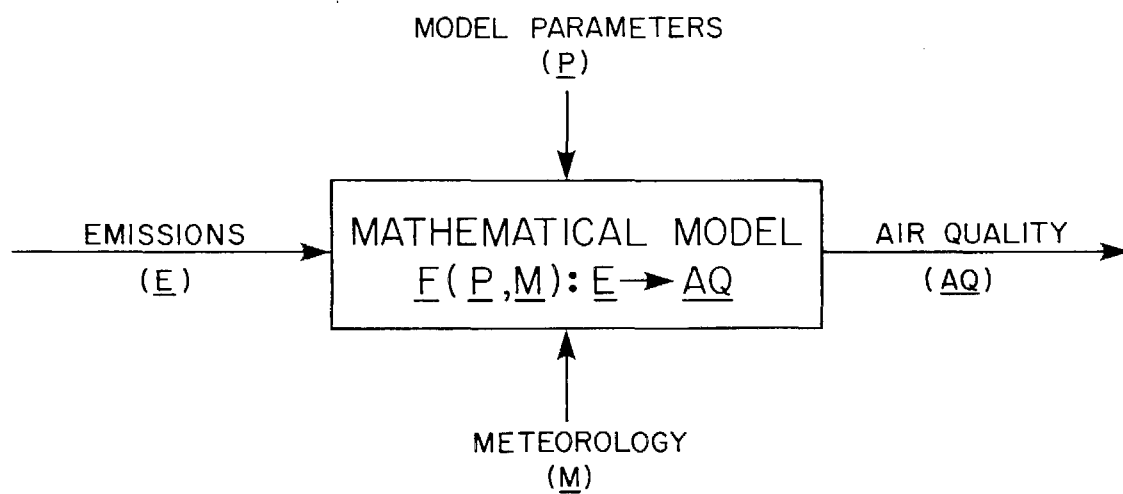


FIGURE 1.2

Schematic Structure of an Air Quality Model

system of arbitrary dimension. Given E, M and a set of additional parameters P, that characterize the atmospheric chemistry, the air quality modeling problem can be represented in a general way by the mapping

$$F(P,M):E \longrightarrow AQ \quad (1.1)$$

As might be expected there is a considerable literature that describes different functional representations for F, some of which are summarized in the reviews by: Roth et al. (1976), National Academy of Sciences (1977), Dimitriadis (1977), Myrabo et al. (1977) and Turner (1979). Despite the diversity of methodologies there two basic types of models. Those which are based on a fundamental description of the physics and chemistry occurring in the atmosphere are classified as a priori approaches. Deterministic models normally incorporate a mathematical treatment of the chemical and meteorological processes and in addition utilize information about emission distributions.

Another class of methods involves the use of a posteriori models in which empirical relationships are deduced from smog chamber or atmospheric measurements. These models are usually very simple and typically bear a close relationship to the actual data upon which they are based. This latter feature is a basic weakness. Because the models do not explicitly quantify the causal phenomena they cannot be reliably extrapolated beyond the bounds of the data from which they were derived. As a result, statistically based models are not ideally suited to the task of predicting the impacts of drastic changes in emissions.

While a detailed evaluation of all the various techniques is beyond the scope of the present study, Tables 1.1 and 1.2 summarize the results of an extensive literature survey conducted to assemble background material for this project. Both a priori and a posteriori methods are useful tools; however as a rule, if data are available to test a model based on scientific fundamentals then that approach is preferable.

#### 1.4 The Atmospheric Diffusion Equation

The various elements which must be linked as part of an a priori methodology for relating emissions to air quality are shown in Figure 1.3 where the mathematical model provides a framework for integrating the following basic components:

- A. A kinetic mechanism describing the rates of atmospheric chemical reactions as a function of the concentration of the various species present.
- B. A source description, giving the temporal and spatial distribution of emissions from significant pollutant sources within the airshed.
- C. A meteorological description, including wind speed and direction at each location in the airshed as a function of time, the vertical temperature structure and radiation intensity.

TABLE 1.1

Empirical Relationships for Predicting the Impact  
of Photochemical Oxidant Control Strategies

Methodology	Selected References
Smog Chamber Data	Dimitriadis (1972, 1976) Hamming, Chass, Dickinson et al. (1973)
Aerometric Data Analysis	Merz, Painter and Ryason (1972) Trijonis (1972, 1974), Trijonis et al. (1978) Paskind and Kinosian (1974) Bailey (1975) Myrabo, Wilson and Trijonis (1977) Tiao, Phadke and Box (1975) Post and Bilger (1978) Trijonis and Hunsaker (1978) Horie, Marians, Trijonis et al. (1979)
U.S. Environmental Protection Agency Recommended Methods	Schuck and Papetti (1973) U.S. Environmental Protection Agency (1971, 1974, 1978)

TABLE 1.2

Physicochemical Models for Predicting the Impact  
of Photochemical Oxidant Control Strategies

Methodology	Selected References	
Kinetic Mechanisms	Hecht, Seinfeld and Dodge (1974) Dodge (1977) Falls and Seinfeld (1978) Lloyd, Lurmann, Godden et al. (1979) Whitten, Hogo, Meldgin et al. (1979)	
Box Models	Graedel, Farrow and Weber (1976, 1978) Demerjian and Schere (1979) McRae, Goodin and Seinfeld (1981)	
Models Trajectory	Eschenroeder and Martinez (1972) Lloyd, Lurmann, Godden et al. (1979) McRae, Goodin and Seinfeld (1981)	} vertically resolved
	Wayne, Kokin and Weisburd (1973) Whitten and Hogo (1978)	} single cell
Grid Models	Reynolds, Roth and Seinfeld (1973) Reynolds, Liu, Hecht et al. (1974) Roth, Roberts, Liu et al. (1974) McRae, Goodin and Seinfeld (1979) McRae, Goodin and Seinfeld (1981)	} vertically resolved
	MacCracken and Sauter (1975) MacCracken, Walton, Duewer et al. (1978) Duewer, MacCracken and Walton (1978) McRae, Goodin and Seinfeld (1981)	} vertically integrated

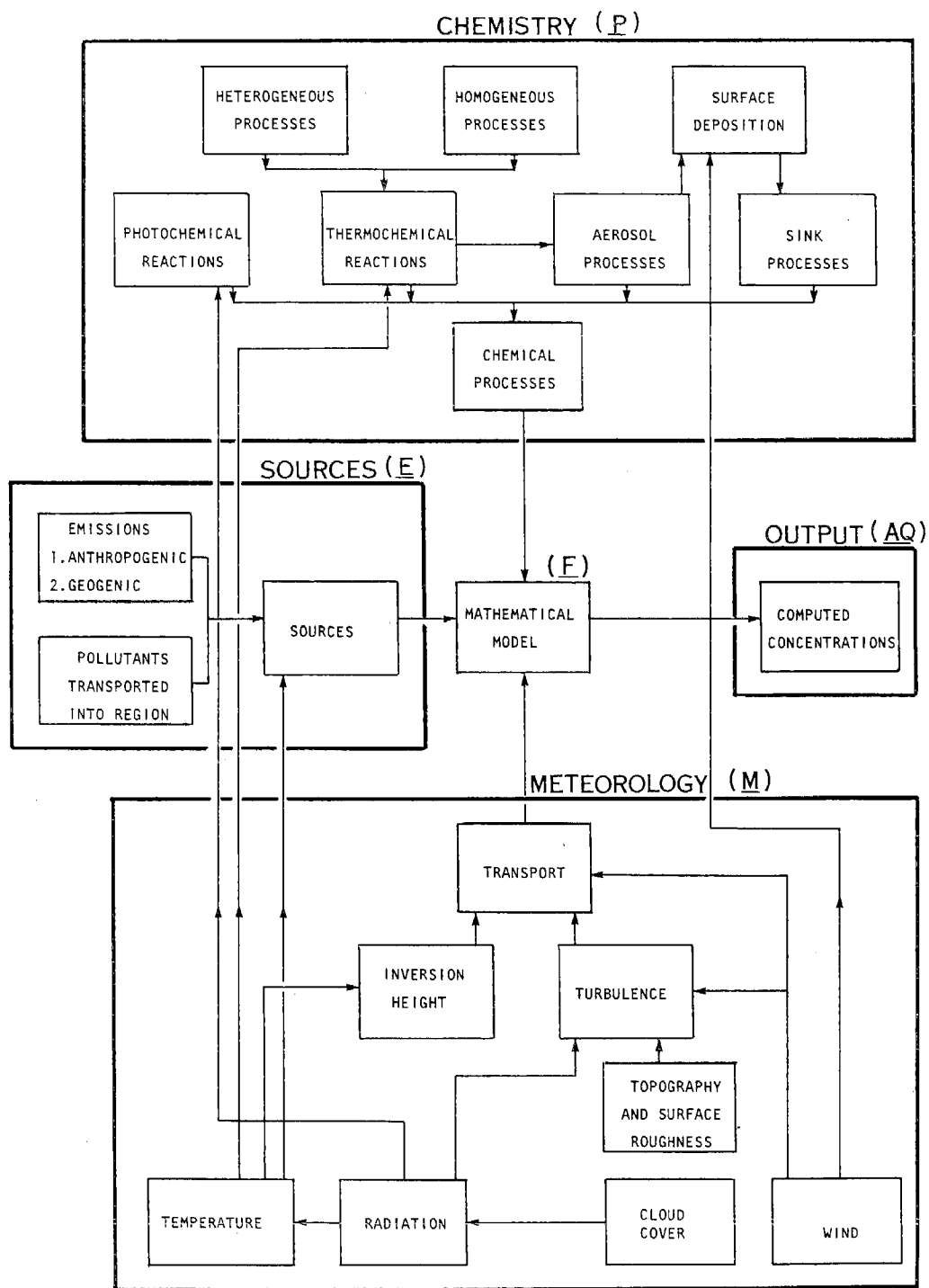


FIGURE 1.3

Elements of a Mathematical Model for Relating Pollutant Emissions to Ambient Air Quality

The detailed formulation of a system which links the components parts, shown in Table 1.3, is a difficult undertaking because it is necessary to maintain a balance between the need for computational economy and the desire for an accurate representation of the underlying physics and chemistry. In this study the formation and transport of chemically-reacting species in the turbulent planetary boundary layer is described by the atmospheric diffusion equation.

$$\frac{\partial c_i}{\partial t} + \nabla \cdot (\underline{u}c_i) = \nabla \cdot (K\nabla c_i) + R_i \quad (1.2)$$

where  $c_i$  is the concentration of the species  $i$ ,  $\underline{u}(\underline{x},t)$  is the prescribed flow field,  $R$  the chemical reaction rate and  $K$  a parameterization of the turbulent mixing. Various reduced forms of the atmospheric diffusion equation (1.2) provide the basis for less complex models. For example the modeling system developed as part of this study incorporates a vertically integrated, a Lagrangian trajectory and single cell box models. Since each model employs common components and input data they can be used in a unified approach to air quality modeling. The simpler formulations can be used for rapid screening calculations and the more complex models for detailed evaluations. Subsequent chapters of this work discuss the validity and practical implementation of these different representations of atmospheric concentration dynamics.

TABLE 1.3

Summary of Inputs Needed to Solve the  
Atmospheric Diffusion Equation

Basic Input	Detailed Components
Meteorology ( <u>M</u> )	Three dimensional wind field Mixing depth Topography and surface roughness Turbulent diffusion coefficients Solar insolation Ultraviolet radiation Temperature Relative humidity
Chemical Kinetics ( <u>P<sup>c</sup></u> )	Reaction mechanism Reaction rate constants Reaction stoichiometry Surface deposition velocities Hydrocarbon lumping procedure
Air Quality Data ( <u>P<sup>a</sup></u> )	Initial and boundary conditions Verification data
Emission Inventory ( <u>E</u> )	Mobile sources Stationary sources

### 1.5 Structure of this Research

A basic goal of this research is the formulation of a practical airshed modeling system that incorporates the the most recent developments in photochemical reaction mechanisms, turbulent diffusion, surface removal processes, numerical solution techniques and objective analysis procedures. The formulation of such a system involves a number of basic steps the first of which is a detailed examination of the validity of the atmospheric diffusion equation as a basis for describing the formation and transport of photochemical air pollution. The second step requires that the form and interaction between the various physical and chemical processes be specified and tested against independent experiments. Once the appropriate mathematical descriptions have been formulated then it is necessary to implement suitable numerical solution procedures. The final step is to assess the ability of the model to predict the actual concentration distributions in an urban airshed.

The following chapters are devoted to these tasks and since this involves a significant amount of material an overall perspective is useful. Table 1.4 presents a summary outline and Figure 1.4 illustrates how each chapter is related to the atmospheric diffusion equation.

TABLE 1.4

## Outline of Contents of Chapters

---

CHAPTER	SUMMARY OUTLINE
2	Model formulation and detailed derivation of the atmospheric diffusion equation
3	Development of objective analysis procedures for specification of wind fields, mixing heights and initial concentration distributions
4,5	Parameterization of the turbulent mixing processes under different meteorological conditions
6	Characterization of the surface removal mechanisms
7	Treatment of point and area source emissions in a grid based model
8,10	Implementation, testing and sensitivity analysis of a photochemical reaction mechanism
9	Numerical solution of the atmospheric diffusion equation using operator splitting and coordinate transformations. Selection of a numerical method for solving the advection-diffusion equation. Solution procedures for the chemical kinetics
12	Evaluation of the model performance in an urban airshed
13,14	Summary and Conclusion

---

Species Continuity Equation

$$\frac{\partial c_i}{\partial t} + \overset{3}{\downarrow} \nabla \cdot (u c_i) = \overset{4,5}{\downarrow} \nabla \cdot (K \nabla c_i) + \overset{8,10}{\downarrow} R_i \quad ; \quad i = 1, 2, \dots, p$$

Initial Conditions

$$c_i(\vec{x}, 0) = \overset{12}{\downarrow} c_i^0 \quad ; \quad t = 0$$

Boundary Conditions (General form of  $\tilde{a}, \tilde{b}, \tilde{f}$  depend on application)

$$\left[ \overset{6}{\downarrow} \tilde{a} c_i + \overset{4}{\downarrow} \tilde{b} \frac{\partial c_i}{\partial x} \right] \cdot \overset{7}{\downarrow} \hat{n} = \tilde{f}$$

FIGURE 1.4

Inputs to the Atmospheric Diffusion Equation and Processes  
Required for Numerical Solution - Numbers Represent Subsequent Chapters.

## CHAPTER 2

## FORMULATION OF AN URBAN SCALE AIRSHED MODEL

2.1 Introduction

Modeling urban scale air pollution is essentially the problem of describing the formation and transport of chemically reactive species in the turbulent planetary boundary layer. As used in this study, an air quality model will be taken to represent a physiochemical model based on theoretical treatments of atmospheric chemistry and meteorology. This chapter presents the basic model formulation and discusses the key assumptions which must be invoked in order to obtain a tractable set of governing equations.

2.2 Species Continuity Equation

A common starting point for most air quality model derivations is a statement of mass conservation. A differential expression of the mass balance for species  $c_i$ , in a  $p$ -component mixture, is given by

$$\frac{\partial c_i}{\partial t} + \nabla \cdot (\underline{u}_i c_i) = R_i(c_1, \dots, c_p, T) \quad (2.1)$$

where  $\underline{u}_i(\underline{x}, t)$  is the velocity of species  $c_i$  at position  $\underline{x}$  at time  $t$  and  $R_i$  is the chemical generation rate. A more useful form of the mass flux  $\underline{u}_i c_i$  can be written in terms of the mass-weighted average velocity  $\underline{u}$  of the mixture as a whole. The velocity of species  $c_i$  relative to the mean  $\underline{u}$  is simply  $\underline{u}_i - \underline{u}$  and so the diffusive flux of  $c_i$  relative to a coordinate system moving with the mean velocity is then  $\underline{j}_i \underline{\tilde{u}} = c_i(\underline{u}_i - \underline{u})$ . Equation (2.1) can then be written in the form

$$\frac{\partial c_i}{\partial t} + \nabla \cdot (\underline{u}c_i) = -\nabla \cdot \underline{j}_i + R_i \quad (2.2)$$

The diffusive flux is represented by Fick's law,  $\underline{j}_i = -D_i \nabla c_i$ , where  $D_i$  is the molecular diffusion coefficient of  $c_i$  with respect to the composite mixture. The molecular diffusion coefficient in general depends upon the temperature and chemical potential gradients of all species in the mixture (Bowen, 1976). If the pollutant species are present in sufficiently dilute amounts, then the conservation of mass for a particular component can be written in the form

$$\frac{\partial c_i}{\partial t} + \nabla \cdot (\underline{u}c_i) = \nabla \cdot (D_i \nabla c_i) + R_i \quad (2.3)$$

The mixture mass balance consists of two parts; the first is a conservation statement (2.3) for each species and the second is a balance for the mixture as a whole. In order to describe the dynamics of the complete system it is necessary to carry out a simultaneous solution of the coupled equations of mass, momentum and energy conservation. Since the appropriate equations of motion for air are extensively discussed in Dutton and Fichtl (1969), Spiegel and Veronis (1960), Businger (1973), Donaldson (1973) they will not be reiterated here.

### 2.3 Decoupling Species and Carrier Fluid Equations

Because of the computational difficulties it is useful to attempt a decoupling of the species continuity equations from the equations of motion of the carrier fluid. While this approach simplifies the solution procedure, the temperature and velocity fields must nevertheless

be externally supplied to the airshed model. A key assumption implicit in the separation is that the presence of pollutant gases and particulate aerosols does not significantly affect the meteorology. The objective of this section is to examine the justification for the decoupling, as it has not been extensively discussed in previous photochemical modeling studies.

Two effects could invalidate the assumption. The direct effect on atmospheric temperature structure from heat released in the chemical reactions can be considered to be negligible as most species are present only in trace quantities. A more serious question arises, however, as to the effect of gaseous pollutants and aerosols on the radiative transfer processes. Recently there have been a number of studies on the effects of pollutant material on the microclimates of urban areas. (Ackerman et al., 1976; Ackerman, 1977; Atwater, 1977; Bergstrom and Viskanta, 1973abc; Viskanta and Daniel, 1980; Viskanta et al., 1977; Welch et al., 1978; Zdunkowski and McQuage, 1972; Zdunkowski et al., 1976.) The results of these studies indicate that gaseous pollutants, which interact primarily in the infrared, tend to heat the earth's surface during the day by increasing the downward thermal radiation and conversely enhancing the cooling at night. While there is general agreement on this result, the conclusions regarding the effects of aerosols on the temperature structure are not so straightforward. The reason for this is that the radiation balance depends on both the surface albedo and the aerosol characteristics.

Ackerman (1977) has presented a model which considers the effects of pollutants on both longwave and shortwave radiation and the interaction of the modified radiation field with the surface fluxes. The results are of particular interest because the model was applied to the Los Angeles Basin. An important conclusion of the study was that there is a strong tendency for self stabilizing compensation. This was particularly evident in the relationship between the atmospheric absorption of shortwave radiation and the heat flux. If the radiation is absorbed by a layer near the ground the heat transfer from the surface to the atmosphere is reduced. This in turn tends to keep the surface and the boundary-layer temperatures approximately the same as if no absorption were taking place. Loss of energy due to backscatter may also result in a reduction of the depth of the boundary layer rather than in a reduction in temperature. An additional compensation occurs within the radiative fluxes. The warming of the atmosphere by shortwave radiation is opposed to a lesser degree by an increase in longwave emission, a phenomenon which also tends to maintain the surface temperature.

A number of different studies (Atwater, 1977; Bergstrom and Viskanta, 1973abc; Ackerman, 1977; Viskanta and Daniel, 1980) indicate that the principal effect of aerosols on the urban climate is to increase the daytime temperatures whereas the gaseous pollutants decrease the boundary layer temperature at night. The changes in both cases are quite small; for example, Viskanta and Daniel (1980) predicted that the mean difference in temperature with and without

radiatively interacting pollutants was  $< 0.5$  °K and the changes in the mixed layer height  $< 10\%$ . In areas with relatively high background particulate concentrations the aerosol heating tends to retard the growth of the mixed layer. Ackerman (1977) showed, however, that for Los Angeles this tendency could cause a strengthening of the sea breeze circulation which in turn would increase the turbulent mixing and tend to raise the inversion base. An increase in the strength of the sea breeze would bring in more cool air and thus oppose the temperature increase caused by the aerosol absorption. In passing it is important to note that most of the above findings are primarily based on theoretical studies. There is a great need for more experimental data, in particular about the optical properties of aerosols, in order to quantify the feedback mechanisms between pollutants and the thermal structure of the atmosphere.

The major inference to be drawn from the preceding literature survey is that the pollutant gases and aerosols have only a minor influence on the urban climate. In particular, the net impact of particles was to decrease the temperature of the atmosphere-earth system, while the influence of absorption and emission of thermal radiation by gases was to increase the system temperature. The effects of gaseous and particulate pollutants are opposite and to a certain extent partially compensating. Under these conditions decoupling the species continuity equation from the equations of motion is a valid approximation in an urban atmosphere. This conclusion should not, however, be interpreted as a statement that the decoupling can be used in all

situations. There is some evidence to suggest that while on an urban scale the effects are minor, the influence on regional climate may be significant (Atwater, 1977).

#### 2.4 Turbulent Flows

A basic problem with any effort to solve the species continuity equation is that the velocity field  $\underline{u}(\underline{x}, t)$  is typically not available as a continuous function of space and time. In most urban airsheds the wind field is sampled only at a discrete set of spatial locations. Lamb and Seinfeld (1973) have shown that only the features of the velocity field with spatial scales larger than about twice the average distance between sampling points can be described explicitly. All smaller features cannot be resolved and therefore must be treated as stochastic variables. The conventional representation for  $\underline{u}$  is as a sum of a deterministic  $\underline{u}$  and a random component  $\underline{u}'$ ,  $\underline{u} = \underline{u} + \underline{u}'$ . Because of the fluctuating component  $\underline{u}'$ , (2.3) is then a stochastic differential equation and  $c_i$  is a random variable. Since the probability density function for  $c_i$  cannot, in general, be determined only statistical moments are available. In order to make meaningful predictions it is necessary to average the equations in such a manner that model outputs can be identified with experimental measurements in the field. Some information, related to the small scale variations, is lost in the process of taking the mean value. Averaging (2.3) over an infinite ensemble of realizations and neglecting molecular diffusion gives

$$\frac{\partial \langle c_i \rangle}{\partial t} + \nabla \cdot (\underline{u} \langle c_i \rangle) + \nabla \cdot \langle \underline{u}' c_i' \rangle =$$

$$\langle R_i(\langle c_1 \rangle + c_1', \dots, \langle c_p \rangle + c_p') \rangle \quad (2.4)$$

where  $\langle c_i(x,t) \rangle$  is the ensemble mean concentration. This result follows from the linear nature of the ensemble averaging operator defined by (2.5) where  $p^i(t)$  is the  $i$ -th realization of a particular process  $p(t)$ . The properties (2.6 - 2.8) are used in the derivation of (2.4).

$$\langle p(t) \rangle = \lim_{N \rightarrow \infty} \frac{1}{N} \sum_{i=1}^N p^i(t) \quad (2.5)$$

$$\langle Ap(t) \rangle = A \langle p(t) \rangle ; A = \text{constant} \quad (2.6)$$

$$\langle p_1(t) + p_2(t) \rangle = \langle p_1(t) \rangle + \langle p_2(t) \rangle \quad (2.7)$$

$$\left\langle \frac{\partial p(t)}{\partial s} \right\rangle = \frac{\partial}{\partial s} \langle p(t) \rangle \quad (2.8)$$

In these expressions  $s$  is an independent variable, for example space or time. There is an important difference between the ensemble average, (2.5), and the temporal (or spatial) average implied by the overbar for  $\underline{u}$ . Mean fluid velocities are normally determined by a process involving temporal and spatial averaging of the form

$$\bar{\underline{u}} = \frac{1}{T} \int_0^T \underline{u}(t) dt \quad (2.9)$$

This average itself will fluctuate depending on the starting point and the duration of the averaging process. The use of the temporal average, (2.9), to define  $\bar{\underline{u}}$  complicates the process of deriving (2.4) for it is necessary to assume that

$$\overline{\langle \underline{u}c' \rangle} = \overline{\underline{u}} \langle c' \rangle \equiv 0 \quad (2.10)$$

Strictly speaking, unless  $\overline{\underline{u}}$  is a constant, this assumption is not satisfied; however, the averaging interval may be chosen in such a way to approximate the equality with comparatively high accuracy. To do this the averaging interval,  $T$ , must be long in comparison with the characteristic periods of the fluctuating quantity  $\underline{u}'(t) = \underline{u}(t) - \overline{\underline{u}}(t)$ . Sheih (1980) discusses how the averaging time can be selected from a knowledge of the spectral distribution of the wind velocity fluctuations. An investigation of the averaging time needed to approximate ensemble average statistics is presented in Wyngaard (1973). Further, if the ergodic hypothesis can be invoked, i.e., that  $\underline{u}(t)$  is independent of starting time, then ensemble and time average are identical. Monin and Yaglom (1971) discuss, in considerable depth, the problem of averaging. Depazo (1977) has considered the more difficult case of intermittent flows.

## 2.5 The Turbulent Closure Problem

Neglecting molecular diffusion, (2.4) is a rigorously valid equation for the ensemble mean concentration. If the variables  $\langle \underline{u}'c_i' \rangle$  and any of those arising from  $R_i$  are known functions of space and time, then (2.4) can, in principle, be solved to yield  $\langle c_i \rangle$ . Unfortunately the  $\langle \underline{u}'c_i' \rangle$  cannot be measured at all points in an atmospheric flow and, in addition, cannot be exactly predicted because of the classic closure problem of turbulent flow. A great deal of research effort has been directed at attempts to resolve this problem. The most well-known

method of approximating the fluctuating transport term  $\langle \underline{u}'c_i' \rangle$  is the so-called gradient transport approximation proposed originally by Bousinesq (1877). With this approach, the transport is based on an analogy to the simplest molecular models in which the flux is assumed to be proportional to the linear mean gradients. The model for a non-isotropic flow is given by

$$\langle \underline{u}'c_i' \rangle = -K \cdot (\nabla \langle c_i \rangle) \quad (2.11)$$

where  $K$  is the second rank eddy diffusion tensor. Ignoring, for the moment, the chemical reaction term, (2.11) can be substituted into (2.4) to give

$$\frac{\partial \langle c_i \rangle}{\partial t} + \nabla \cdot (\underline{u} \langle c_i \rangle) = \nabla \cdot (K \nabla \langle c_i \rangle) \quad (2.12)$$

Considering the almost universal use of (2.11) as a closure approximation in airshed models it is important to outline some of its limitations. Monin and Yaglom (1971) and, in particular, Corrsin (1974) have identified some conditions which are necessary for the valid use of a gradient transport hypothesis. A basic requirement is that the transport mechanism length scale must be much smaller than the distance over which the curvature of the mean transported field gradient changes appreciably. Similar conditions apply to the temporal scales. A more fundamental difficulty occurs when the flows are buoyancy driven. In this situation, particularly for free convection, the fluxes  $\langle \underline{u}'c_i' \rangle$  are no longer described by the local gradient. Under unstable conditions parcels of warm air, displaced from their equilibrium position,

rise to the top of the mixed layer. To compensate for these vertical motions, zones of sinking air occur between the rising air parcels. As a result of this combined motion, positive values of  $w'$  are correlated with positive temperature fluctuations  $\theta'$ . The covariance  $\overline{w'\theta'}$  is positive but the mean vertical temperature gradient is zero (Deardorff; 1966, 1970).

In an attempt to circumvent some of these problems, considerable effort has been expended to develop so-called second moment turbulent closure models in which the governing equations are closed by including terms parameterizing various turbulent correlations. See, for example, Lewellen et al. (1974), Wyngaard and Cote (1974), Yamada and Mellor (1975), Lumley and Khajeh-Nouri (1974), Mellor and Yamada (1974), Zeman and Lumley (1976), Zeman and Tennekes (1977), Manton (1979), Binkowski (1979), Freeman (1977), and Yamada (1977). While many of these models are conceptually very appealing, their inclusion in an urban airshed model imposes an unreasonable computational burden. In addition to the problems associated with the solution economy, many of the models have been verified for only limited flow regimes and some require the determination of a large number of empirical constants. In spite of the possible benefits of employing a second-order closure model there remains a need for a simple scheme that produces results consistent with the known behavior of pollutants in the planetary boundary layer. The approach adopted in this work is to retain the use of the eddy diffusion concept and to develop the components of  $K$  using modern boundary layer theory.

## 2.6 Eddy Diffusivities

In most models the second rank tensor  $K$  is approximated by the diagonal form

$$K = \begin{bmatrix} K_{xx} & 0 & 0 \\ 0 & K_{yy} & 0 \\ 0 & 0 & K_{zz} \end{bmatrix} \quad (2.13)$$

The presence of zeros in the off diagonal elements implicitly assumes that the principal axes of  $K$  are aligned with the Eulerian co-ordinate system, a situation that seldom occurs in the planetary boundary layer (Monin and Yaglom, 1971; Corrsin, 1974). In general the tensor,  $K$ , depends on scalar quantities, such as the turbulent kinetic energy and the magnitude of the vertical shear of the horizontal wind. A major barrier to the inclusion, and parameterization, of the off diagonal elements is the lack of suitable laboratory and field data for a range of stability conditions. Freeman (1977), Yamada (1977) and Manton (1979) have used second-order closure models to calculate the off diagonal components of  $K$  for simplified atmospheric flows. The effects on concentration predictions have not as yet been extensively discussed in the literature.

An alternative approach, which retains the simplicity of the  $K$ -theory formulation, was introduced by Lamb et al. (1975). The basic idea was to develop vertical  $K_{zz}$  profiles which, when used in the atmospheric diffusion equation, reproduced the actual concentration distributions. In their initial work they found expressions for  $K_{zz}(z)$

that yielded accurate estimates of ground level concentrations under neutral and slightly unstable conditions. A similar method, which makes use of field measurements, has been developed by Crane et al. (1977). Using these techniques it is possible to obtain solutions of the diffusion equation which closely match observed concentration profiles. A variant of this procedure has been implemented in the present airshed model and further details are discussed in Chapter 4.

## 2.7 Effect of Turbulence on Chemistry

A major problem in modeling atmospheric concentration dynamics is predicting the species reaction rates in a turbulent fluid. The reason for this is that the true reaction rate  $R_i$  is a function of  $\langle c \rangle + c'$  but only the mean values  $\langle c \rangle$  are available after ensemble averaging. A closure assumption used in most airshed models is that the ensemble mean reaction rate is the same as the rate based on ensemble mean concentrations. There are obvious difficulties with this approach. Consider two elementary mechanism steps and their associated forward reaction rates. Assuming the rate constants  $k$  are fixed, the chemical production terms are given by

$$R_i = \begin{cases} -k_1 c_1 & ; c_1 \xrightarrow{k_1} \text{products} \\ -k_2 c_1 c_2 & ; c_1 + c_2 \xrightarrow{k_2} \text{products} \end{cases} \quad (2.14)$$

Expressing the concentrations as a sum of mean and fluctuating components  $c_i = \langle c_i \rangle + c_i'$  and ensemble averaging gives

$$\frac{\partial \langle c_1 \rangle}{\partial t} = k_1 \langle c_1 \rangle \quad (2.15)$$

$$\frac{\partial \langle c_2 \rangle}{\partial t} = -k_2 \langle c_1 \rangle \langle c_2 \rangle - k_2 \langle c_1' c_2' \rangle \quad (2.16)$$

For the first-order decay it is clear from (2.15) that the turbulence has no effect on the reaction rate. In the multicomponent case, (2.16), there is an interaction between the mean and fluctuating concentration level. The closure assumption  $\langle R(c) \rangle = R(\langle c \rangle)$  will not be valid unless

$$\langle c_1 \rangle \langle c_2 \rangle \gg |\langle c_1' c_2' \rangle| \quad (2.17)$$

An obvious question is: what is the effect of neglecting second order correlations of the form  $\langle c_1' c_2' \rangle$  in determining the reaction rates? Despite the importance of understanding reactive mixing in turbulent shear flows relatively little progress has been made in developing valid theories for use in practical situations. The complexity of the problem and approaches for resolving some of the difficulties are outlined in O'Brien (1974), Murthy (1975), Spalding (1975), Hill (1976), Shu et al. (1978). The few closure models that have been developed either require assumptions about the nature of the underlying concentration probability density functions (O'Brien, 1974; Lamb and Shu, 1978; Shu et al., 1978) or introduce additional differential equations (Donaldson, 1975) which in turn impose an unreasonable burden on an already complex computational problem.

Given the difficulties of developing simple closure models, an alternative approach is to attempt a delineation of the conditions

under which terms of the form  $\langle c_1'c_2' \rangle$  can be expected to be significant. In the absence of mean gradients, two competing processes influence the magnitude of  $\langle c_1'c_2' \rangle$ : molecular diffusion and chemical reactions. For example if the dissipative scale of the turbulence is small and the reaction rate is very slow, then molecular diffusion can be expected to keep  $c_1$  and  $c_2$  well mixed and the correlation term  $\langle c_1'c_2' \rangle$  can be neglected. A numerical measure of the ratio between the diffusive and reaction time scales is given by the Damkohler number  $N_D$  (Hill, 1976). For second-order reactions Shu (1976) evaluated  $N_D$  using

$$N_D = \frac{T_D}{T_R} = \frac{\text{Diffusive Time Scale}}{\text{Reaction Time Scale}} = \frac{k[\langle c_1 \rangle + \langle c_2 \rangle] \lambda^2}{2D} \quad (2.18)$$

where  $D$  is the molecular diffusion coefficient, and  $\lambda$  is the dissipation length scale (Corrsin, 1958). When  $N_D \gg 1$  the characteristic time for chemical reaction is short compared to that for molecular mixing. In this situation  $\langle c_1'c_2' \rangle$  will tend to  $-\langle c_1 \rangle \langle c_2 \rangle$  and so the reactions between  $c_1$  and  $c_2$  will be governed not by the kinetics but by the rate at which the reactants can be brought together by molecular diffusion. If the time scale for reaction is longer than that of dissipation ( $N_D \ll 1$ ) then concentration fluctuations are removed before they can affect the chemistry. For this situation the mean reaction rate can be satisfactorily predicted by  $-k\langle c_1 \rangle \langle c_2 \rangle$ . The Damkohler number has been estimated in Table 2.1 for reactions that often occur in photochemical mechanisms. Further details of rate constants and reaction steps are contained in Chapter 8.



A notable feature of the calculations shown in Table 2.1 is that unless the reactants are well mixed, there exists a possibility that some reaction rates are slower than those inferred directly from the kinetics. The importance of this finding must however be placed in its proper context. A variety of factors are involved: the first of which is that in Table 2.1 only single reaction steps are considered, whereas in the atmosphere, many reactions are occurring simultaneously. In a mixture, some reactions will deplete species and others will generate new material. Those reactions which are diffusion limited are normally so fast that lowering the rate constant to the effective mixing rate does not significantly change the overall kinetics. Another approach is to use sensitivity analysis techniques, like those described in Chapter 12, to examine the mechanism performance when all the diffusion limited kinetic rate constants are reduced.

The degree to which the reactants can be considered to be well mixed has an important practical consequence since steep concentration gradients can often exist in the vicinity of plumes. As an example, emissions from large combustion sources are typically rich in nitric oxide. This material is emitted into a background that typically has a high concentration of ozone and other species. The time required to mix the initially separated reactants ( $\text{NO}$  and  $\text{O}_3$ ) over the whole plume is longer than that required for reaction between  $\text{NO}$  and  $\text{O}_3$ . The macroscopic rate of reaction is controlled by the rate of mixing of the plume with ambient air, rather than by the kinetic rate constant for the reaction. The recent measurements of Hegg et al. (1977) appear to

support this contention. If the closure assumption is to be used for plume modeling then it is necessary to include sufficient computational grid points to resolve the concentration gradients.

In the remainder of this study the approximation  $\langle R(c) \rangle = R(\langle c \rangle)$  will be adopted even though there is some doubt about its validity in all situations. The second-order closure models that are available do not represent satisfactory alternatives, either because of computational cost or uncertainties in their formulations. In addition to the theoretical difficulties the lack of good experimental data is a major barrier to further progress.

## 2.8 The Atmospheric Diffusion Equation

In the previous section, the various assumptions and approximations needed to develop a practical air quality model were presented. For each of the  $p$  species present in the atmosphere the governing differential equation is given by

$$\frac{\partial \langle c_i \rangle}{\partial t} + \nabla \cdot (\bar{u} \langle c_i \rangle) = \nabla \cdot (K \nabla \langle c_i \rangle) + R_i(\langle c_1 \rangle, \dots, \langle c_p \rangle) \quad (2.19)$$

$$i = 1, 2, \dots, p$$

This equation is the starting point for the derivation of almost all airshed models. Since most practical applications entail numerical solutions of (2.19) the airshed must be subdivided into an array of grid cells, where each cell may have horizontal  $(\Delta x, \Delta y)$  and vertical  $(\Delta z)$  dimensions on the order of a few kilometers and several tens of meters, respectively. Before (2.19) can be solved, it must be filtered

to remove all small scale variations that cannot be resolved. This averaging process must be applied to both the concentration fields and the input parameters, such as the wind velocities and eddy diffusivities. In addition, (2.19) must be time-averaged over an interval equivalent of that used in each time step of the numerical solution procedure. The necessary spatial averaging can be accomplished with a filter of the form (2.20) that operates on an ensemble average quantity  $\langle p \rangle$ .

$$\langle \tilde{p}(t) \rangle = \frac{1}{\Delta V} \iiint_{\Delta V} \langle p(t) \rangle \, dx dy dz \quad (2.20)$$

where  $\Delta V$  is the computational cell volume. If it is assumed that  $\underline{u}$  and  $K$  do not possess spatial variations on a scale smaller than the computational grid, then (2.19) can be written in the form

$$\frac{\partial \langle \tilde{c}_i \rangle}{\partial t} + \nabla \cdot (\underline{u} \langle \tilde{c}_i \rangle) = \nabla \cdot (K \nabla \langle \tilde{c}_i \rangle) + \tilde{R}_i \quad (2.21)$$

In a manner similar to the turbulence closure problem of the previous section it is necessary to assume that

$$\tilde{R}_i[\langle c_1 \rangle, \dots, \langle c_p \rangle] \approx R_i[\langle \tilde{c}_1 \rangle, \dots, \langle \tilde{c}_p \rangle] \quad (2.22)$$

This approximation assumes that the volume-average reaction rate is the same as the reaction rate based on the volume average cell concentrations. Until the recent work of Lamb (1975) the validity of this assumption had not been discussed in the air pollution literature. Lamb concluded that in computational cells surrounding large point

sources there are circumstances in which errors in the concentration predictions can arise from the use of (2.22). This is to be expected as the spatial scale of a plume near the source is typically much smaller than the cell volume. In contrast the second-order closure model developed by Lamb indicates that for diffuse area sources and commonly encountered line sources, there are negligible subgrid-scale chemistry effects. His comments and examples were directed at the fast nonlinear reactions of the NO - O<sub>3</sub> system; most other reactions are generally slower and as a result are less affected by subgrid-scale variations. A major area for future research is the development of subgrid-scale models which can be used to embed large point sources into urban scale airshed models. Some initial steps in this direction are discussed in Chapter 7.

The form (2.23) which emerges as a result of the averaging operations and closure approximations is the basis of most airshed models.

$$\frac{\partial \langle \tilde{c}_i \rangle}{\partial t} + \nabla \cdot (\tilde{u} \langle \tilde{c}_i \rangle) = \nabla \cdot (K \nabla \langle \tilde{c}_i \rangle) + R_i(\langle \tilde{c}_1 \rangle, \dots, \langle \tilde{c}_p \rangle) \quad (2.23)$$

The steps in the process used to derive the atmospheric diffusion equation are summarized in Figure 2.1. In order to simplify the notation in subsequent sections, and in the following chapters, symbols indicating the nature of the averaging operation will be omitted.

Species Continuity Equation

$$\frac{\partial c_i}{\partial t} + \nabla \cdot (\underline{u} c_i) = \nabla \cdot (D_i \nabla c_i) + R_i \quad (2.3)$$

Assumptions:  $\underline{u} = \bar{\underline{u}} + \underline{u}'$

$$c_i = \langle c_i \rangle + c_i'$$

$$\underline{u} c_i \gg D_i \nabla c_i$$

$$\frac{\partial \langle c_i \rangle}{\partial t} + \nabla \cdot (\bar{\underline{u}} \langle c_i \rangle) = -\nabla \cdot \langle \underline{u}' c_i' \rangle + \langle R_i \rangle \quad (2.4)$$

Assumptions:  $\langle \underline{u}' c_i' \rangle \approx -K \nabla \langle c_i \rangle$

$$\langle R_i \rangle \approx R_i[\langle c_1 \rangle, \dots, \langle c_p \rangle, T]$$

$$\frac{\partial c_i}{\partial t} + \nabla \cdot (\bar{\underline{u}} \langle c_i \rangle) = \nabla \cdot (K \nabla \langle c_i \rangle) + R_i[\langle c_1 \rangle, \dots, \langle c_p \rangle, T] \quad (2.19)$$

Assumptions:  $\tilde{\underline{u}} \approx \bar{\underline{u}}$

$$\tilde{K} \approx K$$

$$\tilde{R}_i \approx R_i[\langle \tilde{c}_1 \rangle, \dots, \langle \tilde{c}_p \rangle, T]$$

Atmospheric Diffusion Equation

$$\frac{\partial \langle \tilde{c}_i \rangle}{\partial t} + \nabla \cdot (\bar{\underline{u}} \langle \tilde{c}_i \rangle) = \nabla \cdot (K \nabla \langle \tilde{c}_i \rangle) + R_i[\langle \tilde{c}_1 \rangle, \dots, \langle \tilde{c}_p \rangle, T] \quad (2.23)$$

FIGURE 2.1

Summary of the Steps Involved in Deriving the  
Atmospheric Diffusion Equation

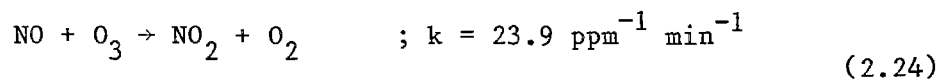
## 2.9 Vertical Extent of the Airshed Boundaries

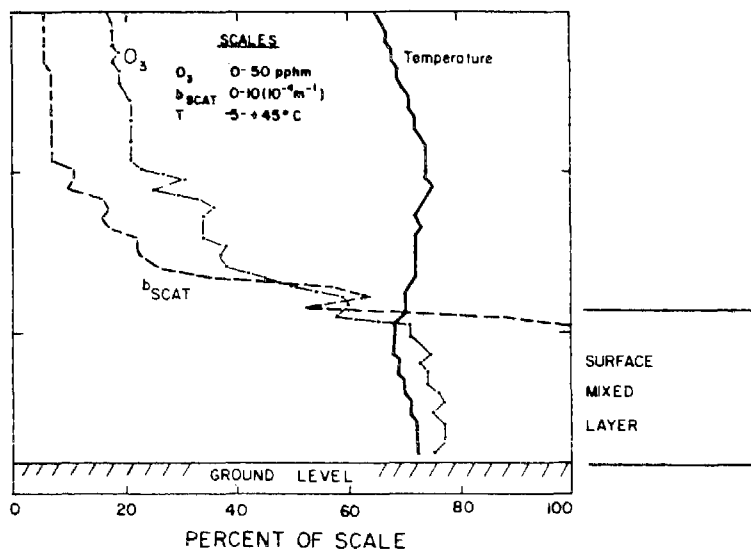
In urban areas the definition of the vertical extent of the airshed has a major influence on the choice of the boundary conditions. In most previous studies the top of the airshed has been defined by the base of an elevated inversion. The justification is that, for surface level releases, the extent of vertical mixing is basically controlled by the lower surface of an elevated temperature inversion. In mid-latitudes, over land, this convective boundary layer reaches a height of 1-2 Km by mid-afternoon and exhibits a near-constant distribution of wind speed and potential temperature. The name 'mixed layer' is often used synonymously with the convective boundary layer in much of the literature. Some controversy exists regarding the choice of the height  $Z_1$  that defines the thickness of the boundary layer. Tennekes (1970), Zilitinkevich (1972), Clarke and Hess (1973) have suggested that the boundary layer thickness is a function of the Ekman layer depth  $u_* / f$ . The modeling studies of Deardorff and Willis (1974) show that the elevation of the lowest inversion base is perhaps a more appropriate measure for unstable conditions.

Use of this height to define the depth of the airshed can, under some conditions, cause great difficulty in establishing appropriate upper level boundary conditions. The calculations by Duewer et al. (1978), using the model described in MacCracken et al. (1978), indicate that ground level predictions for ozone are often quite sensitive to the values chosen for the upper level inflow boundary conditions. Similar findings were noted by Liu et al. (1976). Few concentration

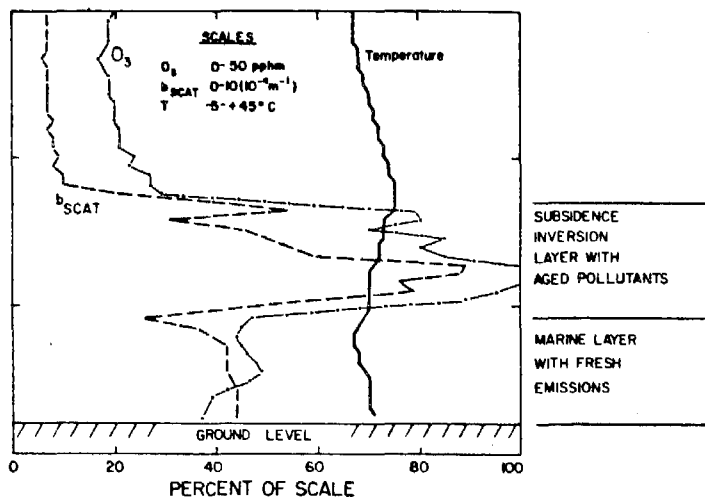
measurements are made above ground level and as a result the upper level boundary conditions are normally set to typical background values. This procedure can severely underestimate the actual concentrations which can exist above the inversion base. Figure 2.2 presents some data measured by Blumenthal et al. (1978) during a special study of the three dimensional structure of concentration distribution over the Los Angeles Basin. The most striking feature, particularly for ozone, is that the concentrations above the inversion base are considerably in excess of normal background levels of 0.04 ppm. These results are similar to the observations made by Edinger (1973) and presented in Figure 2.3. Before discussing how to resolve the difficulties, it is important to understand the origin of the high concentrations and their influence on ground level predictions by the airshed model.

Late in the day the direction of the thermal radiation at the earth's surface changes direction. In particular, after sunset the net heat loss by radiation produces a stable layer close to the ground. With sufficient cooling, the stable layer can extend from the surface to a height of several hundred meters. The stable stratification inhibits vertical mixing and so any ozone trapped aloft is not subject to attack by fresh, ground level,  $\text{NO}_x$  emissions. In the stable layers dark phase reactions occur which can deplete the ozone. The principal mechanism elements and reaction rate constants from Hampson and Garvin (1977) are:





(a)



(b)

FIGURE 2.2

Vertical Profiles of Ozone, Temperature and b<sub>scatter</sub> over El Monte Airport (a) 1247 PDT and (b) 1656 PDT. (Blumenthal et al., 1978)

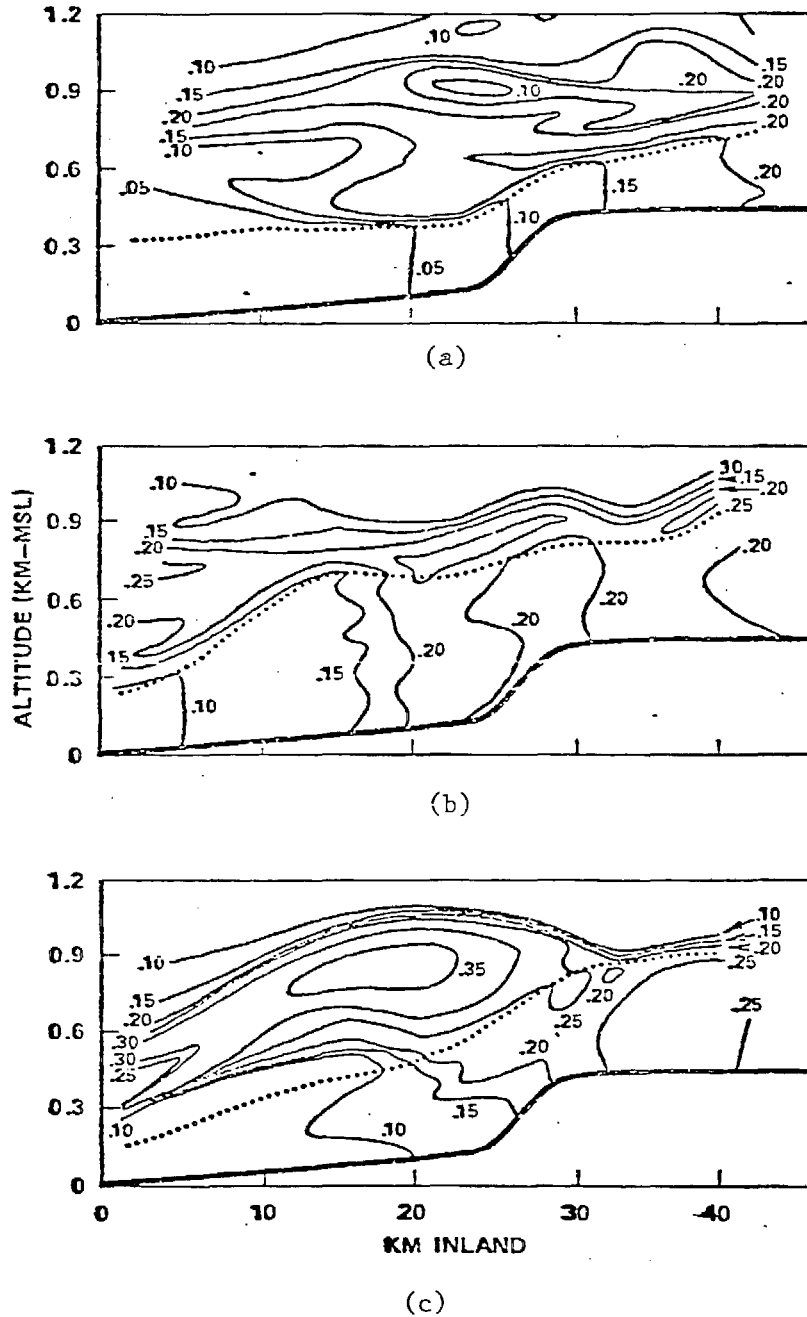
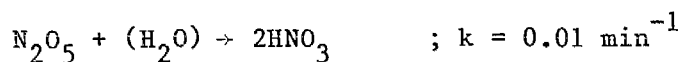
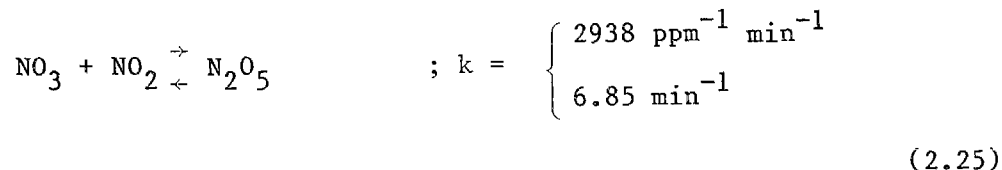


FIGURE 2.3

Contours of Oxidant Concentrations (ppm) in the Vertical Cross Section from Santa Monica to Rialto-Miro, As Observed by Edinger (1973).  
 (a) 0900 PDT, (b) 1200 PDT, (c) 1630 PDT 20 June 1970  
 Dotted Curve Denotes Inversion Base



Since by late afternoon the NO concentration levels are already quite small, substantial levels of O<sub>3</sub> can remain aloft. In addition, the little NO<sub>2</sub> that is left can be removed by:



The details of the reaction steps are not of major importance; what is of significance is that O<sub>3</sub> produced during one day can be trapped aloft and be fumigated to the ground during the next day. The sequence of events is illustrated in a highly simplified form in Figure 2.4. After sunrise ground heating generates a growing mixed layer which eliminates the stable stratification. As the convective layer grows in depth, material is rapidly entrained and mixed downward. As soon as the layer reaches the height of the high O<sub>3</sub> levels, the ground level concentrations of ozone can be abruptly increased. There is a variety of alternate physical mechanisms which can produce fumigation conditions and they, together with some laboratory experiments, are described in Manins (1977). Zeman and Tennekes (1977) have recently reviewed the literature and presented a parameterized model of the entrainment dynamics at the top of the mixed layer. Zeman and Lumley (1976) have used a second-order closure model to investigate stratified turbulent flows with particular applications to buoyancy driven mixed layers.

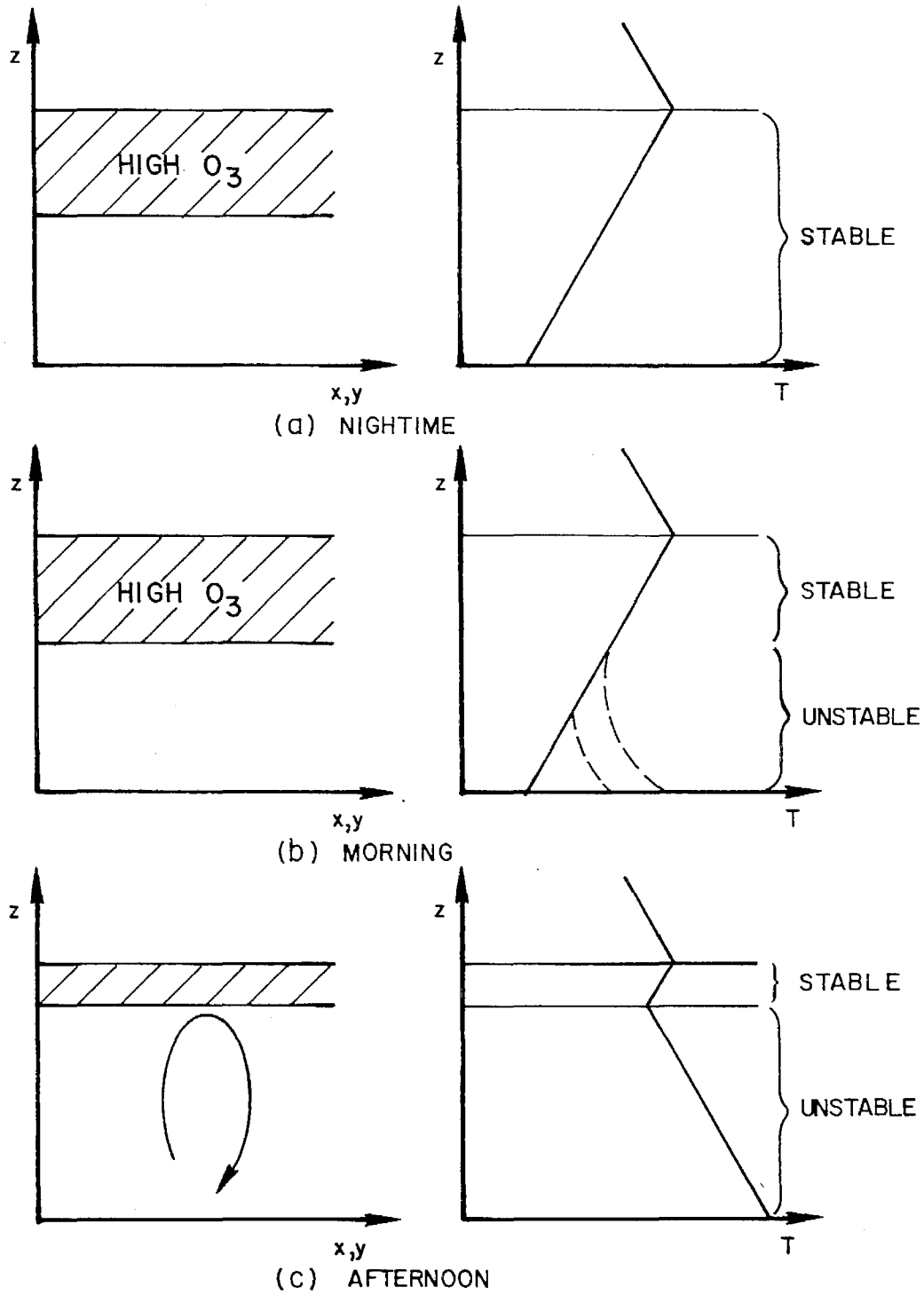


FIGURE 2.4

Sequence of Events Leading to Entrainment of Ozone From Stable Layers Aloft into the Surface Well-Mixed Layer

From the above discussion it is clear that unless upper level concentration data are available, or the airshed is ventilated at night, correct specification of the boundary conditions at the top of the mixed layer is likely to be a difficult problem. An approach which alleviates some of the difficulties is to include computational cells above the mixed layer and to run the airshed model throughout the night. With this method, ozone can be trapped aloft at night and fumigated the next day. Boundary layer growth and entrainment can be modeled by variations in the vertical eddy diffusivity profile. With a combination of time-varying grid spacing and  $K(z)$  profiles, considerable flexibility can be attained in practice.

#### 2.10 Initial and Boundary Conditions

To complete the mathematical formulation of the airshed model both the initial and boundary conditions need to be specified. In general the boundary conditions for the model represent statements of mass continuity across the bounding surfaces of the airshed. For parabolic systems like the atmospheric diffusion equation, the inhomogeneous mixed Neumann and Dirichlet boundary condition covers most cases. Normal to the boundary in direction  $\hat{n}$  this condition can be written in the form

$$[\underline{a}c + \underline{b}\nabla c] \cdot \hat{n} = \underline{f} \quad (2.26)$$

where  $\underline{a}$ ,  $\underline{b}$  and  $\underline{f}$  are defined for the particular application. Consider, first, the ground level boundary conditions

$$[V_g^i c_i - K_{zz} \frac{\partial c_i}{\partial z}] = E_a(x,t) \quad (2.27)$$

where  $E_a$  is the mass flux per unit area of species  $c_i$ ,  $K_{zz}$  the vertical eddy diffusivity and  $v_g^i$  the equivalent pollutant deposition velocity. At the ground the vertical velocity  $w$  is zero. The term  $v_g^i c_i$ , which has been omitted in many previous studies, has been included to parameterize the interaction of the pollutant material with the ground. Chapter 6 presents a model for evaluating the magnitude of the surface removal flux.

The remainder of the boundary conditions are identical to those chosen by Reynolds et al. (1973). At the top of the airshed,  $z = H(x,y,t)$ , the conditions are given by

$$\begin{aligned} [\underline{V}c_i - K\nabla c_i] \cdot \hat{\underline{n}} &= \underline{V}c_i^b \cdot \hat{\underline{n}} & ; \underline{V} \cdot \hat{\underline{n}} \leq 0 \\ -K\nabla c_i \cdot \hat{\underline{n}} &= 0 & ; \underline{V} \cdot \hat{\underline{n}} > 0 \end{aligned} \quad (2.28)$$

where  $\underline{V}$ , the advective velocity of pollutants relative to the top of the airshed, is given by

$$\underline{v} = u\underline{i} + v\underline{j} + (w - \frac{\partial H}{\partial t})\underline{k} \quad (2.29)$$

In (2.28)  $\hat{\underline{n}}$  is the unit vector normal to the surface defining the top of the airshed and  $c_i^b(\underline{x},t)$  is the mean concentration of species  $i$  outside the modeling region. The case of a fixed domain corresponds to the condition  $\partial H / \partial t = 0$ . The two conditions in (2.28) correspond to the case when material is transported into the region,  $(\underline{V} \cdot \hat{\underline{n}}) \leq 0$ , and

out of the region,  $(\underline{V} \cdot \hat{\underline{n}}) > 0$ . This second condition must be carefully evaluated in practical applications of the model when H could be below the top of the convective mixed layer. In most circumstances the top of the airshed is in a stable layer in which case the turbulent transport is likely to be quite small and most material is removed by advection. The horizontal boundary conditions are similar to (2.28) and are given by:

$$\begin{aligned} [\underline{U}c_i - K\nabla c_i] \cdot \hat{\underline{n}} &= U c_i^b \cdot \hat{\underline{n}} & ; \underline{U} \cdot \hat{\underline{n}} \leq 0 \\ - K\nabla c_i \cdot \hat{\underline{n}} &= 0 & ; \underline{U} \cdot \hat{\underline{n}} > 0 \end{aligned} \quad (2.30)$$

where  $\hat{\underline{n}}$  is the unit vector normal to the horizontal boundary,  $c_i^b(x,t)$  is the concentration outside of the airshed and  $\underline{U}$  is the advective velocity  $\underline{U} = u\hat{i} + v\hat{j}$  in the horizontal plane. The second condition ( $\underline{U} \cdot \hat{\underline{n}} > 0$ ) states that the turbulent transport is zero, an approximation that is usually satisfied due to the dominance of the horizontal advection. Outflow boundary conditions are a major source of difficulty in implementing numerical solution procedures and for this reason will be discussed further in Chapter 10.

### 2.11 Validity and Accuracy of the Atmospheric Diffusion Equation

An obvious question after all the preceding simplifications is to ask if the atmospheric diffusion equation is an adequate representation of the ensemble mean concentration  $\langle c_i \rangle$ . Formally, the validity of (2.23) relates to how closely the predicted mean concentration  $\langle c_i \rangle$  corresponds to the true ensemble mean value. If the true ensemble mean

velocities and concentrations are known for a particular flow field, then it is relatively straightforward to assess the model validity for different K, R and S. Unfortunately, in the boundary layer the ensemble mean velocities and concentrations can never be computed because the atmosphere presents only one realization of the flow at any time. Because the true mean velocities, concentrations and source emission rates are not available an unambiguous measure of the validity of (2.23) for any particular flow cannot be obtained.

Using the results of Lamb (1971), Lamb and Seinfeld (1973) and Reynolds et al. (1973) it is possible, however, to establish a set of conditions which must be satisfied if (2.23) is to be a valid representation of atmospheric transport and chemical reaction. The background discussions and data necessary to develop these conditions are extensively discussed in the above references and will not be reiterated here. In summary, however, Reynolds et al. (1973) concluded that the basic model is applicable for resolving those perturbations in the concentration field which have horizontal scales greater than 2 Km, vertical scales greater than 20 m and temporal scales greater than 1000 seconds. These conditions serve as a guide to the choice of grid size and averaging time to be used in the numerical solution procedures.

Table 2.2 summarizes the principal approximations which could be a source of invalidity in an urban scale airshed model. Although the validity cannot be established without question, it is generally accepted that the atmospheric diffusion equation is essentially a correct description of transport, mixing, and chemical reaction

Table 2.2 Sources of Invalidity in Air Quality Models

Source of Error	Comment
A. True form of the turbulent fluxes, $\overline{u'c_1'}$ , $\overline{v'c_1'}$ , $\overline{w'c_1'}$ , is unknown.	Higher order closure models will offer improvement over eddy diffusivities in representing these terms. Such closure methods lead to large computational requirements.
B. Turbulent fluctuating chemical reaction terms are neglected.	Closure models appropriate for turbulent chemistry can be developed but large computational requirements as above may arise.
C. Effect of concentration fluctuations from spatial averaging on chemical reaction rate is neglected.	Introduce "micro-scale model" in regions where strong point and line sources occur.

processes. The major source of invalidity is probably the eddy diffusion representation of the turbulent fluxes. However, as long as the eddy diffusivity functions used in the model have been determined empirically under similar conditions to those to which the equation is applied, then the approximation should be considered valid.

Accepting the validity of the formulation (2.23) the next question which must be addressed is, how accurate are the model predictions? Accuracy-evaluation is an assessment of the errors induced by inaccuracies in the input information. Another term often used in connection with model evaluation is 'verification', referring to the agreement between predictions and observations for the specific case in which the observations used for verification were taken from the same pool of data used to develop the input information for the model. Verification contains elements of both validation and accuracy evaluation.

Accuracy evaluations can be made using estimates of the errors associated with the input information and from numerical sensitivity tests which assess the impact on concentration predictions. The inputs needed to solve the atmospheric diffusion equation together with possible sources of error are shown in Table 2.3. In each instance unless the actual value of the input is known, the level of error in that input can only be estimated. From the standpoint of the effect of errors on the predictions of the atmospheric diffusion equation, joint consideration must be given to the level of uncertainty in each input parameter and the sensitivity of the predicted concentrations to the parameter. Uncertainty relates to the possible error in the parameter

Table 2.3 Sources of Inaccuracy in Air Quality Models

Source of Error	Comment
<p>A. Mean velocities <math>\bar{u}</math>, <math>\bar{v}</math>, <math>\bar{w}</math> are not true ensemble means (usually <math>u</math>, <math>v</math> and <math>w</math> are calculated from data at a finite number of locations).</p>	<p>There <u>is</u> no way to determine the true mean from the data; <math>u</math>, <math>v</math>, <math>w</math> can be calculated in principle from accurate fluid mechanical turbulence model.</p>
<ol style="list-style-type: none"> <li>1. Uncertainties in the measurement of wind speed and direction.</li> <li>2. Inadequate or non-representative spatial measurements of wind speed and direction.</li> <li>3. Uncertainties associated with wind field analysis techniques.</li> </ol>	
<p>B. Source emission function <math>E_i</math> is inaccurate.</p>	<p>More detailed emission inventories needed to reduce this source of inaccuracy.</p>
<ol style="list-style-type: none"> <li>1. Inaccurate or no specification of source location.</li> <li>2. Uncertainties in emission factors.</li> <li>3. Inaccurate or no temporal resolution of emission.</li> <li>4. Inadequate or no verification of emission methodologies.</li> </ol>	

Table 2.3 (continued)

Source of Error	Comment
<p>C. Chemical reaction mechanism does not accurately reflect those chemical processes occurring in the atmosphere.</p> <ol style="list-style-type: none"> <li>1. Uncertainties in experimental determinations of specific reaction rate constants.</li> <li>2. Variations of rate constants with temperature either uncertain or unknown.</li> <li>3. Inadequacies in lumping due to the non-representativeness of lumped class reactions relative to specific species within the class, e.g., reaction rates, products, and stoichiometric coefficients.</li> <li>4. Inaccuracies in the mechanism due to insufficient verification studies.</li> </ol>	<p>Continued study of chemical processes needed to insure that <math>R_1</math> is accurate. Elimination or quantification of smog chamber related errors:</p> <ol style="list-style-type: none"> <li>1. Inadequate or lack of control and measurement of levels of <math>H_2O</math> in the chamber.</li> <li>2. Impurities in background chamber air.</li> <li>3. Inadequate or lack of measurements of the spectral distribution and intensity of the chamber irradiation system.</li> <li>4. Inaccurate or ambiguous analytical methods.</li> <li>5. Non-homogeneity due to inadequate stirring or poor chamber design.</li> <li>6. Absorption and desorption of reactants and products on chamber walls.</li> <li>7. Chemical reactions occurring on chamber surfaces.</li> <li>8. Inadequate control and measurement of chamber temperature.</li> </ol>
<p>D. Boundary conditions inaccurately specified.</p> <ol style="list-style-type: none"> <li>1. Concentrations</li> <li>2. Inversion height</li> </ol>	<p>No remedy except for more extensive data.</p>

from its true value, and sensitivity refers to the effect that variation in that parameter has on the solution of the equation. A parameter may have a large uncertainty associated with it but have little influence on the solution. In such a case, effort at reducing the uncertainty may be unwarranted. Conversely small uncertainties in some parameters may have a large impact on the concentration predictions. Thus, both uncertainty and sensitivity must be considered when evaluating the accuracy of the atmospheric diffusion equation. The issues are discussed in detail in Chapters 12 and 13. Finally it must be noted that discrepancies between predicted and measured concentrations may arise because of the basic difference in the nature of the averaging or experimental uncertainties. Field measurements are typical point estimates whereas model predictions are volume averages.

The basic objective of this section has been to explore some of the background questions related to the validity and accuracy of the atmospheric diffusion equation. These considerations are important factors which influence the nature and scope of the air pollution problems which can be addressed with an airshed model.

## 2.12 Simplified Forms of the Atmospheric Diffusion Equation

The previous discussions were focussed on the development of a single mathematical model which could be used to predict the formation and transport of photochemical air pollution. While the basic objective was to introduce a comprehensive description of atmospheric concentration dynamics there are circumstances where it is desirable to use

less complex forms of the governing equation for screening purposes. This chapter presents a discussion of Lagrangian, vertically integrated and single cell box models, all of which are based on various reduced or averaged forms of the atmospheric diffusion equation. Since these models form subcomponents of the airshed modeling system it is essential to be aware of the limitations imposed by the simplifying assumptions. All of the models to be described incorporate the effects of time dependent emission sources, surface removal phenomena, non-linear chemistry and unsteady meteorology. Unless these processes are included, the contracted formulations are of little use in practical calculations.

While the atmospheric diffusion equation (2.23) is ideally suited for predicting the concentration distribution over extended areas, there are many situations where the air quality impact only needs to be calculated at a particular location. A trajectory model that follows a parcel of air as it traverses the airshed can often be used in these circumstances. Such models are based on a Lagrangian formulation where the co-ordinate system is advected by the horizontal wind field. If the concentration distribution is required over a large area then computational cost associated with multiple trajectories can become comparable to the fixed or Eulerian grid approaches. The most common representation of a trajectory model (Eschenroeder and Martinez, 1972; Lloyd et al., 1979) can be expressed in the form

$$\frac{\partial c}{\partial t} = \frac{\partial}{\partial z} K_{zz} \frac{\partial c}{\partial z} + R(c) \quad (2.31)$$

Given the widespread use of this formulation it is useful to examine the assumptions which must be adopted to derive the model from the atmospheric diffusion equation (2.23). If a column of air is advected by the wind then the appropriate change of variables from the fixed system  $[x,y,z,t]$  to the moving co-ordinate system  $[\xi,\eta,z,t]$  is given by (Aris, 1962)

$$\begin{aligned}\xi &= \xi(x,y,t) \\ \eta &= \eta(x,y,t) \\ z &= z \\ t &= t\end{aligned}\tag{2.32}$$

With this set of transformations the Lagrangian form of the atmospheric diffusion equation, for a divergence-free flow field, is given by

$$\begin{aligned}\frac{\partial c}{\partial t} &= \frac{\partial}{\partial \xi} K_{xx} \frac{\partial c}{\partial \xi} \left(\frac{\partial \xi}{\partial x}\right)^2 + \left[\frac{\partial}{\partial \xi} K_{xx} \frac{\partial c}{\partial \eta} + \frac{\partial}{\partial \eta} K_{xx} \frac{\partial c}{\partial \xi}\right] \left(\frac{\partial \xi}{\partial x}\right) \left(\frac{\partial \eta}{\partial x}\right) + \\ &\frac{\partial}{\partial \eta} K_{xx} \frac{\partial c}{\partial \eta} \left(\frac{\partial \eta}{\partial x}\right)^2 + \frac{\partial}{\partial \xi} K_{yy} \frac{\partial c}{\partial \xi} \left(\frac{\partial \xi}{\partial y}\right)^2 + \left[\frac{\partial}{\partial \xi} K_{yy} \frac{\partial c}{\partial \eta} + \frac{\partial}{\partial \eta} K_{yy} \frac{\partial c}{\partial \xi}\right] \left(\frac{\partial \xi}{\partial y}\right) \left(\frac{\partial \eta}{\partial y}\right) + \\ &\frac{\partial}{\partial \eta} K_{yy} \frac{\partial c}{\partial \eta} \left(\frac{\partial \eta}{\partial y}\right)^2 + \frac{\partial}{\partial z} K_{zz} \frac{\partial c}{\partial z} - w \frac{\partial c}{\partial z} + R(c) - \\ &\left[\frac{\partial \xi}{\partial t} + u \frac{\partial \xi}{\partial x} + v \frac{\partial \xi}{\partial y}\right] \left(\frac{\partial c}{\partial \xi}\right) - \left[\frac{\partial \eta}{\partial t} + u \frac{\partial \eta}{\partial x} + v \frac{\partial \eta}{\partial y}\right] \left(\frac{\partial c}{\partial \eta}\right)\end{aligned}\tag{2.33}$$

This is a more general expression of the model presented in Liu and Seinfeld (1975). Clearly, if this equation is to be reduced to the form (2.32) then a number of simplifying assumptions need to be invoked. The first is that the vertical advective transport must be small in comparison to the turbulent diffusion, i.e.

$$\frac{\partial}{\partial z} K_{zz} \frac{\partial c}{\partial z} \gg \left| w \frac{\partial c}{\partial z} \right|\tag{2.34}$$

If meteorological conditions are such that the vertical component of the wind field is large then the advective transport term  $w \frac{\partial c}{\partial z}$  can be easily retained in the formulation. Another major assumption is that the loss, or gain, of material from horizontal diffusion is negligible. If the horizontal concentration gradients are small then the appropriate terms involving  $K_{xx}$  and  $K_{yy}$  can be justifiably omitted. Since the co-ordinate system  $[\xi, \eta, z, t]$  is advected by the flow field the only way that the column of air can retain its vertical integrity is if the effects of wind shear can be neglected, i.e.

$$u(x, y, z, t) = u(x, y, t) \quad (2.35)$$

$$v(x, y, z, t) = v(x, y, t) \quad (2.36)$$

This is a critical assumption and a major source of error in many trajectory model calculations, especially those which involve long transport times. A quantitative assessment of each of the above simplifications is presented in Liu and Seinfeld (1975).

Another alternative which has been adopted to cut down the computational cost of using the full scale airshed model is to reduce the number of spatial dimensions. For many applications the vertical mixing is sufficiently rapid to enable the atmospheric transport to be considered as a two-dimensional problem. This approach is often used in hydraulic modeling where it is more commonly known as the shallow water analogy (Galloway, 1976; Yotsukura, 1977). Most of the basic concepts were initiated by Taylor (1954) and refined by Aris (1956). Atmospheric

applications of the procedures are described in Saffman (1962), Gallo-way (1976) and MacCracken et al. (1978).

If the functions  $h(x,y)$  and  $H(x,y,t)$  define the lower and upper boundaries of the airshed then the equivalent vertical average value of a variable  $p$  can be defined as

$$\overline{p(t)} = \frac{1}{H(x,y,t) - h(x,y)} \int_h^H p(x,y,z,t) dz \quad (2.37)$$

By integrating (2.23) between the limits  $h(x,y)$ ,  $H(x,y,t)$  and applying the Liebnitz rule for differentiation under the integral sign (Sokol-nikoff and Redheffer, 1958), the equivalent vertically averaged form of the atmospheric diffusion equation is given by

$$\begin{aligned} & \frac{\partial(H-h)\overline{c}}{\partial t} + \frac{\partial(H-h)\overline{uc}}{\partial x} + \frac{\partial(H-h)\overline{vc}}{\partial y} + A \\ = & \frac{\partial(H-h)}{\partial x} \overline{K_{xx} \frac{\partial c}{\partial x}} + \frac{\partial(H-h)}{\partial y} \overline{K_{yy} \frac{\partial c}{\partial y}} + B + (H-h)\overline{R(c)} \end{aligned} \quad (2.38)$$

where

$$\begin{aligned} A = & c(h)\frac{\partial h}{\partial t} - c(H)\frac{\partial H}{\partial t} + u(h)c(h)\frac{\partial h}{\partial x} - u(H)c(H)\frac{\partial H}{\partial x} \\ & + v(h)c(h)\frac{\partial h}{\partial y} - v(H)c(H)\frac{\partial H}{\partial y} - w(h)c(h) + w(H)c(H) \end{aligned} \quad (2.39)$$

$$\begin{aligned} B = & K_{xx}(h)\frac{\partial c}{\partial x}\Big|_h \cdot \frac{\partial h}{\partial x} - K_{xx}(H)\frac{\partial c}{\partial x}\Big|_H \cdot \frac{\partial H}{\partial x} + K_{zz}(H)\frac{\partial c}{\partial z}\Big|_H \\ & + K_{yy}(h)\frac{\partial c}{\partial y}\Big|_h \cdot \frac{\partial h}{\partial y} - K_{yy}(H)\frac{\partial c}{\partial y}\Big|_H \cdot \frac{\partial H}{\partial y} - K_{zz}(h)\frac{\partial c}{\partial z}\Big|_h \end{aligned} \quad (2.40)$$

The terms A and B in (2.39) can be simplified by utilizing the boundary constraints

$$dz = \frac{\partial h}{\partial t} dt + \frac{\partial h}{\partial x} dx + \frac{\partial h}{\partial y} dy \quad (2.41)$$

$$dz = \frac{\partial H}{\partial t} dt + \frac{\partial H}{\partial x} dx + \frac{\partial H}{\partial y} dy \quad (2.42)$$

At the upper surface there are two cases to consider

$$K \nabla c \cdot \hat{\underline{n}} = 0 \quad \text{if} \quad \underline{V} \cdot \hat{\underline{n}} > 0 \quad (2.43)$$

and

$$[\underline{V}c - K \nabla c] \cdot \hat{\underline{n}} = (\underline{V}c^b) \cdot \hat{\underline{n}} \quad \underline{V} \cdot \hat{\underline{n}} \leq 0 \quad (2.44)$$

where  $\underline{V}$ , the relative vertical velocity, is defined by

$$\underline{V} = u \underline{i} + v \underline{j} + (w - \frac{\partial H}{\partial t}) \underline{k} \quad (2.45)$$

and  $\underline{n}$  is the unit normal to the surface  $H(x,y,t)$  which is given by

$$\hat{\underline{n}} = \frac{-\frac{\partial H}{\partial x} \underline{i} - \frac{\partial H}{\partial y} \underline{j} + \underline{k}}{\sqrt{(\frac{\partial H}{\partial x})^2 + (\frac{\partial H}{\partial y})^2 + 1}} \quad (2.46)$$

Combining (2.39 - 2.46) enables the A term to be reduced to

$$A = \begin{cases} 0 & ; \underline{V} \cdot \hat{\underline{n}} > 0 \\ (c - c^b) [(w - \frac{\partial H}{\partial t}) + u(H) \frac{\partial H}{\partial x} + v(H) \frac{\partial H}{\partial y}] & ; \underline{V} \cdot \hat{\underline{n}} \leq 0 \end{cases} \quad (2.47)$$

At the lower level the appropriate boundary condition is given by

$$v_g c - K \nabla c = E_a(\underline{x}, t) \quad (2.48)$$

where  $v_g$  is the deposition velocity and  $E_a(\underline{x}, t)$  is the emission flux term. Using the same procedure used to derive (2.47) the B term becomes

$$B = E_a(\underline{x}, t) - v_g c \quad (2.49)$$

The final averaged form of the atmospheric diffusion equation is then given by

$$\begin{aligned} \frac{\partial (H-h)\bar{c}}{\partial t} + \frac{\partial (H-h)\overline{uc}}{\partial x} + \frac{\partial (H-h)\overline{vc}}{\partial y} = \\ \frac{\partial (H-h)\overline{K_{xx}}}{\partial x} \frac{\partial \bar{c}}{\partial x} + \frac{\partial (H-h)\overline{K_{yy}}}{\partial y} \frac{\partial \bar{c}}{\partial y} + A + E_a - v_g \bar{c} + (H-h)\overline{R(c)} \end{aligned} \quad (2.50)$$

From an inspection of (2.50) it is apparent that the presence of terms of the form  $\overline{uc}$ ,  $\overline{vc}$  and  $\overline{R(c)}$  creates a difficulty similar to the turbulent closure problem described in Section 2.5. Applying the Reynolds averaging rules and a K-Theory closure hypothesis to the differential advective flux terms results in

$$\overline{uc} = \overline{u} \bar{c} + \overline{u'c'} = \overline{u} \bar{c} - K_{xx}^a \frac{\partial \bar{c}}{\partial x} \quad (2.51)$$

$$\overline{vc} = \overline{v} \bar{c} + \overline{v'c'} = \overline{v} \bar{c} - K_{yy}^a \frac{\partial \bar{c}}{\partial y} \quad (2.52)$$

where the primed quantities represent deviations from the vertical average values. If it is further assumed that

$$\overline{K_{xx} \frac{\partial c}{\partial x}} = \overline{K_{xx}} \frac{\partial \bar{c}}{\partial x} \quad (2.53)$$

$$\overline{K_{yy} \frac{\partial c}{\partial y}} = \overline{K_{yy}} \frac{\partial \bar{c}}{\partial y} \quad (2.54)$$

and

$$\overline{R(c_1, \dots, c_p)} \approx R(\bar{c}_1, \dots, \bar{c}_p) \quad (2.55)$$

The final form of the vertically integrated atmospheric diffusion is then given by

$$\begin{aligned} \frac{\partial(H-h)\bar{c}}{\partial t} + \frac{\partial(H-h)\bar{u}\bar{c}}{\partial x} + \frac{\partial(H-h)\bar{v}\bar{c}}{\partial y} = \\ \frac{\partial}{\partial x} K_{xx}^e \frac{\partial \bar{c}}{\partial x} + \frac{\partial}{\partial y} K_{yy}^e \frac{\partial \bar{c}}{\partial y} + A + E_a - v_g \bar{c} + (H-h)R(\bar{c}) \end{aligned} \quad (2.56)$$

where the effective diffusion coefficients are given by

$$K_{xx}^e = (H-h) [ \overline{K_{xx}} + K_{xx}^a ] \quad (2.57)$$

$$K_{yy}^e = (H-h) [ \overline{K_{yy}} + K_{yy}^a ] \quad (2.58)$$

One of the most critical assumptions in the above derivation was that the vertical average reaction rate is the same as the rate based on vertical average concentration profiles. For this approximation to be true, the time scale of the reaction must be much slower than the characteristic mixing time. If there are any persistent steep gradients in the vertical concentration profiles then the closure assumption is clearly violated for nonlinear reaction systems.

In an attempt to circumvent the difficulty MacCracken et al. (1978) proposed that the vertical species distribution be described by an expression of the form

$$c_i(z) = a_i + b_i \ln\left(\frac{z}{z_r}\right) \quad (2.59)$$

where  $z_r$  is a reference height = 1 m and the constants  $a_i$ ,  $b_i$  are determined from the boundary conditions. With an analytic expression for  $c(z)$  it is possible to derive the correct forms of the reaction rates. For example, if the product  $c_j c_k$  appears in  $R_i$  and terms of the order  $O(z_r/H)$  are neglected then the vertical average rate is given by

$$\overline{c_j c_k} = \frac{1}{H-z_r} \int_{z_r}^H c_j c_k dz = \overline{c_j} \overline{c_k} + b_j b_k \quad (2.60)$$

Unfortunately the validity of the profile assumption, (2.59), has not been established for rapidly reacting species.

Whether or not a vertically integrated model is appropriate for a particular application or chemical species depends to a large extent on the characteristic mixing time. For unstable conditions Smith et al. (1976) calculated the frequency distribution of the convective mixing time  $\lambda$  from field measurements in the Los Angeles Basin. The characteristic mixing time is given by

$$\lambda = \frac{Z_i}{w_*} \quad (2.61)$$

where  $Z_i$  is the depth of the convective mixed layer and  $w_*$  is the convective velocity scale defined by

$$w_* = \left(-\frac{1}{k} \frac{z_i}{L}\right)^{1/3} u_* \quad (2.62)$$

In this expression  $k$  is the von Karman constant,  $u_*$  the friction velocity and  $L$  is the Monin-Obukhov length. The results of their correlations are shown in Figure 2.5. For unstable conditions Deardorff and Willis (1974) have shown that material released at the surface becomes nearly well mixed within a travel time of  $3\lambda$ . The mean value of  $\lambda$  is 210 seconds and so within a time step of 0(10 minutes) slowly reacting pollutants can be considered to be well mixed. Thus when the inversion base is low and the mixed layer is unstable (both conditions implicit in the above data) it should be possible to produce acceptable concentration estimates using only a two-dimensional, vertically-integrated model (Smith et al., 1976). This conjecture cannot be satisfactorily generalized until more experimental data becomes available.

There is another approach which can be used to estimate the time after which a surface or elevated pollutant release can be considered to be well mixed. This procedure involves calculating the moments of the concentration distribution, where the  $(n,m)$ -moment is defined by

$$c^{n,m} = \int_{-\infty}^{\infty} \int_{-\infty}^{\infty} x^n y^m c \, dx dy \quad (2.63)$$

Assuming that  $c(\underline{x},t) \rightarrow 0$  sufficiently rapidly with  $x,y$  then the moments can be calculated from the sequence

$$\begin{aligned} \frac{\partial c^{n,m}}{\partial t} + \frac{\partial w c^{n,m}}{\partial z} &= -nuc^{n-1,m} - mvc^{n,m-1} + \frac{\partial}{\partial z} K_{zz} \frac{\partial c^{n,m}}{\partial z} \\ &+ n(n-1)K_{xx} c^{n-2,m} + m(m-1)K_{yy} c^{n,m-2} \end{aligned} \quad (2.64)$$

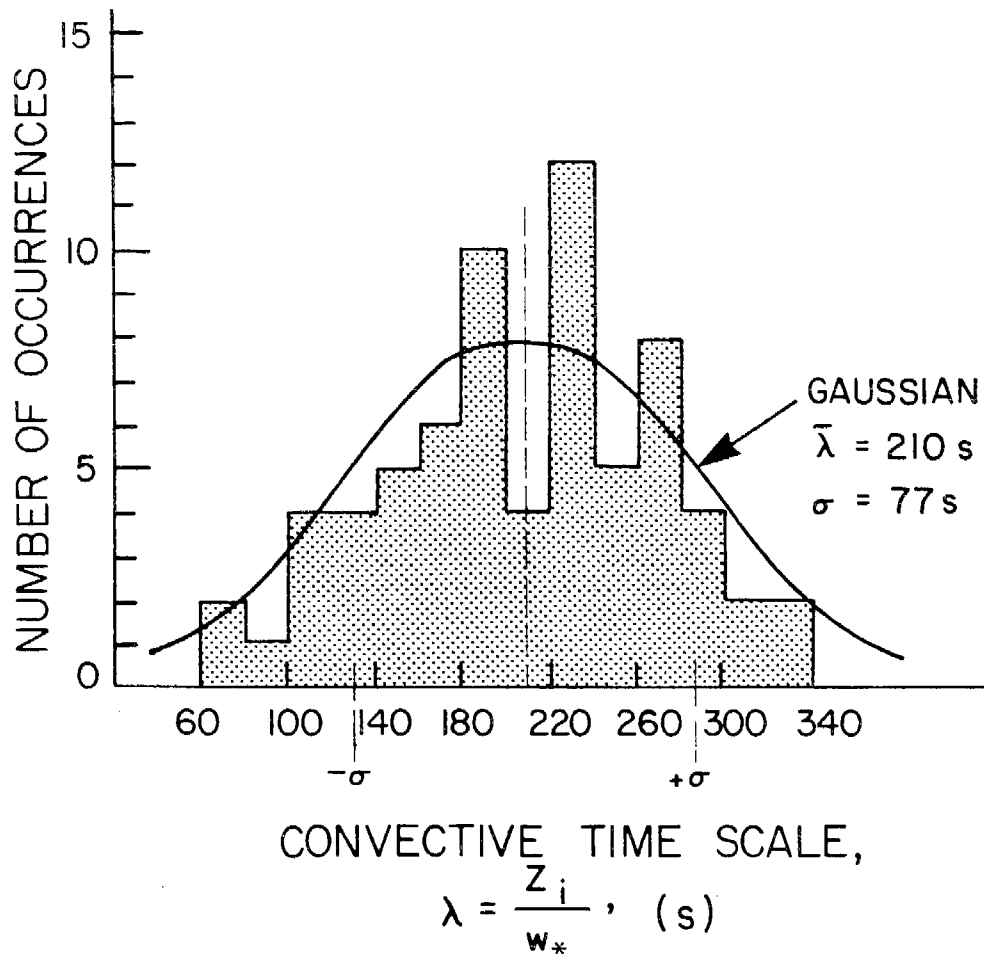


FIGURE 2.5

Frequency Distribution of the Convective Mixing Time Scale  $\lambda$  Observed in the Los Angeles Marine Layer for Different Times (Source: Smith et al. 1976)

Given the moment equations it is possible to solve the Sturm-Liouville problem, formed by (2.64) and its boundary conditions, for the variance of the concentration distribution. The time for the variance to tend to a constant value corresponds to the characteristic mixing time. Saffman (1962) established a bound  $\lambda > Z_i^2 / 2K_{zz}$  for problems in which the vertical profiles of wind and diffusivities can be described by power laws. Unfortunately, for all but the simplest applications (2.64) must be solved numerically. The fact that it is a one-dimensional problem does, however, considerably simplify the computational task.

An even further reduced photochemical model can be derived if the spatial averaging is carried out over the whole airshed and the resulting formulation is a single or box model. While extensive use has been made of box models (Graedel et al., 1976; Whitten and Hogo, 1976), the set of assumptions which must be invoked to justify their use severely limits the range of valid applications. Unless the meteorological and source distributions are sufficiently simple and uniform, the box approach should not be used for modeling concentration distributions in urban airshed. Further details of these models are presented in Chapter 8.

### 2.13 Conclusions

In this chapter most of the basic assumptions required to produce a practical airshed modeling system have been discussed. The formulation of such a system is a difficult undertaking because it is necessary to maintain a balance between the need for computational economy

and the desire for an accurate representation of the underlying physics and chemistry. The atmospheric diffusion equation, and its various reduced forms, form the basis of a set of mathematical models which can be used to describe the formation and transport of urban scale photochemical air pollution. Subsequent chapters in this study are devoted to a detailed treatment of the model components and required inputs.



## CHAPTER 3

## OBJECTIVE ANALYSIS PROCEDURES

3.1 Introduction

A major simplifying assumption adopted in the previous chapter was that the presence of pollutant gases and aerosols does not significantly affect urban scale meteorology. The importance of this approximation is that it allows the concentration dynamics to be decoupled from the equations which describe the flow fields over the airshed. While this approach reduces the complexity of the computational problem it does not remove the need for a priori specification of the velocity and mixing characteristics. In addition the initial concentration distribution is needed as part of the solution procedures. This chapter is devoted to a detailed presentation of the objective analysis techniques which can be used to generate the necessary model inputs.

As with many other aspects of this study the intent is to develop procedures which only employ readily available or routinely measured data. In many cases it is this requirement which limits characterization of the different processes and not the understanding of the physical phenomena. Subsequent sections discuss the interpolation procedures, objective analysis techniques and practical applications of the different methodologies.

3.2 A Comparison of Interpolation Methods for Sparse Data:  
Application to Wind and Concentration Fields

(Reprinted from J. Applied Meteorology, 18, 761-771.)

## A Comparison of Interpolation Methods for Sparse Data : Application to Wind and Concentration Fields

WILLIAM R. GOODIN,<sup>1</sup> GREGORY J. MCRAE AND JOHN H. SEINFELD

*Environmental Quality Laboratory, California Institute of Technology, Pasadena 91125*

(Manuscript received 1 December 1978, in final form 23 February 1979)

### ABSTRACT

In order to produce gridded fields of pollutant concentration data and surface wind data for use in an air quality model, a number of techniques for interpolating sparse data values are compared. The techniques are compared using three data sets. One is an idealized concentration distribution to which the exact solution is known, the second is a potential flow field, while the third consists of surface ozone concentrations measured in the Los Angeles Basin on a particular day. The results of the study indicate that fitting a second-degree polynomial to each subregion (triangle) in the plane with each data point weighted according to its distance from the subregion provides a good compromise between accuracy and computational cost.

### 1. Introduction

A problem common to many disciplines is the development of continuous fields from discrete data sets. For example, in meteorology, wind fields are often generated using a two-step procedure. The first element is the interpolation of the raw station data to a finer mesh. Objective analysis procedures are then employed to adjust the wind vectors at each grid point so that an applied physical constraint, such as minimum field divergence, is satisfied. Much of the literature is devoted to the second step; what is frequently neglected is that the final form of the field is often critically dependent on the results of the initial interpolation. Formally, the objective of this paper is to address the problem: given a bounded region of  $r$ -space containing  $n$ , error-free data values  $C_i$ , at locations  $\mathbf{x}^i = [x_1^i, \dots, x_n^i]$ ,  $i = 1, 2, \dots, n$ , develop a function,  $f(\mathbf{x})$ , which will assign a value of  $C$  at any arbitrary location  $\mathbf{x}$ . While simply stated, there is, in general, no unique solution to the interpolation problem. As a result, when alternative techniques are applied to the same discrete data set, different fields are generated. This study was undertaken to identify and test computationally efficient methods for interpolating sparse data measurements onto a regular mesh.

### 2. A survey of methods for interpolation of sparse data

#### a. Weighted interpolation methods

A common approach to interpolation of sparse data onto a regular grid is to assume that the grid value

is some weighted average of the surrounding data values, i.e.,

$$C_{ij} = \sum_{k=1}^n C_k W_k(r) / \sum_{k=1}^n W_k(r), \quad (1)$$

where  $C_k$  is the measured value at the  $k$ th measuring station,  $W_k(r)$  the weighting function, and  $r$  the distance from the grid point to the station.

In an early study, Cressman (1959) reported on a procedure for use in pressure-surface height analysis which used the weighting factor

$$W(r) = \frac{R^2 - r^2}{R^2 + r^2}, \quad (2)$$

where  $R$  is the distance at which the weighting factor goes to zero, i.e., the "radius of influence." This weighting technique aided the interpolation procedure in areas of sparse data. Decreasing values of  $R$  were used on successive scans to analyze a spectrum of scales. The values obtained from each scan were then averaged to produce the final field.

Endlich and Mancuso (1968) combined both polynomial fitting and distance weighting in their interpolation technique. A least-squares fit to a first-order polynomial was performed using five of the nearest station values, according to

$$W(r) = \frac{a}{(r + r^*)^2 + a}, \quad (3)$$

where  $a$  is a constant,  $r$  the distance to the station and  $r^*$  a distance factor ( $0 \leq r^* \leq r$ ) that indicates whether the observation is in an upwind-downwind ( $r^* = r$ ) or crosswind ( $r^* = 0$ ) direction from the grid point.

<sup>1</sup> Present affiliation: Advanced Technology Group, Dames & Moore, Los Angeles, CA 90024.

Shepard (1968) discussed an interpolation technique in which a direction factor was also included which accounted for shadowing of the influence of one data point by a nearer one in the same direction. The method also included the effect of barriers. If a "detour" of length  $b(r)$ , perpendicular to the line between the point  $(i, j)$  and the  $k$ th measuring station, was required to travel around the barrier between the two points, then  $b(r)$  was considered to be the length of the barrier. An effective distance  $r'$  was defined by

$$r' = [r^2 + b(r)^2]^{1/2} \quad (4)$$

If no barrier separated the two points, then  $b(r) = 0$ .

Shenfeld and Boyer (1974) presented a technique for interpolation of a velocity field similar to that proposed by Endlich and Mancuso. The velocity was computed as in Eq. (1). For example, for the  $x$  component of the velocity at grid point  $(i, j)$ ,

$$u_{ij} = \frac{\sum_{k=1}^n u_k W_k(r)}{\sum_{k=1}^n W_k(r)}, \quad (5)$$

with the weighting function defined by

$$W_k(r) = \exp \left[ - \left( \frac{x_k^2}{S_{xk}} + \frac{y_k^2}{S_{yk}} \right) \right], \quad (6)$$

where  $x_k^2 + y_k^2 = r^2$ . The coordinate system was oriented in the direction of the observed wind with the origin at the  $k$ th station.  $S_{xk}$  was defined by

$$S_{xk} = S_y \left( 1 + \frac{V_k}{V_s} \right), \quad (7)$$

where  $V_k$  was the magnitude of the velocity vector at the  $k$ th station and  $V_s$  a scaling velocity.  $S_y$  was assigned a value between 40 and 70, depending on the density of wind stations. The larger the number of stations, the lower the value of  $S_y$ . For low values of  $S_y$ , the computed wind velocity at any grid point was more dependent on nearby stations. Also since  $S_{xk}$  was always greater than or equal to  $S_y$ , the computed wind velocity was more dependent on downwind distance ( $x_k$ ) than on crosswind distance ( $y_k$ ).

For interpolation in regions of sparse data, Fritsch (1971) used a cubic spline technique. He first fitted spherical surfaces to the data to obtain an initial field, and then iteratively adjusted these values using the splines until convergence was obtained. He compared his technique with that of Cressman using an idealized data set with a known solution, and the mean error ( $\sim 3\%$ ) was approximately half that of Cressman's.

MacCracken and Sauter (1975) used a Gaussian weighting scheme to eliminate complete dominance of a measuring station near a grid point, i.e.,

$$W(r) = \exp(-0.1r^2). \quad (8)$$

Hovland *et al.* (1977) computed wind and temperature fields using data from the Environmental Protection Agency's Regional Air Pollution Study (RAPS) conducted in St. Louis. An iterative scan procedure was used in which the radius of influence was decreased and the number of stations increased empirically on successive iterations. The advantage to this strategy is that small-scale motions which are only detected in an area of dense station coverage are not transmitted to outlying areas. Moreover, during the initial iterations this procedure places significant weight on outlying stations which may be less reliable than those in the center of the region. The weighting function used was

$$W(r) = \begin{cases} \left( \frac{R^2 - r^2}{R^2 + r^2} \right)^4, & r \leq R \\ 0, & r > R. \end{cases} \quad (9)$$

This function decreases rapidly with increasing distance  $r$  from a maximum of 1 at  $W(0)$ .

Recently, Boone and Samuelson (1977) described the application of a distance and directional weighting technique to the display of air pollution data. The weighting factor used in Eq. (1) was

$$W_k(r) = S_k^2 (1 + T_k), \quad (10)$$

where, based on the work of Shepard (1968), the weighting factor was defined by

$$S_k = \begin{cases} 1/r_k, & 0 < r_k \leq R/3 \\ \frac{27}{4R} \left( \frac{r_k}{R} - 1 \right)^2, & R/3 < r_k \leq R \end{cases} \quad (11)$$

where  $r_k$  is the distance from the  $k$ th station to the  $(i, j)$  grid point. The directional weighting factor is computed from

$$T_k = \frac{\sum_{l=1}^m S_l (1 - \cos A)}{\sum_{l=1}^m S_l}, \quad (12)$$

where  $m$  is the number of points within the radius  $R$  and angle  $A$  is defined by the segments  $(x_k, y_k)$ ,  $(i, j)$  and  $(i, j)$ ,  $(x_l, y_l)$ .

#### b. Least-squares polynomial interpolation

The second class of methods for producing a continuous surface over a grid is a least-squares fit of a polynomial to the data points. The technique requires minimization of  $\chi^2$ , the goodness of fit to the data. In a second-degree polynomial, for example,

$$\begin{aligned} \chi^2 &\equiv \sum_{k=1}^n (\Delta C_k)^2 \\ &= \sum_{k=1}^n (C_k - a_1 - a_2 x_k - a_3 y_k - a_4 x_k y_k - a_5 x_k^2 - a_6 y_k^2)^2 \quad (13) \end{aligned}$$

must be a minimum, where  $C_k$  is the measured concentration (or wind speed) at point  $(x_k, y_k)$ . The minimum value of  $\chi^2$  can be determined by setting the derivatives of  $\chi^2$  with respect to each of the coefficients  $a_i$  equal to zero. For a second-degree polynomial, six simultaneous equations must be solved for the optimum coefficients. The concentration  $C(x, y)$  at any grid location  $(x, y)$  can then be computed from

$$C(x, y) = a_1 + a_2x + a_3y + a_4xy + a_5x^2 + a_6y^2. \quad (14)$$

In an early paper, Panofsky (1949) used third-degree polynomials to fit wind and pressure fields for use in weather map construction. The technique was later modified to handle areas with sparse data by Gilchrist and Cressman (1954). These polynomial-fitting procedures were typically applied to the whole grid.

An alternative to applying the polynomial interpolation to the entire grid is to perform the interpolation over areas within the influence of individual stations. Thiessen (1911) defined space-filling polygons over particular areas by assuming that each station measurement is associated with the local region of the area nearer to that station than to any other. Formally, the resultant planar divisions are defined as Dirichlet tessellations although they are sometimes called Voroni or Thiessen polygons. While the recent algorithm of Green and Sibson (1978) simplifies the task of defining the polygons, the attainment of slope continuity in  $C$  from one region to another is a difficult problem.

A simpler technique is to triangulate the region using the station locations for the vertex positions. Lawson (1977) described a number of algorithms which perform this task. Given  $n_b$  points on the convex boundary of the region, the number of non-overlapping triangles  $n_t = 2n_b - 2$  is unique even though the triangulations may be different. Once the triangle vertices have been established, a variety of interpolation schemes can be used. For example,  $C(x, y)$  within each triangle can be determined from the equation of a plane oriented to pass through the three vertex data points.

A natural extension of this idea is to use higher order polynomials to achieve slope continuity between adjacent triangles. Lawson (1977) employed a cubic polynomial based on the finite element method of Clough and Tocher (1965) to obtain

$$C(x, y) = \sum_{i=0}^M \sum_{j=0}^{M-i} a_{ij} x^i y^j, \quad (15)$$

where  $M=3$ . Powell and Sabin (1977) used piecewise quadratic approximation to obtain an interpolation function with continuous first derivatives.

Akima (1975) developed a method of bivariate interpolation and smooth surface fitting for irregularly spaced data based on a fifth-degree polynomial ( $M=5$ ) in  $x$  and  $y$  defined in each triangular cell. For each

polynomial 29 coefficients must be determined. In addition to the values of the function at the data locations, the first- and second-order partial derivatives are also required. Partial derivatives of the function differentiated in the direction perpendicular to each side of the triangle are considered in order that the resulting polynomials intersect smoothly at the triangle edge. Use of higher order polynomials requires more coefficients and accordingly more computer time to solve for the coefficient matrix  $a_{ij}$ .

McLain (1974, 1976) has discussed a different polynomial fitting approach, in which the domain is divided into triangular subregions by connecting the data points. A second-degree polynomial is then fitted to each triangle using all data points with each value weighted according to its distance from the given triangle. The weighting scheme  $r^{-2}$  was used in the present formulation with the radius of influence effectively set to the dimension of the region. At each edge of the triangle,  $C(x, y)$  is required to be the same as that of adjacent polynomials in order that position continuity of the resulting surface is assured.

In each triangle, the final value  $C(x, y)$  is found as the weighted average of the three functions [Eq. (14)] corresponding to the vertices, i.e.,

$$C(x, y) = W_1C_1 + W_2C_2 + W_3C_3. \quad (16)$$

To ensure smooth transition from one triangle to the next, each weight  $W_i$  and its leading derivatives must be identically zero along the side of the triangle opposite to the  $i$ th vertex. This can be achieved by making  $W_i$  proportional to the third power of the distance from that side. The distance  $d_i$  from the point  $(x, y)$  to the side is a linear function of  $x$  and  $y$ , i.e.,

$$d_i = l_i x + m_i y + n_i, \quad (17)$$

where  $l_i$ ,  $m_i$ ,  $n_i$  are the coefficients defining a line through triangle edge opposite vertex  $i$ , scaled such that  $d_i=1$  at vertex  $i$ . The weight  $W_i$ , within the triangle, is then

$$W_i = d_i^3 / (d_1^3 + d_2^3 + d_3^3). \quad (18)$$

### c. Optimum interpolation

A third general technique, first presented by Gandin (1963), known as optimum interpolation, has proved useful for interpolation of synoptic-scale meteorological data (wind and temperature) for initializing global or synoptic circulation models (Dartt, 1972; Schlatter, 1975; Julian and Thiebaut, 1975; Thiebaut, 1975). The technique produces an interpolated field from data points irregularly spaced in both space and time. The interpolation function can be formulated directly in terms of statistical properties of the wind (temperature) field, i.e., past behavior determines the function's form. This implies, however, that a historical record of data values must be available in

TABLE 1. Summary of interpolation methods and their attributes.

Method	Attributes	Applications
Weighted interpolation	1. Easy to implement	Cressman (1959)
(a) $W(r) = \left(\frac{R^2 - r^2}{R^2 + r^2}\right)^n$	2. May be modified if directional influence is important	Endlich & Mancuso (1968)
(b) $W(r) = \exp(-ar^n)$	3. More features of the data are smoothed as $n$ decreases	Shepard (1968)
(c) $W(r) = r^{-n}$	4. Influence of a station becomes very localized as $n$ (or $a$ ) increases	Shenfeld & Boyer (1974)
	5. Radius of influence $R$ may be fixed or variable	MacCracken & Sauter (1975)
		Hovland <i>et al.</i> (1977)
		Boone & Samuelson (1977)
Least-squares polynomial interpolation	1. Complex to implement	Panofsky (1949)
(a) Polynomial of degree $n$ fitted to full grid	2. Resulting field depends strongly on distribution of data points when using (a)	Akima (1975)
(b) Polynomials of degree $n$ fitted to subregions of grid	3. Resulting field is smoothed as $n$ decreases when using (a)	McLain (1974, 1976)
	4. (b) fits data almost exactly	Lawson (1977)
	5. Execution time increases with $n$	
Optimum interpolation	1. Complex to implement	Gandin (1963)
	2. Much historical data may be required	Dartt (1972)
	3. Statistics of the data accounted for	Schlatter (1975)

order to calculate these statistical properties (covariances). Moreover, the variance from the long-term mean of a wind measurement taken at a particular hour may not be useful for a mesoscale flow since the local stability and terrain influences on a particular day may be critically important in determining the flow.

#### d. Summary

Table 1 summarizes the methods that have been discussed in Section 2.

### 3. Optimum radius of influence

Theoretically, the choice of weight function and radius of influence for use in a distance-weighted interpolation procedure depends on the field statistics. Since insufficient measured data are available in most practical applications, the choice of an optimum radius must be based on the average station separation. For a two-dimensional domain of area  $A$  with  $N$  stations randomly distributed over the plane, the average station density  $\rho$  and separation  $d$  are given by  $\rho = N/A$  and  $d = (A/N)^{1/2}$ . Stephens and Stitt (1970) have shown empirically that the optimum search radius  $R$  for large signal-to-noise ratios is  $R/d \approx 1.6$ . A further finding of their work is that  $R$  should be overestimated rather than underestimated. In practice this is important since nonrandom station distributions can lead to situations in which  $R$  is commensurate with the dimension of the data separation. In a separate study, Barnes (1964, 1973) came to similar conclusions and was also able to relate  $R/d$  to  $L/d$ , where  $L$  is the half wavelength of a disturbance. As an example, the parameters  $d$  and  $R/d$  can be calculated for the network of approximately 50 air monitoring stations in the South Coast Air Basin of Southern

California (in 1974). Distributed over an area of about 19 400 km<sup>2</sup>, the average station separation is calculated to be  $\sim 20$  km. This implies that a radius of influence between 20 and 40 km would be optimum. In order to calculate air quality distributions over the ocean and desert areas, which have few measurement stations, a larger radius of influence of 30–50 km must sometimes be used.

Careful consideration must be given to the choice of  $R$ . If the objective is to produce a set of gridded values, then each point must be within the radius of influence of at least one measurement station. While increasing  $R$  reduces the field variance, it does so at an increase of computational cost. For randomly distributed stations the interpolation cost per grid value increases quadratically since the number of data points within each radius of influence is proportional to  $R^2$ . Thus, knowledge of an "optimum" radius of influence is important both from the point of view of accuracy of the final interpolated field as well as cost of the calculation. The simple technique discussed in this section for computing an optimum radius of influence, while developed for a random distribution of points, provides a useful range of values even when the measurement points are not randomly located.

### 4. Comparison of interpolation procedures for scalar fields

The results of interpolating test data sets for which the exact solution is known provide a means to assess the performance of interpolation routines.

A test data set consisting of a hemispherically shaped surface was constructed to compare the various interpolation methods. The hemisphere was arbitrarily centered above the center of a 100×50 grid system overlaying the South Coast Air Basin. Each grid cell was 3.2 km×3.2 km. The height of the surface above

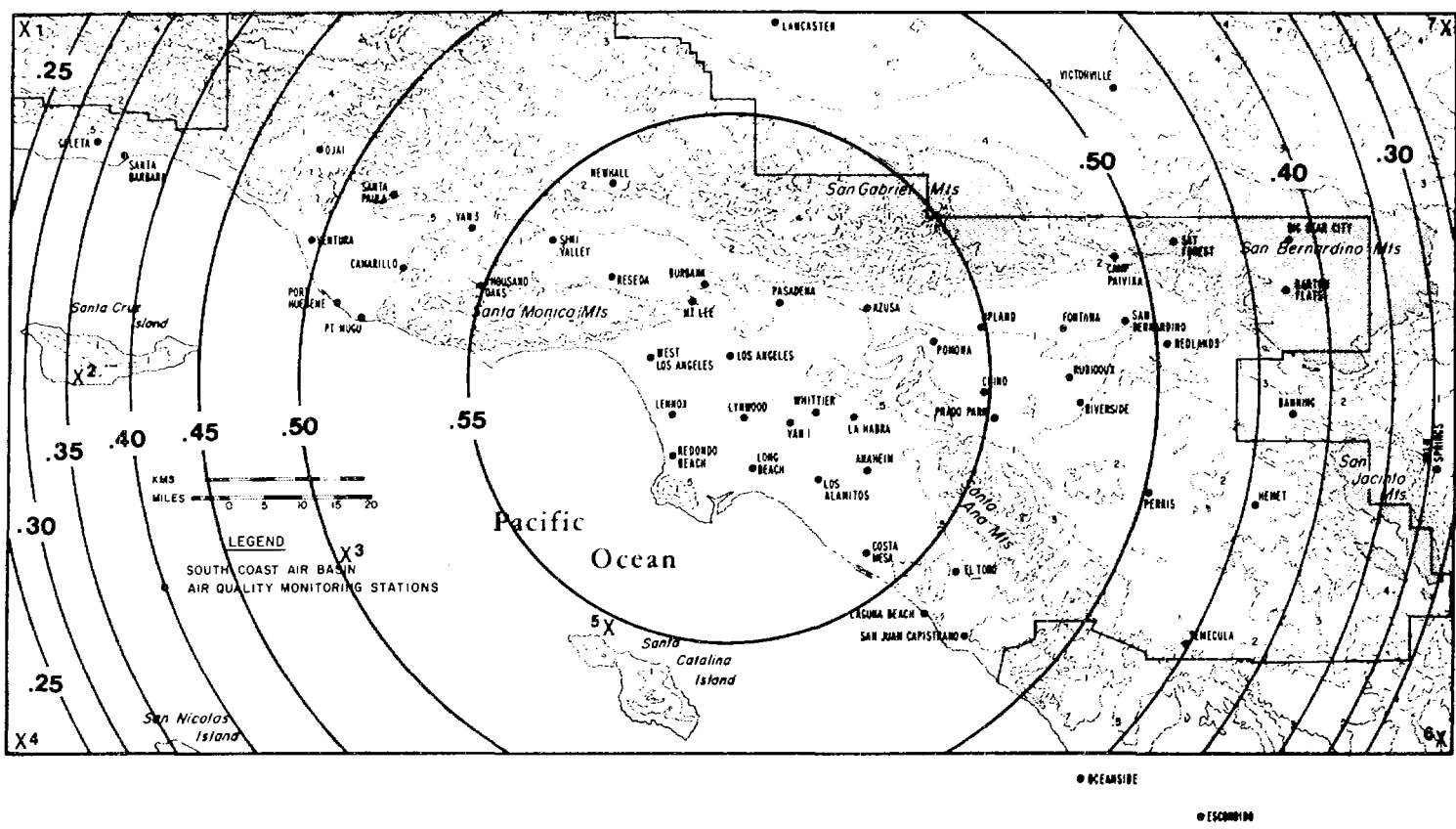


FIG. 1. Distribution of measurement stations and hemispherical test surface.

each grid point corresponded to the field value at that point. The height of the constructed surface was evaluated at each measuring station location (56 points) and these values were used as raw data in the test. Fig. 1 shows the field isopleths and the measuring station locations. The test consisted of attempting to reconstruct the hemispherical surface from these data points (no flow barriers were used).

The methods compared are the second-degree polynomial with  $r^{-2}$  weighting and the simple distance-weighting scheme with various weights, the results of which are shown in Table 2. Statistics are given for the station locations as well as for all grid points; in each case the percentage relative residual error  $E_r$  is computed from

$$E_r = 100 \left[ \frac{C_{\text{comp}}}{C_{\text{act}}} - 1 \right], \quad (19)$$

where  $C_{\text{comp}}$  is the computed surface height and  $C_{\text{act}}$  its actual height. When an interpolation scheme is applied to a set of field data, the residual error at each station is the only measure of the technique's performance. However, for this test data set, the residual error can be computed over the whole grid, indicating the level of accuracy that can be expected away from measuring stations. Such a procedure cannot be expected to resolve sharp gradients which are not reflected in the data.

Contour plots of the reconstructed fields are shown in Fig. 2. Generally, in regions where the number of measuring stations is relatively large, the error is smallest (i.e., toward the center of the region). However, near the boundaries where the data network is less dense the errors can be much larger.

The results indicate that among the simple distance-weighting schemes, the  $(R^2 - r^2)/(R^2 + r^2)$  weighting produces the most hemisphere-like surface. However, the departure from measured values is largest with

this scheme. More accuracy is obtained near the data points with the  $r^{-2}$  and  $\exp(-br^2)$  schemes, but at the expense of accuracy away from measuring stations. The second-degree polynomial fitting procedure provides a compromise. The hemispherical shape is preserved and the accuracy at the measuring station locations is also acceptable. The execution times do not include the square-to-station distance (or formulation of the triangles) calculation times since they need only be calculated once for a given set of stations.

### 5. Application of selected interpolation procedures to air quality data

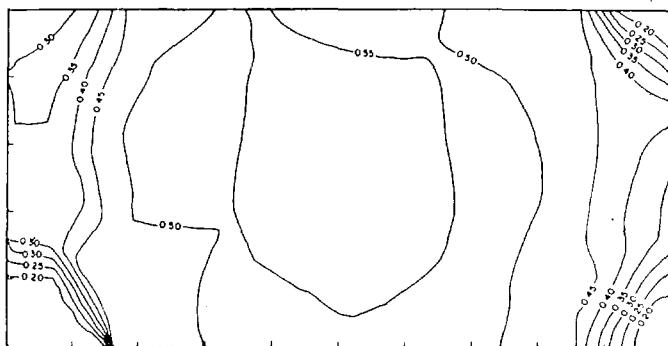
On the basis of the simple problem described above as well as a variety of other test cases, three techniques were selected for further examination using actual measured data. These were distance-weighting schemes  $r^{-2}$  and  $\exp(-0.1r^2)$  and second-degree polynomial fit with  $r^{-2}$  weighting. The distance-weighting schemes were chosen based on a compromise between station accuracy, accuracy over the whole grid, and cost. The actual data chosen for testing purposes were ozone measurements on 26 June 1974 taken within the South Coast Air Basin. All data have been corrected for measurement as well as interference errors. The distance-weighting techniques were tested using a fixed radius of influence of 48 km as well as a variable radius of influence. The variable radius of influence was specified to include at least two data points.

The results of the ozone data interpolation tests are displayed in Fig. 3 and Table 3. The  $r^{-2}$  weighting scheme produces the smallest residuals in the vicinity of the measuring stations whether a fixed or variable radius of influence is used. While minimizing the station residuals, the overall field variance for the  $r^{-2}$  weighting can be much higher than the polynomial fitting procedure as demonstrated in the test problem. Fig. 4 shows a three-dimensional perspective plot of

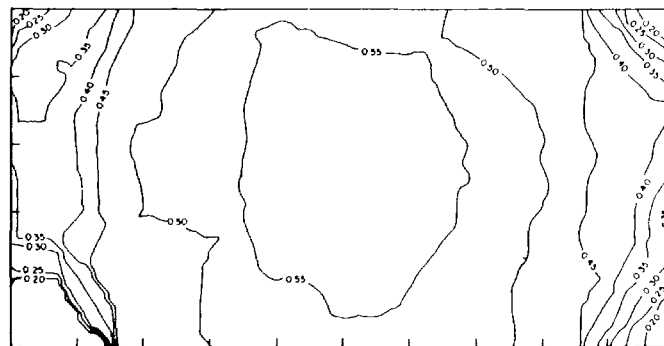
TABLE 2. Percentage relative residual error tabulated for hemispherical surface, for various weighting functions using 56 stations and a radius of influence ( $R$ ) of 48 km.

Weighting function* $W(r)$	Residual error $E_r$ (%) at measuring stations				Residual error $E_r$ (%) at all grid points				Relative computation time
	Mean	Minimum	Maximum	Std. Dev.	Mean	Minimum	Maximum	Std. Dev.	
$r^{-1}$	0.06	-1.27	2.31	0.57	0.52	-52.47	52.12	8.23	2.1
$r^{-2}$	<0.01	-0.14	0.29	0.06	0.03	-52.47	52.10	8.59	1.4
$r^{-3}$	<0.01	-0.04	0.11	0.02	-0.38	-52.47	52.08	9.19	3.4
$\frac{R^2 - r^2}{R^2 + r^2}$	0.93	-9.29	36.64	5.51	-0.06	-52.47	52.08	9.47	1.7
$e^{-0.1r^2}$	0.02	-3.28	3.58	0.72	-1.07	-55.88	54.77	12.42	2.3
$e^{-0.6r^2}$	<0.01	-0.66	0.72	0.16	-1.14	-58.0	58.27	13.15	2.5
Second degree polynomial ( $r^{-2}$ weighting)	0.09	-0.75	0.87	0.32	-1.78	-18.92	10.64	4.0	1.0

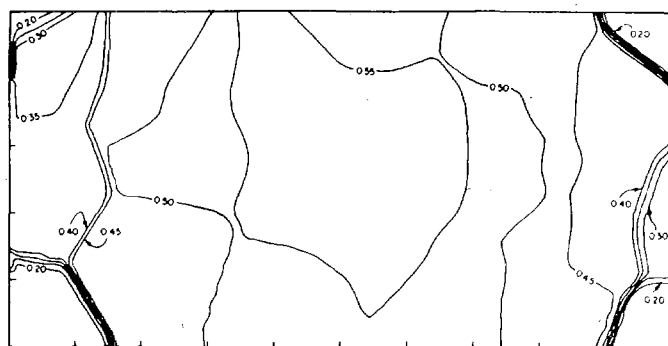
\*  $r$  is the distance from grid point to measuring station; for  $r > R$ ,  $W(r)$  is set to zero.



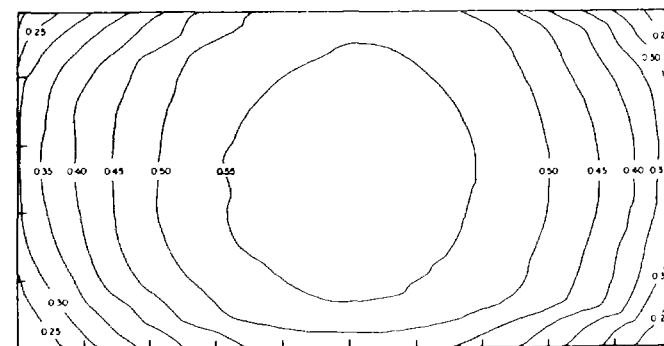
(a)



(b)

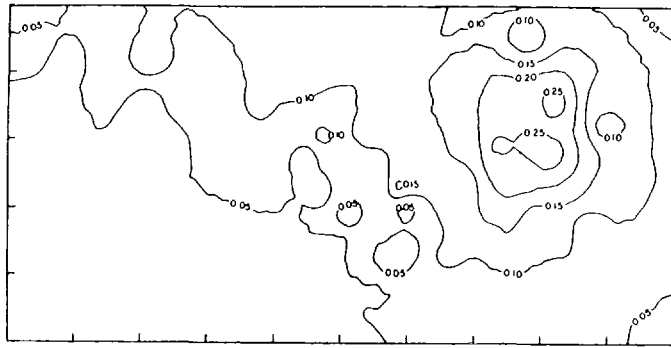


(c)



(d)

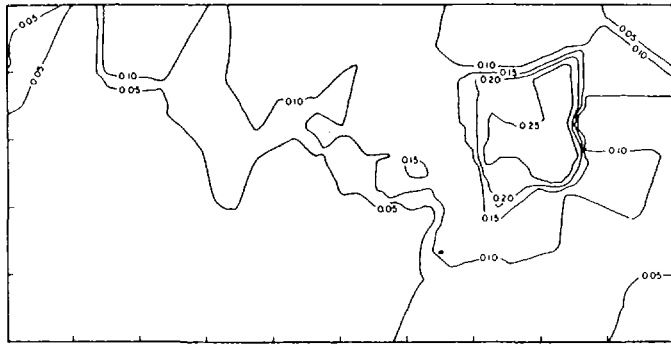
FIG. 2. Surfaces resulting from interpolation of hemispherical data using (a)  $(R^2 - r^2)/(R^2 + r^2)$  weighting of data values, (b)  $r^{-2}$  weighting of data values (similar visual results were obtained for the  $r^{-1}$  and  $r^{-3}$  cases), (c)  $\exp(-0.1r^2)$  weighting of data values (similar visual results were obtained for  $\exp(-0.5r^2)$ ), and (d) polynomial fitting procedure.



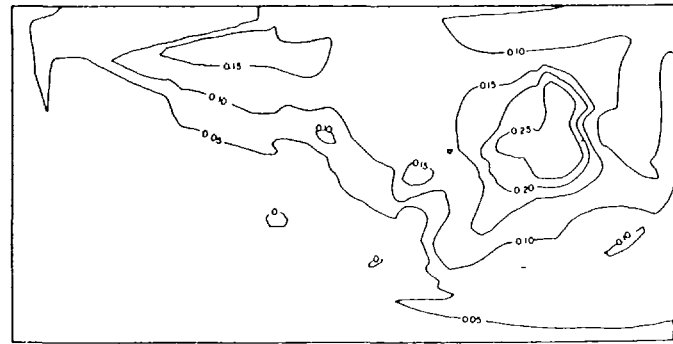
(a)



(b)



(c)



(d)

FIG. 3. Surfaces resulting from interpolation of measured ozone values from 1600 PST 26 June 1974 using (a)  $r^{-2}$  weighting of data values with a fixed radius of influence  $R$ , (b)  $r^{-2}$  weighting of data values with a variable  $R$ , (c)  $\exp(-0.1r^2)$  weighting of data values with a variable  $R$  (similar visual results were obtained with a fixed  $R$ ), and (d) polynomial fitting procedure.

TABLE 3. Percentage relative residual error  $E_r$ , tabulated from ozone data analysis for various weighting functions using 56 stations.

Weighting function* $W(r)$	Residual error $E_r$ (%) at stations with radius of influence $R=48$ km				Residual error $E_r$ (%) at stations with variable radius of influence $R$			
	Mean	Minimum	Maximum	Std. Dev.	Mean	Minimum	Maximum	Std. Dev.
$r^{-2}$	0.67	-3.08	10.42	2.04	0.14	-3.22	3.79	1.00
$e^{-0.1r^2}$	5.56	-28.75	85.48	19.62	3.01	-21.59	71.72	15.69
Second degree polynomial ( $r^{-2}$ weighting)	4.82	-13.02	49.18	12.60				

\*  $r$  is the distance from grid point to measuring station, for  $r > R$ ,  $W(r)$  is set to zero.

the ozone surface generated by the polynomial fitting procedure.

### 6. Application of interpolation procedures to vector fields

The procedures outlined in Section 2 can easily be applied to vector as well as scalar fields, for example, by treating the  $u$  and  $v$  components separately. Based on the results of the hemisphere test data set, the same three techniques used in Section 5 were selected for further detailed examination here. These were distance-weighting schemes  $r^{-2}$  and  $\exp(-0.1r^2)$  and second-degree polynomial fit with  $r^{-2}$  weighting.

The test wind field data set, potential flow over a flat plate inclined at angle  $\alpha$  to the flow, free stream velocity  $v_0$ , was chosen to illustrate the inclusion of a barrier to flow. The exact solution to the problem can be calculated from potential flow theory. The velocity potential  $\phi$  and streamfunction  $\psi$  in an  $x$ - $y$  Cartesian

coordinate system are given by

$$\phi(x,y) = v_0 \left( x + \frac{x \cos 2\alpha - y \sin 2\alpha}{x^2 + y^2} \right), \quad (20)$$

$$\psi(x,y) = v_0 \left( y - \frac{x \sin 2\alpha + y \cos 2\alpha}{x^2 + y^2} \right). \quad (21)$$

The velocity components are computed from the velocity potential

$$u(x) = \frac{\partial \phi}{\partial x} = v_0 \left( 1 + \frac{\cos 2\alpha (y^2 - x^2) + 2xy \sin 2\alpha}{(x^2 + y^2)^2} \right), \quad (22)$$

$$v(y) = \frac{\partial \phi}{\partial y} = v_0 \left( \frac{\sin 2\alpha (y^2 - x^2) - 2xy \cos 2\alpha}{(x^2 + y^2)^2} \right). \quad (23)$$

For the present analysis, the angle of inclination  $\alpha$  was chosen to be  $\pi/4$ . Indicated on Fig. 5 are the

TABLE 4. Percentage relative residual error statistics for interpolation of a potential flow problem.

Weighting function* $W(r)$	Velocity component	Residual error $E_r$ (%) at measuring stations				Residual error $E_r$ (%) at all grid points			
		Mean	Minimum	Maximum	Std. Dev.	Mean	Minimum	Maximum	Std. Dev.
$e^{-0.1r^2}$ $R=8$ squares	$u$	16.36	-57.23	231.43	49.86	3.49	-80.71	281.16	19.87
	$v$	12.43	-81.38	185.68	54.04	18.20	-787.53	544.39	81.04
$r^{-2}$ $R=8$ squares	$u$	0.21	-1.08	2.46	0.63	7.53	-81.26	165.14	14.25
	$v$	-0.10	-1.21	2.86	0.71	-66.27	-989.70	966.45	151.65
Polynomial	$u$	9.72	-40.85	99.13	24.98	1.62	-76.93	170.49	14.17
	$v$	-4.85	-55.76	48.25	24.06	-99.93	-192.21	137.29	19.61
$e^{-0.1r^2}$ $R$ variable (includes 2 data points)	$u$	10.13	-27.64	202.69	39.12	0.70	-81.82	202.69	15.16
	$v$	2.88	-158.82	151.86	62.89	9.43	-819.73	555.60	87.15
$r^{-2}$ $R$ variable (includes 2 data points)	$u$	0.10	-0.31	2.24	0.43	0.23	-81.82	198.00	12.76
	$v$	0.01	-0.59	0.76	0.31	12.47	-702.78	577.71	74.22

\*  $r$  is the distance from grid point to measuring station; for  $r > R$ ,  $W(r)$  is set to zero.

Note: In calculating the error statistics, points on the plate and one grid cell away from the plate were ignored.

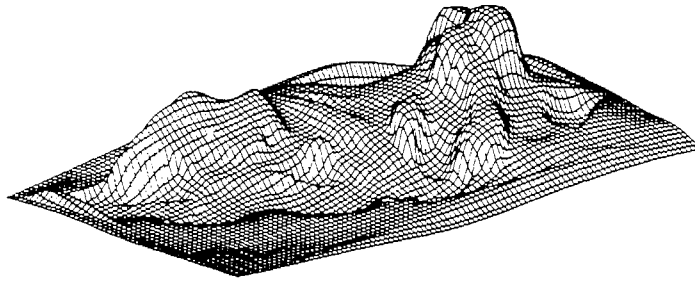


FIG. 4. Perspective plot of ozone distribution generated by polynomial interpolation scheme (a view from the southwest).

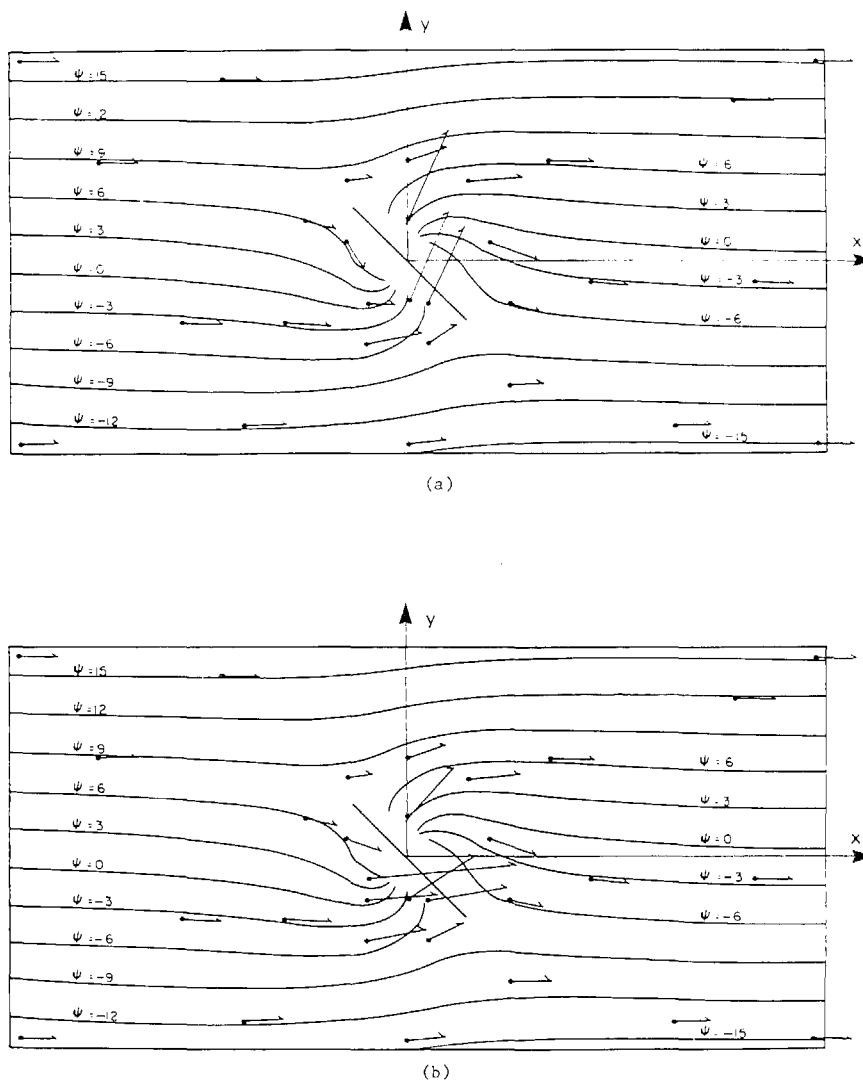


FIG. 5. Streamfunctions and location of velocity data points (solid circles) for potential flow over a flat plate. Reconstructed velocity field for potential flow over a flat plate for (a)  $r^{-2}$  with variable  $R$  and (b) polynomial fitting scheme.

streamfunction and velocity data points together with the calculated velocity vectors developed using the interpolation procedures over a  $40 \times 20$  grid.

In the distance-weighting procedures, a check is made to see whether a line connecting a measuring station to a grid point intersects the barrier. If so, that station's value is not included in the weighting procedure at that grid point. In the polynomial fitting procedure a barrier is treated by requiring that it be an edge of two adjacent triangles. The results of this vector test problem are shown in Table 4 and Fig. 5.

## 7. Conclusions

Since the interpolation of a set of sparse data does not have a unique solution, it is important that the calculation be done carefully, producing physically realistic resulting surfaces. The interpolated field is critical to calculations such as wind field divergence reduction, contouring of data values, and initialization of pollutant transport calculations. A comparison of a number of procedures for interpolating sparse data indicates that the second-degree polynomial fitting procedure with an  $r^{-2}$  distance-weighting scheme provides a good compromise between computational costs and the accuracy of the final surface adjacent to and further away from measurement stations.

*Acknowledgments.* Portions of this work were supported by the California Air Resources Board under Contract A5-046-87, and by the Department of Energy under Institutional Grant EY-76-G-03-1305.

## REFERENCES

- Akima, H., 1975: A method of bivariate interpolation and smooth surface fitting for values given at irregularly distributed points. Dept. of Commerce Rep. 75-70, 51 pp. [NTIS COM-75-10812].
- Barnes, S. L., 1964: A technique for maximizing details in numerical weather map analysis. *J. Appl. Meteor.*, **3**, 396-409.
- , 1973: Mesoscale objective analysis using weighted time-series analysis. NOAA Tech. Memo. ERL NSSL-62, 60 pp. [NTIS COM-73-10781].
- Boone, D. R., and G. S. Samuelson, 1977: Computer mapping of air quality. *J. Environ. Eng. Div. Proc. ASCE*, **103**, EE6, 969-979.
- Clough, R. W., and J. L. Tocher, 1965: Finite element stiffness matrices for the analysis of plates in bending. *Proc. Conf. Matrix Methods in Structural Mechanics*, Air Force Inst. and Tech., Wright Patterson AFB, Ohio.
- Cressman, G. P., 1959: An operational objective analysis system. *Mon. Wea. Rev.*, **87**, 367-374.
- Dardt, D. G., 1972: Automated streamline analysis utilizing optimum interpolation. *J. Appl. Meteor.*, **11**, 901-908.
- Endlich, R. M., and R. L. Mancuso, 1968: Objective analysis of environmental conditions associated with severe thunderstorms and tornadoes. *Mon. Wea. Rev.*, **96**, 342-350.
- Fritsch, J. M., 1971: Objective analysis of a two-dimensional data field by the cubic spline technique. *Mon. Wea. Rev.*, **99**, 379-386.
- Gandin, L. S., 1965: *Objective Analysis of Meteorological Fields*. Israel Program for Scientific Translations. Jerusalem. 242 pp.
- Gilchrist, B., and G. P. Cressman, 1954: An experiment in objective analysis. *Tellus*, **6**, 309-318.
- Green, P. J., and R. Sibson, 1978: Computing Dirichlet tessellations in the plane. *Comput. J.*, **21**, 168-173.
- Hovland, D., D. Dartt and K. Gage, 1977: An objective analysis technique for the regional air pollution study, Part I. EPA, Research Triangle Park, N.C., 44 pp. [NTIS PB 266255].
- Julian, P. R., and H. J. Thiebaut, 1975: On some properties of correlation functions used in optimum interpolation schemes. *Mon. Wea. Rev.*, **103**, 605-616.
- Lawson, C. L., 1977: Software for  $C'$  surface interpolation. *Mathematical Software*, Vol. 3, J. R. Rice, Ed., Academic Press, 161-194.
- MacCracken, M. C., and G. D. Sauter, Eds., 1975: *Development of an Air Pollution Model for the San Francisco Bay Area*, Vol. 2, Appendices. Lawrence Livermore Laboratory, UCRL-51920, 229-230 [NTIS UCRL-51920].
- McLain, D. H., 1974: Drawing contours from arbitrary data points. *Comput. J.*, **17**, 318-324.
- , 1976: Two dimensional interpolation from random data. *Comput. J.*, **19**, 178-181.
- , 1976: Errata. *Comput. J.*, **19**, 384.
- Panofsky, H. A., 1949: Objective weather-map analysis. *J. Meteor.*, **6**, 386-392.
- Powell, M. J. D., and M. A. Sabin, 1977: Piecewise quadratic approximation on triangles. *Mathematical Software*, Vol. 3, J. R. Rice, Ed., Academic Press, 316-325.
- Schlatter, T. W., 1975: Some experiments with a multivariate statistical objective analysis scheme. *Mon. Wea. Rev.*, **103**, 246-257.
- Shenfeld, L., and A. E. Boyer, 1974: The utilization of an urban air pollution model in air management. Paper presented at Fifth Meeting NATO/CCMS Expert Panel on Air Pollution Modeling, Roskilde, Denmark.
- Shepard, D., 1968: A two-dimensional interpolation function for irregularly spaced data. *Proc. 23rd ACM Nat. Conf.*, Las Vegas, 517-524.
- Stephens, J. J., and J. M. Stitt, 1970: Optimum influence radii for interpolation with the method of successive corrections. *Mon. Wea. Rev.*, **98**, 680-687.
- Thiebaut, H. J., 1975: Experiments with correlation representations for objective analysis. *Mon. Wea. Rev.*, **103**, 617-627.
- Thiessen, A. H., 1911: Precipitation averages for large areas. *Mon. Wea. Rev.*, **39**, 1082-1084.

### 3.3 Weighted Interpolation Procedures

An important element of the interpolation procedure presented in the previous section was the distance weighting function

$$c(p) = \frac{\sum_{k=1}^n c_k W_k(r)}{\sum_{k=1}^n W_k(r)} \quad (3.1)$$

where  $c(p)$  is the interpolated value of  $c$  at the point  $p=(x,y)$ ,  $c_k$ ;  $k=1,2,\dots,n$  are the data values at the points  $p_k$ ,  $W_k(r)$  the weighting function

$$W(r) = \frac{1}{r^a} \quad (3.2)$$

and  $r$  a suitably chosen distance metric of the form

$$r(p,p_i) = [(x-x_i)^2 + (y-y_i)^2]^{\frac{1}{2}} \quad (3.3)$$

Some other functional forms of  $W(r)$ , which are used in practice, are shown in Figure 3.1. Subsequent to the publication of the paper by Goodin et al. (1979) a discussion was received from Glahn (1981). In the process of preparing a reply, Goodin et al. (1981), it was discovered that (3.1) could be written in the equivalent form

$$c(p) = \sum_{i=1}^n F_i c_i \quad (3.4)$$

where

$$F_i = \frac{\prod_{\substack{j=1 \\ j \neq i}}^n r_j^a}{\sum_{m=1}^n \prod_{\substack{j=1 \\ j \neq m}}^n r_j^a} \quad (3.5)$$

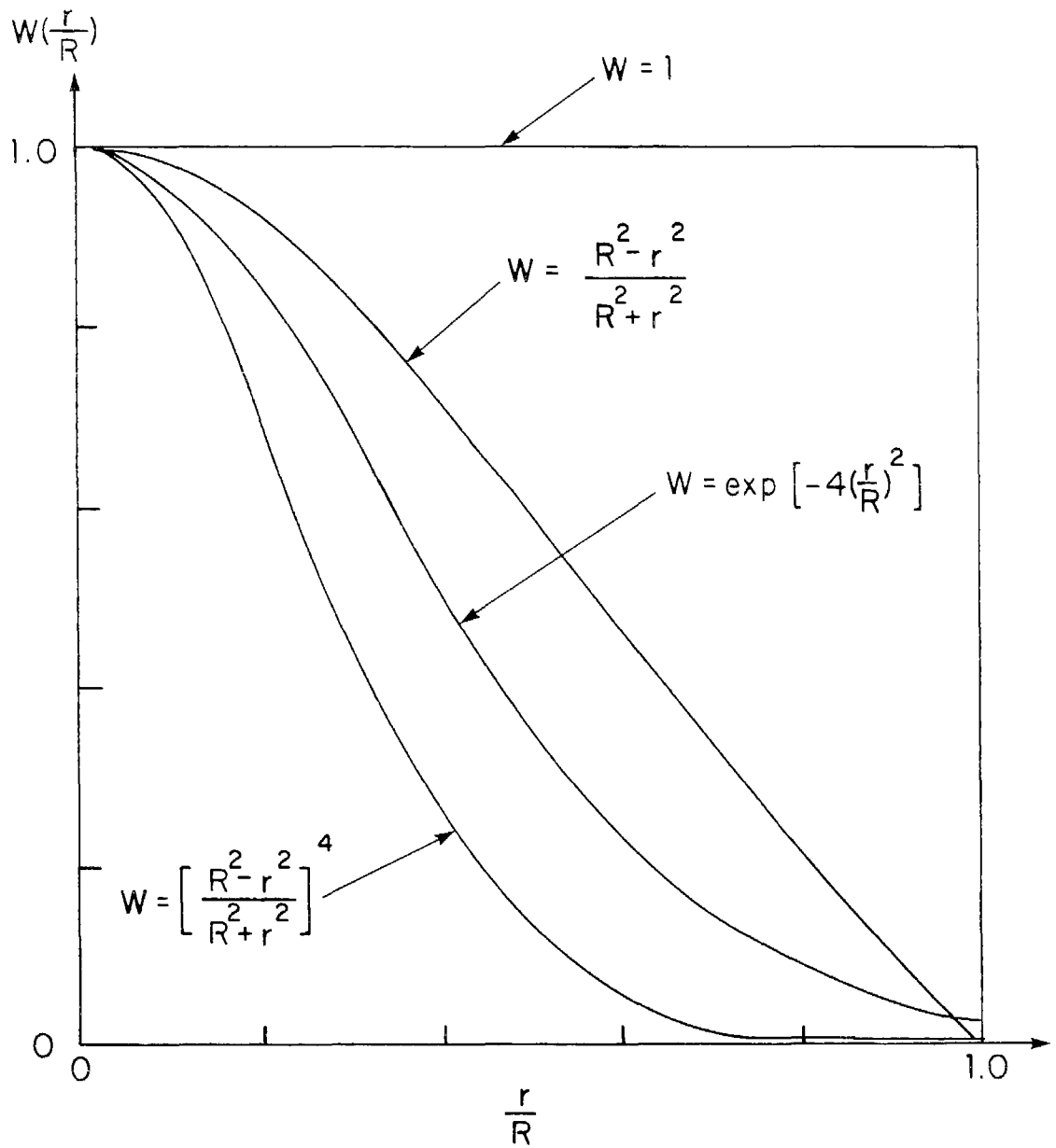


FIGURE 3.1

Some Examples of Different Weighting Functions of the Form  $W(r/R)$  Where  $R$  is the Radius of Influence

This section presents some of the results which can be readily derived from the alternate representation of interpolation procedure.

A particular concern of Glahn (1981) was the behaviour of (3.1) in between data points. Using the rearranged form it is a straightforward task to evaluate the partial derivatives of  $c(p)$  in the neighborhood of the data points and to show that for  $a > 1$

$$\lim_{p \rightarrow p_i} \frac{\partial c}{\partial x} = \lim_{p \rightarrow p_i} \frac{\partial c}{\partial y} = 0 \quad (3.6)$$

and for  $0 < a \leq 1$  that the partial derivatives do not exist. These results have important practical consequences because it is evident that for  $0 < a \leq 1$  there will be cusps at the data points and when  $a > 1$  the surface slope in the vicinity of each  $c_k$  will be zero. These properties are illustrated in Figure 3.2. From a practical point of view it is desirable to avoid the cusps at the data points and so it is customary to choose  $a > 1$ . As  $a$  is increased the surface tends to become flat near the data points and consequently, quite steep in between. A number of experiments were conducted using different data sets and it was concluded that  $a = 2$  represents a good compromise.

One interesting feature of Figure 3.2 is that as the exponent is increased the interpolated result approximates a piecewise constant function. Since this result will also apply in two dimensions it suggests a simple and direct method for testing if a point is within the tessellation surrounding a particular data point. Gordon and Wixom (1978) and Schumaker (1976) discuss the properties of interpolation

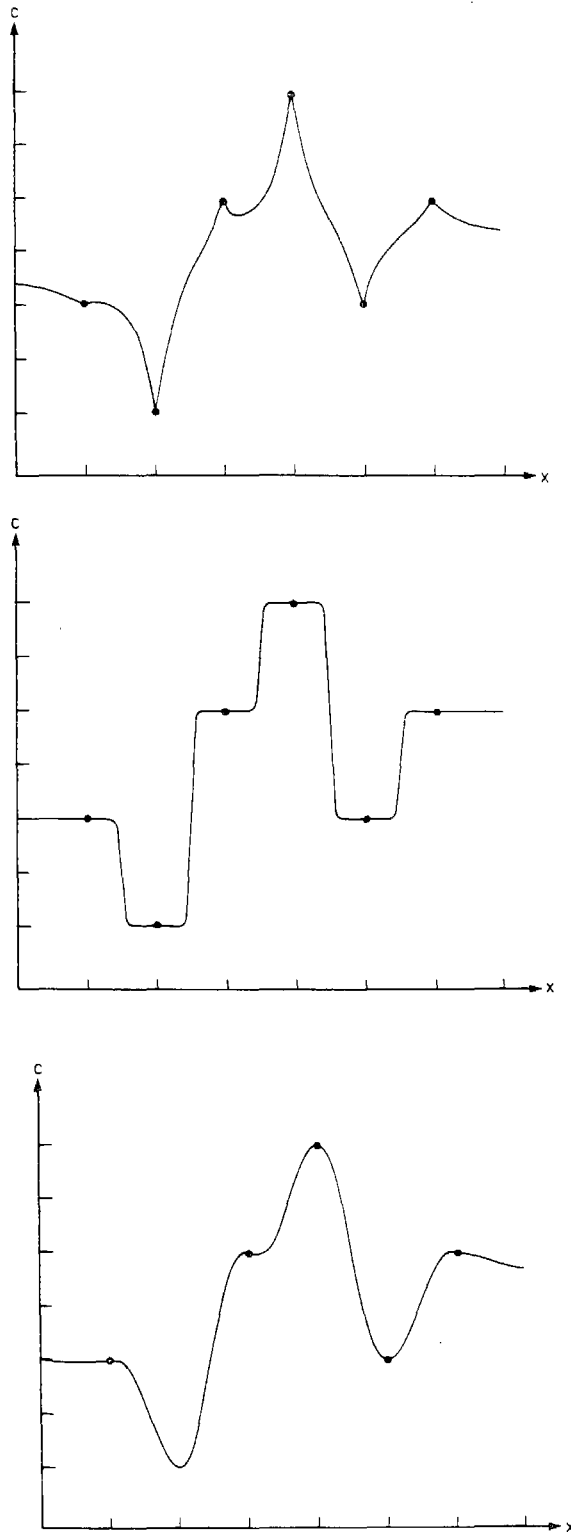


FIGURE 3.2

Results of Using Different Exponents in the Weighting Function  $W(r) = 1/r^a$ . The three cases correspond to (a)  $1/r$ , (b)  $1/r^{10}$  and (c)  $1/r^2$  (After Gordon and Wixom, 1978)

schemes based on (3.1) and in particular show that for the case  $a = 1$

$$\min_i [c_i] < c(p) < \max_i [c_i] \quad (3.7)$$

Further Gordon and Wixom (1978) show that if  $c_i \geq 0$  for all  $i=1,2,\dots,n$  then  $c(p) \geq 0$  for all  $p$ . This is a very desirable result when interpolating concentration fields.

If information about the slope of the surface is available then the procedure developed by Shepard (1968) can be used to overcome the problems associated with flat spots for  $a > 1$ . The interpolation formula is given by

$$c(p) = \sum_{i=1}^n F_i [c_i + (x-x_i)c_x + (y-y_i)c_y] \quad (3.8)$$

where the derivatives in each direction are given by

$$c_x = \left. \frac{\partial c}{\partial x} \right|_{p=p_i}$$

$$c_y = \left. \frac{\partial c}{\partial y} \right|_{p=p_i} \quad (3.9)$$

Franke (1977) and Barnhill (1977) have carried out extensive comparisons of different weighted interpolation schemes and present numerous test cases that have analytic results.

### 3.4 Generation of Triangulated Computational Domains

One step in the interpolation technique introduced in the previous section involves constructing a mesh of non-overlapping triangles whose vertices correspond to the data point locations. While manual construction of the mesh is straightforward the sheer volume of measurement information which must be processed in typical applications necessitates an automated procedure. This section presents an algorithm which will construct the required triangulation given a set  $S$  of  $n$  distinct spatial points  $P_i(z,y)$ ;  $i=1,2,\dots,n$ .

While there are many possible triangulations they all contain the same number of triangles. This can be readily deduced, for a bounded polygon, from the Euler-Poincare formula

$$F + V = E + 1 \quad (3.10)$$

In this expression  $F, V$  and  $E$  are respectively the number of faces, vertices and edges. For the particular problem under consideration  $F = n_t$ , the number of triangles, and  $V = n$  the number of vertices. Since each internal edge is common to two triangles and the  $n_b$  points which define the edges of convex hull of  $S$  appear only once then

$$3n_t = 2E - n_b \quad (3.11)$$

Eliminating the number of edges from (3.10-3.11) gives a simple expression for the number of triangles

$$n_t = 2n - n_b - 2 \leq 2n \quad (3.12)$$

There are two basic problems in constructing triangulated meshes: establishing suitable selection criteria for identifying preferred triangulation and avoiding overlap. In general there is no single "best" triangulation although it is clearly desirable to maximize the smallest interior angles in each triangle. The reason for this is to avoid illconditioning the matrices which arise during the polynomial fitting procedures. One procedure that can be used to generate nonoverlapping triangulations that satisfies the minimum angle criterion is due to Green and Sibson (1978). They start by constructing a convex polygon around each data point  $p_i$ . Each polygon or tile is defined by

$$T_i = \{(x,y): r(p,p_i) < r(p,p_j) \text{ for all } i \neq j\} \quad (3.13)$$

$$i = 1, 2, \dots, n$$

where  $r(p,p_i)$  is the Euclidean distance (3.3). The resulting pattern is known by a variety of different names: a Dirichlet tessellation, the Thiessen diagram (Thiessen, 1911), or Voronoi polygons (Finney, 1979; Brostow et al. 1978). The diversity of names is a consequence of their independent development in various different applications. Within any polygon each point is closer to the data point than any other in  $S$ . In general tiles meet in threes at vertices. The lines joining data points in contiguous polygons define triangles the perpendicular bisectors of which define the tile boundaries and the circumcenters, the polygon vertices. Figure 3.3 illustrates a typical Dirichlet tessellation and its associated dual, the Delaunay triangulation (Rodgers, 1964). This configuration satisfies the local equiangularity property suggested by

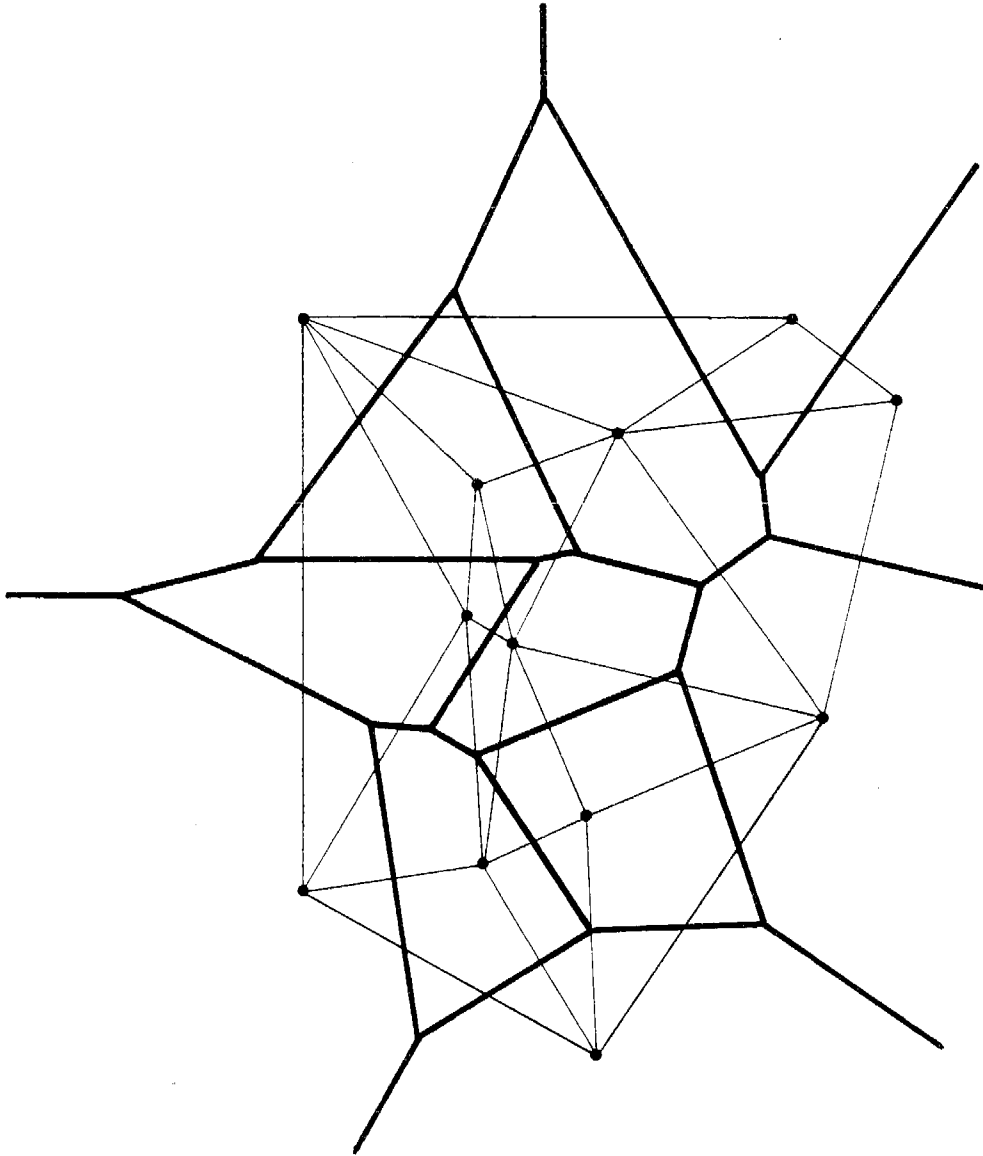


FIGURE 3.3

The Dirichlet Tessellation (bold lines) and  
Delaunay Triangulation (fine lines) for a Small Scale Configuration.  
(After Green and Sibson, 1978)

Lawson (1977) which requires that in every convex quadrilateral formed by two adjacent triangles, the minimum of the six angles in the two triangles is not less than it would have been had the alternative diagonal and pair of triangles been chosen. Unfortunately while it is relatively easy to define the tiles, construction of an efficient general purpose algorithm is not straightforward. An alternative, and the procedure adopted in this study is to construct the triangles one at a time using an algorithm due to McLain (1976ab), Nelson (1978) and Thacker (1979). Operationally the technique is easy to implement and Lawson (1977) has shown that it produces the same Delaunay triangulation generated by the Green and Sibson (1978) algorithm.

Consider a triangle  $T^k$  formed by the three points ABC in Figure 3.4. Let  $\overline{AB}$  be an edge and  $S_k$  the subset of  $S$  consisting of the points on the opposite side of  $\overline{AB}$  from C. McLain (1976a) introduced a simple test for identifying the point in  $S_k$  that could be used to construct the next triangle  $T^{k+1}$ . The test is as follows. For each point  $p_i$  in  $S_k$  construct the circumcircle which passes through A, B and  $p_i$  and determine the signed distance of the circumcenter from  $\overline{AB}$ . The signed distance from  $\overline{AB}$  is positive on the side of AB opposite to C. The point  $\overline{p}_i$  which has the minimum value of  $\overline{ABp}_i$  is the one to use in extending the triangulation. If any of the points in  $S_k$  satisfying this criterion are found to lie on the same circumcircle then they are triangularized in a right hand order. The procedure is terminated when there are no remaining points in  $S_k$  and all edges have been tested.

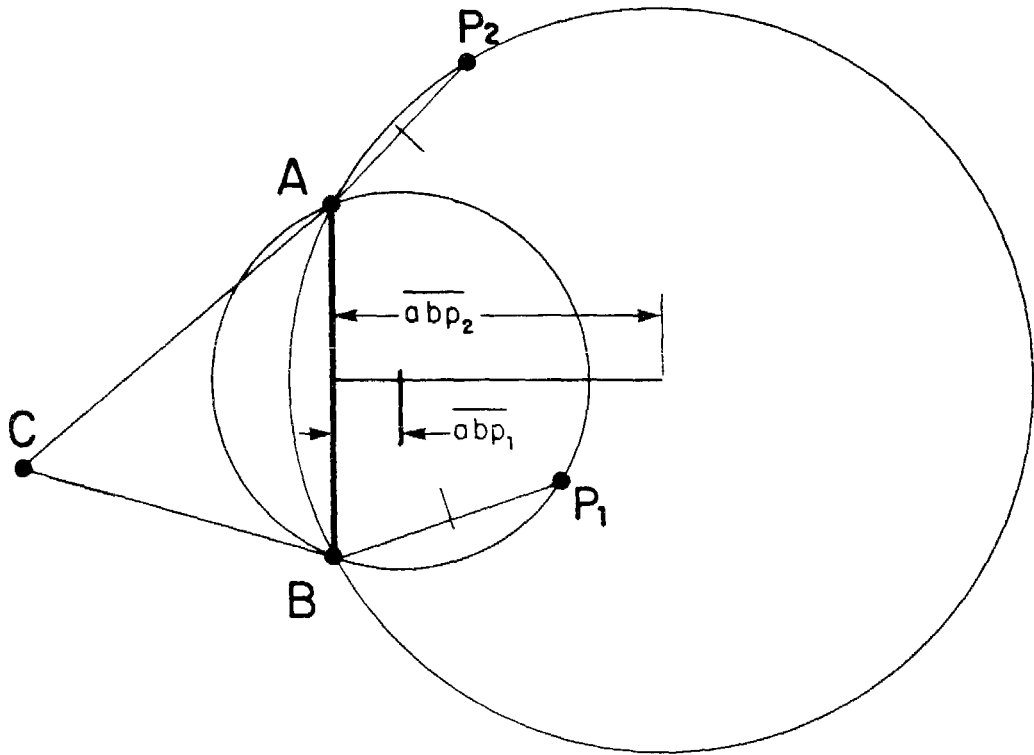
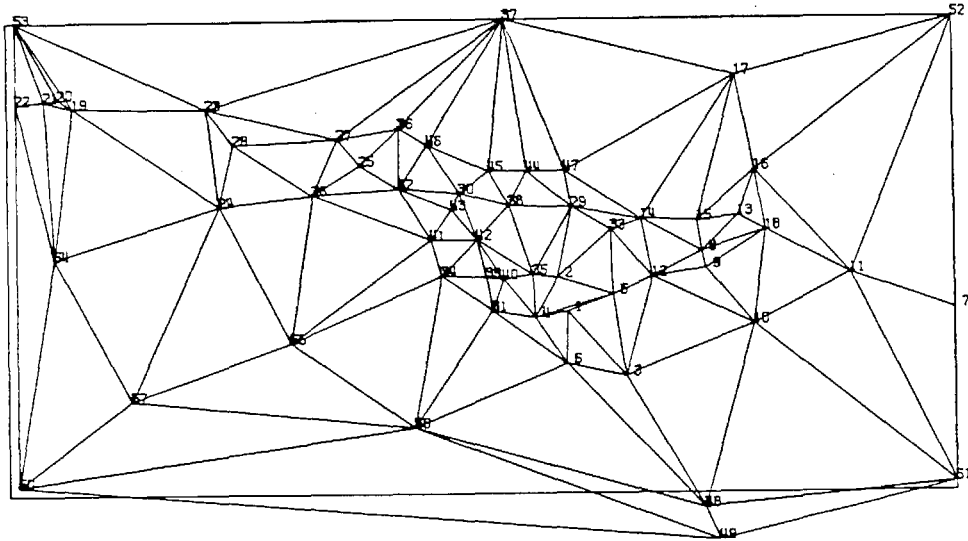
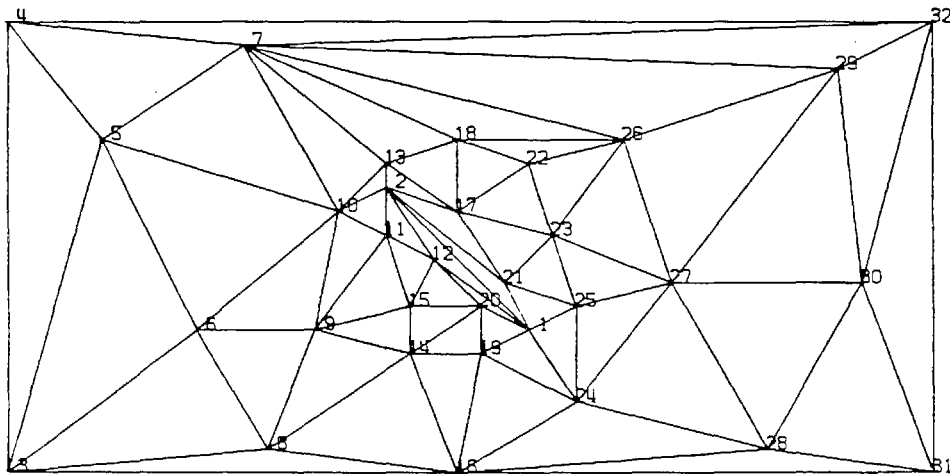


FIGURE 3.4  
 Procedure for Identifying Triangle Vertices.



(a)



(b)

FIGURE 3.5

Triangulations of the Plane for Examples Presented in Section 3.3

(a) Air Quality Interpolation ( $n = 53$ ,  $n_b = 8$ ,  $n_t = 96$ )

(b) Flow Over a Flat Plate ( $n = 32$ ,  $n_b = 5$ ,  $n_t = 57$ )

There are a variety of ways to start the algorithm, the simplest of which is to specify an initial triangle. Another approach is to identify the nodes and edges which form the convex hull of  $S$ . The methods of Graham (1972), Jarvis (1973) or Green and Silverman (1979) can be used for this task. Given the boundary edges then the interior triangles can be constructed using the McLain algorithm. A third method is to evaluate the Euclidean distances from the origin or some point outside the convex hull to each data point. A starting triangle can then be formed by using the three points closest to the origin. Figure 3.5 presents some examples of triangulations produced with the above procedure. Once the region has been triangulated the convex hull can be readily determined by identifying those edges which are common to only one triangle.

Given the convex hull then it is possible to easily evaluate moments of the form

$$I^{nm} = \iint x^n y^m dx dy \quad (3.14)$$

using Green's theorem (3.14) can be written in the equivalent form

$$I^{nm} = \frac{1}{2(n+1)} \int x^{n+1} y^m dy - \frac{1}{2(m+1)} \int x^n y^{m+1} dx \quad (3.15)$$

Since the boundary of the convex hull is defined by a series of straight line segments (3.15) can be written as

$$I^{nm} = \frac{1}{2(n+1)(m+1)} \sum_{i=1}^{n_b} (x_i^{n+1} y_{i+1}^{m+1} - x_{i+1}^{n+1} y_i^{m+1}) \quad (3.16)$$

For example the area inside the convex hull is given by  $I^{00}$ .

### 3.5 Polynomial Interpolation over Triangles

Once the plane has been triangulated the next step is to develop the interpolation functions over each triangle. The basic objective is to construct from the nodal values  $c_i$  a function  $c(p) = c(x,y)$  that interpolates  $c$  into the triangle interior. This section has been provided to supplement the necessarily brief discussion of polynomial interpolation procedures presented in Section 3.2.

The simplest surface corresponds to a linear variation over the triangle. For a triangle with vertices at the points (ijm) such a surface is defined by

$$c(x,y) = \frac{1}{D} [(a_0^i + a_1^i x + a_2^i y)c_i + (a_0^j + a_1^j x + a_2^j y)c_j + (a_0^m + a_1^m x + a_2^m y)c_m] \quad (3.17)$$

where

$$a_0^i = x_j y_m - x_m y_j \quad (3.18)$$

$$a_1^i = y_j - y_m \quad (3.19)$$

$$a_2^i = x_m - x_j \quad (3.20)$$

The remaining coefficients in (3.17) can be obtained by cyclic permutation of the subscripts (ijm). The determinant  $D$  in (3.17) is given by

$$2D = \det \begin{bmatrix} 1 & x_i & y_i \\ 1 & x_j & y_j \\ 1 & x_m & y_m \end{bmatrix} = 2 \text{ (area } ij\text{m)} \quad (3.21)$$

This procedure produces a piecewise linear surface composed of plane facets as shown in Figure 3.6. Because (3.17) reduces to straight lines joining the vertices the surface is globally continuous.

While the construction of interpolating functions which have higher-order smoothness  $C^1$  or  $C^2$  across element boundaries is not straightforward there is an extensive literature which discusses the subject because of its importance in finite element modeling. Some general reviews can be found in Akima (1975), Schumaker (1976), Barnhill (1977), Powell and Sabin (1977) and Lawson (1977). The approach adopted in this study (McLain, 1974; 1976ab) is to construct a local quadratic approximation to  $c_i(x,y)$  and then to form the  $c(x,y)$  as a weighted average of the functions at the three nodes. There are two reasons for adopting this method, the low computational cost and the general lack of information about the derivatives and function values at points other than the vertices. If these data are available then it is possible to use higher order elements of the type discussed by Barnhill (1977).

In the present work the variation at  $c_i$  is of the form

$$c_i(x,y) = a_{00} + a_{10}x + a_{01}y + a_{11}xy + a_{20}x^2 + a_{02}y^2 \quad (3.22)$$

where the six coefficients are determined from a weighted least squares fit to the surrounding data points. By setting  $a_{00} = c_i$  and solving for the remaining five coefficients the interpolating surface passes through the data points. In the surface fitting procedure distant data values are weighted using schemes of the type discussed in Section 3.3.

Once the polynomials have been constructed for each node they can be combined as follows

$$c(x,y) = W_i c_i + W_j c_j + W_m c_m \quad (3.23)$$

where the weighting functions  $W$  are chosen to ensure smooth transitions across each of the triangle edges. In the present work the weighting for each polynomial is proportional to the distance  $d_i$  of the point from the side of the triangle. The distance from the point  $(x,y)$  to the side is a linear function of  $x$  and  $y$

$$d_i = a_0 + a_1 x + a_2 y \quad (3.24)$$

where  $a_0$ ,  $a_1$  and  $a_2$  are the coefficients defining a line through the triangle edge opposite vertex  $i$ , scaled such that  $d_i = 1$  at the point  $i$ . The weight  $W_i$  used in the present study is given by

$$W_i = \frac{d_i^3}{(d_i^3 + d_j^3 + d_m^3)} \quad (3.25)$$

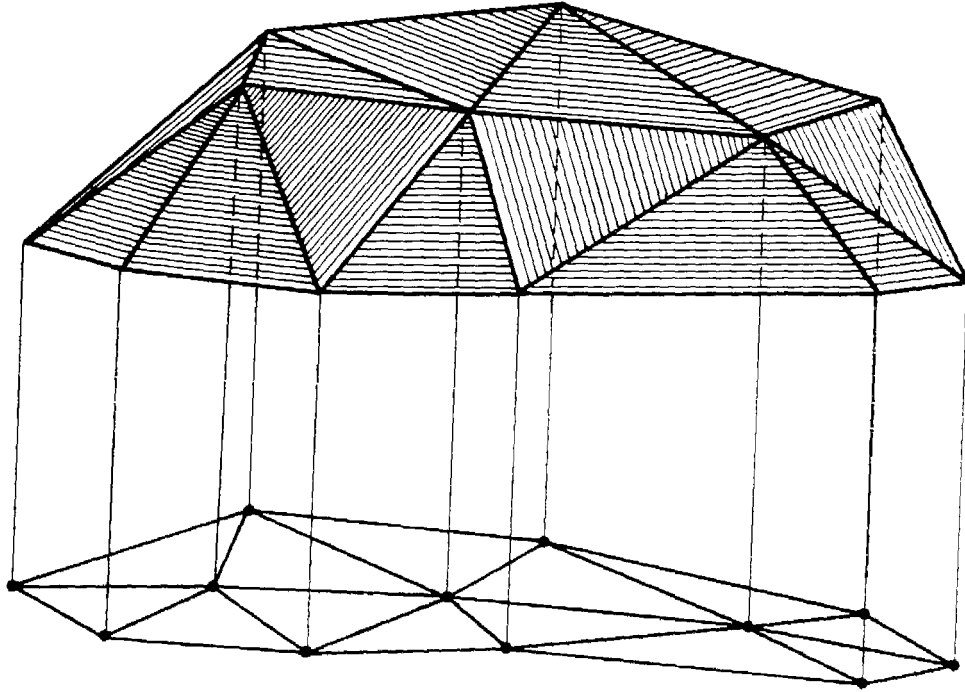


FIGURE 3.6  
An Example of a Linear Functional Variation  
Over each Triangular Element

### 3.6 Generation of Three-dimensional Wind Flow Fields

Advective transport and turbulent mixing are two of the physical processes that dominate pollutant dispersion over an urban area. In the airshed model they are characterized by the velocity field  $\underline{u}(\underline{x},t)$  and the eddy diffusion tensor  $K$ . Considerable research effort has been devoted to developing general procedures for specifying these inputs. Two common approaches for generating the required wind fields are: numerical solution of the governing equations of motion and objective analysis procedures which employ measured data. This section describes some of the different methods for constructing velocity distributions and is intended as an introduction to the material to be presented in the following section.

In the planetary boundary layer the flow dynamics can be described by the conservation equation for mass, momentum, energy and state. Dutton and Fichtl (1969), Busch (1973) and Donaldson (1973) have derived systems for boundary layer flows and in particular have discussed the validity of various simplifying assumptions. Despite the desirability of developing flow fields from solutions of the governing equations, relatively little progress has been made in developing models which can be used on a routine basis for generating three-dimensional mesoscale wind fields. There are two reasons for this, severe computational difficulties and practical problems associated with establishing the boundary conditions. For example Nickerson's (1979) model requires a priori specification of all thermodynamic variables at the boundaries. Maher and Pielke (1977) have a more realistic treatment of the heat flux at

the ground but their formulation is only applicable for steady state conditions. Most of the other available models are valid only for two-dimensional flow problems.

An operational constraint on the development of wind field models is the requirement that the input data be either routinely available or readily estimated. In a typical urban area the following data can usually be obtained: synoptic meteorological charts, geostrophic winds, terrain height, surface roughness, cloud cover, solar insolation, temperature, relative humidity, surface winds, and estimates at 850, 700 and 500 mb heights. The availability of this information was an important factor in selecting the objective analysis procedure to be presented in the following section.

There are two basic approaches to objective analysis. One is to use the field data and interpolate them in a manner such that mass conservation or other physical constraints are satisfied directly. This method has been used by Wahba and Wendelberger (1979) to develop 500 mb pressure surfaces. Another scheme, and the focus of Section 3.7, is to interpolate the measurements to a regular grid and then apply variational procedures to minimize the field divergence. The latter procedure has the advantage that any knowledge about measurement errors can be directly incorporated into the formulation. Figure 3.7 summarizes the general approaches that have been adopted to generate three-dimensional wind flow fields.

APPROACHES FOR GENERATING  
WIND FIELDS

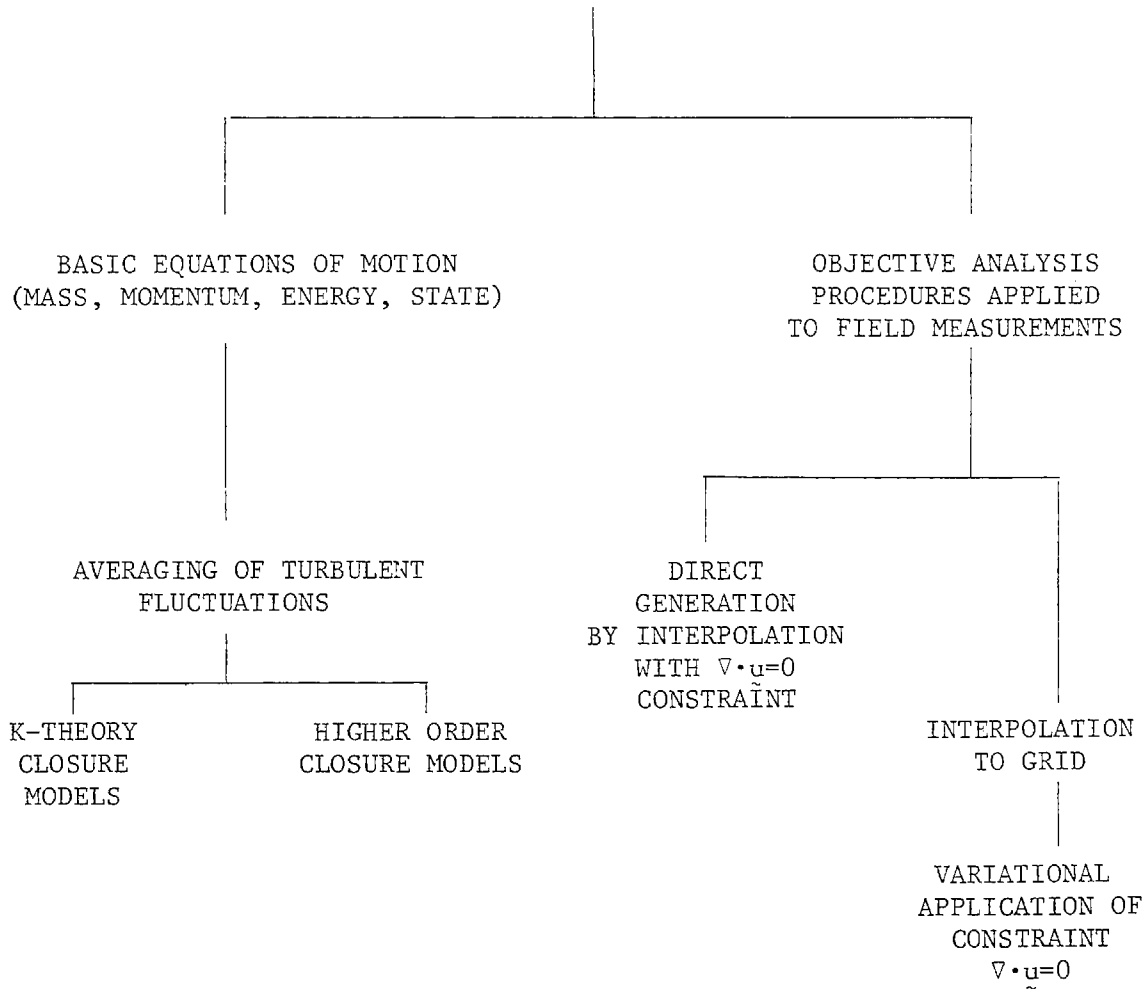


FIGURE 3.7

Summary of Approaches for Generating Wind Fields

3.7 An Objective Analysis Technique for Constructing  
Three-Dimensional Urban-Scale Wind Fields

(Reprinted from J. Applied Meteorology, 19, 98-108.)

## An Objective Analysis Technique for Constructing Three-Dimensional Urban-Scale Wind Fields

WILLIAM R. GOODIN,<sup>1</sup> GREGORY J. MCRAE AND JOHN H. SEINFELD

*Environmental Quality Laboratory, California Institute of Technology, Pasadena 91125*

(Manuscript received 10 January 1979, in final form 8 September 1979)

### ABSTRACT

An objective analysis procedure for generating mass-consistent, urban-scale three-dimensional wind fields is presented together with a comparison against existing techniques. The algorithm employs terrain following coordinates and variable vertical grid spacing. Initial estimates of the velocity field are developed by interpolating surface and upper level wind measurements. A local terrain adjustment technique, involving solution of the Poisson equation, is used to establish the horizontal components of the surface field. Vertical velocities are developed from successive solutions of the continuity equation followed by an iterative procedure which reduces anomalous divergence in the complete field. Major advantages of the procedure are that it is computationally efficient and allows boundary values to adjust in response to changes in the interior flow. The method has been successfully tested using field measurements and problems with known analytic solutions.

### 1. Introduction

A key input to most urban-scale air pollution models is an accurately specified, mass-consistent wind field. In most practical situations numerical solution of the full Navier-Stokes equations is not feasible as a means of constructing such a field. As a result, simpler objective analysis procedures must be used. The most common approach for generating a gridded wind field consists of a two-step procedure, the first step of which is interpolation of the sparse and discrete measurements within the airshed to a finer mesh (Goodin *et al.*, 1979). Once the initial field has been established, the next step is to employ an objective analysis procedure to adjust the wind vectors at each grid point so that appropriate physical constraints are satisfied. We present here a new technique for constructing three-dimensional velocity fields with a minimum of anomalous divergence.

### 2. Previous work on wind field divergence reduction

Only a limited number of divergence reduction procedures have appeared in the literature. Endlich (1967) used a point-iterative method to reduce the two-dimensional divergence in a wind field while retaining the vorticity in the original field. Fankhauser (1974) approached the three-dimensional divergence reduction problem from the point of view of accounting for measured data errors; in particular,

those which increase with altitude. Liu and Goodin (1976) adapted the technique of Endlich to a two-dimensional mesoscale wind field. The flow field within the mixed layer was assumed to be vertically integrated and divergence was adjusted point by point with the capability of holding wind station values fixed. More recently, Sherman (1978) devised a procedure called MATHEW for constructing three-dimensional mass-consistent wind fields. Based on the variational calculus approach of Sasaki (1958, 1970), the method involves solution of a Lagrange multiplier equation. A two-dimensional vertically integrated version of MATHEW called MASCON (Dickerson, 1978) was incorporated into the LIRAQ model (MacCracken, *et al.*, 1978). The influences on the flow field of topography, surface roughness and temperature gradients were accounted for in a technique developed by Yocke *et al.* (1978) which uses empirically determined coefficients to weight the contributions of the various processes responsible for the flow field divergence.

While each of the above techniques has advantages, several shortcomings are apparent. In a number of cases the final form of the flow field is critically dependent on empirically chosen constants. Little guidance is given in the literature as to how some of these values can be developed for new regions. Another problem with some formulations is the initial estimates of horizontal velocities at region boundaries often force the nature of the interior flow solution. This can be a serious problem because, typically, few measurements are available

<sup>1</sup> Present affiliation: Advanced Technology Group, Dames & Moore, Los Angeles, CA 90024.

at boundaries and so there can be large uncertainties associated with specification of the initial velocity field. From an operational point of view, none of the above techniques employ variable vertical grid spacing or terrain-following coordinate systems. The present paper introduces an algorithm which avoids most of the above limitations.

### 3. The basic algorithm

The present wind field generation algorithm consists of several basic steps. As a starting point, the region boundaries, vertical extent and basic grid cell sizes must be chosen. These are frequently dictated by the nature of the intended application. Once the grid has been established, the surface level velocity measurements and upper level wind and temperature data are interpolated to specify initial values for each computational point. The final step is to adjust the velocity field with the objective of minimizing anomalous divergence.

#### a. Surface wind field generation

The surface wind field is constructed from the measured data (converted to  $u$  and  $v$  components) by interpolation to a regular grid using inverse distance-squared weighting (Goodin *et al.*, 1979). A fixed radius of influence  $R$  is specified which indicates the distance beyond which the influence of a station's value is no longer felt. The influence of gross terrain features (e.g., mountain ranges) is accounted for by the use of barriers to flow during interpolation of the wind components. This procedure, however, does not incorporate the effects of local terrain features that have scales less than one grid cell length. Following the interpolation procedure, a local terrain-adjustment technique, which is similar to that of Anderson (1971, 1973), is used in the wind field calculation. This adjustment procedure involves solution of Poisson's equation

$$\nabla^2 \phi = \psi(x, y), \quad (1)$$

where  $\phi$  is a velocity potential and  $\psi$  a forcing function based on layer thickness and terrain gradients. An evaluation of solution techniques for Eq. (1) was made which included a Fourier series method (Dorr, 1970), the successive overrelaxation (SOR) method (Roache, 1972), and the alternating-direction-implicit (ADI) method (Peaceman and Rachford, 1955). Based on efficiency, programming and accuracy considerations, the ADI method was chosen.

As a test of the surface wind field calculation procedure,  $u$  and  $v$  component data from 63 wind stations in the South Coast Air Basin (SCAB) in California for 1600 PST 26 June 1974 were interpolated to a  $100 \times 50$  square grid. The grid spacing was 3.2 km and the radius of influence used was 25 grid squares (a size large enough to include at least

two data points). The measured data together with barriers to flow are shown in Fig. 1. Terrain data were obtained at 200 ft horizontal intervals from the National Cartographic Information Center, U.S. Geological Survey. From these data an average height for each 3.2 km square was then computed. Fig. 2 shows a three-dimensional plot of the terrain, the highest point of which is  $\sim 3000$  m MSL.

The results of the interpolation and terrain adjustment procedure are displayed in Fig. 3. For most stations, the agreement between computed and measured values, both for magnitude and direction, is quite good. The mean error in magnitude is  $0.7 \text{ m s}^{-1}$  which is less than a 20% relative error, while the mean direction error is  $11.5^\circ$ ; this is within the  $22.5^\circ$  sector to which the wind data are given. Among the stations operated by the South Coast Air Quality Management District (SCAQMD) (from which the most reliable data are obtained), the maximum error in magnitude occurs at Prado Park, a station which may be unduly influenced by localized channeling effects of Santa Ana Canyon. The computed magnitude is  $5.1 \text{ m s}^{-1}$ , and the measured value is  $6.7 \text{ m s}^{-1}$ . The largest error in magnitude occurring at any station is at CT33, a station operated by California Department of Transportation (CALTRANS). This station is in the vicinity of a convergence zone behind the Laguna Hills. The computed magnitude is  $3.0 \text{ m s}^{-1}$  and the measured magnitude is  $5.8 \text{ m s}^{-1}$ .

The maximum error in direction among the SCAQMD stations occurs at Reseda, where the computed and measured vector differ by  $44^\circ$ . At 1600 PST, Reseda appeared to be near the location of the so-called San Fernando convergence zone, where air from Ventura encounters air from the Los Angeles basin. The measured vector at Reseda probably represents an average of a local fluctuating velocity and is, therefore, less representative of a 3.2 km square for that hour. The largest error in direction occurring at any station is at Station CT35 where the difference in direction is  $69^\circ$ . The location of this station, which is downwind of the pass near Camarillo and adjacent to the Santa Monica Mountains, may not be representative of a larger area.

All the station measurements and calculated results for the sample problem are displayed in Figs. 4a and 4b. Two conclusions are apparent from an inspection of the scatter plots. The first is that there is little or no systematic bias in either the magnitude or direction of the calculated results. The second is that there is a high degree of correlation between observed and predicted,  $r = 0.86$  for the wind magnitudes and  $r = 0.90$  for direction.

#### b. Interpolation of the upper level wind and temperature data

Before the transport of urban pollutants can be adequately modeled some knowledge of the vertical



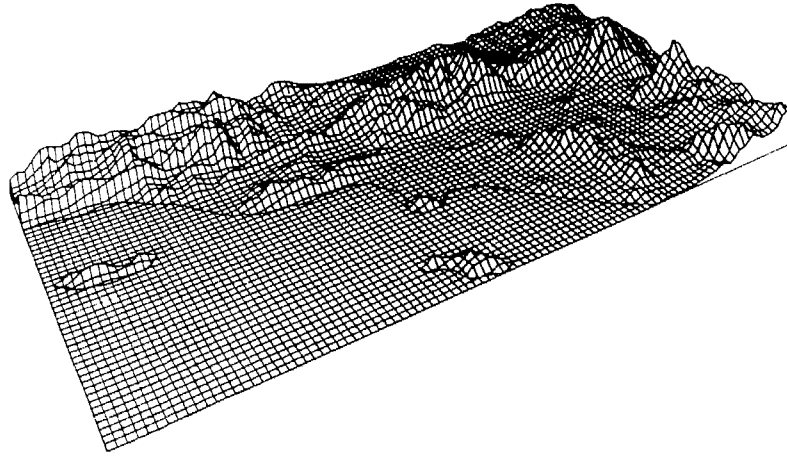


FIG. 2. Topography of Los Angeles basin viewed from the southwest.

temperature structure and the three-dimensional flow field is required. These quantities are known with much less precision than the surface quantities since fewer measurements are customarily available. As an example of available data in the Los Angeles area, Fig. 1 shows the measurement stations for upper level data in the SCAB. This data set includes stations in operation: Los Angeles International Airport (LAX), Pt. Mugu, San Nicolas Island, El Monte, Riverside and Edwards Air Force Base (off grid); sites with data calculated for the days of interest using the Limited-Area Fine Mesh Model (Gerrity, 1976); Victorville, Escondido, Ventura; and stations which have recorded upper level data in the past, providing "typical" data: Long Beach, Burbank, Santa Monica and March Air Force Base. An average of two measurements per day are available at each station except for El Monte where an acoustic sounder records the depth of the mixed layer continuously.

The approach taken for spatial interpolation of mixing depth and upper level wind data is slightly different from that used for the surface quantities. Imprecision in the measured data makes a highly accurate interpolation procedure unnecessary; as a result  $r^{-1}$  weighting was chosen since it produces a smoother field than  $r^{-2}$  weighting. In performing the interpolation of mixing depth, the height above sea level is first computed at all grid points. The height of the terrain surface is then subtracted to give mixing depth above the surface. This procedure is used because the height of the mixed layer above sea level tends to be a smooth surface while the terrain changes more abruptly. Contours of mixing depth tend to follow the coastline since the degree of heating of air moving inland depends mainly on the distance travelled over land. The mixing depth data

for 1600 PST 26 June 1974 were interpolated using the  $r^{-1}$  procedure and then smoothed using a simple five-point filter in which the new value at a given point is the average of the value at the point itself and the values at the four adjacent points,

$$h_{ij}^{n+1} = 0.20(h_{ij}^n + h_{i-1,j}^n + h_{i+1,j}^n + h_{i,j-1}^n + h_{i,j+1}^n). \quad (2)$$

The maximum depth was set at 1100 m since a depth greater than this is generally assumed to be unlimited. A three-dimensional plot of mixing depth above sea level is shown in Fig. 5. The mixing depth follows the contours of the terrain at high elevations since negative mixing heights cannot occur.

In order to follow pollutants as they move above the mixed layer, the top of the region was set at a high level (above the mixed layer). The top of the mixed layer was allowed to fluctuate both temporally and spatially within this region. Its only real purpose is a reference height above which vertical diffusion is very small. In addition, to eliminate the difficulty in specifying vertical velocity boundary conditions, a coordinate system which follows the terrain surface was chosen rather than sea level based coordinates. The transformation from sea level to terrain-following coordinates produces a new vertical velocity,  $W$ , i.e.,

$$W = w - u \left( \frac{\partial h}{\partial x} + \rho \frac{\partial \Delta H}{\partial x} \right) - v \left( \frac{\partial h}{\partial y} + \rho \frac{\partial \Delta H}{\partial y} \right) - \rho \frac{\partial \Delta H}{\partial t}, \quad (3)$$

where  $\Delta H(x, y, t) = H(x, y, t) - h(x, y)$  is the height of the top of the region above the terrain surface, and  $\rho$  is the new vertical coordinate ( $0 \leq \rho \leq 1$ ).

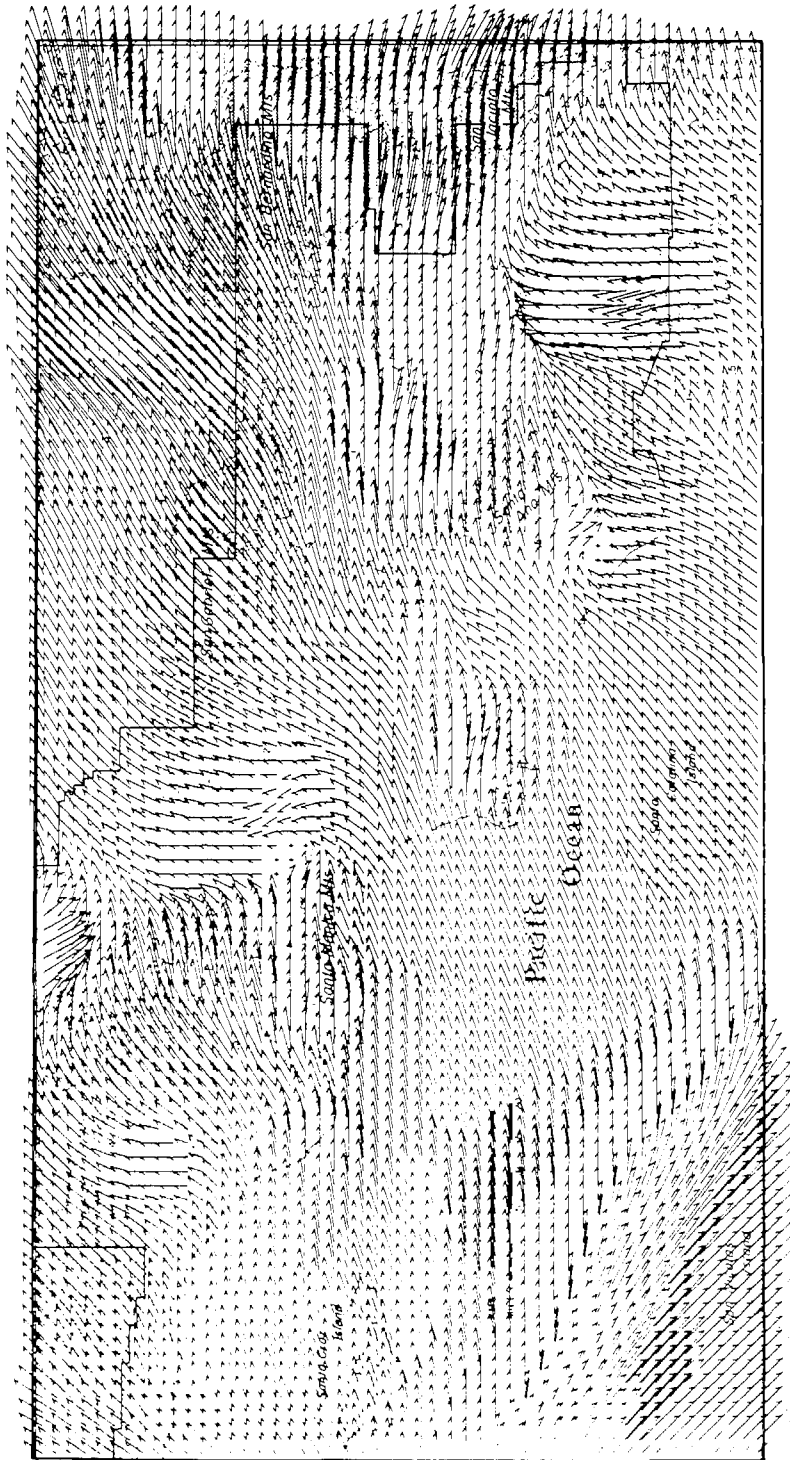


FIG. 3. Flow field in the surface layer following interpolation and adjustment for terrain effects.

Fig. 6a shows the general case where  $\Delta H$  is a function of space as well as time. In order to eliminate complications introduced into the advection scheme by nonparallelepiped grid volumes in  $x, y, z$  space,  $\Delta H$  is used for normalization. Figs. 6b and 6c show the transformation from the  $x, y, z$  space to  $x, y, \rho$  space.

In the new coordinate system, the continuity equation is

$$\frac{\partial W}{\partial \rho} + \frac{\partial(u\Delta H)}{\partial x} + \frac{\partial(v\Delta H)}{\partial y} = 0. \quad (4)$$

Given the horizontal velocities at each vertical level from  $r^{-1}$  interpolation of the measured data,  $W$  can be calculated at each level using Eq. (4). Unfortunately, this simple solution produces unrealistically large values of  $W$  at the top of the region since all residual divergence in the field is propagated upward. Therefore, a procedure is required that will reduce the divergence in the flow field to an acceptable level while maintaining small upper level vertical velocities.

### c. New divergence reduction procedure

Once the surface level flow field has been established and the upper level wind data have been interpolated to the three-dimensional grid, the next step is to reduce the divergence in the total flow field. The proposed procedure involves three steps:

1) The divergence in each of the interpolated  $u$  and  $v$  fields at each vertical level above the lowest layer is first reduced using a slightly modified version of the simple five-point filter discussed above. The equation for smoothing is

$$u_{ij}^{n+1} = 0.20(u_{ij}^n + u_{i+1,j}^n + u_{i-1,j}^n + u_{i,j+1}^n + u_{i,j-1}^n)(1 - \alpha_k) + \alpha_k u_{ij}^n, \quad (5)$$

where  $\alpha_k$  is a parameter which allows the user to keep the measured velocity at station  $k$  fixed ( $\alpha_k = 1$ ) or keep only some of its original influence ( $\alpha_k < 1$ ). This parameter is zero at all non-measuring station points. This first step is designed to reduce as much of the anomalous divergence as possible. The number of passes through the smoothing step is related to the relative atmospheric stability at that level and will be determined empirically. A relatively unstable (generally near ground level) layer requires few iterations since less of the divergence present is anomalous, while a more stable upper layer must be smoothed more times. The more smoothing a field of values is subjected to, the more initial anomalous divergence is dissipated horizontally within that layer, i.e., the more the vertical velocity above that layer (which will be computed from the divergence within the layer) will be suppressed.

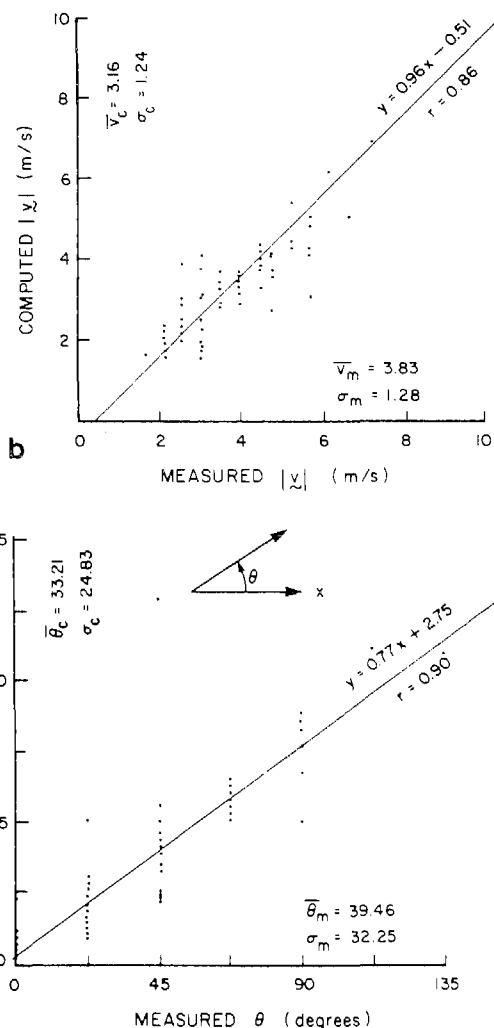


FIG. 4. Comparison of field observations against calculated results: (a) Wind direction. (b) wind magnitude.

2) Following this initial smoothing step, the vertical velocity above each layer is computed from the divergence within that layer. The layers are temporarily disconnected from each other during this calculation so that the calculated vertical velocity above a layer depends only upon the divergence within that layer. This prevents velocities at the top of the region from becoming unrealistically large. These vertical velocities will be held fixed throughout the rest of the divergence reduction procedure.

3) The final refinement reduces the remaining divergence which exists within each layer by application of a two-dimensional technique to each layer similar to that of Liu and Goodin (1976). The equation solved is (with  $\Delta H = \text{constant}$ )

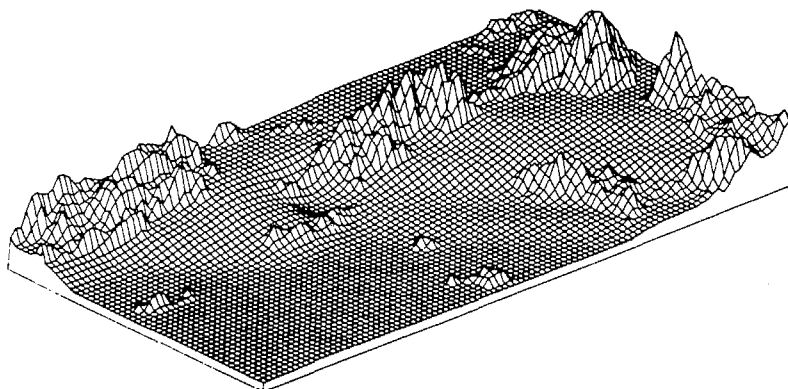


FIG. 5. Mixing heights above sea level computed from measured data for 1600 PST 26 June 1974.

$$\frac{\partial W}{\partial \rho} + \Delta H \left( \frac{\partial u}{\partial x} + \frac{\partial v}{\partial y} \right) = D_R(x, y, \rho), \quad (6)$$

where  $D_R(x, y, \rho)$  is a measure of the remaining divergence. At grid point  $(i, j, k)$ , Eq. (6) can be written as

$$D_{ijk}^{n+1} = \frac{W_{i,j,k-1,2} - W_{i,j,k-1,2}}{\Delta \rho} + \Delta H \left[ \frac{u_{i+1/2,j,k}^{n+1} - u_{i-1/2,j,k}^{n+1}}{\Delta x} + \frac{v_{i,j-1/2,k}^{n+1} - v_{i,j+1/2,k}^{n+1}}{\Delta y} \right], \quad (7)$$

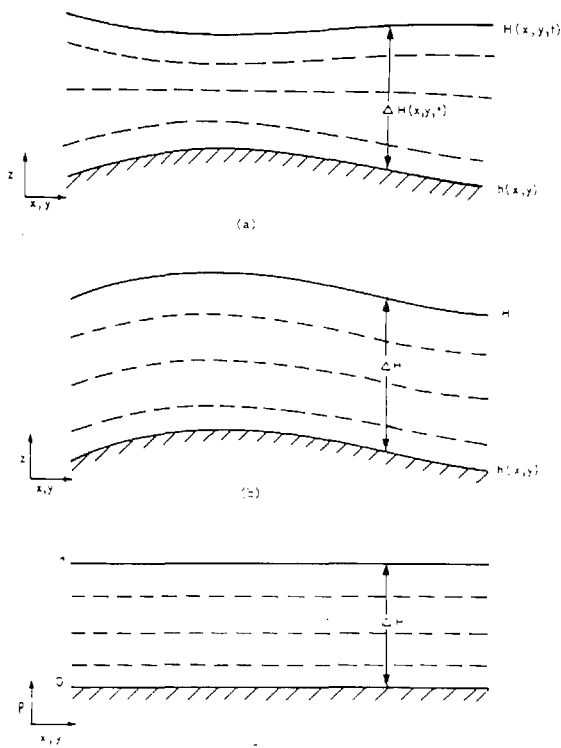


FIG. 6. A terrain-following coordinate system: (a) general case  $H = H(x, y, t)$ ; (b)  $H$  is a constant height above the terrain; (c) transformed  $x, y, \rho$  coordinate system.

where the superscript  $n + 1$  indicates the values are computed for the  $(n + 1)$ st iteration, and the subscript  $R$  is dropped from  $D_R$  for convenience.

To remove the divergence at the point  $(i, j, k)$ , adjustments are made to the  $u$  values at  $(i + 1/2, j, k)$  and  $(i - 1/2, j, k)$  and the  $v$  values at  $(i, j + 1/2, k)$  and  $(i, j - 1/2, k)$  in order that the divergence is exactly zero at  $(i, j, k)$ . Since this procedure will add additional divergence to surrounding points, the whole grid must be scanned iteratively. The adjustments to the velocity components are

$$\left. \begin{aligned} u_{i+1/2,j,k}^{n+1} &= u_{i+1/2,j,k}^n + u_T \\ u_{i-1/2,j,k}^{n+1} &= u_{i-1/2,j,k}^n - u_T \\ v_{i,j+1/2,k}^{n+1} &= v_{i,j+1/2,k}^n + v_T \\ v_{i,j-1/2,k}^{n+1} &= v_{i,j-1/2,k}^n - v_T \end{aligned} \right\}, \quad (8)$$

where  $u_T$  and  $v_T$  are the adjustment velocities. These velocities are computed by substitution in Eq. (7).

$$0 = D_{ijk}^{n+1} - \Delta H \left( \frac{2u_T}{\Delta x} + \frac{2v_T}{\Delta y} \right). \quad (9)$$

Assuming that  $\Delta y = \Delta x$  and that the velocity adjustments are equally weighted in each direction, Eq. (9) can be solved to give

$$u_T = \frac{-D_{ijk}^{n+1} \Delta x}{4\Delta H}. \quad (10)$$

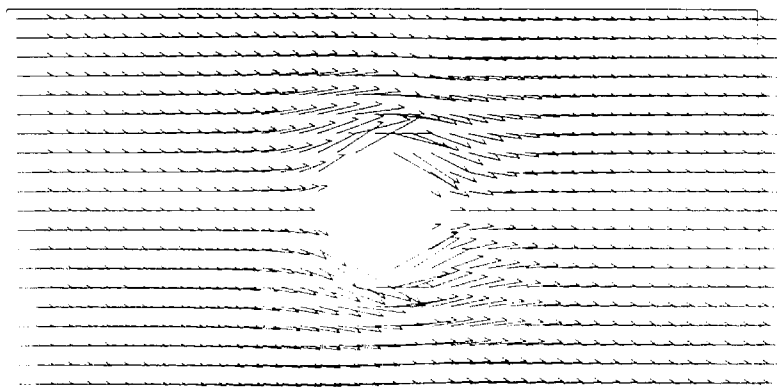


FIG. 7. Idealized three-dimensional flow field—initial state in layer 1.

Thus, the complete three-dimensional divergence reduction procedure consists of 1) smoothing at each level using an empirically determined number of smoothing passes based on local atmospheric stability, 2) followed by solution of Eq. (7) at each level for  $W_{i,j,k-1,2}$ , temporarily assuming  $W_{i,j,k-1,2}$  is zero; and 3) Eqs. (7), (10) and (6) are then solved repeatedly using the calculated values for  $W$  until the maximum divergence is reduced to an acceptable level, i.e., the magnitude of the divergence should be less than the local vertical velocity and less than the estimated errors in the horizontal velocity components.

The interaction between the flow field and the change in depth of the mixed layer has not been accounted for in the above procedure because of a lack of upper air data, i.e., mixing depth and vertical velocity are never measured simultaneously, and because attempts to tie the vertical cell heights to the mixing depth resulted in large horizontal wind velocities as the mixing depth approached zero.

#### 4. Test of present divergence reduction procedure

A hypothetical flow field was constructed to test the divergence reduction procedure just discussed and estimate the approximate number of smoothing passes corresponding to each Pasquill stability class. The grid chosen was  $40 \times 20 \times 2$  points. The upper layer contained uniform horizontal flow at  $5 \text{ m s}^{-1}$ . In the lower layer the flow consisted of potential flow around a circular disk located at the center of the grid. Each layer was of equal thickness with a horizontal grid spacing of 2 km. Fig. 7 shows the initial flow pattern in the lower layer.

The test consisted of reducing the divergence in the flow following removal of the disk. First, the smoothing step reduced the gross divergence in the lower layer (the upper layer required no smoothing). The vertical velocity between the layers was then

calculated from the divergence in the lower layer using Eq. (10), temporarily assuming zero velocity at the bottom of that layer. (The vertical velocity above layer 2 was identically zero since there was no divergence present initially.) Finally, the refined, iterative divergence-reduction step was performed within each layer as described in Section 3c.

The results for number of smoothing passes ranging from 1 to 40 are shown in Table 1. As expected, the final divergence, as well as maximum  $W$ , is a strong function of number of initial smoothing passes. The iterative divergence reduction procedure then reduces the remaining divergence by a factor of 20–40 after 100 iterations. A maximum vertical velocity of  $0.28 \text{ m s}^{-1}$  approximately corresponds to vertical velocities observed within the mixed layer during the daytime hours in the Los Angeles Basin (Angell *et al.*, 1972), while typical subsidence motion within the inversion is on the order of  $0.02 \text{ m s}^{-1}$ .

The set of upper air data collected in Los Angeles on 1600 PST 26 June 1974 was then used to test the present procedure. The data measurement locations are indicated in Fig. 1. Five vertical levels were

TABLE 1. Results of the present divergence reduction procedure on an idealized data set.

Number of smoothing passes	Maximum divergence in layer 2		Maximum $W$ above layer 1 ( $\text{m s}^{-1}$ )
	Following initial smoothing ( $\times 10^6 \text{ s}^{-1}$ )	Following 100 iterations ( $\times 10^6 \text{ s}^{-1}$ )	
1	350.0	8.3	0.28
5	41.7	1.1	0.04
10	16.7	0.3	0.01
20	11.1	0.3	0.01
40	5.5	0.3	0.004

TABLE 2. Results of present divergence reduction procedure on wind data from 1600 PST 26 June 1974.

Layer	Thickness of layer (m)	Number of smoothing passes during first step	rms divergence		
			After initial smoothing ( $\times 10^6 \text{ s}^{-1}$ )	After 100 iterations ( $\times 10^6 \text{ s}^{-1}$ )	After 200 iterations ( $\times 10^6 \text{ s}^{-1}$ )
1	50	0	151	149	148
2	150	5	27	20	20
3	300	10	27	17	14
4	550	20	25	14	11
5	450	20	51	28	20

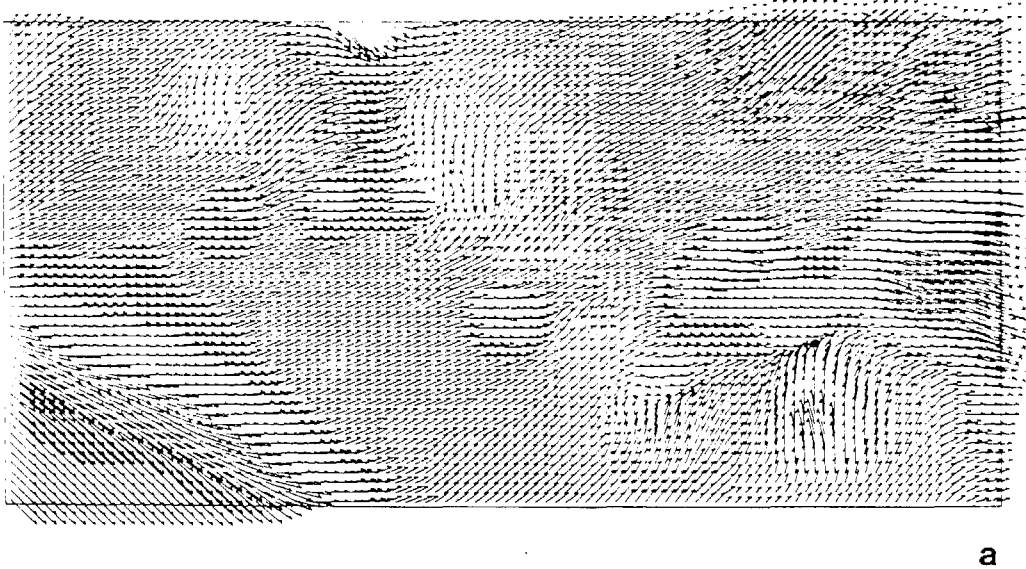
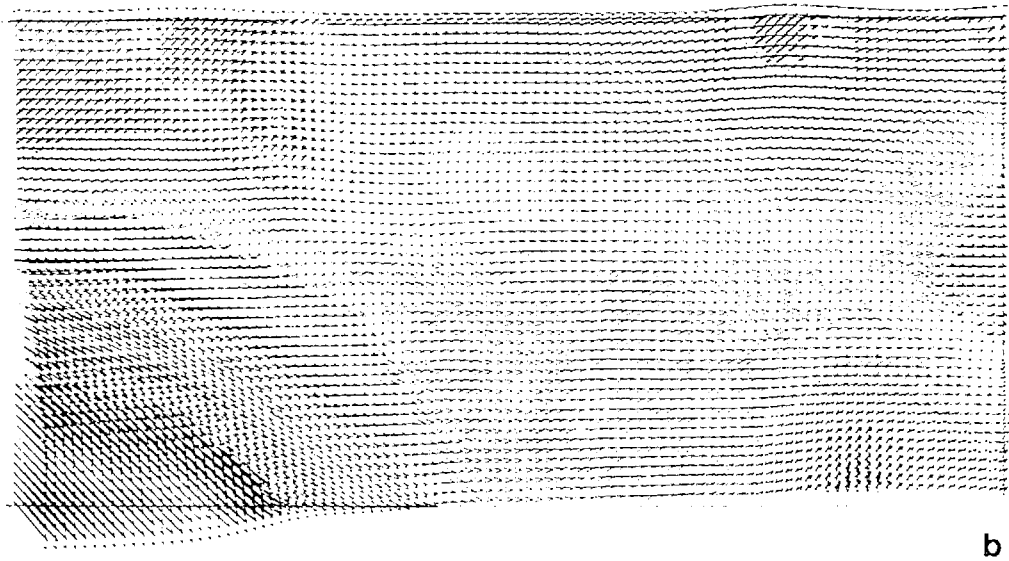


FIG. 8. (a) Horizontal flow field in layer 2 (550 ft above terrain) at 1600 PST 26 June 1974 and (b) horizontal flow field in layer 3 (1200 ft above terrain) at 1600 PST 26 June 1974.

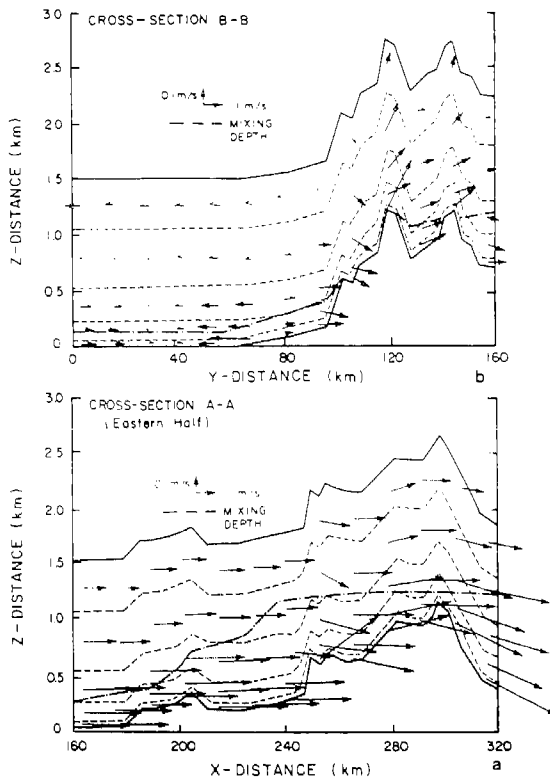


FIG. 9. Vertical velocity cross sections corresponding to locations indicated in Fig. 1. (Note exaggeration of vertical scale.) (a) Eastern half of cross section AA, (b) cross section BB.

chosen with thicknesses of 50, 150, 300, 550 and 450 m, respectively. The lowest layer, of depth 50 m, was the surface layer, the flow pattern of which had been calculated previously from the surface data network. The interpolated  $u$  and  $v$  fields in layers 2–5 were smoothed 5, 10, 20 and 20 times, respectively. These numbers were obtained empirically from the calculation of the flow around the disk and correspond approximately to Pasquill stability classes B, D and E.

The results of the calculation procedure are displayed in Table 2 and Figs. 8a, 8b, 9a and 9b. The algorithm reduced the divergence to  $<0.001 \text{ s}^{-1}$  in all layers; in the vicinity of downtown Los Angeles, an area of relatively flat terrain, the divergence is of order  $10^{-5} \text{ s}^{-1}$ . The largest divergence in each layer occurs over mountainous regions, especially the San Jacinto and San Gabriel mountains. In these areas, upper air data are nonexistent, so the interpolation procedure has generated a smoothed flow field which does not accurately reflect the influence of the steep terrain in these regions. Most of the divergence was reduced during the initial smoothing step. The last two columns in Table 2 indicate that 100 iterations were sufficient to refine the divergence reduction during the second step. Very little additional reduction was obtained after 200 iterations. The algorithm has been extensively tested against analytic problems, the results of field releases of  $\text{SF}_6$  and has been used to generate 72 different hours of wind fields for use in the modeling study by McRae *et al.* (1980).

TABLE 3. Comparison of attributes of three-dimensional divergence reduction procedures.

Attribute	Present technique	MATHEW
Coordinate system	Terrain-following coordinates	Coordinate system parallel to sea level
Treatment of flow over complex terrain	Barriers to flow are used during interpolation procedure. Surface layer flow is adjusted using $\nabla^2 \phi = D$ , where $D$ is magnitude of vertical perturbation.	Obstacle cells are used to represent terrain. They are treated as no-flow-through boundaries.
Interpolation procedure	$1/r^2$ weighting of station data at surface. $1/r$ weighting at each level above surface.	$1/r^2$ weighting at surface. Upper level values are obtained from synoptic analysis.
Treatment of horizontal boundary conditions during divergence reduction procedure	Normal component of velocity at boundary is adjusted according to value at adjacent interior point. (Same procedure as at all other interior points.)	Program accepts $\partial \lambda / \partial n = 0$ or $\lambda = 0$ as boundary conditions. Derivative is approximated by three-point difference.
Treatment of atmospheric stability	Number of smoothing passes through interpolated field at each vertical level is related to the stability at that level. Amount of smoothing required for a given stability class is obtained empirically.	Gaussian precision moduli, $\alpha_1, \alpha_2$ , which are functions of measurement errors must be determined empirically.
Variable vertical grid spacing	Yes	No
Computer time required	25 000 points ( $100 \times 50 \times 5$ ) Divergence $\rightarrow 10^{-4} \text{ s}^{-1}$ 5 min on IBM 370	23 000 points ( $25 \times 33 \times 28$ ) Divergence $\rightarrow 10^{-12} \text{ s}^{-1}$ 2–5 min on CDC 7600 (20–50 min on IBM 370)

### 5. Comparison with previous divergence reduction procedures

Table 3 presents a comparison of the proposed method with MATHEW. Each procedure uses an inverse-distance weighting procedure to interpolate the measured values. MATHEW, however, relies on a synoptic analysis to determine the horizontal velocities at the upper boundary. If a vertical profile of wind speed and direction is not available, a linear variation is assumed between the surface layer winds and the upper boundary.

The use of obstacle cells in MATHEW for flow over complex terrain affects the computer time required for solution, since the computer time increases with the complexity of the terrain. The use of terrain-following coordinates in the present technique avoids this difficulty. A major advantage of the present technique is that it allows the boundary values to adjust in response to the interior flow. Each of the techniques requires an empirically determined parameter. Its value is calculated based on atmospheric stability. The choice of the value to be used in each procedure must be determined by the experience of the user.

### 6. Conclusions

A new technique for constructing a three-dimensional, urban-scale, mass-consistent wind field has been introduced. The interpolation method relies on measured upper air data (when available) for constructing the flow field. If little or no upper air data are available, the user may construct velocity profiles using some assumed profile such as a power law for input to the program. The problem of large vertical velocity at the top of the region has been avoided by reducing divergence significantly at the lower levels rather than allowing it to propagate out of the top of the region. Variable vertical grid spacing is also permitted allowing the user greater flexibility in the concentration calculations. The present technique is easy to implement, computationally efficient, and offers promise as an attractive method for routine meteorological applications.

*Acknowledgments.* Portions of this work were supported by the California Air Resources Board under Contract A5-046-87, and by Institutional

Grant EY-76-G-03-1305 from the Department of Energy.

### REFERENCES

- Anderson, G. E., 1971: Mesoscale influences on wind fields. *J. Appl. Meteor.*, **10**, 377-386.
- , 1973: A mesoscale windfield analysis of the Los Angeles Basin. EPA-650/4-73-001. The Center for Environment and Man, Inc., Hartford, Conn., 56 pp.
- Angell, J. K., D. H. Pack, L. Machta, C. R. Dickson and W. H. Hoecker, 1972: Three-dimensional air trajectories determined from tetron flights in the planetary boundary layer in the Los Angeles Basin. *J. Appl. Meteor.*, **11**, 451-471.
- Dickerson, M. H., 1978: MASCON—A mass consistent atmospheric flux model for regions with complex terrain. *J. Appl. Meteor.*, **17**, 241-253.
- Dorr, F. W., 1970: The direct solution of the discrete Poisson equation on a rectangle. *SIAM Rev.*, **12**, 248-263.
- Endlich, R. M., 1967: An iterative method for altering the kinematic properties of wind field. *J. Appl. Meteor.*, **6**, 837-844.
- Fankhauser, J. C., 1974: The derivation of consistent fields of wind and geopotential height from mesoscale rawinsonde data. *J. Appl. Meteor.*, **13**, 637-646.
- Gerrity, J. F., Jr., 1977: The LFM model: A documentation. NOAA Tech. Memo. NWS NMC 60, National Meteorological Center, 66 pp.
- Goodin, W. R., G. J. McRae and J. H. Seinfeld, 1979: A comparison of interpolation methods for sparse data: Application to wind and concentration fields. *J. Appl. Meteor.*, **18**, 761-771.
- Liu, C. Y., and W. R. Goodin, 1976: An iterative algorithm for objective wind field analysis. *Mon. Wea. Rev.*, **104**, 784-792.
- MacCracken, M. C., D. J. Wuebbles, J. J. Walton, W. H. Duerwer and K. E. Grant, 1978: The Livermore regional air quality model: I. Concept and development. *J. Appl. Meteor.*, **17**, 254-272.
- McRae, G. J., W. R. Goodin and J. H. Seinfeld, 1980: Development of a second generation mathematical model of photochemical air pollution. Final Report to the California Air Resources Board under Contract A5-046-87.
- Peaceman, D. W., and H. H. Rachford, Jr., 1955: The numerical solution of parabolic and elliptic differential equations. *J. SIAM*, **3**, 28-41.
- Roache, P. J., 1972: *Computational Fluid Dynamics*. Hermosa Publ., 434 pp.
- Sasaki, Y., 1958: An objective analysis based on the variational method. *J. Meteor. Soc. Japan*, **36**, 77-88.
- , 1970: Some basic formalisms in numerical variational analysis. *Mon. Wea. Rev.*, **98**, 875-898.
- Sherman, C. A., 1978: A mass-consistent model for wind fields over complex terrain. *J. Appl. Meteor.*, **17**, 312-319.
- Yocke, M. A., M. K. Liu and J. L. McElroy, 1978: The development of a three-dimensional wind model for complex terrain. *Proc. Joint Conf. Application of Air Pollution Meteorology*, Salt Lake City, Amer. Meteor. Soc., 209-214.

### 3.8 Extensions of the Wind Field Generation Procedure to Incorporate the Effects of Surface Roughness

In situations where little or no upper air wind data are available it is often necessary to use the surface measurements to estimate vertical velocity profiles. This section summarizes the procedure of Goodin and McRae (1980) which incorporates the influence of local surface roughness and stability in a determination of the vertical variation of the wind speed.

A variety of methods have been used, with varying success, for calculating the wind profile in the lowest layers of the atmosphere ( $z < 100$  m). The profiles are either represented by a power-law expression of the form,

$$u(z) = u(z_r) \left(\frac{z}{z_r}\right)^\alpha \quad (3.26)$$

or alternatively,

$$u(z) = \frac{u_*}{k(1-\beta)} \left[ \left(\frac{z}{z_o}\right)^{1-\beta} - 1 \right] \quad (3.27)$$

where the parameters  $\alpha$  and  $\beta$  must be determined empirically. Tables of values for these parameters as a function of surface roughness and/or stability have been developed by Deacon (1949), Davenport (1960), Touma (1977), and Irwin (1979). The values for  $\alpha$  range from 0.05 to 0.60 increasing with stability and roughness. The parameter  $\beta$  ranges from approximately 0.8 to 1.2 increasing with decreasing stability. The familiar logarithmic profile can be obtained from (3.27) by using a

series expansion and setting  $\zeta = 1$  i.e.

$$u(z) = \frac{u_*}{k} \ln \left( \frac{z}{z_0} \right) \quad (3.28)$$

Equation (3.28) is only valid for near neutral conditions. Given the wide variability in  $\alpha$  and  $\beta$  there is a clear need for a direct approach that incorporates more recent boundary layer measurements. The technique adopted in this study is to use Monin-Obukhov similarity solution in the surface layer. The integral form of the velocity gradient is given by

$$u(z) = u(z_r) + \frac{u_*}{k} \int_{z_r}^z \phi \left( \frac{z}{L} \right) \frac{dz}{z} \quad (3.29)$$

where  $\phi(z/L)$  is a universal function of atmospheric stability, the Monin-Obukhov length and the height above the ground. The functional form of these expressions is discussed in considerable detail in the following chapter. Given the  $\phi$  functions, (3.29) can be integrated from a reference height  $z_r$  to some other elevation  $z < 2|L|$ .

Above the surface layer ( $z > L$ ) a logarithmic profile is used for stable conditions (Webb, 1970). The procedure involves matching the similarity solution at  $z=L$  so that the gradient is continuous. The resulting equation is

$$u(z) = \frac{5.7u_*}{k} \ln \left( \frac{z}{L} \right) + u_L ; \frac{z}{L} > 0 \quad (3.30)$$

where  $u_L$  is the velocity at  $z = L$  computed from (3.29). Above the mixed layer the velocity is assumed to be constant with height. Similarly, for unstable conditions a logarithmic profile is matched to the

similarity solution at  $z = L$  to give

$$u(z) = \frac{0.5 u_*}{k} \ln\left(-\frac{z}{L}\right) + u_L; \frac{z}{L} < 0 \quad (3.31)$$

Under neutral conditions the wind profile appears to follow the logarithmic law to heights greater than the scale height (Panofsky, 1973). Therefore, the simple logarithmic law is used up to the top of the mixed layer here.

In order to evaluate the performance of the proposed algorithm wind profile data obtained from a 1,420 foot (430 m) tower and reported by Thuillier and Lappe (1964) were used. In that study a total of 274 profiles representing four observation times were used in the analysis. Each profile was determined from thirty minute averages of the wind speed at 11 vertical levels. The data were normalized by means of  $u_*$  as well as a reference height velocity,  $u(z_r)$ , computed at the lowest observation level (9.15 m). Profiles for those wind speeds were grouped according to shape characteristics. For each group, an average profile was computed and the vertical variation of mean wind speed was compared to a logarithmic or power law profile form. The surface roughness,  $z_o$ , height at the site was estimated to be 3 cm. The reference velocity, reference height and roughness height from three typical profiles presented in the above mentioned work were used to construct wind profiles using the present algorithm.

Figures 3.8 - 3.10 show selected data from Thuillier and Lappe (1964) together with the profiles computed using the present algorithm.

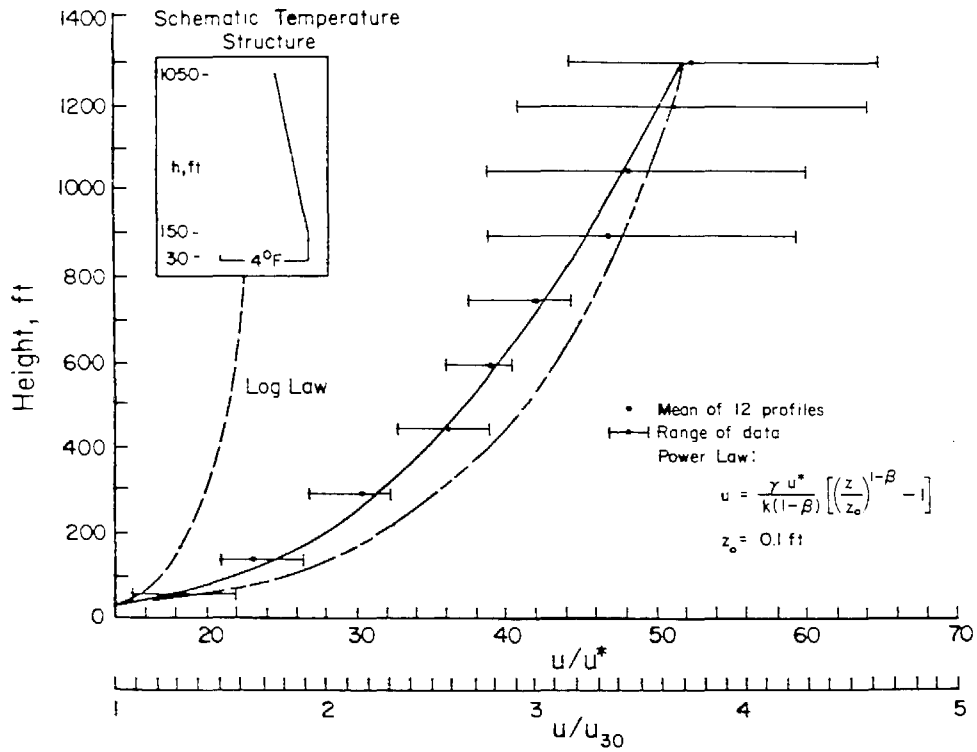


FIGURE 3.8

Plot of Measured Data and Calculated Profiles for E Stability from Thuillier and Lappe (1964) (solid lines) as Well as Results Calculated by Present Algorithm (dashed lines).

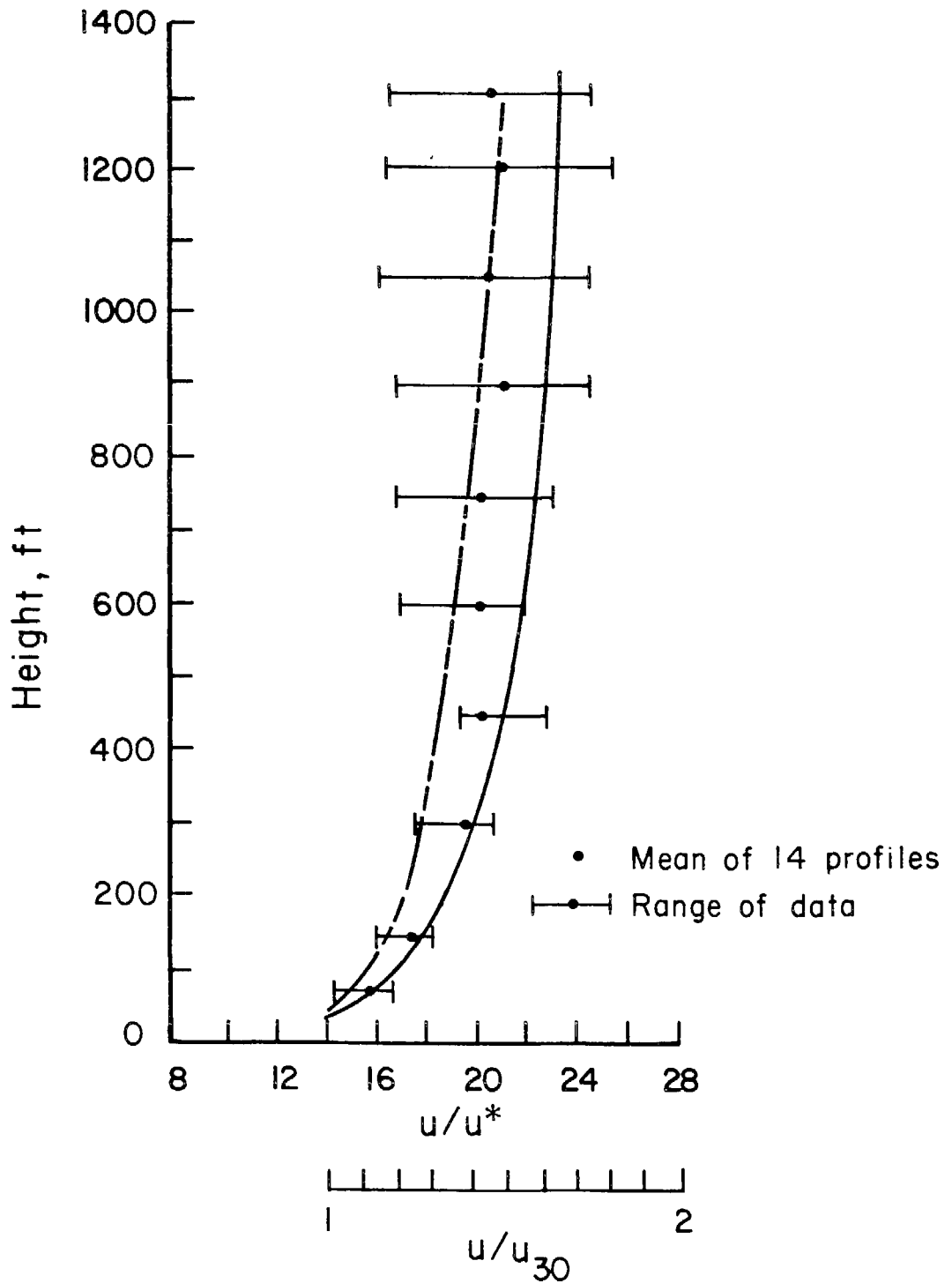


FIGURE 3.9

Plot of Measured Data and Calculated Profiles for C-D Stability from Thuillier and Lappe (1964) as Well as Results Calculated by Present Algorithm (dashed line).

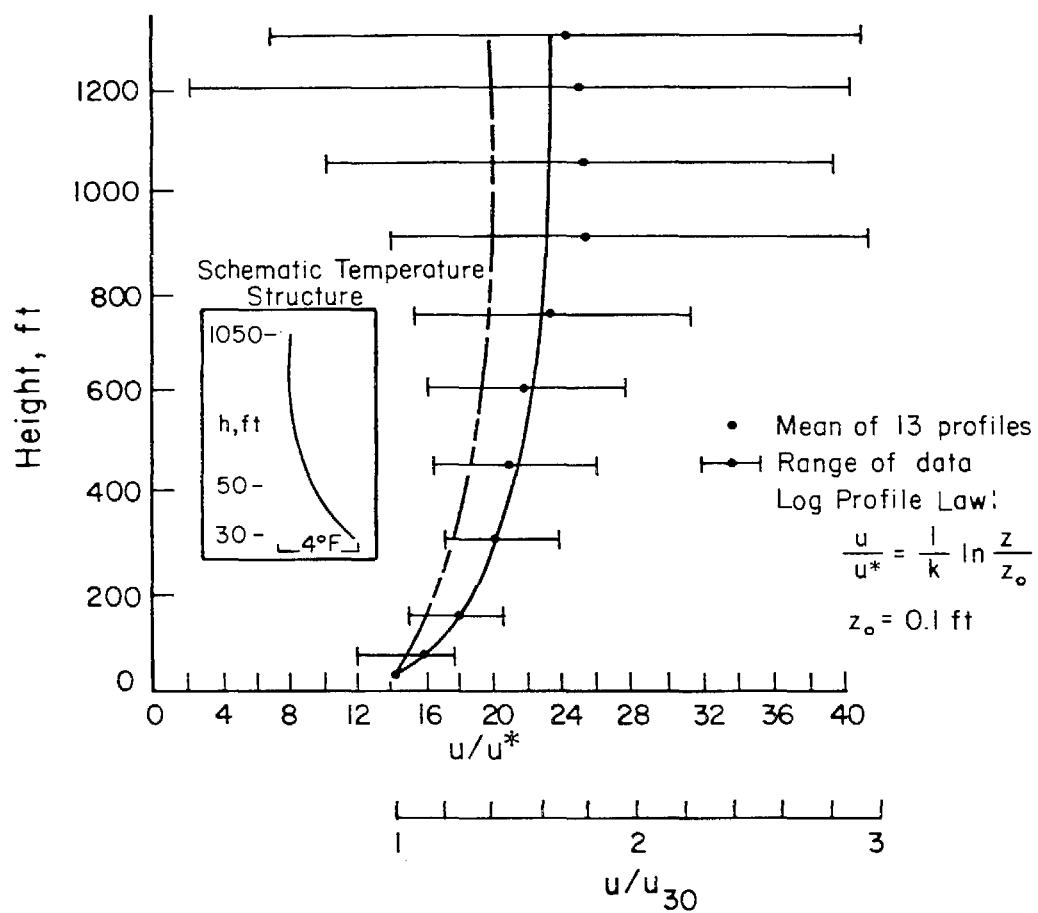


FIGURE 3.10

Plot of Measured Data and Calculated Profiles for B-C Stability from Thuillier and Lappe (1964) (solid lines) as well as Results Calculated by Present Algorithm (dashed lines).

Generally, the wind profiles computed using the present algorithm fit the data as well as the profiles computed by the authors. A major advantage of the present algorithm is the lack of dependence on parameters such as  $\alpha$  or  $\beta$  that were adjusted by Thuillier and Lappe to obtain a good fit. The intent of the present algorithm was to develop procedures for estimating the vertical variation in the absence of any upper air data. Because of the complexity of inversions and wind shear effects aloft, surface data cannot be expected to be indicative of flow aloft at all times.

### 3.9 Solution of the Poisson Equation

An important element of the wind field generation procedure involves repeated solution of the Poisson equation and its associated Dirichlet boundary conditions over the two-dimensional rectangle  $R$ .

$$\nabla^2 f = g \quad x \in R \quad (3.32)$$

$$f = 0 \quad x \in \partial\Omega \quad (3.33)$$

In (3.32) the function  $g(x,y)$  represents the vertical component of the flow field induced by the terrain and  $f(x,y)$  is the velocity potential which is used to adjust the initial estimates of the horizontal velocities  $(u_0, v_0)$  to account for the topographic effect. Given  $f(x,y)$  the variations in the initial field are given by

$$u = u_0 + \frac{\partial f}{\partial x} \quad (3.34)$$

$$v = v_0 + \frac{\partial f}{\partial y} \quad (3.35)$$

Because solution of the Poisson equation forms part of a procedure, which is repeated many times, it is important to minimize the computational time for an individual step. This section is devoted to a brief evaluation of three different numerical techniques and the selection of one which is suitable for inclusion in the wind field generation program. The methods to be discussed are: successive over relaxation (SOR), Fourier Series and the alternating direction implicit (ADI) methods. These and many other highly efficient techniques are evaluated in the reviews by: Dorr (1970), Buzbee et al. (1970), Roache

(1976), Swarztrauber (1977) and Temperton (1979)

The basis of most approaches to solving the field problem is to approximate the system (3.32) with the second-order finite difference approximation

$$\frac{f_{i-1,j} - 2f_{i,j} + f_{i+1,j}}{(\Delta x)^2} + \frac{f_{i,j-1} - 2f_{i,j} + f_{i,j+1}}{(\Delta y)^2} = g_{i,j} \quad (3.36)$$

$$2 < i < n-1, \quad 2 < j < m-1$$

and the boundary conditions

$$\begin{aligned} f_{0,j} &= 0 & f_{n,j} &= 0 & 1 < j < m \\ f_{i,0} &= 0 & f_{i,m} &= 0 & 1 < i < n \end{aligned} \quad (3.37)$$

If  $\Delta x = \Delta y$  these difference expressions can be expressed in the more compact block tridiagonal form

$$[M]\underline{f} = \underline{y} \quad (3.38)$$

where the matrix  $M$ , of dimension  $(n-2) \times (m-2)$ , is given by

$$M = \begin{bmatrix} D & I & & & \\ I & D & & & \\ & & \cdot & \cdot & \cdot \\ & & & \cdot & I \\ & & & & I & D \end{bmatrix} \quad (3.39)$$



conditions. For a rectangular region an estimate of the optimum value can be found from (Roache, 1976)

$$w_0 = 2 \left( \frac{1 - \sqrt{1-a}}{a} \right) \quad (3.42)$$

where

$$a = \left[ \frac{\cos(\pi/n) + \beta^2 \cos(\pi/n)}{1 + \beta^2} \right]^2 \quad (3.43)$$

The major advantages of this particular procedure are that it is extremely easy to program and has minimal core storage requirements. Even though the cost per iteration is small there are circumstances where the convergence can be slow especially if a strongly sheared flow is predominantly aligned in one coordinate direction.

Another iterative approach for finding a solution to the Poisson equation is to convert (3.32) to the parabolic problem

$$\frac{\partial f}{\partial t} = \nabla^2 f - g \quad (3.44)$$

and then solve for the steady state solution. This is the basis of the classic alternating direction implicit (ADI) method introduced by Peaceman and Rachford (1955). The procedure makes use of the fact that [M] can be split into two linear operators A and B both of which can be easily decomposed. Starting with an initial guess  $f^0$  (3.44) is discretized in time, with a time step  $\Delta t$ , and the system is solved on odd numbered steps (k+1) implicitly in A and explicitly in B,

$$f^{k+1} - f^k = \Delta t [ Af^{k+1} + Bf^k - g ] \quad (3.45)$$

The process is reversed on even numbered steps ( $k+2$ ), solving implicitly in B and explicitly in A,

$$f^{k+2} - f^{k+1} = \Delta t [ Af^{k+1} + Bf^{k+2} - g ] \quad (3.46)$$

The combined operations (3.45 - 3.46) make one double sweep of the ADI iteration. The sequence of tridiagonal equations which need to be solved are as follows.

$$[1 \quad -(2+\alpha) \quad 1]f^{k+1} = -\beta^2 [1 \quad -(2-\alpha) \quad 1]f^k + \Delta x^2 g \quad (3.47)$$

$$[1 \quad -(2+\alpha) \quad 1]f^{k+2} = -\frac{1}{\beta^2} [1 \quad -(2-\alpha) \quad 1]f^{k+1} + \Delta y^2 g \quad (3.48)$$

where  $\alpha = 2\Delta x^2/\Delta t$  and as before  $\beta = \Delta x/\Delta y$ . If the same  $\Delta t$  is used in both directions then convergence is assured. The procedure is computationally quite efficient because there are fast algorithms available for solving tridiagonal systems of linear equations. Unfortunately there is no general theory for selecting  $\Delta t$ , and in fact a variable sequence is required to take full advantage of the ADI procedure. Roache (1976) discusses different time stepping strategies and Doss and Miller (1979) describe a completely automatic procedure. The ADI algorithm is straightforward to implement, requires little storage and with the appropriate choice of time steps is extremely fast.

In addition to the ADI and SOR iterative procedures there are a number of very efficient direct methods. Most of the direct approaches

for solving the Poisson equation can be divided into two basic categories: those based on Fourier decomposition in one dimension, and those based on cyclic reduction. Dorr (1970) discusses block, cyclic reduction, tensor product and Fourier series methods. The Fourier series methods are based on the fact that an exact solution to the finite difference equation (3.36), in one space dimension (say rows), can be expressed in terms of finite eigenfunction expansions. Consequently the problem is reduced to a set of tridiagonal matrix equations, which couple the variables across the rows, each of which may be solved separately.

The procedure is to Fourier analyse the source function  $g_{ij}$  along one dimension to obtain the Fourier coefficients for each  $j$ .

$$\hat{g}_j(k) = \sqrt{\frac{2}{m}} \sum_{j=1}^m g_{ij} \sin\left(\frac{\pi k_i}{m}\right) ; 2 \leq j \leq n-2 \quad (3.49)$$

The appropriate tridiagonal equations with the known right-hand sides are then given by

$$[1 - (2-2\beta^2) - \{\cos(\frac{\pi i}{m}) - 1\}] \hat{f}_j = \Delta y^2 \hat{g}_i(k) ; 2 \leq j \leq n-2 \quad (3.50)$$

After solving each of the tridiagonal equations the potential at each mesh point is then recovered by using

$$f_{ij} = \sqrt{\frac{2}{m}} \sum_{k=1}^m \hat{f}_j(k) \sin\left(\frac{\pi k_i}{m}\right) ; 2 \leq j \leq n-2 \quad (3.51)$$

The Fourier method, described by (3.49 - 3.51) is easy to program and has the major advantage that the solution does not involve any iterative steps. If the number of grids points in one or the other direction can be expressed as a integer of the form  $2p$  then the most expensive element of the computation, the decomposition, can be performed using Fast Fourier Transform (FFT) algorithms. Unfortunately this does not often occur in practical applications of the type discussed in the previous section. More sophisticated procedures have been developed and in particular there is a trend towards combining the Fourier analysis and  $r$  steps of cyclic reduction producing composite algorithms which are denoted by FACR( $r$ ) (Temperton, 1979; Swarztrauber, 1977).

Each of the above methods were coded and tested on a series of sample problems one example of which is given by

$$\nabla^2 f = -2\pi \sin(\pi x) \sin(\pi y) ; x, y \in R \quad (3.52)$$

$$f = 0 ; x, y \in \partial\Omega \quad (3.53)$$

This test case has the exact solution

$$f(x, y) = \sin(\pi x) \sin(\pi y) \quad (3.54)$$

The computational time required to solve (3.52) for each of the three

methods is given in Table 3.1. In the case of the SOR method the optimum relaxation factor was determined to be 1.6 (Figure 3.11) as compared to the value of 1.9 estimated by (3.42). The convergence parameter for the ADI was obtained from a series of numerical experiments the results of which are shown in Figure 3.12. For this and a number of other test problems the ADI method was more efficient than either the SOR or Fourier series methods and so it was selected for initial implementation in the wind field generation procedure. After publication of the paper reprinted in Section 3.7 the computational algorithm was modified to make use of the direct solution scheme described by Swarztrauber (1977). The cyclic reduction technique has proved to be both extremely efficient and reliable.

TABLE 3.1  
Results of Test Case Comparing Three Poisson  
Equation Solving Algorithms

METHOD	CONVERGENCE CRITERION	CONVERGENCE PARAMETER	NUMBER OF ITERATIONS	RELATIVE EXECUTION TIME
Fourier				18.8
SOR	$10^{-4}$	1.6	50	1.7
	$10^{-4}$	1.9	139	4.8
ADI	$10^{-4}$	0.1	9	1.0

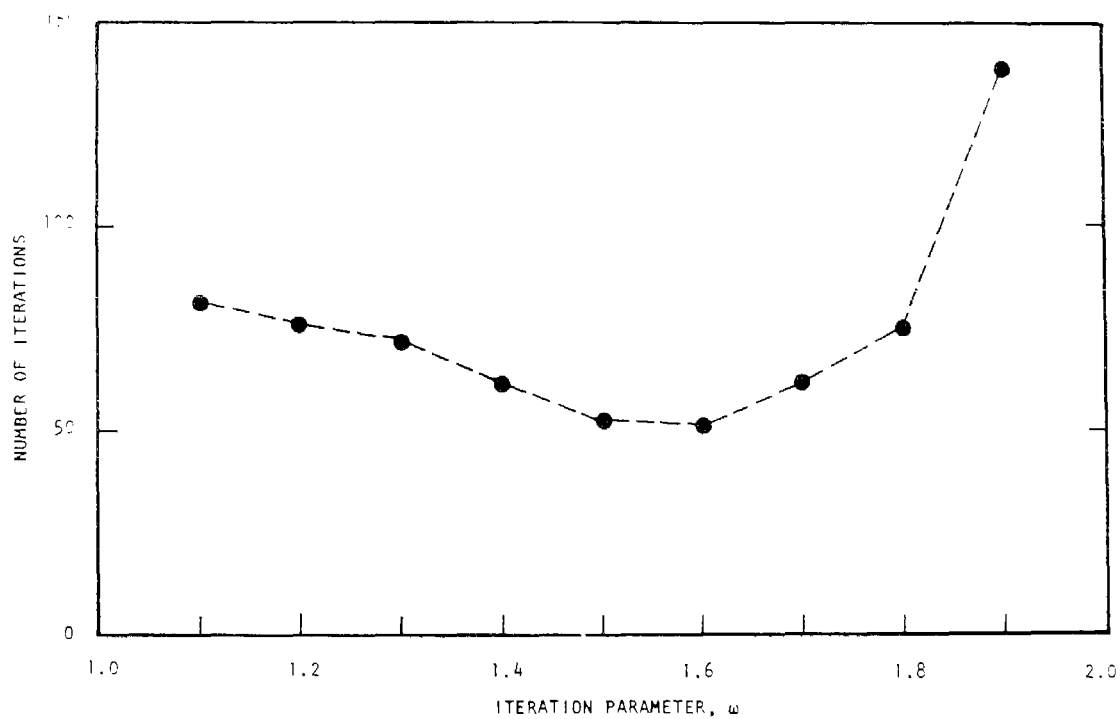


FIGURE 3.11

Number of Iterations Required for Convergence  $V$  as a Function of  $\omega$  of the Successive Over Relaxation (SOR) Method.

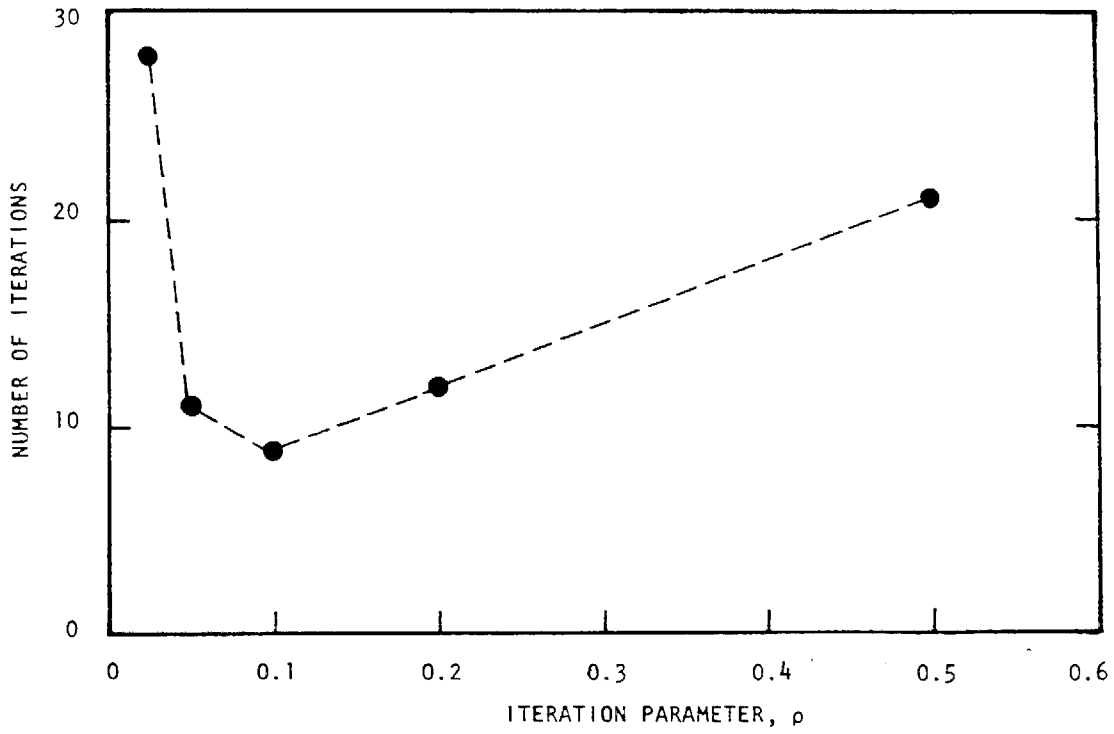


FIGURE 3.12

Number of Iterations Required for Convergence of the Alternating Direction Implicit (ADI) Method as a Function of  $\rho$

### 3.10 Trajectory Integration Procedure

Once the wind field  $\underline{u}(\underline{x},t)$  has been established it is extremely useful to be able to follow the paths of individual air parcels as they traverse the airshed. There are two reasons for this. For the trajectory model introduced in Chapter 2, the spatial location of the column of air is needed to specify the emission inputs and the appropriate meteorological data. A second application of a trajectory integration procedure is to specify the horizontal boundaries for three-dimensional airshed models. For example, by locating the model boundaries beyond the extent of return air flow, in regions subjected to land-sea breeze reversals, the effect of uncertainties in inflow boundary conditions can be minimized as background values are more likely to apply. This section describes a procedure for calculating the movement of air parcels within flow fields generated by objective analysis techniques of the type presented in Section 3.7.

The spatial position of the air parcel at time T relative to an initial starting location  $\underline{x}(0)$  is given by

$$\underline{x}(T) = \underline{x}(0) + \int_0^T \underline{u}(\underline{x},t) dt \quad (3.55)$$

Since the velocity field  $\underline{u}(\underline{x},t)$  is usually only available at discrete locations, objective analysis procedures of the type discussed in previous section must be used to characterize the flow in between grid points. The method adopted in this study is to calculate the velocity at the current trajectory position  $p(\underline{x},t)$  as a distance-weighted

function of the wind field at the nearest grid points. A two-dimensional example is shown in Figure 3.13, where  $\underline{u}(\underline{p},t)$  is formed as a weighted mean of the wind field at the four nearest grid points. The velocity components at  $\underline{p}(\underline{x},t)$  are given by

$$\underline{u}_k(\underline{x},t) = \frac{\sum_{i=1}^n u_i^k/d_i}{\sum_{i=1}^n 1/d_i} \quad (3.56)$$

where  $n$  is the number of nearest grid point (=4 for two-dimensional problems and 8 for three-dimensional cases) and  $\underline{u}_i^k$  are the  $k$ -th components of the velocity field at each of the grid points.

A variety of techniques can be used to integrate the initial value problems (3.55); the simplest numerical scheme is given by

$$\underline{x}(t + \Delta t) = \underline{x}(t) + \Delta t \underline{u}[\underline{x}(t),t] \quad (3.57)$$

Although the Euler integration method is only first-order accurate in time ( $O(\Delta t)$ ), with sufficiently small time steps  $O(10$  minutes) the positional errors using hourly averaged wind fields are negligible. The reasons for this are that  $\Delta t$  is small compared to the averaging time for  $\underline{u}(\underline{x},t)$  and the spatial gradients in the velocity field over a distance of  $\underline{u}\Delta t$ . Figure 3.14 illustrates an application of the procedure to tracking a sulfur hexafluoride ( $\text{SF}_6$ ) tracer release. After 12 hours, the predicted position of the concentration centroid is almost coincident with the field measurements.

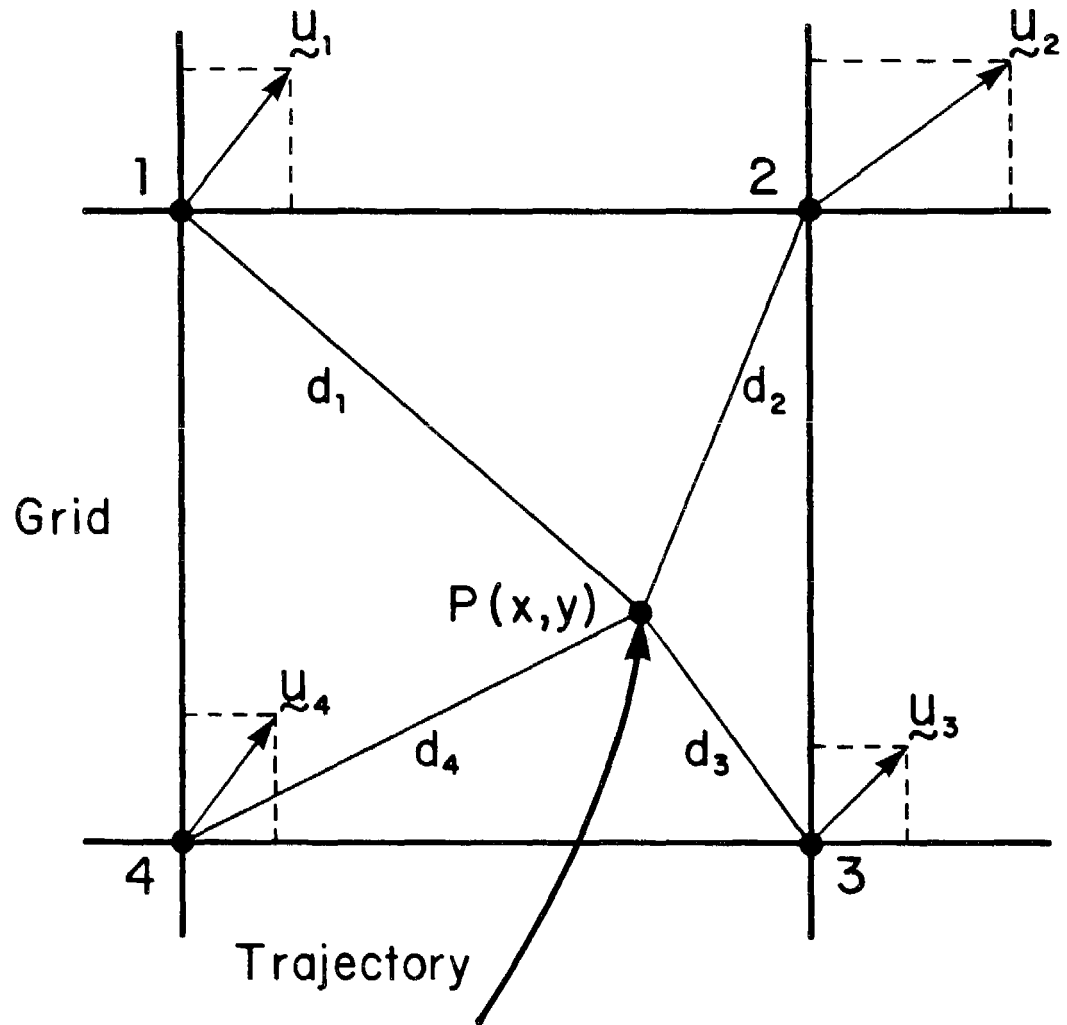


FIGURE 3.13

Velocity at Current Position  $P(x,y)$  is Determined as a Distance Weighted Mean of Wind Velocity at the Four Nearest Grid Points.

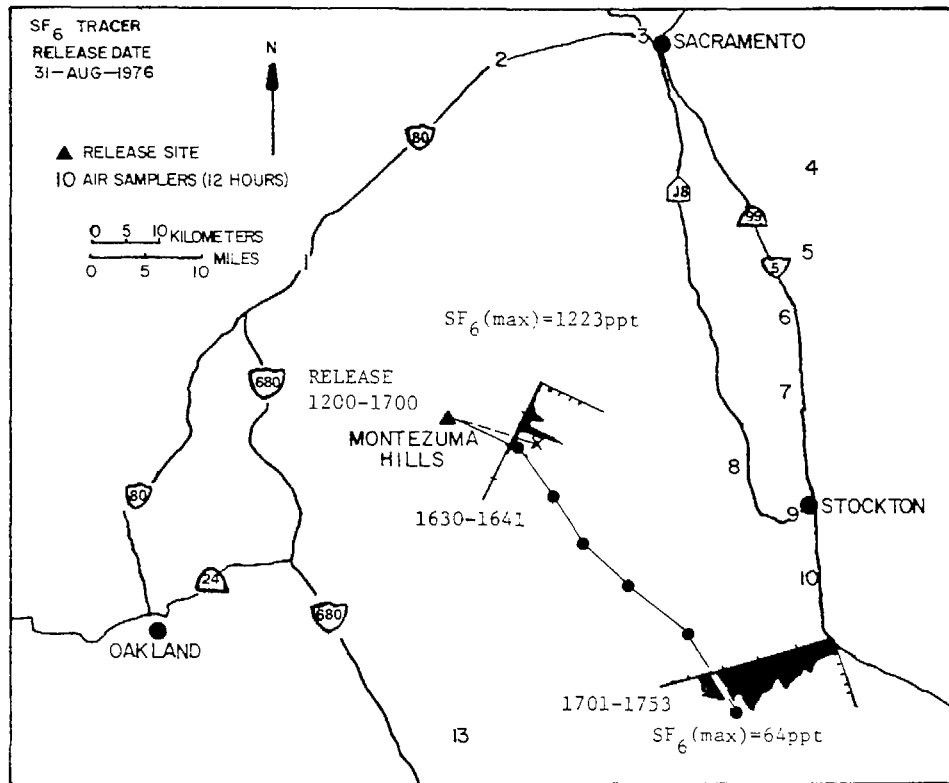


FIGURE 3.14

Forward Air Parcel Surface Trajectories.  
 Each Point ● Represents One Hour of Transport.  
 Source: Lamb and Shair (1977)

In order to assess the effects of errors in the wind field a number of numerical experiments were conducted in which grid values were randomly perturbed and the trajectory path recalculated. In these calculations the velocity magnitudes were assumed to be normally distributed about the old field value with a standard deviation of  $\pm 20\%$ . Angular errors were assumed to be uniformly distributed in a segment of  $\pm 11.25^\circ$ . The error growth  $e(t) = [\underline{x}^P(t) - \underline{x}^O(t)]$  for these problems is defined as the distance between the nominal path  $\underline{x}^O(t)$  and the trajectory  $\underline{x}^P(t)$  calculated with the perturbed wind field. This error is derived from two components, a positional error  $V_p$  due to the uncertainty in the wind field  $\underline{u}$  and the other arising from spatial gradients in the velocity field  $V_g$  i.e.

$$\frac{de(t)}{dt} = V_p + V_g = V_p + \frac{d}{dt}[\underline{x}^P(t) - \underline{x}^O(t)] \quad (3.58)$$

Sykes and Hatton (1976) assumed that when  $e(t)$  is small compared to the large scale features of the flow field,  $V_g$  can be approximated by  $e(t)S$  where  $S$  is the horizontal shear or vorticity.

$$\frac{de(t)}{dt} = V_p + e(t)S \quad (3.59)$$

With this formulation it can be seen that the error growth is linear when  $e(t) \ll V_p/S$  and exponential when  $e(t) = V/S$ . In urban regions where the topography is reasonably flat, the error growth is linear. For example, in Los Angeles a typical velocity error is  $0(1 \text{ m/s})$  and the vorticity of flows with scales greater than  $10 \text{ km}$  is  $0(10^{-4} \text{ s})$  so

the error growth is in the linear regime. This observation is confirmed by the sample calculation displayed in Figure 3.15 where the maximum error at the end of a 24 hr integration is 0( 5 km), the size of a typical computational cell. When one of the trajectories in Figure 3.15 encountered mountainous terrain the error exhibited an exponential like growth.

### 3.11 Conclusion

In this chapter a new method for constructing three-dimensional, mass-consistent wind fields has been introduced. Two steps are involved in the generation process. The first involves interpolating irregularly spaced monitoring data to a regular computational mesh. Objective analysis procedures are then employed to adjust the wind vectors at each grid point so that an applied physical constraint such as minimum field divergence is satisfied. A major advantage of the technique is that it only requires, as input, routinely measured information. In addition, the interpolation algorithms can also be used to establish the initial concentration distributions and mixing height over the airshed. The procedures are easy to implement, computationally efficient and can be easily applied to a wide range of other meteorological applications.

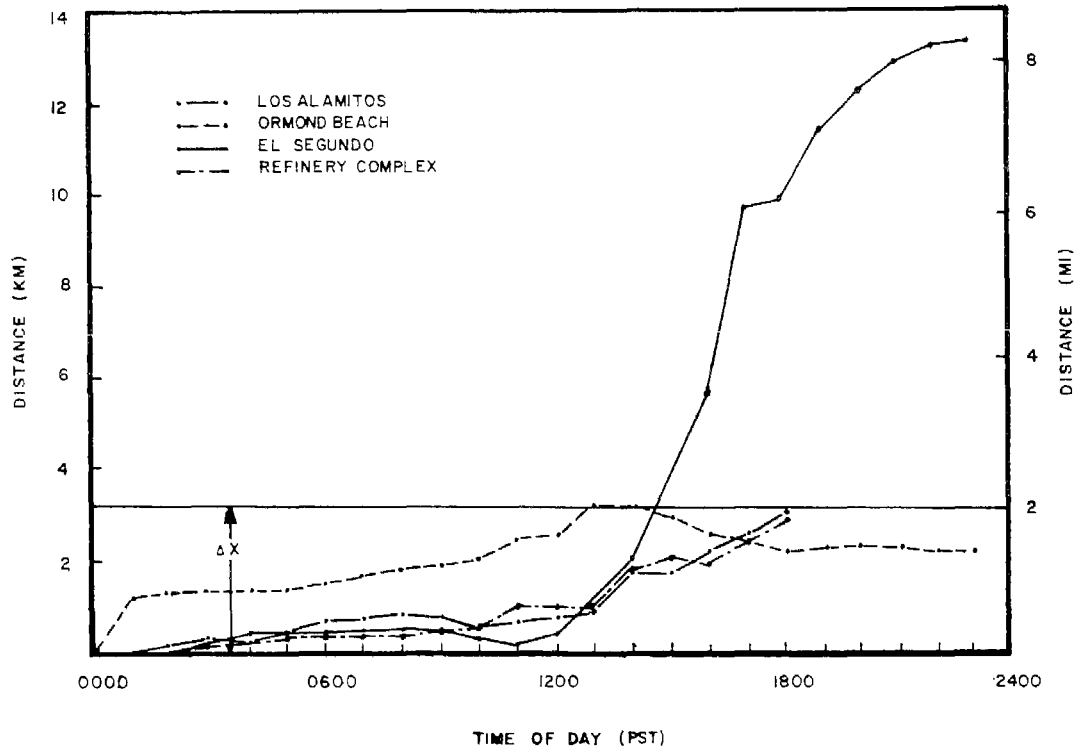


FIGURE 3.15  
 Plot of Distance Between Actual and Perturbed  
 Trajectories as a Function of Time.

## CHAPTER 4

## TURBULENT DIFFUSION COEFFICIENTS

4.1 Introduction

Closure of the species continuity equation has been accomplished in the present model by a gradient-diffusion or K-theory hypothesis. This chapter is devoted to a presentation of the formulation adopted for the vertical ( $K_{zz}$ ) and horizontal ( $K_{xx}, K_{yy}$ ) diffusion coefficients. At the outset it should be remarked that a variety of different formulations exist. Yu (1977), for example, presents a comparative evaluation of 14 different approaches. A particular complication in the selection or development of a model is the lack of suitably detailed measurements of vertical wind shear and temperature profiles. As a result a guiding principle in formulating the present model was to employ only those parameters that are readily available or can be easily estimated.

4.2 Turbulent Diffusion in the Atmosphere

The K-Theory model was introduced to describe the fluxes of material which occur on spatial scales smaller than those which can be resolved either by an observational network of wind stations or by the computational grid points. In this model the fluxes  $\langle \underline{u}'c'_i \rangle$  are assumed to be proportional to the mean concentration gradient  $\nabla \langle c_i \rangle$ .

$$\langle \underline{u}'c'_i \rangle = K \nabla \langle c_i \rangle \quad (4.1)$$

Specification of the components of the second-rank eddy diffusion tensor  $K$  requires an understanding of the turbulent processes occurring in the atmosphere. The planetary boundary layer is commonly divided into three layers. In most models these regions are: the constant flux layer next to the ground, a deeper layer in which the fluxes generally decrease with height and the free atmosphere. These regions are illustrated in Figure 4.1 for an atmospheric state characteristic of daytime conditions. During daytime conditions the mixed layer has a reasonably well defined upper boundary. This height,  $Z_i$ , is commonly associated with the base of an elevated temperature inversion. Solar heating causes the convective layer to increase in thickness at a rate determined by the heat flux radiated at the ground. Above the mixed layer there is a quasi-permanent layer of non-turbulent flow. Stable layers can also exist close to the ground as a result of nocturnal cooling.

Many processes are involved in turbulent transport. For example, above the planetary boundary layer, diffusion is associated with internal wind shear and the effect of topography on a scale large enough to cause upward propagation of energy. In the surface or "constant flux" layer the fluxes of heat, momentum and water vapor are approximately constant with height. Over most of the boundary layer the small scale turbulence is induced by wind shear and/or thermal convection. The relationship between mean values and vertical gradients of such properties as wind, temperature, humidity and surface properties was the subject of a major workshop project (Haugen, 1973).

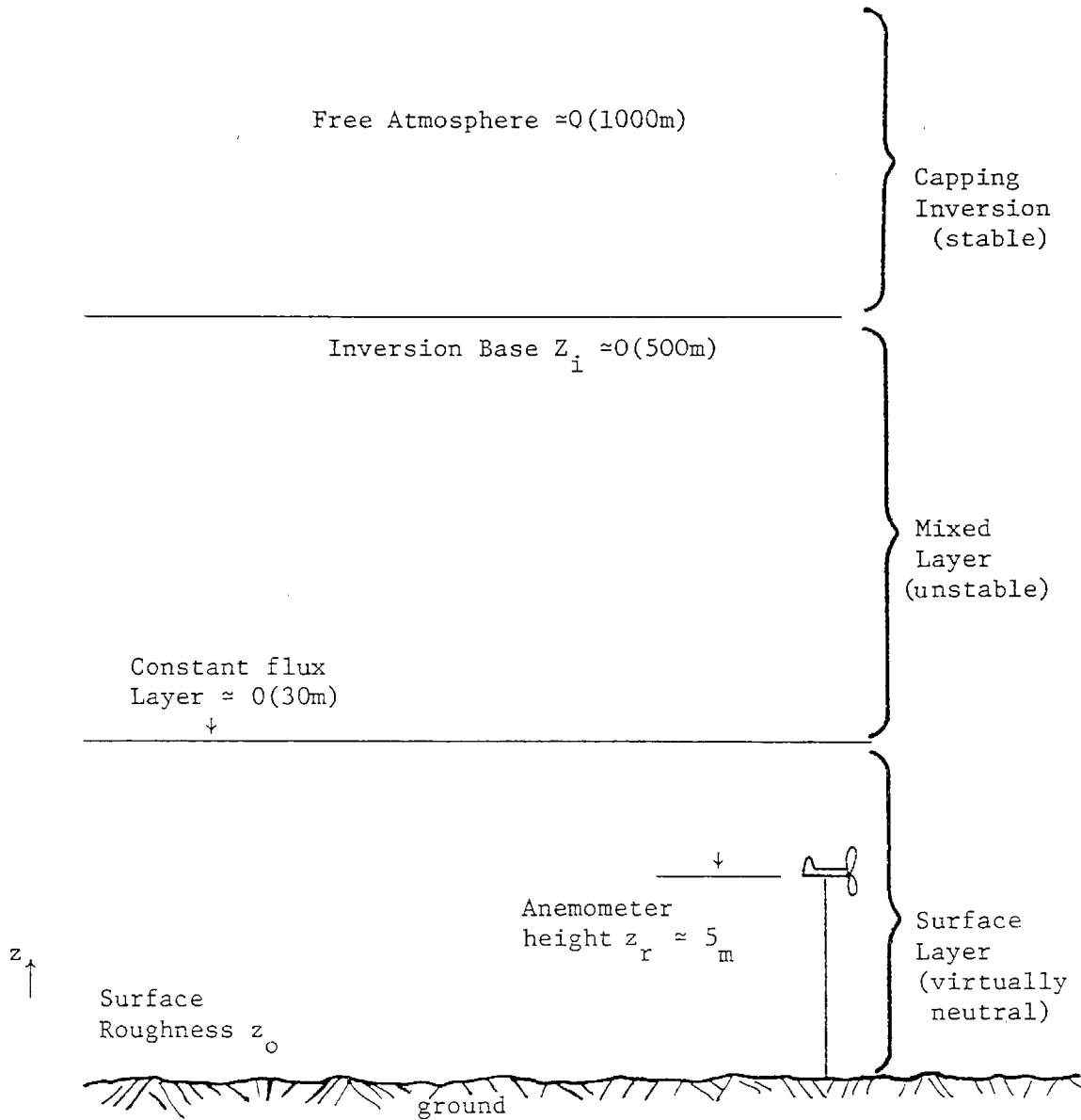


FIGURE 4.1  
Structure of the Atmospheric Boundary  
for Typical Daytime Conditions

### 4.3 Turbulent Transport Parameters

In this study primary attention is directed at the turbulent processes that occur in the mixed layer as a result of the interaction between shear and buoyancy driven flows. The flux Richardson number  $R_f$  gives a measure of the relative importance of the buoyancy terms in the equations of motion  $\frac{g}{T} \overline{w'\theta'}$  as compared to the shear production terms  $\overline{u'w'} \frac{\partial \overline{u}}{\partial z}$  i.e.,

$$R_f = \frac{\frac{g}{T} \overline{w'\theta'}}{\overline{u'w'} \frac{\partial \overline{u}}{\partial z}} \quad (4.2)$$

where  $\overline{w'\theta'}$  is a measure of the kinematic sensible flux and  $\overline{u'w'}$  is the x-component of vertical momentum flux. Clearly when  $R_f$  is large the flow is dominated by buoyancy effects. The flux Richardson number is a function of the distance from the ground and is thus a measure of the local stability property of the turbulent flow. Richardson (1920) suggested that turbulence should occur in the atmosphere when the production of turbulent energy by the wind shear is just large enough to counterbalance its consumption by buoyancy forces.

A major deterrent to the use of (4.2) as a measure of atmospheric stability is the need for simultaneous determinations of both the heat and momentum flux. Another approach is to define a quantity similar to (4.2) called the gradient Richardson number  $R_i$ .

$$R_i = \frac{\frac{g}{T} \frac{\partial \theta}{\partial z}}{\left(\frac{\partial \overline{u}}{\partial z}\right)^2} \quad (4.3)$$

where  $\phi$  is the potential temperature and  $T$  the absolute air temperature. The relationship between  $R_f$  and  $R_i$  is

$$R_f = \frac{K_H}{K_m} R_i \quad (4.4)$$

where  $K_m$  and  $K_H$  are the eddy diffusion coefficients for momentum and heat respectively.  $R_i$  determines the stability of a stratified fluid subjected to small perturbations and so it is a measure of the onset of turbulence (Plate, 1971).

Another stability parameter often used in micro-meteorology is the Monin-Obukhov length

$$L = - \frac{u_*^3 c_p \rho T}{kHg} \quad (4.5)$$

where  $c_p$  is the specific heat at constant pressure,  $\rho$  the air density,  $k$  the von Karman constant,  $T$  the absolute air temperature,  $g$  acceleration of gravity,  $H$  is the vertical heat flux and  $u_*$  is the friction velocity. Physically the Monin-Obukhov length is the approximate height above the surface at which buoyancy effects become comparable to the shear effects. For neutral conditions,  $L$  is related to the flux Richardson number  $R_f$  by

$$R_f = \frac{z}{L} \quad (4.6)$$

The Monin-Obukhov length, like  $R_f$ , provides a measure of the stability of the surface layer since:

$$\begin{array}{ll} L > 0 & \text{Stable} \\ L = \infty & \text{Neutral} \\ L < 0 & \text{Unstable} \end{array} \quad (4.7)$$

#### 4.4 Estimation of the Monin-Obukhov Length

The Monin-Obukhov length  $L$  is a key parameter in the present model and indeed in many other approaches. Golder (1972) established a relation between the stability classes of Pasquill and Turner, the roughness height and  $L$ . The results of his investigation are shown in Figure 4.2. With this technique, the local wind speed and cloud cover measurements are used to estimate the Pasquill stability class (Table 4.1). In addition, Golder developed a nomogram for relating the gradient Richardson number  $R_i$  to the more easily determined bulk Richardson number  $B$

$$B = \frac{g}{T} \frac{\partial \theta}{\partial z} \left[ \frac{z}{u} \right]^2 \quad (4.8)$$

In order to simplify calculation of  $1/L$ , within the airshed model, each stability class was approximated by a single straight line of  $1/L$  against surface roughness. The error induced by this approximation is quite small, for example, in calculating the convective velocity scale  $w_*$

$$w_* = \left( -\frac{1}{k} \frac{z_i}{L} \right)^{\frac{1}{3}} u_* \quad (4.9)$$

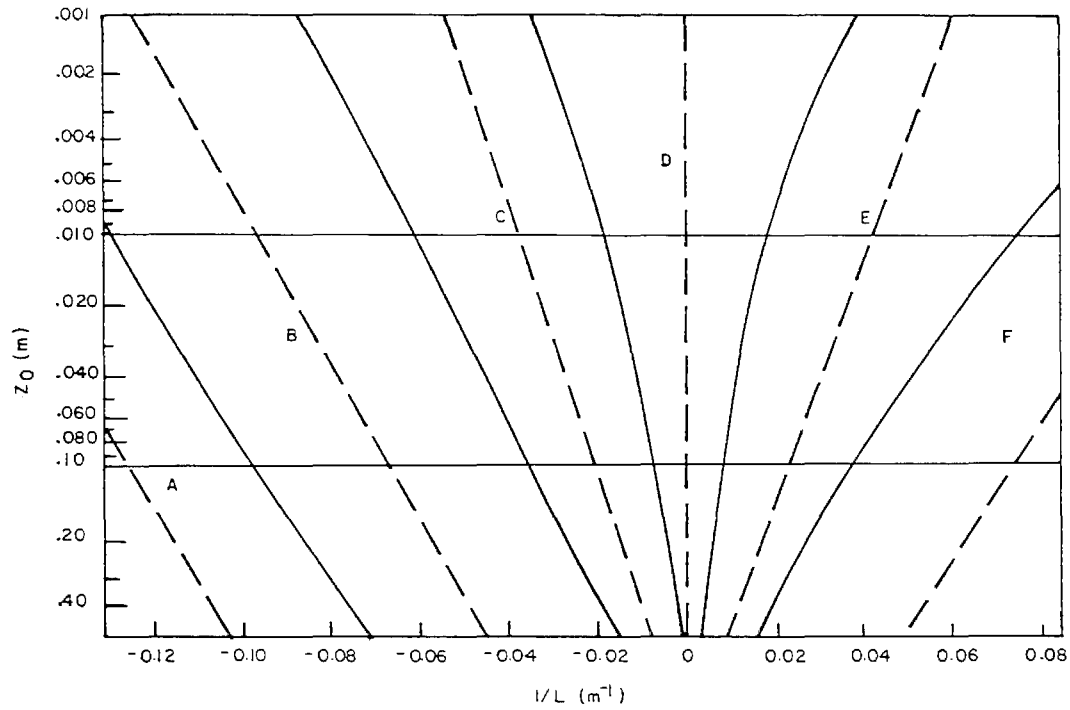


FIGURE 4.2

Relationship between Pasquill Stability Classes, Surface Roughness, and Monin-Obukhov Length. (Solid lines define stability classes, dotted lines used to approximate stability region).

TABLE 4.1

Estimation of Pasquill Stability  
Classes. (Source: Turner, 1969)

Surface Wind Speed at 10m (m-sec <sup>-1</sup> )	Solar Radiation*			Night Time Cloud Cover Fraction	
	Strong	Moderate	Slight	Low cloud $\geq \frac{4}{8}$	cloud $\leq \frac{3}{8}$
< 2	A	A - B	B		
2 - 3	A - B	B	C	E	F
3 - 5	B	B - C	C	D	E
5 - 6	C	C - D	D	D	D
> 6	C	D	D	D	D

\*

Incoming Radiation (Category)	Solar Insolation	
	(Langley min <sup>-1</sup> )	(W - m <sup>-2</sup> )
Strong	I > 1.0	I > 700
Moderate	0.5 ≤ I ≤ 1.0	350 ≤ I ≤ 700
Slight	I < 0.5	I < 350

Since the parameter  $l/L$  is raised to the one third power, large variations do not lead to rapid variations in  $w_*$ . The parameters for the straight line approximations to the stability classes are shown in Table 4.2.

There is a variety of factors that could influence the location of the lines approximating each stability class. An important factor is the presence of water vapor in the atmosphere. If suitable data are available, the Monin-Obukhov length  $L$  can be redefined as

$$L_w = \frac{1}{\left[1 + \frac{m}{B_o}\right]} \quad (4.10)$$

where  $B_o$  is the Bowen ratio and  $m$  is a constant the value of which is given by  $m = 0.61 c_p T/\bar{L}$  where  $\bar{L}$  is the latent heat of vaporization of water (for  $T = 300^\circ\text{K}$ ,  $m \approx 0.07$ , Lumley and Panofsky, 1964). The water vapor flux can exert a considerable influence on diffusion, particularly over the ocean and heavily vegetated areas. Increased levels of evaporation act to shift the lines to the right and so, for a given surface roughness, larger values of  $\bar{L}$  can be expected.

#### 4.5 Surface Roughness Estimation

In the present model the effects of small-scale surface irregularities on the boundary layer transfer processes are incorporated only through the surface roughness parameter  $z_o$ . As a result,  $z_o$  must be specified at each grid point within the modeling region. The range of variation of  $z_o$  over different land types is quite large, and the

TABLE 4.2

Coefficients for Straight Line Approximation to  
Golder's Plot as a Function of Stability Classes

$$\frac{1}{L} = a + b \log_{10} z_0$$

	Pasquill Stability Class	Coefficients	
		a	b
Extremely Unstable	A	-0.096	0.029
Moderately Unstable	B	-0.037	0.029
Slightly Unstable	C	-0.002	0.018
Neutral	D	0	0
Slightly Stable	E	+0.004	-0.018
Moderately Stable	F	+0.035	-0.036

measurements required to estimate the effective roughness are quite complex. As an alternative, Plate (1971) proposed a simple formula that relates  $z_o$  to the mean canopy height  $h_c$ .

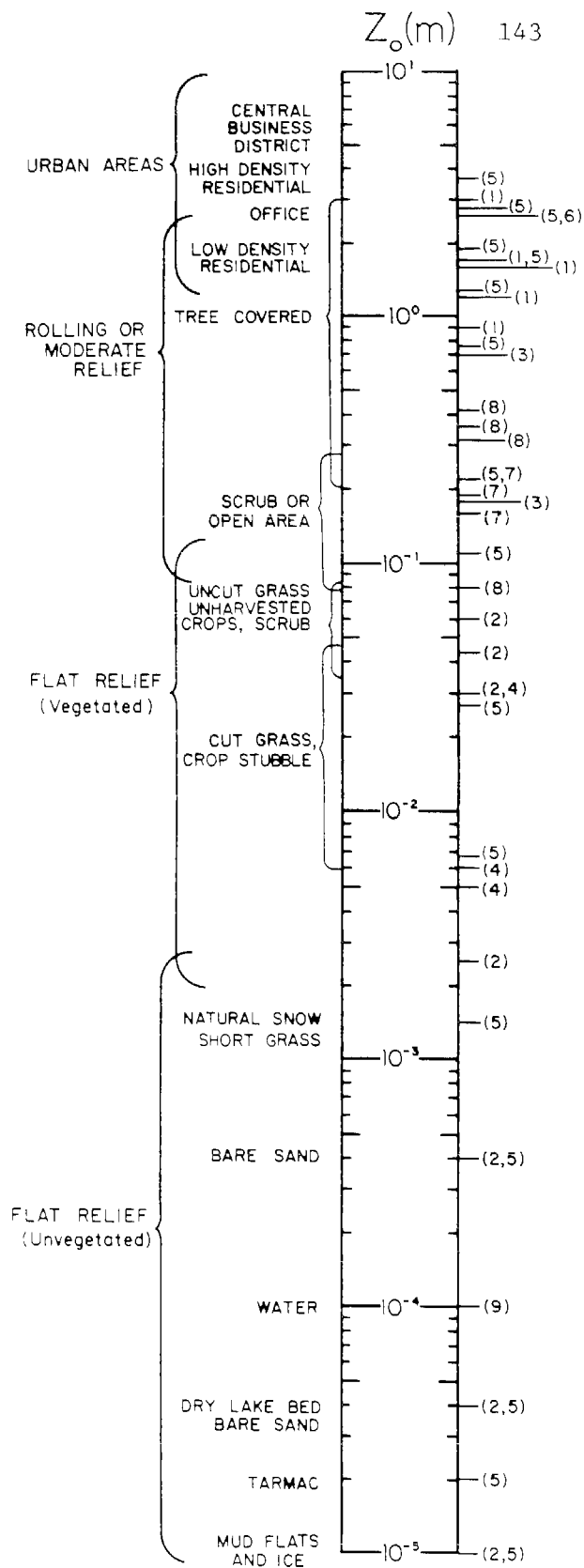
$$z_o = 0.15 h_c \quad (4.11)$$

Depending on the conditions, the 'constant' 0.15 varied from 1/7 to 1/30. Figure 4.3 presents surface roughness values for a variety of land use categories compiled primarily from the reviews by Myrup and Ranzieri (1976) and Hodgkin (1980). The precision implied by some entries on the figure is deceptive because there is considerable scatter in many of the underlying experimental data.

When a modeling region includes a large body of water, the roughness cannot be characterized by simply associating  $h_c$  with the wave height. Unlike the land, the effective roughness of the water surface is a dynamic variable whose magnitude is influenced by factors such as the wave state and wind stress. There is a variety of models of the air-sea interaction and its influence on  $z_o$ . The studies by Gent, (1977), Hsu (1974) and Kitaigorodskii (1970) illustrate some of the complexities. Arya (1977) has recently reviewed some of the more simple parameterizations that are applicable to the present study. For example, Wipperman (1972) has suggested the following formula for smooth as well as rough conditions:

$$z_o = 0.1 \frac{\nu}{u_*} + b \frac{u_*^2}{g} \quad (4.12)$$

Where  $\nu$  is the kinematic viscosity of air and  $b$  is a constant whose



REFERENCES

1. COUNIHAN (1975)
2. DEACON (1949)
3. FICHTL and McVEHIL (1970)
4. GOLDER (1972)
5. MYRUP and RANZIERI (1976)
6. SLADE (1969)
7. TOUMA (1977)
8. WEBER et al. (1975)
9. SEE TEXT

FIGURE 4.3

Variation of Surface Roughness as a Function of Surface Type

magnitude  $\approx 0.02$ . The formula implies a considerably increasing trend in  $z_0$ ; the results of Stewart (1974) and calculations by Gent (1977) imply a more or less constant value of  $z_0 \approx 0.01 - 0.02$  cm for 10 m wind speeds in the range  $6-12$  m s $^{-1}$ . For the purposes of this study, a value of  $z_0$  for the ocean was set to be 0.01 cm.

#### 4.6 Determination of the Friction Velocity $u_{*}$

Close to the ground, in the constant flux layer,  $u_{*}$  is a measure of the turbulent eddying and of the transfer of momentum due to these fluctuations. The friction velocity  $u_{*}$  is used in many situations and this section presents some simple formulae that can be used under a variety of meteorological conditions. The friction velocity is defined by

$$u_{*}^2 = \frac{\tau_0}{\rho} = -\overline{u'w'} \quad (4.13)$$

where  $\tau_0$  is the shear stress per unit area of the boundary and  $\rho$  is the density of the fluid. A K-Theory approximation for the momentum flux  $\overline{u'w'}$  and a Monin-Obukhov similarity expression can be used to develop the following form.

$$u_{*} = \frac{k u(z_r)}{\int_{z_0}^{z_r} \phi_m \left( \frac{z}{L} \right) \frac{dz}{z}} \quad (4.14)$$

where  $u(z_r)$  is the velocity at a reference elevation  $z_r$ , typically the elevation of the wind measuring instrument and  $\phi_m$  an experimentally determined function. The velocity at the height of the momentum sink,

$z_0$ , is assumed to be zero. Businger et al. (1971) developed a series of  $\phi_m$  functions from field data, the results of which are given by:

$$\phi_m \left( \frac{z}{L} \right) = \begin{cases} 1 + 4.7 \left( \frac{z}{L} \right) & ; \frac{z}{L} > 0 \\ 1 & ; \frac{z}{L} = 0 \\ [1 - 15 \left( \frac{z}{L} \right)]^{-\frac{1}{4}} & ; \frac{z}{L} < 0 \end{cases} \quad (4.15)$$

Substituting these expressions into (4.14) gives the friction velocity. The necessary integrals are summarized in Table 4.3.

#### 4.7 Vertical Diffusivity Profile for Unstable Conditions

Transport of pollutant material in the vertical direction is often dominated by turbulent diffusion. Only diagonal components of the eddy diffusion tensor  $K$  are used in the airshed model and, as a consequence, the specification of  $K_{zz}$  has an important bearing on the performance of the airshed model. Many approaches have been tried to establish vertical profiles of  $K_{zz}$  within the boundary layer. The wide range of meteorological regimes encountered in practice considerably complicates the task. This section is devoted to a discussion of the mathematical model adopted for  $K_{zz}$  under unstable conditions, i.e., when  $L < 0$ .

Monin-Obukhov similarity theory predicts that the surface layer eddy diffusion coefficient is given by Monin and Yaglom (1971)

$$K_{zz} = \frac{k u_*^* z}{\phi \left( \frac{z}{L} \right)} \quad (4.16)$$

TABLE 4.3

Momentum and Pollutant Integrals of Different Stability Conditions

INTEGRAL	STABILITY CONDITION		
	STABLE $\frac{z}{L} > 0$	NEUTRAL $\frac{z}{L} = 0$	UNSTABLE $\frac{z}{L} < 0$
MOMENTUM $\int_{z_0}^{z_r} \phi_m \left(\frac{z}{L}\right) \frac{dz}{z}$	$\ln\left(\frac{z_r}{z_0}\right) + \frac{4.7}{L}(z_r - z_0)$	$\ln\left(\frac{z_r}{z_0}\right)$	$\ln\left[\frac{\left(1-15\frac{z_r}{L}\right)^{\frac{1}{4}} - 1}{\left(1-15\frac{z_r}{L}\right)^{\frac{1}{4}} + 1}\right] - \ln\left[\frac{\left(1-15\frac{z_0}{L}\right)^{\frac{1}{4}} - 1}{\left(1-15\frac{z_0}{L}\right)^{\frac{1}{4}} + 1}\right]$ $+ 2 \arctan\left(1-15\frac{z_r}{L}\right)^{\frac{1}{4}} - 2 \arctan\left(1-15\frac{z_0}{L}\right)^{\frac{1}{4}}$
POLLUTANT $\int_{z_0}^{z_r} \phi_p \left(\frac{z}{L}\right) \frac{dz}{z}$	$0.74 \ln\left(\frac{z_r}{z_0}\right) + \frac{4.7}{L}(z_r - z_0)$	$0.74 \ln\left(\frac{z_r}{z_0}\right)$	$0.74 \left\{ \ln\left[\frac{\left(1-9\frac{z_r}{L}\right)^{\frac{1}{2}} - 1}{\left(1-9\frac{z_r}{L}\right)^{\frac{1}{2}} + 1}\right] - \ln\left[\frac{\left(1-9\frac{z_0}{L}\right)^{\frac{1}{2}} - 1}{\left(1-9\frac{z_0}{L}\right)^{\frac{1}{2}} + 1}\right] \right\}$

where  $\phi$  is an experimentally determined function that basically corrects for buoyancy effects on the turbulence. Businger et al. (1971) have constructed  $\phi$  expressions for momentum  $\phi_m$  and heat  $\phi_H$  from an analysis of field data. For unstable conditions  $z/L < 0$  the formulae for  $\phi_m$  and  $\phi_H$  are

$$\phi_m\left(\frac{z}{L}\right) = \left[1 - 15\left(\frac{z}{L}\right)\right]^{-\frac{1}{4}} \quad (4.17)$$

$$\phi_H\left(\frac{z}{L}\right) = \phi_m^2 \quad (4.18)$$

The findings of Galbally (1971) and Crane et al. (1977) indicate that eddy transport of matter is more closely related to that of heat rather than momentum. Using the above results, an approximate expression for  $K_{zz}$  can be derived in terms of the momentum diffusivity  $K_{zz}^m$ .

$$K_{zz} = K_{zz}^m \left[1 - 15\left(\frac{z}{L}\right)\right]^{\frac{1}{4}} \quad (4.19)$$

This result indicates that the common assumption, adopted in many air pollution studies, that  $K_{zz} \approx K_{zz}^m$  can lead, under typical meteorological conditions, to an underestimate of  $K_{zz}$  by a factor of 3. Carl et al. (1973) suggested an expression for  $K_{zz}^m$  that closely fits a second order closure model calculation by Zeman and Lumley (1976).

$$K_{zz}^m = 2.5 w_* z_i \left[k \frac{z}{z_i}\right]^{\frac{4}{3}} \quad (4.20)$$

Combining the last two equations gives the distribution of  $K_{zz}$  in the surface layer under unstable conditions.

$$K_{zz} = 2.5 w_* z_i \left[ k \frac{z}{z_i} \right]^3 \left[ 1 - 15 \frac{z}{L} \right]^{\frac{1}{4}} \quad (4.21)$$

Above the surface layer there is considerable uncertainty about the magnitude and height dependence of  $K_{zz}$ . Some observed features of atmospheric flow, for example, are not consistent with the basic K-Theory formulation of turbulent transport. For example, the difficulty of describing counter gradient fluxes of pollutant material has been discussed by Willis and Deardorff (1976). A basic problem with the K-Theory model, particularly for convectively driven flows, is that the turbulent transport is no longer described by local concentration gradients.

With these limitations in mind, Lamb et al. (1975) derived empirical expressions for  $K_{zz}$  using the numerical turbulence model of Deardorff (1970). Their work was directed at finding expressions for the vertical eddy diffusivity that were: positive definite, functions only of the height above the ground and that yielded solutions of the diffusion equation in good agreement with more refined turbulence models. The methodology employed Lagrangian diffusion theory and optimal control techniques to develop the profiles. An optimal  $K_{zz}$  was considered to be one for which a solution to the steady state diffusion equation  $c_s(x,t)$  minimized the mean square difference from a known concentration field  $c_K(x,t)$ . Formally the objective was to find a  $K_{zz}$  which

minimized the index J where

$$J(t) = \int_D [c_K(\underline{x}, t) - c_S(\underline{x}, t)]^2 dD \quad (4.22)$$

The data used for determining  $K_{zz}$  were limited to the stability conditions  $z/L = 0$  and  $z/L = -4.5$ . Recently Lamb and Durran (1978) improved the numerical procedures and extended the stability range to  $z/L = -1100$ . The calculations for each of these studies are displayed in Figure 4.4. When scaled with  $w_*$  the convective velocity and  $Z_i$ , the diffusivity profiles are sufficiently similar in shape to suggest that a single profile of the form

$$\tilde{K}_{zz} = \frac{K_{zz}}{w_* Z_i} = f\left(\frac{z}{Z_i}\right) \quad (4.23)$$

might be applicable. Convective scaling is appropriate because  $L$  is small compared with  $Z_i$ . The function  $f$  can be assumed to be universal under the following conditions: (i) the turbulence structure within the mixed layer is self similar and in equilibrium with the current boundary conditions and (ii) the normalized eddy diffusion  $K_{zz}$  is independent of the nature of the pollutant source distribution (Crane et al. 1977). In practice, the equilibrium condition is usually satisfied since it requires that the mixed layer depth varies slowly, i.e. that  $\partial Z_i / \partial t \ll w_*$ . Willis and Deardorff (1976a) indicate that self similarity occurs after  $w_* x / u Z_i$  exceeds 2.5 (where  $x$  is the distance covered after the material has been released and  $u$  the mean wind speed). This latter condition is satisfied for grid cell spacing 0(5Km). Condition

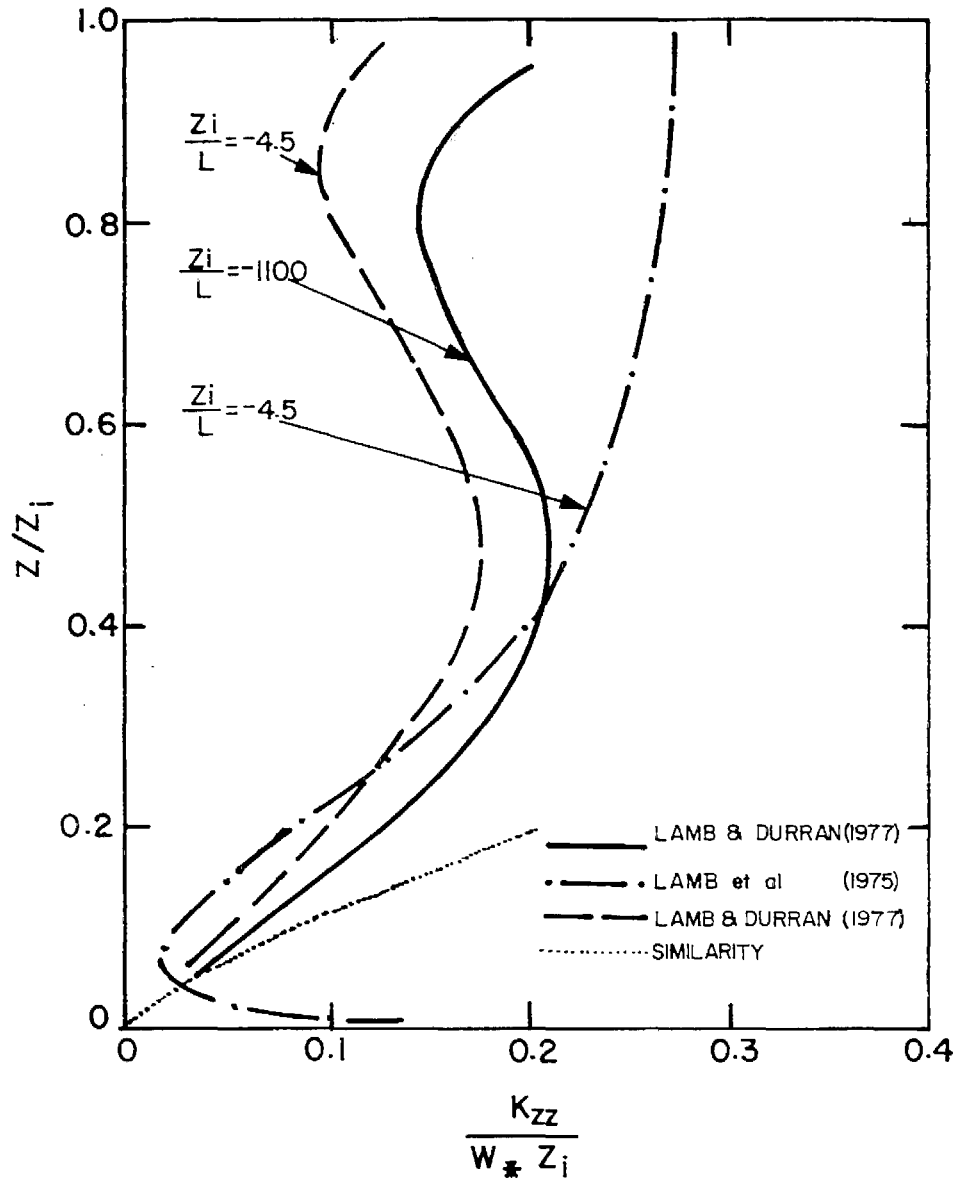


FIGURE 4.4

Vertical Diffusivity Profiles for a Range of Stability Conditions Derived from Turbulence Model of Deardorff (1970)

(ii) is not, in general, satisfied in convectively driven flows. If the eddy diffusivity were truly a local property of the turbulent flow, then  $K_{zz}$  would be independent of the height of source emissions. Lamb and Durran (1978) determined that the form of the  $K_{zz}$  profile is quite dependent on the source height. With this proviso it can be recognized that most emissions are released at or near ground level and so a single profile is applicable. The numerical form of the profile is given by (4.24) for stability conditions in the range  $Z_1/L < -10$ . (The same profile may also apply for  $-10 < Z_1/L < 0$ .)

$$K_{zz} = w_* Z_i \left[ 0.021 + 0.408 \left( \frac{z}{Z_i} \right) + 1.352 \left( \frac{z}{Z_i} \right)^2 - 4.096 \left( \frac{z}{Z_i} \right)^3 + 2.560 \left( \frac{z}{Z_i} \right)^4 \right] \quad (4.24)$$

Field data for  $c_K(x,t)$  were used by Crane et al. (1977) in a similar approach to estimate the optimal diffusivity profile. Their results are shown in Figure 4.5. However, since they neglected the effects of vertical advection and lateral diffusion,  $K_{zz}$  was underestimated by a factor of 2. The dotted line in Figure 4.5 is intended to reflect this correction. The shaded region in the center of the plot was excluded because of measurement difficulties when  $\partial c / \partial z$  was small and the effective diffusivity was large ( $0(100 \text{ m}^2 \text{ s}^{-1})$ ). An important feature of their results was that the diffusivity was quite small near the top of the mixed layer. The divergence of (4.24) for  $z/Z_i > 0.8$  is most likely due to the numerical treatment of the profile in the solution process, since no boundary slopes were imposed. There is no a priori reason why the diffusivity should be a maximum at the top of the mixed layer; indeed the results of Zeman and Lumley (1976), and the study of Stull (1973) would tend to suggest a small value.

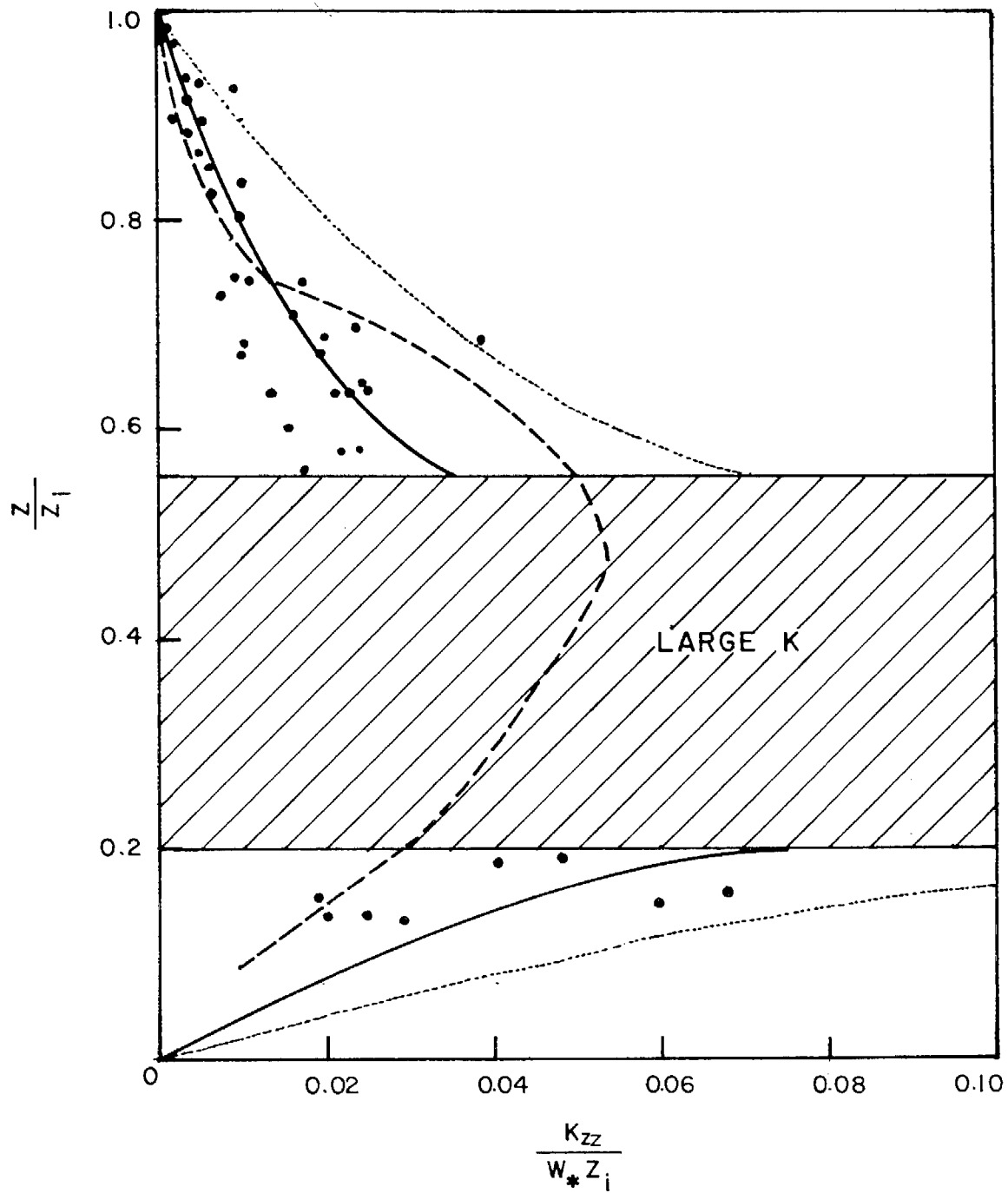


FIGURE 4.5

Vertical Turbulent Diffusivity Profiles, Derived from Field Measurements and a Second Order Closure Calculation.

For this reason (4.24) was modified for  $z > Z_i > 0.6$  to the following form

$$K_{zz} = 0.2 w_* Z_i \exp[6 - 10(\frac{z}{Z_i})] \quad (4.25)$$

This function smoothly reduces the profile to a small value at the top of the mixed layer. For  $z > 1.1Z_i$  the diffusivity is held constant at a value of  $0.0013w_*Z_i$  which is approximately one percent of the maximum value in the mixed layer.

Summarizing, the vertical eddy diffusivity profile under unstable conditions used in this study is shown in Figure 4.6 and is given by:

$$\frac{K_{zz}}{w_* Z_i} = \begin{cases} 2.5 \left(\frac{z}{Z_i}\right)^{4/3} \left[1 - 15\left(\frac{z}{Z_i}\right)\right]^{1/4} & ; 0 < \frac{z}{Z_i} < 0.05 \\ 0.021 + 0.408\left(\frac{z}{Z_i}\right) + 1.352\left(\frac{z}{Z_i}\right)^2 - 4.096\left(\frac{z}{Z_i}\right)^3 + 2.560\left(\frac{z}{Z_i}\right)^4 & ; 0.05 \leq \frac{z}{Z_i} \leq 0.6 \\ 0.2 \exp[6 - 10\left(\frac{z}{Z_i}\right)] & ; 0.6 < \frac{z}{Z_i} < 1.1 \\ 0.0013 & ; \frac{z}{Z_i} \geq 1.1 \end{cases} \quad (4.26)$$

Near the ground the profile matches the similarity solution quite closely. The maximum value of the diffusivity occurs when  $z/Z_i \approx 0.5$  and has a magnitude  $\approx 0.21w_*Z_i$ . For typical meteorological conditions this corresponds to a diffusivity of  $0(100 \text{ m}^2 \text{ s}^{-1})$  and a diffusion time defined by  $Z_i^2/K_{zz}$  of  $0(5Z_i/w_*)$ . While the diffusivities appear to be high they are in accord with the results of some recent boundary layer

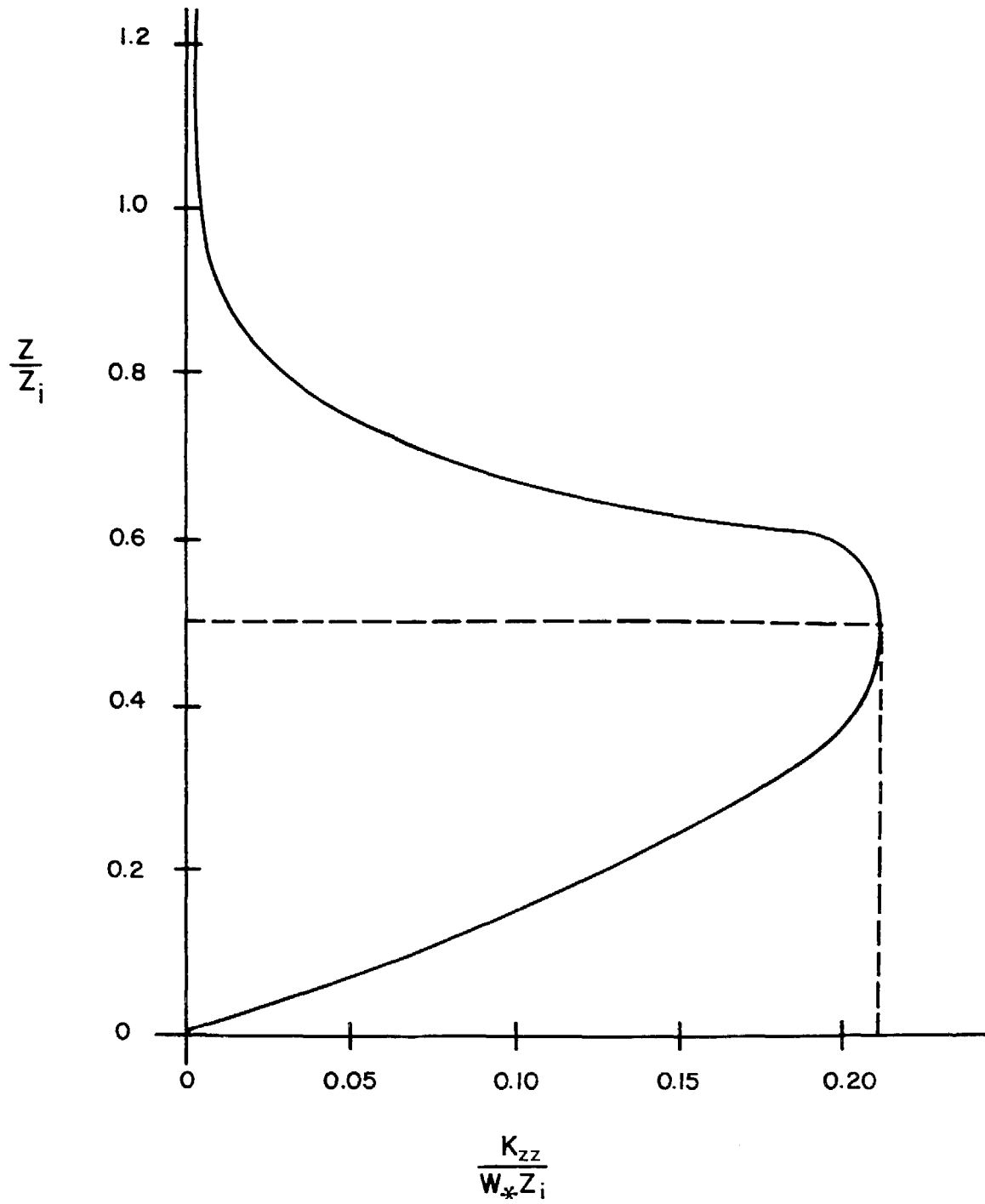


FIGURE 4.6  
Vertical Turbulent Diffusivity Profile  
Corresponding to (4.26)

models. Yamada (1977), for example, has observed maximum diffusivities of  $O(100 \text{ m}^2 \text{ s}^{-1})$  when modeling the Wangara day 34 field experiment. Above the surface layer the observational evidence is inadequate to verify more than an order of magnitude estimate of the diffusivity. Clearly there is a need for more field data to establish the shape of the profile in the upper portions of the mixed layer.

A number of other models for unstable conditions have been used in airshed modeling studies, notably the formulations of O'Brien (1970) and Myrup and Ranzieri (1976). O'Brien's model defines a cubic polynomial variation of  $K_{zz}$  above the surface layer. Boundary conditions are established by matching a similarity solution at the top of the surface layer and fixing profile gradients at  $z = |L|$  and  $Z_i$ . The expression for the diffusivity is given by

$$K_{zz} = K(Z_i) + \left[ \frac{Z_i - z}{Z_i - |L|} \right]^2 \left[ K(|L|) - K(Z_i) + (z - |L|) \left\{ \frac{\partial K}{\partial z} \Big|_{z=|L|} + 2 \left( \frac{K(|L|) - K(Z_i)}{Z_i - |L|} \right) \right\} \right] \quad (4.27)$$

where the height of the top of the surface layer is given by  $z = |L|$ .

The similarity solution can be used to evaluate  $K(|L|)$ , the gradient  $\partial K / \partial z$ , and the maximum diffusivity in the mixed layer.

$$K_{zz}(|L|) = 5.0 w_* Z_i \left( \frac{k|L|}{Z_i} \right)^{\frac{4}{3}} = 2u_* |L| \quad (4.28)$$

$$\frac{\partial K_{zz}}{\partial z} \Big|_{z=|L|} = 8.23 kw_* \left( \frac{k|L|}{Z_i} \right)^{\frac{1}{3}} = 3.3 u_* \quad (4.29)$$

Assuming  $Z_i \gg |L|$  the maximum diffusivity occurs at  $z/Z_i \approx 0.3$  and is given by

$$K_{zz}(\text{max}) \approx \frac{4}{27} \left[ K_{zz}(|L|) + Z_i \left. \frac{\partial K}{\partial z} \right|_{z=|L|} \right] = 0.5 u_* Z_i \quad (4.30)$$

Myrup and Ranzieri (1976) developed an approach based on similarity theory and a set of empirical formulae. For unstable conditions ( $z/L < -5$ ) their profile is specified by

$$K_{zz} = k u_* z [1 - 15 \frac{z}{L}]^{\frac{1}{4} q} \quad (4.31)$$

where

$$q = \begin{cases} 1 & ; \frac{z}{Z_i} < 0.1 \\ 1.1 - \frac{z}{Z_i} & ; 0.1 \leq \frac{z}{Z_i} \leq 1.1 \end{cases} \quad (4.32)$$

For the above conditions the maximum diffusivity occurs at  $z/Z_i \approx 0.5$  with a value  $K_{zz}(\text{max}) \approx 0.4 u_* Z_i$ . Figure 4.7 presents a comparison of the three different diffusivity models for a set of typical meteorological conditions. A striking feature of the plot is the similarity, in the upper and lower regions of the mixed layer, between (4.27) and the O'Brien model. The maximum diffusivity for all models is quite large which in turn implies that the vertical mixing is quite rapid.

#### 4.8 Vertical Diffusivity Profile for Neutral Conditions

Under neutral conditions the atmospheric lapse rate is adiabatic. Close to the ground the vertical eddy diffusivity profile can be based

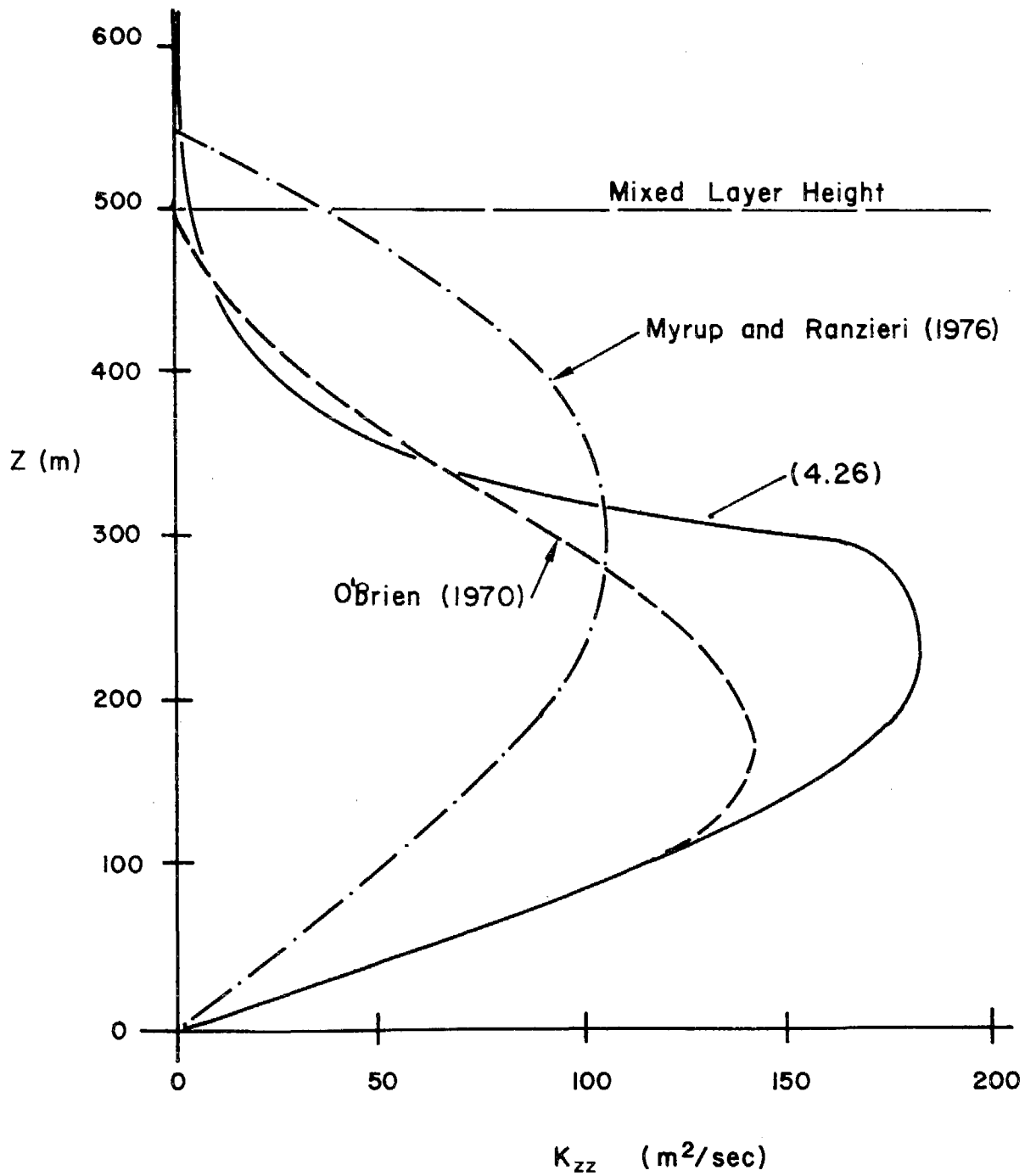


FIGURE 4.7

Comparison of Diffusivity Profiles for Unstable Conditions  
 ( $L = -30\text{m}$ ,  $u_* = 0.5\text{m/sec}$ ,  $Z_i = 500 \text{ m}$ )

on Monin-Obukhov similarity theory in which case  $\phi_m = 1$  and  $K_{zz} = ku_* z$ . With this formulation  $K_{zz}$  increases without limit, clearly a physically unrealistic situation. Myrup and Ranzieri (1976) proposed a set of empirical 'roll off' functions for extending the model to altitudes above the surface layer.

$$K_{zz} = \begin{cases} ku_* z & ; \frac{z}{Z_i} < 0.1 \\ ku_* z (1.1 - \frac{z}{Z_i}) & ; 0.1 \leq \frac{z}{Z_i} \leq 1.1 \\ 0 & ; \frac{z}{Z_i} > 1.1 \end{cases} \quad (4.33)$$

The form implied by (4.33) is some what arbitrary. Shir (1973) developed the following relationship from a study of a one-dimensional version of a turbulent transport model for extrapolation above the surface layer,

$$K_{zz} = ku_* z \exp\left[-\frac{8fz}{u_*}\right] \quad (4.34)$$

where  $f = 2\omega \cos(\phi)$  is the Coriolis parameter corresponding to the latitude  $\phi$  of the airshed. Under neutral conditions  $L = \infty$  and so the Monin-Obkuhov length is not an appropriate choice for the vertical length scale. An alternative is to define the scale in terms of the Ekman layer height  $u_*/f$ . Another formulation was proposed by Businger and Ayra (1974) for neutral and stable conditions.

$$K_{zz} = \frac{ku_* z}{1 + \alpha \phi_m \left(\frac{z}{L}\right)} \exp\left[-|V_g| \frac{zf}{u_*^2}\right] \quad (4.35)$$

where  $v_g$  is the geostrophic wind component orthogonal to the surface wind and  $\alpha$  a constant. Note that if  $v_g$  is approximately  $8u_*$ , as has been predicted by the turbulence models of Wyngaard (1973) and Deardorff (1970), then both (4.34) and (4.35) are very similar. Lamb et al. (1975) calculated the eddy diffusivity of virtual particles by employing the same techniques described in the previous section. Their polynomial form for the neutral case is given by

$$K_{zz} = \begin{cases} \frac{u_*^2}{f} [7.396 \times 10^{-4} + 6.082 \times 10^{-2} \left(\frac{zf}{u_*}\right) + 2.532 \left(\frac{zf}{u_*}\right)^2 - 12.72 \left(\frac{zf}{u_*}\right)^3 \\ \quad + 15.17 \left(\frac{zf}{u_*}\right)^4] & ; 0 \leq \left(\frac{zf}{u_*}\right) \leq 0.45 \\ \approx 0 & ; \left(\frac{zf}{u_*}\right) > 0.45 \end{cases} \quad (4.36)$$

The predictions of the various models are shown in Figure 4.8 where the scale height has been replaced with

$$H = \begin{cases} 0.5 \frac{u_*}{f} & \text{Shir (1973)} \\ z_i & \text{Myrup and Ranzieri (1976)} \\ \frac{u_*}{f} & \text{Lamb et al. (1975)} \end{cases} \quad (4.37)$$

From an examination of the profiles it is clear that there are substantial differences in the magnitudes of  $K_{zz}$  predicted by the various models. Unlike the unstable case discussed in the previous section, the similarity solution and the form proposed by Myrup and Ranzieri (1976) appear to be much larger than the 'optimal' profile.

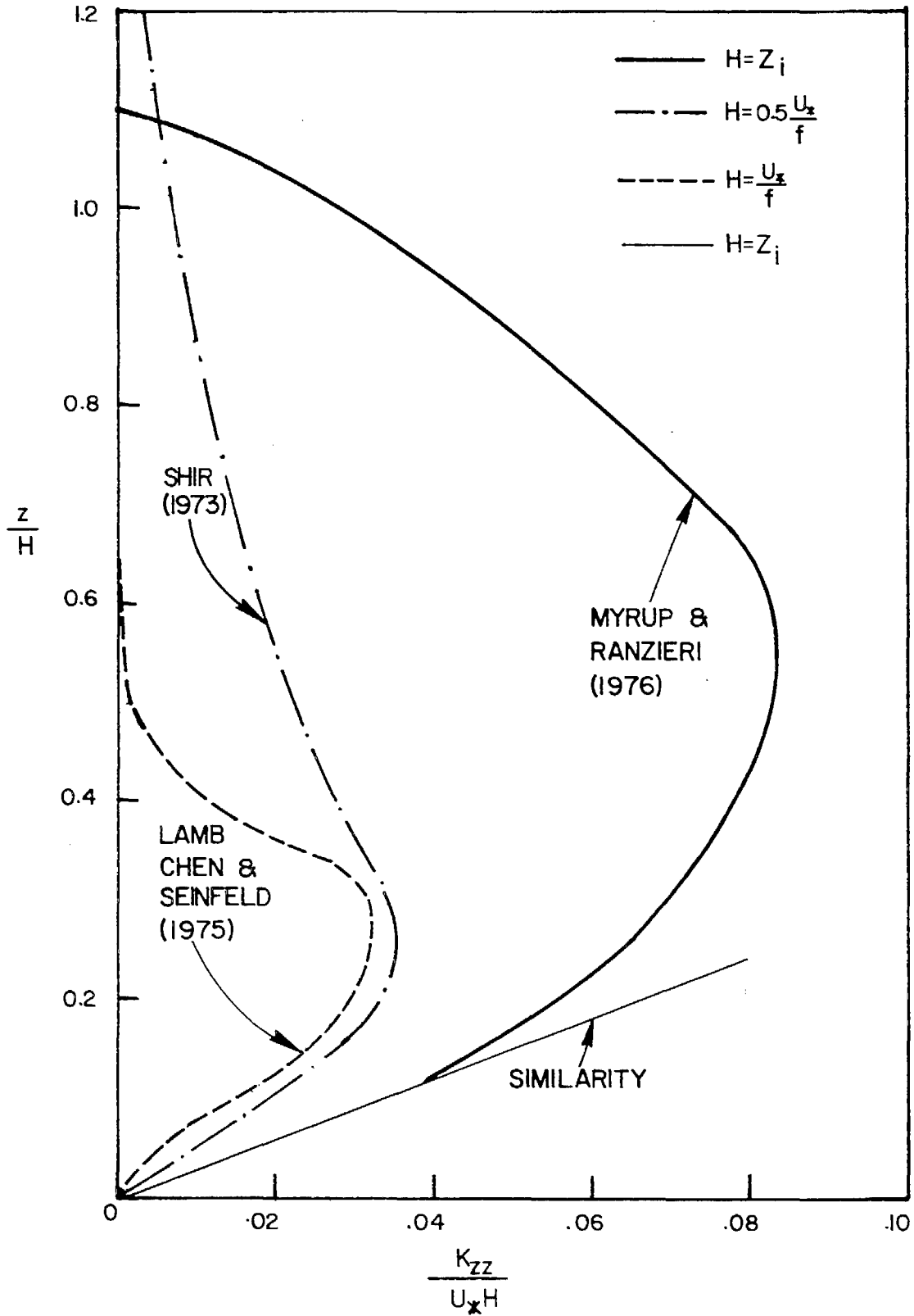


FIGURE 4.8

Comparison of Various Models for Vertical Diffusivity Profile Under Neutral Conditions

The diffusivity estimates at the top of the boundary layer predicted by the similarity solution are excessively large. The profiles of Shir (1973) and Lamb et al. (1975) are in quite close agreement up to a height of  $z/H \approx 0.3$ . Above this elevation the polynomial profile is considerably smaller. For the purposes of the present model the vertical diffusivity profile under neutral conditions will be represented by (4.34).

#### 4.9 Vertical Diffusivity Profile for Stable Conditions

Stable conditions, which typically occur at nighttime, are an important determinant of pollutant carryover effects. When  $z/L > 0$  the nature of the mixing processes is quite different from either the neutral or unstable cases. For example, in a stably stratified shear flow, turbulent energy can be transferred by internal gravity waves. These waves can become unstable and break into isolated patches of turbulence. Wyngaard (1975) has postulated that wave-induced instabilities are probably responsible for a large fraction of scalar diffusion. The intermittent nature of these instabilities considerably complicates the modeling problem because waves, as well as the turbulent patches, can transport momentum. The models discussed below do not predict these local disturbances since they are intended to represent an ensemble average diffusivity.

Even under the most stable conditions it is likely that turbulent mixing occurs at the surface. For example the maximum shear at the surface under a light geostrophic wind,  $V_g \approx 1 \text{ m-s}^{-1}$ , is given by

$$\frac{\partial \bar{u}}{\partial z} = V_g \sqrt{\frac{f}{2\nu}} \quad (4.38)$$

where  $f = 2\omega \cos(\phi)$  is the Coriolis parameter ( $\approx 10^{-4} \text{ s}^{-1}$ ) and  $\nu$  is the kinematic viscosity ( $\approx 1.5 \times 10^{-5} \text{ m}^2 \text{ s}^{-1}$ ). Assuming that the critical Richardson number for transition from a turbulent to a laminar flow is 0.25 then (4.3) can be combined with (4.38) to give an expression for the surface temperature gradient.

$$\frac{\partial \theta}{\partial z} > \frac{V_g^2 f T}{8g\nu} \quad (4.39)$$

For the stated conditions, the temperature gradient must exceed a physically unrealistic value of  $\approx 25^\circ\text{C/m}$  to maintain a laminar flow. Far from the surface the conditions are much less stringent and laminar regimes can exist. In the surface layer, similarity theory can be used to give an expression for momentum and heat diffusivity. Using the field data of Businger et al. (1971) and (4.16) the expressions are given by

$$K_{zz}^m = \frac{k u_* z}{1 + 4.7 \left(\frac{z}{L}\right)} \quad (4.40)$$

and

$$K_{zz} = \frac{k u_* z}{0.74 + 4.7 \left(\frac{z}{L}\right)} \quad (4.41)$$

Again, as in the previous cases, the above results are not applicable for  $z/L > 1$ . Under stable conditions, mixing above the surface layer can be expected to be quite different from local free convection where the eddies scale with the depth of the mixed layer  $Z_1$ . When  $z > L$  the appropriate scale for the eddies is  $L$  because buoyancy inhibits vertical excursions of air parcels over larger distances. This emphasizes that under stable conditions there is a minimum of turbulent exchange in the vertical direction. Businger and Arya (1974) proposed a modification of (4.31) to extend the model above  $z = L$ .

$$K_{zz} = \frac{ku_*z}{0.74 + 4.7\left(\frac{z}{L}\right)} \exp \left[ - \left| \frac{v_g}{u_*} \right| \frac{fz}{u_*} \right] \quad (4.42)$$

The maximum value of the diffusivity for this model is given by the empirical expression.

$$K_{zz}(\max) \approx 0.03 \frac{u_*^2}{f} \left( \frac{fL}{u_*} \right)^{0.9} \quad (4.43)$$

For typical meteorological conditions the maximum diffusivity can be expected to be in the range  $0.5 - 5 \text{ m}^2/\text{sec}$ . The magnitude is considerably smaller than the equivalent values encountered under strongly unstable conditions. A limitation of the above formulation is the need for a knowledge of the geostrophic wind velocity  $V_g$ . Unless this is available, (4.42) must be solved simultaneously with the equations of motion for a steady-state barotropic layer. If the assumption  $V_g \approx 8u_*$ ,

discussed in the previous section, is employed then (4.43) can be written in the form

$$K_{zz} = \frac{ku_* z}{0.74 + 4.7 \left(\frac{z}{L}\right)} \exp\left[-\frac{8fz}{u_*}\right] \quad (4.44)$$

This model is quite similar to the Myrup and Ranzieri (1976) form except that the exponential decay is replaced by the 'roll-off' functions defined by (4.30). An alternative approach is to modify the O'Brien formula noting that the expression (4.27) enables a unique polynomial profile to be established by matching the applied boundary conditions. From (4.41) the slope at  $z = L$  is given by

$$\left. \frac{\partial K_{zz}}{\partial z} \right|_{z=L} = 0.025 ku_* \quad (4.45)$$

Substituting this result into (4.27) and defining the scale height to be  $H$ , the vertical diffusivity variation is

$$K_{zz} = K(H) + \left[ \frac{H-z}{H-L} \right]^2 \left[ K(L) - K(H) + (z-L) \left\{ \left. \frac{\partial K}{\partial z} \right|_{z=L} + 2 \left( \frac{K(L) - K(H)}{H-L} \right) \right\} \right] \quad (4.46)$$

where  $K(L) = 0.025ku_*L$ . If  $K(H)$  is set equal to  $K(L)$  then (4.46) can be further simplified to

$$K_{zz} = 0.025 ku_* L \left[ 1 + 0.025 \left( \frac{z}{L} - 1 \right) \left( \frac{H-z}{H-L} \right)^2 \right] \quad (4.47)$$

The form and magnitude of the scale height  $H$  clearly depends on the meteorological conditions. Wyngaard (1975) concluded that turbulence

is confined to a layer of thickness  $H$  given approximately by

$$H = 0.22 \frac{u_*}{f} \sqrt{\frac{fL}{u_*}} \quad (4.48)$$

This result is the same form as the power law predicted by Zilitinkevich (1972) and, apart from a different constant  $\approx 0.74$ , is identical to the Businger and Ayra (1974) K-Theory model. Within the airshed model the form (4.46) was adopted with  $K(H) \approx 0.05 K(L) = 0.01 ku_*L$ . Above  $z = H$ ,  $K_{zz}$  is held fixed at  $K(H)$  which results in diffusivities  $0(0.1 \text{ m}^2 \text{ s}^{-1})$ , a value consistent with the modeling studies of Yu (1977). The diffusivity profiles for the above models are very similar to the forms shown in Figure 4.8. Considering the magnitude of the diffusivities, the associated mixing times and grid cell spacing, the simplest profile is a constant value of  $K_{zz} = K(L)$  for  $0 < z < H$  and  $K_{zz} = pK(L)$  for  $z > H$  where  $p$  is a small fraction  $\approx 0.05$ .

Evaluation, selection or development of a model for stable conditions is, at present, considerably hampered by a lack of suitable field data. An interesting topic for further research is to develop an understanding of the role of density stratification in inhibiting turbulent mixing and transport.

#### 4.10 Horizontal Eddy Diffusion Coefficients

Completion of the eddy diffusion model requires specification of the horizontal components  $K_{xx}$ ,  $K_{yy}$ . Unlike the vertical direction, the contribution from turbulent fluxes is small compared to the advection.

For typical urban meteorological conditions and grid cell spacings, a simple scale analysis indicates that:

$$\frac{\partial uc}{\partial x} \gg \frac{\partial}{\partial x} K_{xx} \frac{\partial c}{\partial x} \quad ; \quad \frac{\partial vc}{\partial y} \gg \frac{\partial}{\partial y} K_{yy} \frac{\partial c}{\partial y} \quad (4.49)$$

With this result it is evident that the model formulation for  $K_{xx}$ ,  $K_{yy}$  is not as critical as in the case for  $K_{zz}$ . Liu et al. (1977) studied the influence of changes in  $K_{xx}$ ,  $K_{yy}$  (0 - 500 m<sup>2</sup>/sec) and concluded that the effect on concentration predictions for area wide averages is quite small, < 2%. This result should, however, be interpreted in the light of the observation that when simple numerical solution techniques are employed the effective diffusion coefficient  $K_e$  is the sum of two terms. One term,  $K_n$ , is due to the numerical truncation error and the other is the real physical component,  $K_p$ , i.e.

$$K_e = K_n + K_p \quad (4.50)$$

Unless special precautions are taken  $K_n$  can exceed  $K_p$  and so large changes in  $K_p$  do not influence  $K_e$ . As an extreme example the simple upwind difference scheme for the advection equation has  $K_n = (u\Delta x - u^2\Delta t)/2 \approx 0(1000 \text{ m}^2\text{-s}^{-1})$ . A consequence of using more refined numerical techniques is that more attention must be given to  $K_p$  since  $K_p > K_n$ .

Many previous studies have either ignored the horizontal diffusion terms or have assumed, as in the case of Reynolds et al. (1973), a constant value  $\approx 50 \text{ m}^2 \text{ s}^{-1}$ . The influence of stability and grid size was incorporated into the MacCracken et al. (1978) model using the scale dependent diffusion approach of Batchelor (1950) and Walton (1973).

The bases for the formulation adopted in this study are the classic work of Taylor (1938), the laboratory studies of Willis and Dear-dorff (1976b) and some suggestions by Lamb (1977). If  $x_i(t)$  is the displacement of a particle in the  $i$ th direction due to an eddy velocity  $u_i'(t)$  then the rate of change of dispersion is a stationary and homogeneous turbulent field given by

$$\frac{d\langle x_i^2(t) \rangle}{dt} = 2\langle x_i(t)u_i'(t) \rangle = 2\langle u_i'^2(t) \rangle \int_0^t R_{ii}(t-\tau) d\tau \quad (4.51)$$

where  $\langle \rangle$  represents an ensemble average and  $R_{ii}$  is the Lagrangian velocity correlation coefficient defined as

$$R_{ii}(t-\tau) = \frac{\langle u_i'(t)u_i'(\tau) \rangle}{\langle u_i'^2 \rangle} \quad (4.52)$$

From this expression the integral scale of the turbulence can be defined as

$$T_L = \int_0^{\infty} R(\xi) d\xi \quad (4.53)$$

$T_L$  is a measure of the time over which  $u_i'$  is correlated with itself. Now integrating (4.52) with respect to time gives

$$\langle x_i^2(t) \rangle = 2\langle u_i'^2(t) \rangle \int_0^t \int_0^{t'} R_{ii}(t-\tau) d\tau dt \quad (4.54)$$

which in the limit of small and large times leads to the results

$$\langle x_i^2(t) \rangle = \begin{cases} \langle u_i'(t) \rangle^2 t^2 & ; t \rightarrow 0 \\ & (t < T_L) \\ 2K_{ii}t & ; t \rightarrow \infty \\ & (t \gg T_L) \end{cases} \quad (4.55)$$

Where

$$K_{ii} = \langle u_i'(t) \rangle^2 \lim_{t \rightarrow \infty} \int_0^t R(\tau) d\tau \quad (4.56)$$

$K_{ii}$  has the dimensions of a diffusion coefficient, since for  $t \gg T_L$

$$K_{ii} = \frac{1}{2} \frac{d\langle x_i^2(t) \rangle}{dt} \quad (4.57)$$

Measurements of  $T_L$  in the atmosphere are extremely difficult and it is not at all clear whether the condition  $t \gg T_L$  holds for urban scale flows. The time  $t$  in the case of the present model is equal to the numerical time step  $\Delta t \sim 0(1000 \text{ sec})$ . Csanady (1973) indicates that a typical eddy which is generated by shear flow near the ground has a Lagrangian time-scale of the order of 100 sec. Lamb and Neiburger (1971) in a series of measurements in the Los Angeles Basin estimated the Eulerian time-scale  $T_e$  to be  $\sim 50 \text{ sec}$ . In a discussion of some field experiments Lumley and Panofsky (1964) suggested that  $T_L < 4 T_e$  and so an approximate upper limit of  $T_L$  for the Los Angeles data is 200 seconds. If the averaging interval is selected to be equal to the travel time then an approximate value for  $K_H$  can be deduced from the

measurements of Willis and Deardorff (1976b). Their data indicate that for unstable conditions ( $L > 0$ ) and a travel time  $t = 3Z_i/w_*$

$$\frac{\langle y(t)^2 \rangle}{Z_i^2} \approx 0.64 \quad (4.58)$$

Employing the previous travel time estimate and combining this result with (4.58) gives

$$K_H = K_{xx} = K_{yy} = \frac{1}{6} \frac{y(t)^2}{Z_i^2} w_* Z_i \approx 0.1 w_* Z_i \quad (4.59)$$

This latter result can be expressed in terms of the friction velocity,  $u_*$  and the Monin-Obukhov length  $L$

$$K_H \approx 0.1 Z_i^{\frac{4}{3}} (-kL)^{-\frac{1}{3}} u_* \quad (4.60)$$

For a range of typical meteorological conditions this formulation results in diffusivities  $0(50-100 \text{ m}^2/\text{sec})$ . Some typical results, plotted in Figure 4.9, are in quite close agreement with field measurements and the formulae recommended by Briggs (1974) for city conditions. In the above model  $K_H$  varies as a function of the surface conditions at different spatial locations but is assumed to be invariant with height. This latter assumption is based on the observation that the energy dissipation rate  $\varepsilon(z)$  is a weak function of elevation with  $K_H \sim \varepsilon^{1/3}$  and for most practical purposes can be ignored.

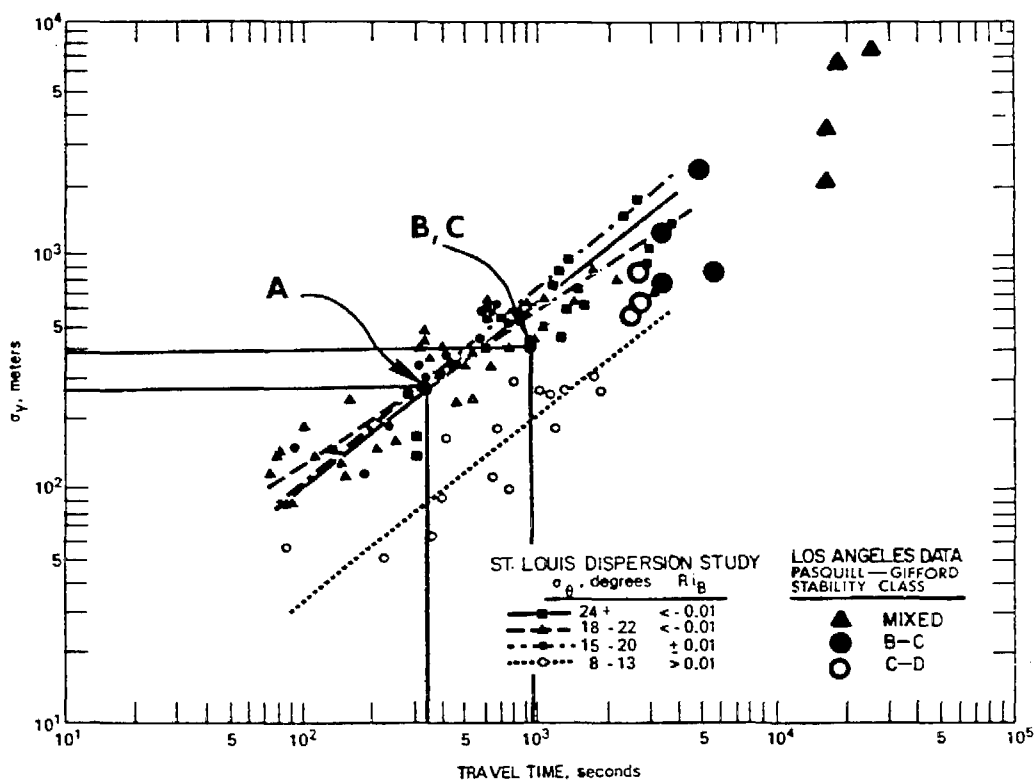


FIGURE 4.9

Cross Wind Standard Deviation  $\sigma_y$  as a Function of Travel Time  
 (Labeled points correspond to examples in Table 4.4)  
 (St. Louis data derived from McElroy and Pooler, 1968; Los Angeles data derived from Drivas and Shair, 1975; Shair, 1977)

TABLE 4.4

Typical Horizontal Eddy Diffusivities  
and Cross Wind Standard Deviations

Stability Class	$z_o$ (m)	L (m)	$\bar{u}$ (m/sec)	$u_*$ (m/sec)	$Z_i$ (m)	$w_*$ (m/sec)	$K_H$ (m <sup>2</sup> /sec)	$\sigma_y$ (m)	Travel Time (sec)
A	0.5	-14	2	0.42	300	2.44	73	231	368
B	1.08	-29	2	0.43	500	1.58	79	387	949
C	1.75	-250	4	0.83	500	1.48	74	387	1013

#### 4.11 Application and Validity of the Diffusion Coefficients

Previous sections have been devoted to surveys and a detailed discussion of the various diffusivity expressions embedded in the airshed model. The inputs required to calculate the components of  $K$  are as follows: surface wind speed  $u$ , roughness height  $z_0$ , solar intensity  $I$ , mixed layer depth  $Z_i$ , latitude and vertical extent of the airshed. A summary of the steps in the calculational procedure for each stability regime is presented in Figure 4.10.

In constructing the models for  $K_{zz}$  and  $K_H$  a number of critical assumptions were invoked. The first was to assume that the temporal variations in the components of  $K$  rapidly adjust to changes in the meteorological condition. A formal validation of this condition would be quite complex. As an alternative it is useful to observe that the characteristic time scales for unstable, neutral and stable conditions ( $Z_i/w_*$ ,  $Z_i/u_*$ ,  $L/u_*$ ) are all in the range of 100-500 seconds. The temporal scales of the processes driving the boundary layer dynamics are much longer, particularly if it is noted that most meteorological data used in airshed modeling studies are hourly averaged. An implication of this discussion is that the turbulence levels change with time but in such a way that at any instant the flow can be considered stationary. Certain non-stationary conditions can exist, however, at sunrise and sunset.

An assumption, possibly more restrictive than stationarity, is that within the surface grid cells an equilibrium state has been assumed between the fluxes and gradients. As air parcels move over the airshed they experience the effects of changes in surface roughness. The adjustment process is relatively slow, implying that the transition



region occupies a significant portion of the area above the new surface. In the transition region the diffusivities are a function of the downwind fetch from the edge of the change as well as the parameters discussed previously. Mulhearn (1977) has recently developed a set of relationships between the surface fluxes and mean profiles of concentration downwind of a change in  $z_0$ . The results indicate that if horizontal homogeneity is assumed within each computational cell the  $K_{zz}$  values will be overestimated for the case of a rough to smooth transition and underestimated for the opposite case. With a sufficiently large grid cell spacing the effects of inhomogeneities are small.

#### 4.12 Conclusions

Turbulent diffusion is an important process which influences the airshed concentration distributions. In this chapter the parameterization of the components of  $K$  has been presented. A different model for each of the stable, neutral and unstable conditions was introduced. Particular emphasis was given to developing models for  $K_{zz}$ ,  $K_H$  under convectively driven conditions. In all cases the guiding principle in model formulation was to employ only those data which are commonly available or readily estimated. Within the airshed model the diffusivity expressions have been implemented as separate modules and so incorporation of any modifications is quite straightforward.

CHAPTER 5

CONVECTIVE DOWNMIXING OF PLUMES IN A COASTAL ENVIRONMENT

(Reprinted from J. Applied Meteorology, 20, 1312-1324)

## Convective Downmixing of Plumes in a Coastal Environment

GREGORY J. MCRAE, FREDRICK H. SHAIR<sup>1</sup> and JOHN H. SEINFELD<sup>1</sup>

*Environmental Quality Laboratory, California Institute of Technology, Pasadena 91125*

(Manuscript received 30 April 1981, in final form 2 August 1981)

### ABSTRACT

This paper describes the results of an atmospheric tracer study in which sulfur hexafluoride ( $\text{SF}_6$ ) was used to investigate the transport and dispersion of effluent from a power plant located in a coastal environment. The field study demonstrated that material emitted into an elevated stable layer at night can be transported out over the ocean, fumigated to the surface, and then be returned at ground level by the sea breeze on the next day. At night when cool stable air from the land encounters the warmer ocean convective mixing erodes the stable layer forming an internal boundary layer. When the growing boundary layer encounters an elevated plume the pollutant material, entrained at the top of the mixed layer, can be rapidly transported in  $\sim 20$  min to the surface. Various expressions for the characteristic downmixing time ( $\lambda = Z_i/w_*$ ) are developed utilizing the gradient Richardson number, the Monin-Obukhov length and turbulence intensities. Calculations using these expressions and the field data are compared with similar studies of convective mixing over the land.

### 1. Introduction

A major influence on pollutant dispersion and transport in coastal environments is the presence of land/sea breeze circulation systems. Unfortunately the characterization of turbulent transport is complicated by the presence of flow reversals and differing atmospheric stabilities. Since many large sources are located in shoreline environments, it is important to understand the mixing characteristics within the boundary layer. A field experiment designed to determine the fate of pollutants emitted into the offshore flow associated with a land/sea breeze circulation system, was carried out by Shair *et al.* (1981). In that study it was found that tracer material emitted into an elevated stable layer at night could be transported out over the ocean, fumigated to the surface, and then be returned at ground level by the sea breeze on the next day. The objectives of this work are to examine the vertical transport processes responsible for this rapid downmixing and to characterize the mixing rates within the internal boundary layer formed when cool air from the land is advected out over a warm ocean surface.

### 2. Description of field experiment

Because of the complexity of atmospheric flows, the only direct way to relate the emissions from a particular source to observed concentrations is to tag the source exhaust gases so they can be uniquely identified. Over the last few years a variety of

atmospheric tracers, including sulfur hexafluoride ( $\text{SF}_6$ ), fluorescent particles, halocarbons and deuterated methane, have been used in transport and diffusion studies. Sulfur hexafluoride was used in this experiment because it is gaseous, physiologically inert, chemically stable, and easily detected using electron-capture gas chromatography (Simmonds *et al.*, 1972). Drivas and Shair (1974), Lamb *et al.* (1978a,b) and Dietz and Cote (1973) have successfully demonstrated the utility of  $\text{SF}_6$  as a tracer in large-scale field studies. Current analysis techniques have achieved detection limits of  $2 \times 10^{-13}$  parts  $\text{SF}_6$  per part of air. From a practical point of view both the release techniques and sampling protocols are well established and reliable.

Each experiment was carried out by injecting the tracer gas into the number 4 stack of the Southern California Edison El Segundo power plant located on the shore of Santa Monica Bay (Fig. 1). This particular chimney is 61 m high and 4.3 m in diameter. The tracer was released at a time when the flow, at the effective stack height, was offshore. Before each experiment an initial estimate of the plume rise was determined using Briggs' formulas (Briggs, 1969; 1975) for neutral conditions. For the particular load conditions (0.57 of capacity), an exhaust gas temperature of 365 K and a gas flow rate of  $230 \text{ m}^3 \text{ s}^{-1}$ , the plume rise was estimated to be 250 m. This information, together with the vertical wind distribution obtained from pibal releases, was used to establish the time to initiate the tracer injection so that the material was released into the offshore flow. After the experiment a more detailed calculation,

<sup>1</sup> Department of Chemical Engineering.

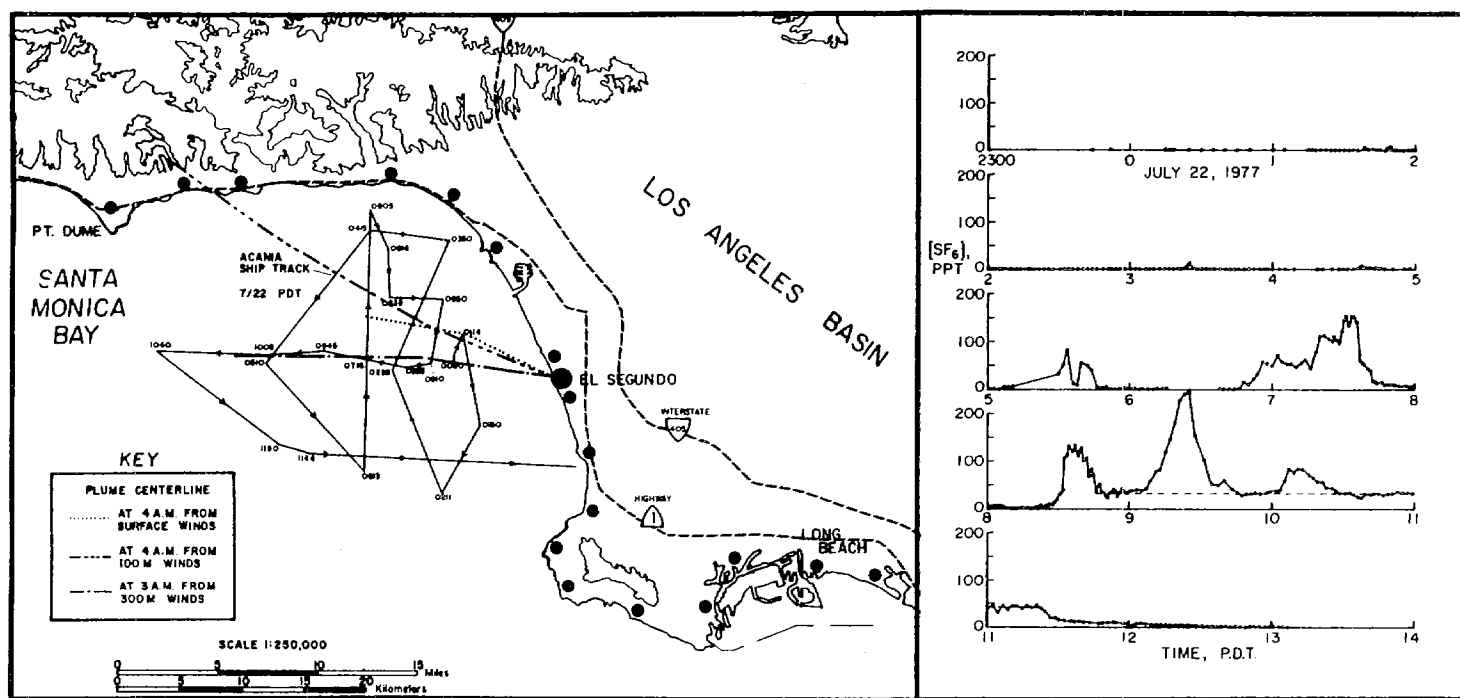


FIG. 1. Sulfur hexafluoride (SF<sub>6</sub>) measurements made on board R/V *Acania* 22 July 1977 coordinated with ship course and possible plume trajectories derived from surface and elevated wind measurements: (●), release site; (○) onshore monitoring sites.

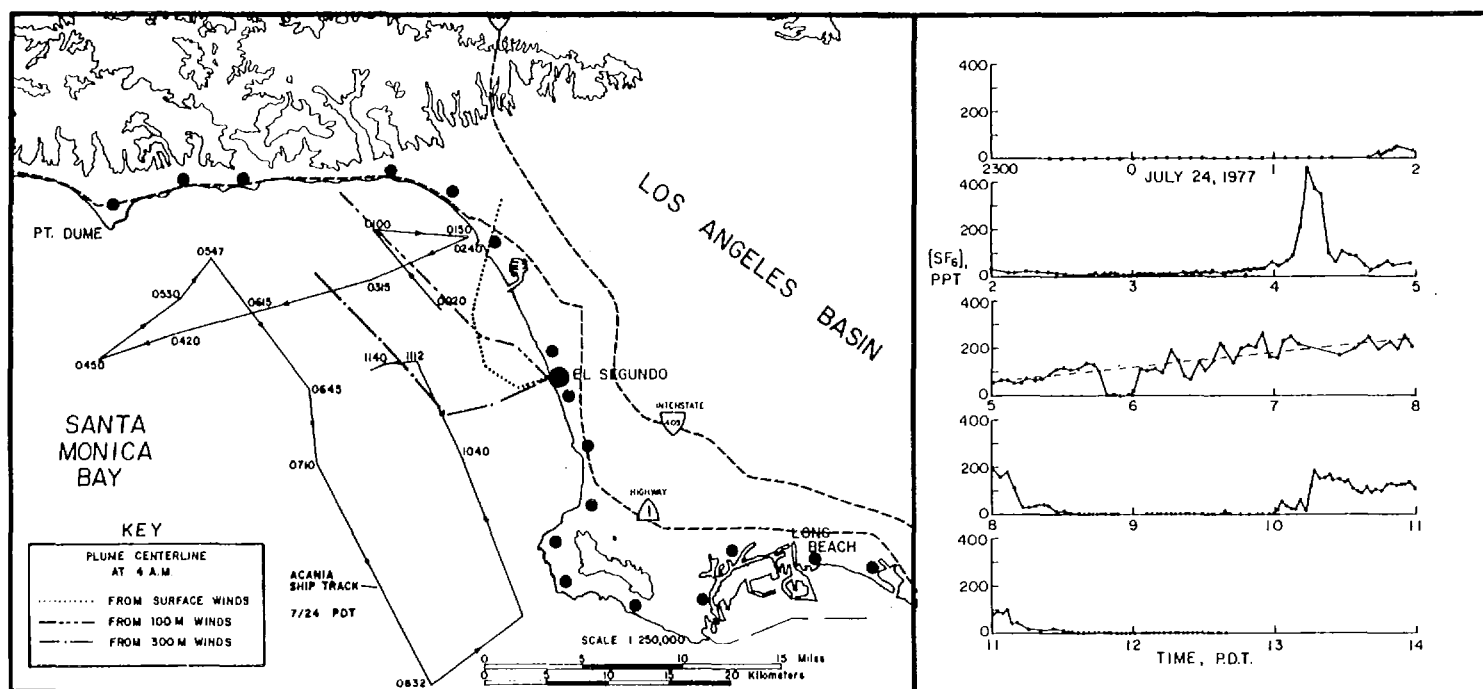


FIG. 2. Sulfur hexafluoride ( $\text{SF}_6$ ) measurements made on board R/V *Acania* 24 July 1977 coordinated with ship course and possible plume trajectories derived from surface and elevated wind measurements: (●) release site; (●) onshore monitoring sites.

accounting for the actual vertical variations in wind and temperature profiles, was carried out using the Schatzmann (1979) integral plume rise model, using meteorological data from Schacher *et al.* (1978). During the first test, on 22 July 1977, 90 kg of SF<sub>6</sub> was released at a rate of 5.0 g s<sup>-1</sup> from 0005–0500 (all times PDT). During the second test 245 kg of SF<sub>6</sub> were released, at a higher rate of 13.6 g s<sup>-1</sup>, from 2303 on 23 July 1977 until 0400 on 24 July.

The amount and release rates for each experiment were selected so that there was sufficient material to distinguish the source from the background at the maximum sampling distance. If the total amount of tracer released during each experiment were to be uniformly distributed throughout a volume of 1600 km<sup>2</sup> × 300 m (i.e., the area of Santa Monica Bay times the estimated plume rise above the ocean surface), then the average tracer concentration would have been 50 ppt<sup>2</sup>, a value well above both the detection limit and normal background levels. Most of the current world background concentration of <0.5 ppt is a result of leakages from high-voltage power transformers and switching systems where SF<sub>6</sub> is used for corona discharge suppression.

Hourly averaged air samples were collected continuously, from 0500–1700 during each of the test days, at 29 coastal sites located from Ventura to Corona del Mar (Figs. 1 and 2). This was to observe the tracer flux across the coast during the sea breeze on the day following the nighttime release. Subsequent mass balance calculations using these measurements were able to account for virtually 100% of the material released during both experiments (Shair *et al.*, 1981). Samples were analyzed using the methodology described in Lamb *et al.* (1978a,b). In addition, grab samples were collected every 5 min on board a ship traversing Santa Monica Bay and analyzed using portable electron-capture gas chromatographs. This sampling protocol provided rapid feedback on the tracer concentrations and plume position during each experiment. The measurements taken on board the ship are shown in Figs. 1 and 2. Sampling on board the ship was started 1 h before each release so that any possible background levels could be detected. All samples were collected in 30 cm<sup>3</sup> plastic syringes and were analyzed within one day of each experiment. At the coastal monitoring sites battery-powered sequential samplers were used to determine the hourly averaged SF<sub>6</sub> concentration levels. In addition automobile sampling traverses were conducted periodically along coastal highways between 1000–1427 on 22 July and between 0235–1540 on 24 July. Grab samples were collected at 0.8–3.2 km intervals along the coastal highway between Redondo Beach and Malibu. The results from the shore measure-

ments and automobile traverses were used by Shair *et al.* (1981) to calculate the flux of SF<sub>6</sub> across the coast.

The tracer experiments were carried out in collaboration with investigators from the Environmental Physics Group at the Naval Postgraduate School in Monterey, California. The research vessel *Acania* was used as a platform to collect meteorological data in the vicinity of Santa Monica Bay. The ship was equipped with a complete suite of meteorological equipment capable of multilevel measurements (4.2, 7.0 and 22.5 m above the ocean) of mean and fluctuating quantities. Since complete details of the instrumentation can be found in Houlihan *et al.* (1978) and Schacher *et al.* (1978), the material will not be repeated here. For the particular study of the mixing rates over the ocean, measurements were made of sea surface temperature  $T_s$ , air temperature  $T_a$ , humidity/dew point  $T_d$ , true wind speed  $u$ , direction  $\theta$ , and temperature inversion height  $Z_i$ . The wind direction  $\theta$  is particularly useful since it can be used to differentiate local (land and sea breeze) circulations. Both the wind speed and direction have been corrected to account for the ship motion. In addition, during the period 19–26 July, 14 radiosondes were released to examine the vertical temperature structure. During each tracer experiment pibals were released each hour at a site close to the release point so that the horizontal winds as a function of elevation could be determined. Observations made at the 100 and 300 m levels were used to calculate plume trajectories from the release point. Some of these results are superimposed on Figs. 1 and 2. The complete data sets describing the meteorological conditions are contained in the reports by Schacher *et al.* (1978, 1980). For convenience a summary of key information from these sources, together with the calculated virtual heat flux  $Q_0$ , is presented in Table 1.

Since the pattern of results observed on board R/V *Acania* on both days were similar it suffices to discuss the experiment conducted on 22 July. A more detailed discussion of the concentration levels measured at the coastal monitoring stations is contained in Shair *et al.* (1981). Prior to 0530 PDT, when the mixing depth was below 200 m, the ship passed under the calculated plume positions at 0100, 0325 and 0438 and no significant concentrations of SF<sub>6</sub> were observed. At 0530, when the ship was 6.4 km south of the plume, the first significant peak (80 ppt) was recorded at a time when the mixed layer was growing above the 200 m level. From 0600 onward all the concentration peaks at 0730, 0835 and 0925 were observed when the ship was in the vicinity of the plume and the mixed-layer height was above 200 m. From 0830 to 1130 the SF<sub>6</sub> exceeded 20 ppt and the ship was always within 3 km of the plume. Lower concentrations were observed when the ship

<sup>2</sup> Parts per trillion.

TABLE 1. Basic meteorological data collected during the period 19–26 July 1977.\*

Date	Time (PDT)	Humidity (%)	$T_a$ (°C)	$T_s$ (°C)	$T_a - T_s$ (°C)	$Q_0$ ( $10^3 \text{ m s}^{-1} \text{ K}$ )	Date	Time (PDT)	Humidity (%)	$T_a$ (°C)	$T_s$ (°C)	$T_a - T_s$ (°C)	$Q_0$ ( $10^3 \text{ m s}^{-1} \text{ K}$ )
19	0000	90	16.4	19.1	-2.75	8.7	21	0945	89	17.5	18.8	-1.26	2.8
19	0020	92	16.0	18.5	-2.53	5.6	21	1005	88	17.4	18.2	-0.72	2.1
19	0100	92	16.0	17.6	-1.61	2.4	21	1025	88	17.6	18.5	-0.38	0.8
19	0140	93	15.9	16.7	-0.80	0.7	21	1045	88	17.6	18.4	-0.80	1.6
19	1620	79	18.7	21.1	-2.39	14.9	21	1105	89	17.4	17.7	-0.33	2.1
19	1650	79	18.5	21.1	-2.57	19.4	21	1305	90	17.7	17.7	-0.05	2.2
19	1710	79	18.3	21.0	-2.72	18.8	21	1325	90	17.5	17.7	-0.24	3.0
19	1730	79	18.1	20.9	-2.77	19.4	21	1345	90	17.5	17.9	-0.40	3.0
19	2000	84	18.2	18.8	-0.59	5.8	21	1405	90	17.7	18.2	-0.54	4.6
19	2040	87	17.5	19.8	-2.26	11.8	21	1505	88	18.2	18.9	-0.68	7.9
19	2120	87	17.5	19.8	-2.26	7.3	21	1620	86	18.3	18.8	-0.47	6.6
19	2140	87	17.6	19.9	-2.33	7.5	21	1720	85	18.0	18.7	-0.69	6.4
19	2200	87	17.6	19.8	-2.20	8.9	21	1945	79	18.6	19.9	-1.30	10.4
							21	2030	85	18.2	19.8	-1.66	7.5
20	0700	86	17.0	18.7	-1.67	9.9	21	2110	84	18.3	19.7	-1.35	3.4
20	0740	86	17.3	19.2	-1.93	8.5	21	2130	85	18.3	19.5	-1.21	3.8
20	0900	85	17.8	19.3	-1.46	4.6							
20	0920	85	17.9	19.3	-1.42	4.4	22	0550	93	17.1	17.3	-0.19	0.5
20	1240	78	19.0	20.2	-1.20	5.2	22	0610	94	16.9	17.2	-0.34	0.7
20	1300	79	19.0	19.8	-0.78	3.2	22	0710	96	16.5	17.3	-0.77	0.5
20	1320	88	19.0	19.7	-0.63	2.3	22	0730	97	16.6	17.3	-0.68	0.4
20	1800	84	18.8	18.2	0.56	-3.9	22	0750	97	16.5	17.3	-0.76	0.5
20	1900	83	18.3	17.8	0.48	-4.3	22	0810	97	16.7	17.3	-0.57	0.3
20	1920	84	18.4	17.7	0.65	-6.4	22	0830	96	16.6	17.3	-0.72	2.1
20	1940	84	18.3	18.4	-0.12	2.5	22	0910	97	16.5	17.3	-0.78	1.4
20	2000	85	18.2	18.3	-0.09	2.1	22	0930	97	16.6	17.3	-0.71	0.8
20	2020	86	17.7	18.3	-0.56	3.7	22	1030	96	17.1	18.5	-1.46	4.6
20	2040	87	17.9	18.3	-0.45	2.5	22	1050	94	17.5	18.6	-1.09	1.4
20	2120	88	17.8	18.2	-0.41	2.3							
20	2140	89	17.7	18.2	-0.53	2.8	23	1440	87	19.2	18.2	0.92	-1.4
20	2220	90	17.6	19.0	-1.38	4.8	23	1505	85	19.5	18.7	0.76	-2.9
20	2230	91	17.6	18.4	-0.83	2.7	23	1645	83	19.9	20.4	-0.43	5.1
20	2300	91	17.2	18.2	-1.00	2.9	23	1725	85	19.1	19.2	-0.08	1.9
							23	1745	87	18.8	19.1	-0.28	1.2
21	0000	94	16.6	17.2	-0.63	2.5	23	2340	90	18.5	18.0	0.53	-0.5
21	0040	94	16.2	16.9	-0.70	2.5							
21	0100	93	15.9	16.6	-0.72	2.0	24	0040	91	19.1	18.6	0.50	-0.7
21	0405	98	16.2	17.7	-1.46	6.3	24	0100	90	19.0	18.6	0.39	-0.5
21	0425	97	16.4	18.1	-1.65	6.2	24	0120	90	19.0	18.7	0.28	-0.3
21	0445	96	16.8	18.4	-1.57	6.0	24	0240	87	19.0	18.7	0.25	-0.3
21	0505	94	17.1	18.4	-1.33	4.5	24	0300	86	19.0	18.7	0.28	-0.3
21	0545	91	17.4	18.2	-0.81	2.2	24	0420	88	18.8	18.7	0.06	0.0
21	0605	89	17.4	18.3	-0.84	0.7	24	1000	78	19.3	19.2	0.06	0.5
21	0645	89	17.3	18.3	-0.96	2.0							
21	0705	89	17.3	18.2	-0.86	2.4	25	2220	83	19.3	17.7	1.57	-8.8
21	0845	91	17.7	19.0	-1.31	6.4	25	2320	84	19.1	17.9	1.27	-7.1
21	0905	89	17.8	18.9	-1.14	3.9	26	0420	90	18.6	18.1	0.49	-0.2

\* Source: Schacher *et al.* (1980).

and the plume separation increased to more than 15 km. The only major difference between the two tests was the increased wind speeds and mixing heights on 23–24 July. While this, together with the wind shear, enhanced the horizontal dispersion of  $\text{SF}_6$  there were no significant differences in the observed vertical mixing rates.

Although the power plant effluent was emitted well above the surface into an elevated stable layer where vertical mixing could be expected to be quite small, large amounts of tracer suddenly appeared at the sampling sites close to the ocean surface. The remaining sections of this work are devoted to a discussion of the reasons for the rapid transport of tracer material to the surface.

### 3. Vertical mixing over the ocean

The problem of dispersion and transport near coastlines and large lakes has received considerable attention in the literature (See, e.g., Lyons, 1975; Businger, 1975; Misra, 1980; Raynor *et al.*, 1980; Orgill, 1981). The purpose of this section is to examine the results from prior observations applicable to the present field experiment, since few, if any, studies have been made of convective activity over the ocean at night. Since the ocean temperatures during the experiments were greater than that of the air, it can be seen that the conditions are similar to those observed over the land during the day.

Under the action of buoyancy forces induced by

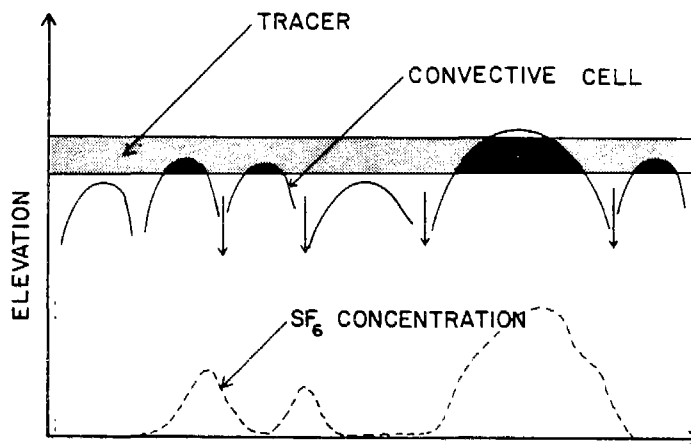


FIG. 3. Intermittent entrainment of tracer material by convective cells.

surface heating, parcels of warm air, displaced by mechanical turbulence, rise all the way through the mixed layer and impinge at the inversion base. To compensate for these vertical motions, zones of sinking air fill the spaces between rising air parcels. Close to the top of the mixed layer the net flux is directed downward. Adiabatic transport of air through the capping inversion would produce the negative flux, which in turn suggests a mechanism for substantial entrainment of air and tracer material into the mixed layer from above (Ball, 1960; Kaimal *et al.*, 1976; Deardorff *et al.*, 1980). The regions of upward flux are obviously thermals which originate near the surface shear layer and the transport is thus occurring over a scale  $Z_i$ .

The updraft regions in the thermals resembles the three-dimensional convection patterns observed by Frisch *et al.* (1975) with dual-Doppler radar. Kaimal *et al.* (1976) suggested that the rising air spreads out laterally as it reaches the inversion base, producing a domelike depression at the interface, and returns as a downdraft along the "side wall" of the thermal. These structures can be observed with acoustic sounders and radars. Arnold *et al.* (1975) found that domelike structures are collocated with the thermals detected simultaneously by an acoustic sounder. The strong returns from the side walls indicate the presence of entrained air from the inversion. The inverted U structures in the vertical section and the doughnut-shaped patterns in plan views observed by Hardy and Ottersten (1969), Konrad (1970), Arnold and Rowland (1976) and Agee and Chen (1973) in radar returns indicate the presence of convective cells.

Arnold and Rowland (1976) conclude that most of the entrainment takes place along the top of the dome. Here either the Kelvin-Helmholtz instability

or wavelike overturning of the dome structures could provide the mechanism for entrainment. This process is illustrated in Fig. 3 where the tops of the convective cells can rise to the elevation of the  $SF_6$ . Entrainment of this material and its subsequent transport to the surface lead to the large concentration increases. Areas of low concentration would then result when the ship went beyond the bounds of the cloud or when the convective cells did not reach the height of the tracer. A detailed examination of the mechanism of entrainment and mixed-layer growth is beyond the scope of this work and for details the reader is referred to Stull (1973), Venkatram (1976), Zeman and Tennekes (1977), Heidt (1977) and Deardorff (1978). Convective entrainment has been studied in the laboratory by Willis and Deardorff (1976a), Manins (1977) and Deardorff *et al.* (1980). The characteristic separation distance of the thermals given by Kaimal *et al.* (1976) is  $1.3-1.4Z_i$ , with the diameter-to-depth ratio for the Rayleigh cells being of the order of 40:1 (Agee and Chen, 1973).

With this background it is now possible to advance an explanation of the findings from the tracer experiments. When the cool stable air from the land encounters the warmer ocean surface, convective mixing begins to erode the overlying stable layer forming an internal boundary layer (Fig. 4). (The growth of this layer as a function of distance from the shore can be seen in the acoustic sounder traces.) Convective mixing in the surface layer entrains air from the stable layer aloft causing the inversion base to rise from the surface. Heating of the mixed layer is due to the combined effects of an upward heat flux from the ocean and a downward flux from the warmer air in the inversion. Continued growth of the mixed layer ultimately leads to a situa-

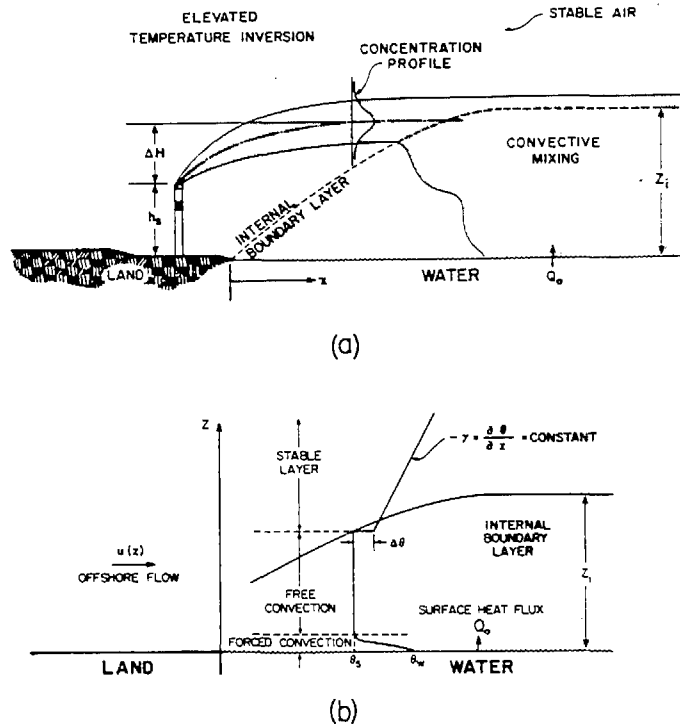


FIG. 4. Schematic representation of (a) fumigation process and (b) notation for mixing model.

tion where the internal boundary layer intercepts the elevated plume and the tracer materials. Since below the inversion base the mixing is rapid, the entrained SF<sub>6</sub> is quickly transported to the surface. Except for the strength of the convective mixing, the conditions of the experiment are similar to those that occur over the land during the day. Subsequent sections of this work are devoted to an estimate of the rate at which the tracer material is transported to the surface.

4. Mixing times under convective conditions

Under convective conditions a variety of interacting processes are involved in the mixing within the boundary layer. The relative role of buoyancy  $w'T_v'$ , in comparison with the transfer of energy from the mean motion  $u'w'\partial u/\partial z$ , can be expressed in terms of the flux Richardson number  $R_f$  (Monin and Yaglom, 1971; Kraus, 1972), as

$$R_f = \frac{\frac{g}{T} \overline{T_v'w'}}{\overline{u'w'} \frac{\partial \bar{u}}{\partial z}}, \tag{1}$$

where  $T_v$  is the virtual temperature. A more commonly used expression is the gradient Richardson number  $Ri$

$$Ri = \frac{g \left( \frac{\partial \bar{T}_v}{\partial z} + \Gamma \right)}{T_v \left( \frac{\partial \bar{u}}{\partial z} \right)^2} = \frac{g}{\theta_v} \frac{\frac{\partial \bar{\theta}_v}{\partial z}}{\left( \frac{\partial \bar{u}}{\partial z} \right)^2} = \frac{N^2}{\left( \frac{\partial \bar{u}}{\partial z} \right)^2}, \tag{2}$$

where  $N$  is the Brunt-Väisälä frequency,  $\theta_v$  the potential temperature, and  $\Gamma$  the adiabatic lapse rate. The relationship between  $R_f$  and the more easily measured Richardson number  $Ri$  is simply  $R_f = \alpha Ri$ , where  $\alpha$  is the ratio of the turbulent eddy diffusion coefficients for heat and momentum. Under a spatial homogeneity assumption temporal changes in the total mean kinetic energy are negligible if synoptic and mesoscale forces driving the boundary layer vary slowly (Caughy *et al.*, 1978). In particular, if the time scales for the large-scale processes are long compared to the time required for the boundary layer to adjust then the rate of change of turbulent kinetic energy per unit mass is negligible. If the contribution from the flux divergence term in the energy equation is small,

TABLE 2. Additional data and calculated results for period 19-26 July 1977.\*

Date	Time (PDT)	$u$ (m s <sup>-1</sup> )	$\theta$ (K)	$Z/L$	$u_*$ (m s <sup>-1</sup> )	$T_*$ (K)	$Z_i$ (m)	$w_*$ (m s <sup>-1</sup> )	$\lambda$ (min)
19	0000	1.5	283	-4.840	0.060	-0.117	280	0.436	11
19	0020	1.0	308	-8.206	0.044	-0.104	330	0.397	14
19	0100	0.5	317	-18.190	0.025	-0.075	320	0.296	18
19	0140	0.3	11	-29.206	0.014	-0.035	190	0.166	19
19	1620	3.1	294	-1.125	0.112	-0.077	470	0.585	13
19	1650	3.9	272	-0.754	0.142	-0.085	500	0.663	13
19	1710	3.6	275	-0.929	0.132	-0.093	490	0.659	12
19	1730	3.7	285	-0.889	0.136	-0.096	480	0.665	12
19	2000	4.4	277	-0.216	0.156	-0.023	500	0.477	17
19	2040	3.0	280	-1.134	0.108	-0.082	540	0.597	15
19	2120	1.5	5	-4.174	0.060	-0.092	590	0.525	19
19	2140	1.5	318	-4.291	0.060	-0.096	600	0.534	19
20	0700	3.6	285	-0.542	0.129	-0.051	160	0.369	7
20	0740	2.5	260	-1.433	0.089	-0.068	230	0.400	10
20	0900	1.5	250	-2.852	0.058	-0.053	160	0.290	9
20	0920	1.5	250	-2.502	0.058	-0.044	180	0.286	10
20	1240	2.0	195	-1.645	0.071	-0.036	360	0.385	16
20	1300	1.8	206	-1.459	0.064	-0.020	360	0.332	18
20	1320	2.0	220	-0.773	0.069	-0.013	280	0.264	18
20	1800	7.2	186	0.045	0.259	0.036	80		
20	1900	6.2	275	0.079	0.213	0.042	140		
20	1920	7.2	250	0.058	0.257	0.041	160		
20	1940	7.2	270	-0.004	0.267	0.013	260	0.069	
20	2000	5.7	270	-0.024	0.203	0.007	280	0.228	20
20	2020	5.1	270	-0.056	0.183	-0.001	240	0.273	15
20	2040	3.6	280	-0.158	0.123	-0.005	200	0.248	13
20	2120	3.6	270	-0.150	0.123	-0.005	240	0.258	15
20	2140	3.5	260	-0.186	0.120	-0.009	240	0.272	15
20	2220	2.0	280	-1.606	0.071	-0.048	340	0.378	15
20	2230	2.0	290	-0.931	0.069	-0.023	340	0.305	19
20	2300	2.3	302	-0.356	0.080	-0.030	300	0.328	15
21	0000	2.6	255	-0.470	0.087	-0.020	280	0.288	16
21	0040	2.6	259	-0.441	0.087	-0.019	310	0.290	18
21	0100	1.8	305	-0.876	0.063	-0.019	200	0.227	15
21	0120	1.0	141	-1.656	0.039	-0.014	270	0.193	23
21	0405	3.1	85	-0.595	0.108	-0.048	240	0.370	11
21	0425	2.5	125	-1.106	0.088	-0.058	320	0.406	13
21	0445	2.6	142	-0.994	0.090	-0.054	380	0.425	15
21	0505	2.1	125	-1.443	0.073	-0.049	360	0.380	16
21	0545	1.5	160	-1.497	0.056	-0.025	455	0.319	24
21	0605	0.2	160	-43.572	0.012	-0.031	460	0.213	36
21	0645	1.0	100	-3.625	0.040	-0.030	480	0.310	26
21	0705	1.5	100	-1.691	0.055	-0.026	460	0.326	23
21	0845	3.1	95	-0.583	0.108	-0.040	475	0.457	17
21	0905	2.1	91	-1.158	0.072	-0.032	430	0.368	19
21	0945	1.0	129	-4.270	0.041	-0.040	360	0.310	19
21	1005	1.5	135	-1.164	0.055	-0.014	310	0.252	21
21	1025	0.2	200	-39.449	0.012	-0.024	300	0.176	28
21	1045	0.8	235	-3.474	0.033	-0.015	280	0.212	22
21	1105	3.6	270	-0.035	0.120	0.006	260	0.143	30
21	1305	7.2	258	0.006	0.264	0.012	180		
21	1325	7.0	260	0.000	0.256	0.009	210		
21	1345	6.5	280	-0.003	0.237	0.008	200	0.079	42
21	1405	6.7	285	-0.020	0.246	0.000	200	0.244	14
21	1505	6.5	280	-0.045	0.240	-0.007	200	0.318	10
21	1620	7.0	260	-0.021	0.260	0.003	200	0.258	13
21	1720	5.5	270	-0.058	0.198	-0.003	120	0.239	8
21	1945	4.0	250	-0.397	0.144	-0.038	250	0.428	10
21	2030	2.5	225	-1.328	0.089	-0.059	150	0.336	7
21	2110	1.0	220	-5.585	0.042	-0.053	300	0.325	15
21	2130	1.5	220	-2.618	0.056	-0.043	310	0.341	15
22	0550	2.0	130	-0.209	0.065	0.000	205	0.143	24
22	0610	1.5	130	-0.550	0.053	-0.006	220	0.169	22
22	0710	0.2	140	-35.247	0.012	-0.030	240	0.157	26

TABLE 2. (Continued)

Date	Time (PDT)	$u$ (m s <sup>-1</sup> )	$\theta$ (K)	$Z_i/L$	$u_*$ (m s <sup>-1</sup> )	$T_*$ (K)	$Z_i$ (m)	$w_*$ (m s <sup>-1</sup> )	$\lambda$ (min)
22	0730	0.2	120	-29.493	0.012	-0.024	240	0.144	28
22	0750	0.2	140	-32.846	0.012	-0.028	240	0.152	26
22	0810	0.2	150	-21.592	0.011	-0.015	245	0.126	33
22	0830	2.1	180	-0.631	0.070	-0.018	230	0.238	16
22	0910	1.0	307	-2.365	0.040	-0.024	210	0.205	17
22	0930	0.5	270	-6.285	0.023	-0.020	220	0.165	22
22	1010	2.6	260	-0.763	0.089	-0.040	240	0.330	12
22	1030	2.0	250	-1.369	0.071	-0.045	260	0.326	13
22	1050	0.5	305	-10.055	0.024	-0.033	260	0.213	20
23	1440	2.5	250	1.332	0.050	0.031	280		
23	1505	3.9	215	0.285	0.114	0.039	310		
23	1645	4.6	275	-0.086	0.163	0.001	320	0.307	17
23	1725	4.9	262	-0.011	0.170	0.012	355	0.112	
23	1745	2.1	244	-0.268	0.068	0.004	350	0.188	31
23	2340	1.7	260	1.943	0.029	0.017	500		
24	0040	2.1	281	0.527	0.052	0.017	155		
24	0100	1.8	270	0.776	0.043	0.017	120		
24	0120	1.5	236	0.767	0.037	0.014	170		
24	0240	1.7	140	0.381	0.046	0.016	120		
24	0300	1.5	136	0.455	0.041	0.016	160		
24	0420	1.0	210	0.044	0.032	0.011	140		
24	1000	1.0	269	-0.091	0.034	0.021	165		
25	2220	5.0	270	0.340	0.150	0.068	160		
25	2320	5.0	280	0.231	0.157	0.054	160		
26	0420	1.4	340	3.147	0.019	0.012	90		

\* Source: Schacher *et al.* (1980).

then, with the above assumptions, the turbulent kinetic energy equation reduces to

$$-u'w' \frac{\partial \bar{u}}{\partial z} (1 - R_f) - \epsilon = 0, \quad (3)$$

where  $\epsilon$  is the dissipation or the rate of conversion of kinetic into internal energy by the viscous forces in the smallest eddies. Since  $\epsilon > 0$  and  $-u'w' \partial \bar{u} / \partial z$  is practically always greater than zero, stationary, undamped turbulence is possible only if  $R_f < 1$ . This result is often used as an approximate criterion for defining the transition to turbulence in a stratified medium. For the purpose of analyzing the experimental results within this framework it is useful to identify the appropriate length and velocity scales. A key scaling parameter is the Monin-Obukhov length  $L$  defined by

$$\frac{1}{L} = - \frac{kgQ_0}{u_*^3 T} = - \frac{kg}{u_*^2 T} \left( Q + 0.61 \frac{TM_0}{\rho} \right) = \frac{1}{L_T} + \frac{1}{L_q}, \quad (4)$$

where  $Q_0 = (\overline{T_v'w'})_0$  is the virtual surface heat flux that accounts for the influence of humidity fluctuations on buoyancy,  $k$  the von Kármán constant,  $u_*^2 = -\overline{u'w'}$  the friction velocity, and  $L_T$

and  $L_q$  are the Monin-Obukhov lengths calculated from the surface heat and evaporative fluxes. Physically,  $L$  is the height at which the two production terms are approximately of equal magnitude. One of the major differences in examining conditions over the ocean or other large bodies of water is that the density stratification is controlled not only by the surface heat flux but also by the water vapor flux. The measurements made by McBean and MacPherson (1975) over Lake Ontario indicate that there can be a significant difference between  $L_q$  and  $L_T$ , that in turn have a major influence on  $L$ .

Above the surface layer a more appropriate length scale for the eddies is the mixed layer depth  $Z_i$ . While there is some controversy associated with a formal definition of  $Z_i$ , in this work it is defined as the elevation of the lowest inversion base. The studies of Deardorff (1972) and Deardorff *et al.* (1980) indicate that this is an appropriate boundary layer height for momentum and heat. Under convective conditions the appropriate velocity scale, above the surface layer, is given by

$$w_* = \left( \frac{g}{T} Z_i Q_0 \right)^{1/3} = \left[ \frac{g}{T} Z_i (\overline{w'T_v'})_0 \right]^{1/3} = \left( - \frac{1}{k} \frac{Z_i}{L} \right)^{1/3} u_* \quad (5)$$

The characteristic time scale under convective conditions is then given by  $\lambda = Z_i/w_*$ . Willis and Deardorff (1976b) have shown that material released instantaneously at the surface becomes nearly well mixed within a travel time of  $\sim 3\lambda$ . In the field experiment the tracer material was "released" at the top of the mixed layer. Apart from the small contribution due to mechanical mixing the characteristic mixing time can be expected to be similar to that for a surface release. The reason for this is that the effective aerodynamic roughness of the ocean is very small.

There are a variety of means of estimating the fluxes needed to evaluate the above expressions. Three of the more common techniques are 1) the profile or gradient method, 2) the variance budget or dissipation technique, 3) and bulk aerodynamic calculations using air-sea differences. Schacher *et al.* (1978, 1980) employed the latter approach in reducing the meteorological data from the field experiment. A detailed discussion of these and other procedures is presented in Busch (1977). The key results from Schacher *et al.* (1978, 1980) are summarized in Table 2. In particular the frequency distribution of convective mixing times observed during the period 19-23 July is shown in Fig. 5 together with a similar distribution for daytime conditions over the land. The characteristic mixing times for both experiments were very similar. The influence of a much larger surface heat flux during the day is readily apparent.

In the surface layer, the velocity distribution can be expressed in terms of Monin-Obukhov similarity theory as

$$\frac{\partial \bar{u}}{\partial z} = \frac{u_*}{kz} \phi_m \left( \frac{z}{L} \right), \quad (6)$$

where  $\phi_m$  is an experimentally determined function that corrects for the effects of buoyancy on turbulence. Businger *et al.* (1971) have constructed expressions for momentum  $\phi_m$  and heat  $\phi_h$  from an analysis of field data. For unstable conditions  $z/L < 0$  the formulas are given by

$$\phi_m \left( \frac{z}{L} \right) = \left[ 1 - 15 \left( \frac{z}{L} \right) \right]^{-1/4}, \quad (7)$$

$$\phi_h^2 \left( \frac{z}{L} \right) = \phi_m \left( \frac{z}{L} \right). \quad (8)$$

These results, together with (3), the definition of  $u_*$  and the relation  $Ri = \alpha R_f$ , can be combined to give

$$u_*^3 = \frac{kz}{(1 - \alpha Ri) \phi_m \left( \frac{z}{L} \right)}. \quad (9)$$

The characteristic mixing time  $\tau_m$  can be defined

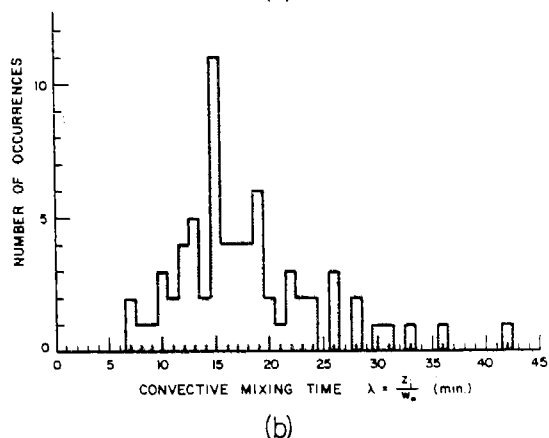
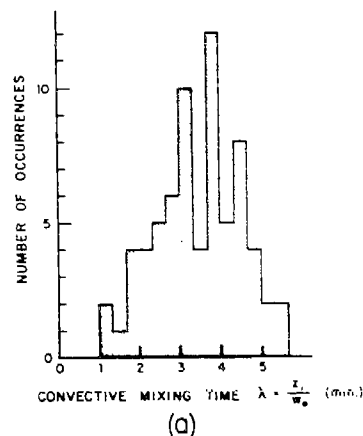


FIG. 5. Distribution of convective mixing times for (a) daytime conditions over land (source: Smith *et al.*, 1976) and (b) nighttime conditions over ocean.

in terms of the convective time scale  $\lambda$  as  $\tau_m = 3\lambda = 3Z_i/w_*$ . Using (5), and the expression  $\phi_m Ri = z/L$ , Eq. (9) can be manipulated to give an estimate of the mixing time in terms of the measured dissipation rate and gradient Richardson number  $Ri$ :

$$\tau_m = 3 \left[ \frac{Z_i^2}{\epsilon} \left( 1 - \frac{1}{\alpha Ri} \right) \right]^{1/3}. \quad (10)$$

For near-neutral conditions, Businger *et al.* (1971) determined that  $\alpha = 1.35$ ; thus a simple upper bound on (10) is  $\tau_m \approx 3[-Z_i^2/\epsilon Ri]^{1/3}$ . For unstable conditions when  $|Ri| \gg 1$ , a lower bound is given by  $\phi_m = 3[Z_i^2/\epsilon]^{1/3}$ . Using the data tabulated in Appendix B of Schacher *et al.* (1978) the limits on the convective mixing times can be calculated and are shown in Table 3 for the experiment conducted on 22 July. The important result from the tracer experiments is that the calculated mixing rates using

TABLE 3. Convective mixing times based on turbulence intensities for 22 July 1977.

Date	Time (PDT)	$Z_i/L$	$u_*$ (m s <sup>-1</sup> )	$Z_i$ (m)	Ri	$\epsilon$ (10 <sup>-4</sup> m s <sup>-3</sup> )	$\left[\frac{Z_i^2}{\epsilon}\right]^{1/3}$ (min)	$\left[-\frac{Z_i^2}{\epsilon Ri}\right]^{1/3}$ (min)
22	0550	-0.209	0.065	205	-0.04	1.8	10	30
22	0610	-0.550	0.053	220	-0.09	3.6	8	19
22	0710	-35.247	0.012	240	-0.16	3.6	9	17
22	0730	-29.493	0.012	240	-0.08	4.0	9	20
22	0750	-32.846	0.012	240	-0.18	2.9	10	17
22	0810	-21.592	0.011	245	-0.21	5.1	8	14
22	0830	-0.631	0.070	230	-0.10	4.6	8	17
22	0910	-2.365	0.040	210	-0.02	7.1	7	24
22	0930	-6.285	0.023	220	-0.03	7.3	7	22

either the bulk or dissipation methods produces results consistent with the observed fumigation times. The rapid concentration increases were measured during times when the ship was beneath the plume and the mixed layer height exceeded 200 m.

### 5. Eddy diffusion coefficients

A basic problem with modeling convectively driven flows is that the turbulent mixing is no longer described by local concentration gradients. Nevertheless, there are some circumstances in which it is desirable to parameterize the diffusive fluxes by a

$K$ -theory model. The objective of this section is to present a simple formulation that produces transport times consistent with observed fumigation rates. Some recent work by Crane *et al.* (1977) and McRae *et al.* (1981) indicates that vertical eddy diffusivity profiles for unstable conditions can be scaled by a single profile of the form

$$K_{zz} = w_* Z_i f\left(\frac{z}{Z_i}\right). \quad (11)$$

Lamb *et al.* (1975) derived an expression for  $f$  using the numerical turbulence model of Deardorff (1970). The profile adopted by McRae *et al.* (1981) is given by

$$\frac{K_{zz}}{w_* Z_i} = \begin{cases} 2.5 \left(\frac{kz}{Z_i}\right)^{4/3} \left[1 - 15 \left(\frac{z}{L}\right)\right]^{1/4}, & 0 < \frac{z}{Z_i} \leq 0.05 \\ 0.021 + 0.408 \left(\frac{z}{Z_i}\right) + 1.352 \left(\frac{z}{Z_i}\right)^2 - 4.096 \left(\frac{z}{Z_i}\right)^3 + 2.560 \left(\frac{z}{Z_i}\right)^4, & 0.05 < \frac{z}{Z_i} \leq 0.6 \\ 0.2 \exp\left[6 - 10 \left(\frac{z}{Z_i}\right)\right], & 0.6 < \frac{z}{Z_i} \leq 1.1 \\ 0.0013, & \frac{z}{Z_i} > 1.1. \end{cases} \quad (12)$$

As can be seen from Fig. 6 the maximum value of the diffusivity occurs when  $z/Z_i \approx 0.5$  and has a magnitude  $\sim 0.21 w_* Z_i$ . For typical conditions this corresponds to a diffusion time, defined by  $Z_i^2/K_{zz}$ , of  $\sim 5Z_i/w_*$  that is quite consistent with the bounds shown in Tables 2 and 3.

### 6. Conclusions

There are a number of important findings from the tracer study that are of direct relevance to air pollution studies, first of which is that close to the shoreline different stabilities can exist above the land and water surfaces. Under these conditions atmospheric stability cannot be easily determined in terms of conventional classifications. A second finding is that the

presence of convective activity can cause down-mixing or fumigation of material that can return the next day as a significant increment to the onshore ground-level concentration. The process by which this occurs is as follows. During the night, cool stable air is advected out over the ocean. When this air encounters the warmer ocean surface convective mixing begins to erode the stable layer. Once the internal boundary layer has grown to the height of the plume the tracer material, entrained at the top of the mixed layer, is rapidly fumigated to the surface. The characteristic mixing time, inferred from the concentration records, is consistent with an estimate based on the convective time scale  $\lambda = Z_i/w_*$  that, for the conditions of the experiment, was  $\sim 20$  min.

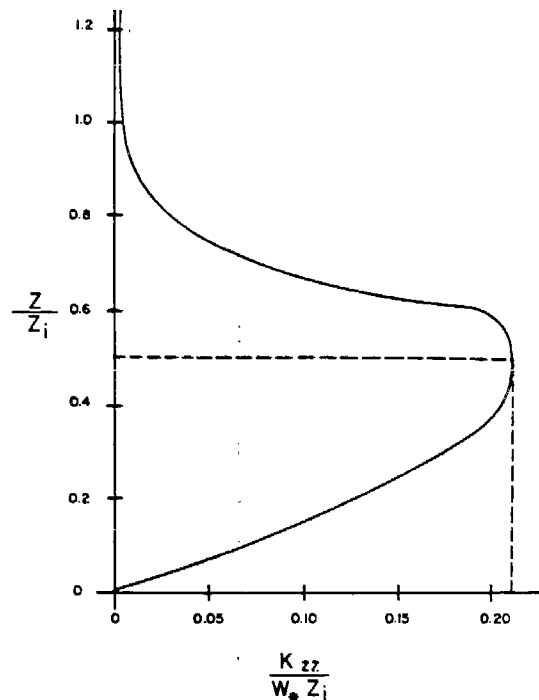


FIG. 6. Vertical turbulent diffusivity profile for unstable conditions (source, McRae *et al.*, 1981).

Understanding of these mixing processes and convective activity over the ocean will improve the ability to predict atmospheric dispersion in coastline environments.

*Acknowledgments.* This work was supported by the California Air Resources Board under contracts A5-187-30, A5-046-87 and A7-187-30. The assistance of Gordon Schacher of the Naval Postgraduate School, who supplied descriptions of data reduction procedures and measurement equipment, and Charles Bennett of the California Air Resources Board is appreciated.

#### REFERENCES

- Agee, E. M., and T. S. Chen, 1973: A model for investigating eddy viscosity effects on mesoscale convection. *J. Atmos. Sci.*, **30**, 180-189.
- Arnold, A., and J. R. Rowland, 1976: Fine scale observation of free convection in the atmospheric boundary layer. *Preprints Third Symp. Atmospheric Turbulence Diffusion and Air Quality*, Raleigh, Amer. Meteor. Soc., 1-8.
- , T. G. Konrad, J. H. Richter, D. R. Jensen and V. R. Noonkester, 1975: Simultaneous observation of clear air convection by a pulse radar, an FM-CW radar, an acoustic sounder and an instrumented aircraft. *Preprints 16th Radar Meteorology Conf.*, Houston, Amer. Meteor. Soc., 290-295.
- Bali, F. K., 1960: Control of inversion height by surface heating. *Quart. J. Roy. Meteor. Soc.*, **86**, 483-494.
- Briggs, G. A., 1969: *Plume Rise*. Atomic Energy Commission Review Series, 81 pp. [NTIS TID-25075].
- , 1975: Plume rise predictions. *Lectures on Air Pollution and Environmental Impact Analysis*, D. A. Haugen, Ed. Amer. Meteor. Soc., 59-111.
- Busch, N. E., 1977: Fluxes in the surface boundary layers over the sea. *Proceedings of a NATO Advanced Study Institute. Urbino, Italy. (1975)*, Pergamon Press, 72-91.
- Businger, J. A., 1975: Interactions of sea and atmosphere. *Rev. Geophys. Space Phys.*, **13**, 720-726, 817-822.
- , J. C. Wyngaard, Y. Izumi and E. F. Bradley, 1971: Flux-profile relationship in the atmospheric surface layer. *J. Atmos. Sci.*, **28**, 181-189.
- Caughey, S. J., B. A. Crease, D. N. Asmakopoulos and R. S. Cole, 1978: Quantitative bistatic acoustic sounding of atmospheric boundary layer. *Quart. J. Roy. Meteor. Soc.*, **104**, 147-161.
- Crane, G., H. A. Panofsky and O. Zeman, 1977: A model for dispersion from area sources in convective turbulence. *Atmos. Environ.*, **11**, 893-900.
- Deardorff, J. W., 1970: A three-dimensional numerical investigation of the idealized planetary boundary layer. *Geophys. Fluid Dyn.*, **1**, 377-410.
- , 1972: Numerical investigation of neutral and unstable planetary boundary layers. *J. Atmos. Sci.*, **29**, 91-115.
- , 1978: Prediction of convective mixed-layer entrainment for realistic capping inversion structure. *J. Atmos. Sci.*, **36**, 424-436.
- , G. E. Willis and B. H. Stockton, 1980: Laboratory studies of the entrainment zone of a convectively mixed layer. *J. Fluid Mech.*, **100**, 41-64.
- Dietz, R. N., and E. A. Coté, 1973: Tracing atmospheric pollutants by gas chromatographic determination of sulfur hexafluoride. *Environ. Sci. Tech.*, **7**, 338-342.
- Drivas, P. J., and F. H. Shair, 1974: A tracer study of pollutant transport and dispersion in the Los Angeles area. *Atmos. Environ.*, **8**, 1155-1163.
- Frisch, A. S., R. B. Chadwick, W. R. Moninger and J. M. Young, 1975: Observation of boundary layer convection cells measured by dual-Doppler radar and echosounder and by microbarograph array. *Bound.-Layer Meteor.*, **3**, 199-226.
- Hardy, K. R., and H. Ottersten, 1969: Radar investigation of convective patterns in the clear atmosphere. *J. Atmos. Sci.*, **26**, 666-672.
- Heidt, F. D., 1977: The growth of the mixed layer in a stratified fluid due to penetrative convection. *Bound.-Layer Meteor.*, **12**, 439-461.
- Houlihan, T. M., K. L. Davidson, C. W. Fairall and G. E. Schacher, 1978: Experimental aspects of a shipboard system used in investigation of overwater turbulence and profile relationships. Naval Postgraduate School Rep. No. NPS61-78-001, 254 pp.
- Kaimal, J. C., J. C. Wyngaard, D. A. Haugen, O. H. Coté and Y. Izumi, 1976: Turbulence structure in the convective boundary layer. *J. Atmos. Sci.*, **33**, 2152-2169.
- Kraus, E. B., 1972: *Atmosphere-Ocean Interaction*. Clarendon Press, 275 pp.
- Konrad, T. G., 1970: The dynamics of the convective process in clear air as seen by radar. *J. Atmos. Sci.*, **27**, 1138-1147.
- Lamb, B. K., A. Lorenzen and F. H. Shair, 1978a: Atmospheric dispersion within coastal regions—Part I. Tracer study of power plant emissions from the Oxnard Plain. *Atmos. Environ.*, **12**, 2089-2100.
- , F. H. Shair and T. B. Smith, 1978b: Atmospheric dispersion within coastal regions—Part II. Tracer study of industrial emissions in the California Delta region. *Atmos. Environ.*, **12**, 2101-2118.
- Lamb, R. G., H. W. Chen and J. H. Seinfeld, 1975: Numerico-empirical analysis of atmospheric diffusion theories. *J. Atmos. Sci.*, **32**, 1754-1807.

- Lyons, W. A., 1975: Turbulent diffusion and pollutant transport in shoreline environments. *Lectures on Air Pollution and Environmental Impact Analysis*, D. A. Haugen, Ed., Amer. Meteor. Soc., 59-111.
- Manins, P. C., 1977: Fumigation and a laboratory experiment. *Weather*, June, 221-228.
- McBean, G. A., and J. I. MacPherson, 1975: Turbulence above Lake Ontario: velocity and scalar statistics. *Bound.-Layer Meteor.*, **10**, 181-197.
- McRae, G. J., W. R. Goodin and J. H. Seinfeld, 1981: Development of a second generation mathematical model for urban air pollution: I Model formulation. *Atmos. Environ.*, (in press).
- Misra, P. K., 1980: Dispersion from tall stacks into a shore line environment. *Atmos. Environ.*, **14**, 397-400.
- Monin, A. S., and A. M. Yaglom, 1971: *Statistical Fluid Mechanics: Mechanics of Turbulence*, Vol. I. MIT Press, 769 pp.
- Orgill, M. M., 1981: Atmospheric studies in complex terrain: A planning guide for future studies. Rep. PNL-3656, Pacific Northwest Laboratories, Richland, WA, U.S. Department of Energy Contract DE-AC06-76RLO 1830.
- Raynor, G. S., P. Michael and S. SethuRaman, 1980: Meteorological measurement methods and diffusion models for use at coastal nuclear reactor sites. *Nuclear Safety*, **21**, 749-765.
- Schacher, G. E., K. L. Davidson and C. W. Fairall, 1980: Atmospheric marine boundary layer mixing rates in the California coastal region. Naval Postgraduate School Rep. No. NPS61-80-003, 115 pp.
- , C. W. Fairall, K. L. Davidson and T. M. Houlihan, 1978: Experimental investigation of the marine boundary layer in support of air pollution studies in the Los Angeles air basin. Naval Postgraduate School Rep. No. NPS61-78-002, 257 pp.
- Schatzmann, M., 1979: An integral model of plume rise. *Atmos. Environ.*, **13**, 721-731.
- Shair, F. H., E. Sasaki, D. Carlan, G. R. Cass, W. R. Goodin, J. Edinger and G. E. Schacher, 1981: Transport and dispersion of airborne pollutants associated with the land breeze-sea breeze system. *Atmos. Environ.* (in press).
- Simmonds, P. G., G. R. Shoemaker, J. E. Lovelock and H. C. Lord, 1972: Improvements in the determination of sulfur hexafluoride for use as a meteorological tracer. *Anal. Chem.*, **44**, 860-863.
- Smith, T. B., S. L. Marsh, W. H. White, T. N. Jerskey, R. G. Lamb, P. A. Durbin and J. P. Killus, 1976: Analysis of the data from the three-dimensional gradient study. Final Report to the California Air Resources Board under Contracts ARB-4-051 and ARB-4-250, Meteorology Research, Inc., Pasadena, and Systems Applications, Inc., San Rafael, 124 pp.
- Stull, R. B., 1973: Inversion rise model based on penetration convection. *J. Atmos. Sci.*, **30**, 1092-1099.
- Venkatram, A., 1976: Internal boundary layer development and fumigation. *Atmos. Environ.*, **11**, 479-482.
- Willis, G. E., and J. W. Deardorff, 1976a: Visual observations of horizontal planforms of penetration convection. *Preprints Third Symp. Atmospheric Turbulence Diffusion and Air Quality*, Raleigh, Amer. Meteor. Soc., 1-8.
- , and —, 1976b: A laboratory model of diffusion into the convective planetary boundary layer. *Quart. J. Roy. Meteor. Soc.*, **102**, 427-445.
- Zeman, O., and H. Tennekes, 1977: Parameterization of the turbulent energy budget at the top of the daytime atmospheric boundary layer. *J. Atmos. Sci.*, **34**, 111-123.